Electromechanical Drivetrain Simulation.

Gallego Calderon, Juan Felipe

Publication date:
2015

Document Version
Publisher's PDF, also known as Version of record

Electromechanical drivetrain simulation

PhD Thesis

Juan F. Gallego Calderon
DTU Wind Energy PhD-051 (EN)
July 2015

DTU Wind Energy
Department of Wind Energy

Electromechanical drivetrain simulation

Juan F. Gallego-Calderon

DTU Wind Energy
Technical University of Denmark
July 2015

DTU Wind Energy
Department of Wind Energy

Author: Juan F. Gallego-Calderon
Title: Electromechanical Drivetrain Simulation

Department: DTU Wind Energy

This thesis was submitted in partial fulfillment of the requirements for obtaining the PhD degree at the Technical University of Denmark (DTU).
The PhD project was carried out between the years 2012-2015 at the Wind Turbines Section (VIM) of DTU Wind Energy, Department of Wind Energy. The dissertation was submitted in March 2015, and successfully defended on July 6th, 2015.

Main Supervisor:
Anand Natarajan, DTU Wind Energy
Co-Supervisor:
Kim Branner, DTU Wind Energy
Co-Supervisor:
Nicolaos A. Cutululis, DTU Wind Energy
Co-Supervisor:
John M. Hansen, DTU Mechanical Engineering

Thesis Examiners
Dorte Juul Jensen, DTU Wind Energy
Carlo L. Bottasso, Technical University of Munich
Eduard Muljadi, NREL

DTU Wind Energy PhD-0051(en)
July 2015

ISBN:
978-87-93278-42-4

Sponsorships:
Strategic Research Center *REWIND - Knowledge based engineering for improved reliability of critical wind turbine components*, Danish Research Council for Strategic Research, grant no. 10-093966

pages: 185
tables: 41
figures: 109
references: 110

Technical University of Denmark
DTU Wind Energy
Risø Campus
Frederiksborgvej 399
Building 115
DK-4000 Roskilde
jugc@dtu.dk
www.vindenergi.dk

Abstract

Wind turbines structures are exposed to inclement loading conditions varying from the turbulent wind field to fluctuations in the electric grid. The variation of these conditions, in addition to special events such as emergency stops, has a great impact of the life time of the components. In multi-MW wind turbines, it is common to find a geared drivetrain, which is the interface between the mechanical and electrical domain. Due to the varying conditions, the drivetrain can suffer accelerated damage reducing the target 20 years life of the turbine.

This Ph.D. thesis focuses on the implementation of advanced models that consider the electromechanical interaction of the wind turbine structure, namely the main shaft and tower top, along with the gearbox and the generator. This is done with the purpose to advance the integrated analysis of wind turbines; something that is not common until recently. The state-of-the-art in wind turbine simulation is to consider the wind turbine structure with a simplified model of the drivetrain. Therefore, the main purpose of this Ph.D. is to develop a simulation tool capable of estimate the loading in the drivetrain internal components, with special attention to the planet bearings in the planetary stage. In brief, the tool is used for the dynamic analysis of the drive-train components under different loading conditions following certification guidelines.

Several numerical simulations demonstrate the capabilities of the tool, and new results show how the lifetime of the bearings are affected by different load cases. The fatigue damage experienced by the planet bearings in the planetary stage is assessed for the normal operation of the wind turbine, by computing the damage equivalent loads for a 20 years period. Several operational modes are identified as the main contributors to the fatigue of the bearings. Second, the ultimate design loads obtained by extreme events such as Low-Voltage Ride through (LVRT), emergency stop and normal stop due to grid loss are investigated. A method to simulate the LVRT based on the grid code requirements from different countries is presented, along with results that highlight the importance of the voltage recovery and its relation to the effect on the bearing loads. Several recommendations are made for the three extreme events in terms of possible load reduction in the bearings. The main goal is to minimize the long-term damage that can be induced by the extreme cases. And finally, reliability analysis using FORM is performed based on two different types of bearing configurations. For this purpose, a bearing stiffness matrix corresponding to each configuration is used in the electromechanical drivetrain simulation tool. Thus, using a parametric study with different dynamic rating

values, it is found that this parameter has an important influence in the reliability, and hence, in the preliminary design of the components. Furthermore, the difference between the damage equivalent loads of both types of bearings is minimal. Therefore, the dynamic rating parameter is found to have higher influence on the bearings reliability.

The methods presented in this dissertation can be used to model different drivetrain configurations for preliminary design, based on standard load cases used in wind turbine certification. In addition, it is possible to carry out reliability analysis, which ultimately, is one of the main focus areas when analyzing and designing such complex and cost-sensitive systems.

Resumé

Vindmøllers strukturelle komponenter udsættes for barske belastningsforhold hidrørende fra turbulens i vindfeltet og fluktuationer i el-nettet. Variationen i disse belastningsforhold, ud over særlige hændelser såsom nødstop, har en stor indflydelse på levetiden af komponenterne. I multi-MW-vindmøller, er det almindeligt at finde et gearet drivtog. Gearkassen er i grænsefladen mellem det mekaniske og elektriske domæne, og komponenterne kan opleve hurtig udvikling af skader, hvilket reducerer levetiden for vindmøllen til under de normalt forventede 20 år. Denne ph.d. afhandling fokuserer på udviklingen af avancerede modeller for den elektromekaniske vekselvirkning mellem vindmøllens struktur, nemlig hovedakse og tårn top samt gearkasse og generator. Dette gøres med det formål at fremme den integrerede analyse af vindmøller; noget der ikke har været almindelig indtil for nyligt. State-of-the-art i vindmølle simulering er at modellere vindmøllens struktur med en simpel model af drivtoget. Derfor er det vigtigste formål med denne ph.d. at udvikle et værktøj, der kan estimere belastninger for drivtogets interne komponenter, med særlig vægt på lejerne omkring planet gear. Kort fortalt anvendes værktøjet til dynamisk analyse af drivtog komponenter under forskellige last situationer specificeret i certificerings guidelines. Flere numeriske simuleringer viser mulighederne for værktøjet og nye resultater for effekten af forskellige last situationer på lejernes levetid er opnået. Først er udmattelse af planet gear lejer vurderet for den normale drift af vindmøllen ved at bruge ækvivalente laster for en 20 årig periode. Flere bidragsydere til udmattelse af lejerne er identificeret ud fra resultaterne. Dernæst er ultimative design belastninger fundet ved at analyserer ekstreme hændelser så som Low-Voltage Ride Through (LVRT), nødstop og normal stop ved tab af nettet. En metode til at simulere LVRT baseret på net-kode krav fra forskellige lande præsenteres sammen med resultater, som understreger betydningen af spændings stabilisering efter net-fejl og dennes relation til lejernes levetid. Flere anbefalinger beskrives i relation til de tre typer af hændelser, der muliggør reduktion af belastningerne på lejerne. Målet er at minimere de langsigtede skader, som kan opstå ved ekstreme hændelser. Endelig er pålidelighedsanalyse med FORM udført baseret på to forskellige leje design. Til dette formål beskrives hvert leje design med en stivhedsmatrix, som input til det elektromekaniske drivtog simulerings værktøj. Ved hjælp af et parameter studie med forskellige dynamisk rating værdier er det fundet at denne parameter har stor indflydelse på pålideligheden og dermed vigtig ved præliminær leje design. Forskellen mellem ækvivalente laster for de to leje design er minimal, så det er den dynamiske rating værdi der har størst indflydelse på lejernes pålidelighed. De

metoder der præsenteres i denne afhandling, kan udvides til forskellige drivtog konfigurationer i den indledende designfase, som baseres på de standard lasttilfælde der bruges i vindmølle-certificering. Desuden er det muligt at foretage pålidelighedsanalyse, som i sidste ende er et af de vigtigste fokusområder, når komplicerede og omkostningsfølsomme systemer analyseres.

Preface

"What you get by achieving your goals is not as important as what you become by achieving your goals."

– Henry David Thoreau

This thesis is submitted in partial fulfillment of the requirements for obtaining the degree of Doctor of Philosophy. The work was carried out at the Wind Turbine Structures section in the Department of Wind Energy at the Technical University of Denmark from March 2012 to March 2015. The Ph.D. project was supported by the Strategic Research Center "REWIND - Knowledge based engineering for improved reliability of critical wind turbine components", Danish Research Council for Strategic Research, grant no. 10-093966.

During the length of the Ph.D., I went through ups and downs that have helped me grow as a professional and as a person. However, this was not achieved on my own. Many, many, thanks to my wife Katie. With your infinite patience, love and devotion to maintain my sanity, you have made this journey truly awesome. Thanks to my family and friends back home for their constant support and encouragement. Thanks to my adventure buddies Carlo, Leo and Rogier for the amazing climbing outings and experiences in the outdoors. Those times were crucial to keep my internal peace, and to introduce me to a new lifestyle that I intend to maintain. Many thanks to my friends Susana and Maria for their continuous encouragement, advice, ham, tortillas de patatas, empanadillas and many laughs. Also, thanks to my office mates Philip and Alem for the nice conversations and laughs during our small coffee breaks.

I will like to express my immense gratitude to my main supervisor Anand, whose guidance help me direct the project in the right direction, in addition to fruitful discussions on load analysis. To my co-supervisors: Nikos for his constant support and discussions in electrical machines; to Kim, for giving me such a privilege to be a Ph.D. student at DTU Wind Energy; and to John for the initial help on understanding the theory of multibody dynamics, and for the initiation into the fascinating field of computational mechanics.

My research stay was carried out at the National Wind Technology Center from NREL in amazing Boulder, CO. Many thanks to Jon and Yi for allowing me to visit and work along your side, where I learned a lot about gearbox modeling and testing.

Juan Felipe Gallego Calderon
Roskilde, Denmark. July 2015

To Katie.

List of Acronyms

BRF Bending Rotating Fatigue. 46

CDF Cumulative Density Function. 100

CRB Cylindrical Roller Bearings. 18, 86, 132, 135–138

DEL Damage Equivalent Load. 99, 100

DFIG Double-Fed Induction Generator. 11, 13, 17, 32, 34, 43, 44, 91, 106, 108, 109, 114, 115, 128, 191, 192

DLC Design Load Case. 13, 14, 17, 18, 20, 30, 33, 34, 39, 99, 105, 107, 110–112, 114, 115, 117, 120, 122–124, 136

DOF Degrees of Freedom. 24, 27, 29, 30, 51, 53, 58, 63, 65, 67, 70, 73, 93, 94, 102, 106, 111, 147, 152, 154, 177, 183, 188, 191, 193

EOG Extreme Operating Gust. 111, 115

EOM Equations of Motion. 25, 26, 30, 34, 51, 52, 61, 67, 68, 70, 71, 83, 87, 91, 95, 101, 147–152, 180–182, 193

FAST Fatigue, Aerodynamics, Structures and turbulence code. 25, 26, 29, 30

fnCRB Full-Complement Cylindrical Roller Bearings. 86

FORM First-Order Reliability Method. 35, 133, 134, 139

FRT Fault Ride Through. 13, 14, 17, 32, 33, 106, 107, 109, 110, 120, 121

GRC Gearbox Reliability Collaborative. 13, 17, 27, 29, 34, 86, 87, 91

HAWC2 Horizontal axis Wind turbine simulation Code 2nd generation. 25, 26, 29, 49, 79, 82–84, 91, 93–98, 100, 101, 103, 105, 106, 114, 147, 148

HCF High Cycle Fatigue. 45, 46

HSS High-Speed Shaft. 29, 30, 37, 42, 70, 86, 112, 113, 117, 193

LCF Low Cycle Fatigue. 45, 46

LSS Low-Speed Shaft. 13, 25, 37, 70, 87, 88, 113, 193

LTI Linear Time Invariant. 27, 28, 70

LTV Linear Time Variant. 28

LVRT Low-Voltage Ride Through. 13, 14, 17, 20, 30, 33, 34, 94, 105, 106, 109, 110, 114, 115, 117–120, 122, 127, 128

NREL National Renewable Energy Laboratory. 17, 25–28, 34, 38, 48, 49, 84, 91, 95, 99, 112, 114

NTM Normal Turbulence Model. 136

NWTC National Wind Technology Center. 25

PMSG Permanent Magnet Synchronous Generator. 11, 12, 32, 43, 44, 79–81, 91, 95, 191, 195, 196

TRB Tapered Roller Bearings. 18, 86, 132, 135–138, 140

VHCF Very High Cyclic Fatigue. 46

WTDUDE Wind Turbine and Drivetrain Under Dynamic Excitation code. 95–97, 100, 101, 103

List of Figures

List of Tables

Contents

1

Introduction

"Begin at the beginning," the King said, gravely, "and go on till you come to an end; then stop."

– Lewis Carroll, *Alice in Wonderland*

1.1 Background

For the past decade, society has seen an increase on energy demand that is targeted to be met in a considerable amount by renewable resources. Different studies have investigated the advantages of using wind energy specially focusing on the cost to generate and transmit power [13], which indicates the large potential of wind energy within a context of clean energy supply. In addition, as society's energy demand increase, there is a need for more efficient, reliable and clean sources of energy. This means that, in the context of wind energy, the wind turbine industry and research institutions need to improve the designs of wind turbines for a more efficient and cost-effective capture of energy. To achieve such a goal, through out the last two decades society has witnessed an increase in size of the wind turbines (Figure 1-1), and bigger technical challenges that need to be addressed.

One of the biggest challenges today is to design reliable wind turbines, specially with the expansion on offshore wind farm development, where the repair and maintenance of a wind turbine is very costly due to the logistical constraints. Thus, the cost of energy tends to be increased due to turbine downtime, unplanned maintenance, replacement of equipment, etc.. Today, most of the downtime of wind turbines are accredited to the drivetrain (gearbox and generator), which is considered the most critical sub-system in terms of reliability [1, 14]. This is no surprise given the complexity of the system: in a multi-stage gearbox, a number of bearings support the operation of the torque and speed transfer to the generator, in addition to the mating gear teeth that are directly exposed to torque variations. A damaged component can generate an array of failures inside the drivetrain with costly and inconvenient consequences. Therefore, special attention must be given to the estimation of the internal loads in the gearbox and their interaction to

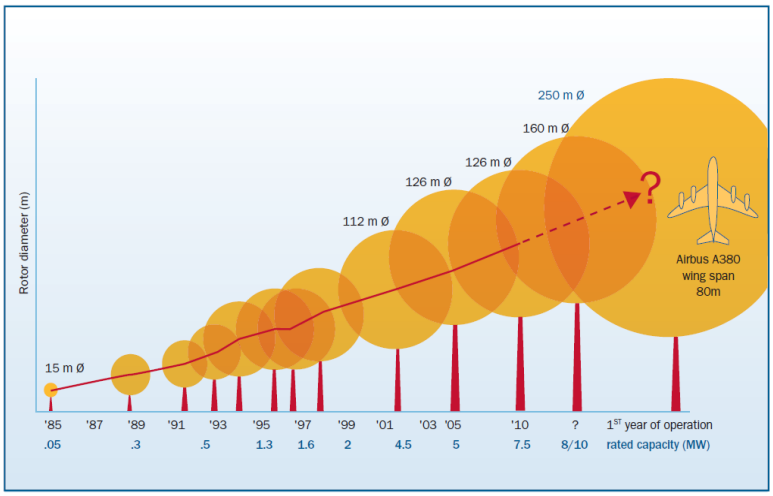

Figure 1-1: Wind turbine sizes throughout the years by Rated power and rotor diameter. It is clear that the trend on the construction of wind turbine is to increase the rotor size and capacity to meet the demand of energy with a larger participation of wind energy (reproduced from [1]).

the rest of the wind turbine under different loading conditions such as: wind turbulence, aerodynamics, controls, grid events and emergency stops. From this, it is clear that the drivetrain dynamics must be analysed in a context where all the components of the wind turbine are taken into account, to develop a framework for reliability focused on the wind turbine drivetrain.

1.2 Literature review

1.2.1 Existing software

There are several codes in the market, which main purpose is to be used for wind turbine design and certification. The majority of the codes are used mostly for commercial purposes, with the exception of a couple which are used in research as well. This section focuses on describing the type of models used to describe the drivetrain dynamics on relevant existing software, with a general explanation of the wind turbine model formulation. Firstly, let us defined the types of formulation [15]:

- **Modal** – It is based on the mode shapes of beams that represent the blades and tower. It requires isotropic materials and is fast to solve given the low amount of Degrees of Freedom (DOF).
- **Multi-body** – Each main body can be described by several elements. This add complexity to the model, thus increases computational time. However, it is possible to include anisotropic materials, which gives a more realistic description of the components in the wind turbine.

When comparing the performance of different codes based on the previous formulations [16], it was observed that those based on modal formulation predict different results concerning the higher order modes than the codes with higher fidelity. In addition, the modal damping was shown to be one of the factors that drove the difference of the codes. In multibody it is an issue since the reduction of the damping by tunning of Rayleigh parameters can lead to numerical instabilities.

Next, the wind turbine simulation codes are presented:

- **HAWC2** – The Horizontal axis Wind turbine simulation Code 2nd generation (HAWC2) is currently developed at DTU Wind Energy [17]. In here, the structure of the wind turbine is described using a multibody formulation, where each body is described by an assembly of Timoshenko beam elements. In order to construct the wind turbine, each body is interconnected by mathematical constraints that represent mechanical joints. The code finds the time-domain solution to the Equations of Motion (EOM) using the Newmark-beta method for numerical integration. Like in most of the aerolastic codes, the drivetrain is treated as an ideal component, and thus its internal dynamics are not included in the simulation. From the aerolastic point of view, it is seen as a component with much higher dynamics than those of interest in these types of simulation. Thus, it is formulated as a concentrated inertia attached to the main shaft with a value equivalent to the generator inertia times the gear ratio squared (Equation (1.1)). This corresponds to the generator seen from the LSS.

$$J_{drivetrain} = n^2 J_{gen} \tag{1.1}$$

  In addition, it is possible to define external systems, such as the gearbox, and to couple it to the wind turbine for a full-system simulation. This is possible in two ways: first, with an integrated interface [18] in where HAWC2 exchanges states with MATLAB/Simulink in co-simulation interface (more details on this in Section 3.5); and second, an external systems interface in where the EOM of the external system are combined with those from HAWC2 at every time step. A comprehensive description of the details of the later, along with examples, is presented in Appendix A.

- **FAST** – The Fatigue, Aerodynamics, Structures and turbulence code (FAST) is developed at the National Wind Technology Center (NWTC) from the NREL. Uses a modal/multibody formulation to describe 2- and 3-bladed horizontal-axis wind turbines. The advantages of this code is that it is possible to interface it with Simulink, and can be used as a pre-processor for ADAMS. The drivetrain is described as shaft in between the rotor hub and the generator. The restoring moment due to the presence of a gearbox is given by Equation (1.2):

$$T_r^{FAST} = K_{shaft}\left(\theta_r - \theta_{gb}\right) + C_{shaft}\left(\dot{\theta_r} - \dot{\theta_{gb}}\right) \tag{1.2}$$

where K_{shaft}, C_{shaft}, θ_r, θ_{gb}, $\dot{\theta_r}$, and $\dot{\theta_{gb}}$ are the low-speed shaft torsional stiffness and damping, rotor position, rotor angular speed, gearbox position and gearbox angular speed, respectively. In addition, the gearbox efficiency can be specified so the losses are accounted for. This value will be included in the final power calculations [19].

- **FLEX5** – Developed at DTU, it is one of the most popular wind turbine certification modes given that its simplicity and fast simulation time. Moreover, it is an open source code, which makes it attractive to companies for further development and coupling with their in-house software (this is the same case for FAST). It uses a modal formulation and the solution to the EOM is found using a Runge-Kutta solver [20, 16].

- **BLADED** – This is an industry standard software package for the design and certification of onshore and offshore wind turbines. Like other codes, BLADED formulates the wind turbine structure by using a multibody dynamics approach. In addition, it contains special modules for applications such as interaction with the electric network and model linearization for control design. As in HAWC2, there is the possibility to define an external gearbox and couple it directly to BLADED for a full-system simulation [21].

- **AdWiMo** – The Advanced Wind turbine Modeling tool is multibody code that uses the capabilities of the general purpose multibody software MSC ADAMS [22]. It has been coupled with NREL tools such as a FAST pre-processor and AeroDyn for aerodynamic analysis of horizontal axis wind turbines. One of the advantages of AdWiMo is that it is a module in the ADAMS software, and therefore, it is possible to develop further the model in different levels of details. For instance, it is possible to use ADAMS Machinery to build a detailed gearbox with different levels of complexity such as: analytical and 3D-contact based gear teeth forces; and different bearing types modeled as kinematic joints, linear/non-linear forces, solid contact or analytical formulas.

- **SIMPACK** – It is a general purpose multibody code that has developed a module focused on the wind energy industry [23]. Like AdWiMo, it is scalable in its complexity given the general purpose multibody code it is built-on. It is also possible to define only the drivetrain model for stand-alone simulation and analysis with high complexity formulations such as FEM [24].

- **SAMCEF** – The software provides a fully coupled simulation environment. It includes aerodynamics, hydrodynamics and hydrostatic loads; finite element components; multibody elements; and controller. Because of its flexibility, the user can modify the model to add different levels of complexity [25].

1.2.2 Drive-train modeling

When turbines became bigger, and costly, special attention was given to the gearbox given it is the system that is responsible for the most downtime. Several major studies over the last decade have been dedicated to investigate the gearbox dynamics and its subcomponents within the wind turbine context [3, 2, 26, 27, 28, 29].

The major contributions from these studies are:

1. Gearbox dynamics had been studied for over 20 years and the literature is extensive, in where researchers such as Lin and Parker [30, 31] and Kahraman, A. [32, 33, 34] (these previous studies are discussed later in detail) developed linear and non-linear lumped-parameters models for the helicopter and automotive industry. From this extensive knowledge, Peeters [3] applied different types of modeling techniques in increasing complexity, focusing on Linear Time Invariant (LTI) and extended the models to helical gears, thus he presented a study in a complete gearbox of a wind turbine. First, he verified the different vibration modes present on a planetary gearbox such as rotational, translational and planetary. Secondly, he extended the current modeling techniques to the use of *flexible multibody models*, which included additional DOF; this could be seen as a mix between rigid body and finite element modeling, since it is possible to represent the elastic deformation of some of the components of the body, while maintaining the rigid body characteristics. Finally, there was a small study involving a grid disturbance present in a start-up situation by using a sinusoidal excitation, where different values of stiffness for the coupling in the high speed pinion were used. This showed the effects of the grid disturbance mainly in the bearings of the pinion: a high peak torque, high levels of acceleration for the bearings and an axial displacement of the pinion in its bearings.

2. Since 2007, NREL started the GRC project. In this project, the general objective read as: "*...developing integrated gearbox analytical tools that will bridge the gap between gearing/bearing designers and wind turbine designers.*" The major contributions from their research is a combination of different modeling techniques of increasing complexity: torsional, multibody and finite element [2]; and a solid experimental research facility, along with the collaboration of different industrial partners that provide their insight on the real operation issues of the gearboxes in the field. In addition, a failure database has been made available in where several wind farm operators and gearbox re-builders can document the observed failures and categorize them into bearing or gear failures [27]. The failure database is an important contribution given that it identifies the root causes of the failures and analyses the bearing failure mechanisms, in order to propose methods for improvement of the gearbox design. Consequently, the data included in this database can be used to increase the reliability of the overall wind turbine.

   The GRC project has focused entirely in testing the gearbox under different conditions in their 2.5 MW dynamometer, very detailed modeling and field data. Their most relevant contributions to the problem of gearbox failure are:

(a) The studies presented in [35, 36] are a comprehensive investigation of the effects of non-torque loads, gravity, bearing clearance, fluctuating mesh stiffness, nonlinear tooth contact and input torque in the planetary gear loads. It was demonstrated by simulation, and experimental verification, that the bending moments caused by non-torque loads such as tower shadow, rotor weight, wind induced moments, thrust and the tilting of the nacelle, can produce external excitations in the carrier frame leading to an increment in the gearbox internal loads and uneven distribution of the load shared among the planets. These loads have negative effects, such as tooth wedging, in the gear teeth and planet bearings reducing the gearbox service life. Another conclusion of their study, is that with carrier bearing clearance the bending moments have a disruptive effect in the gear meshes and planet bearings. In addition, the planet bearing clearance affects the symmetry of the planets, creating asymmetric bearing loads.

(b) Another major contribution by NREL is their failure findings presented in [27]. The test gearbox was disassembled and several damages were identified: scuffing and fretting corrosion; poor load distribution among the teeth of the sun spline with 50% of the teeth carrying the load; overheating of the high-speed stage (HSS) bearing due to lubricant starvation, among others. The common phenomenon that causes these effects was found to be lubricant starvation, which makes the condition monitoring of operational wind turbines very attractive as a way to identify these failures at an early stage[1].

3. The literature on modeling gearbox dynamics is extensive with models developed in the 90s and early 2000 by Kahraman [33, 32, 34] and Lin [30, 31]. In these studies the authors developed different models for the dynamic analysis of planetary gears and two-stage gear systems. The models can be used in the LTI case to find the global dynamics to identify the natural frequencies and natural modes of the system, while the Linear Time Variant (LTV) models were used to study the parametric instabilities caused by varying mesh stiffness. The previous models were used mostly in the automotive and helicopter industry. Later, Guo and Parker [26] proposed additions to the existing model targeted to the wind energy industry. In their work, they analysed a spur planetary gear stage using a 2D lumped-parameter model, with two translations and one rotation, including non-linearities such as tooth wedging (simultaneous contact in a gear tooth on the drive-side and back-side) and bearing clearance (space between the inner race and the rolling element). With their work, it was identified that tooth wedging resulted in elevated planet bearing forces due to the translational vibrations of the planets caused by gravity and bearing clearance. The later model as been given continuity by the work of Guo with NREL explained in item 2(a).

4. Helsen [37, 38] continued Peeters work by analysing the dynamics of a full wind

[1]Condition monitoring is not considered in this dissertation, given that the main purpose is the modeling and simulation of a wind turbine drivetrain, along with experimental validation of the models.

turbine gearbox in different levels of complexity: torsional models, 6 DOF rigid body models with discrete flexibility and full flexible models. Although the more detailed models at the global level provide a good insight in the load dynamics experienced by the drivetrain, the author calls for the need of models that describe the dynamics at the component level. These internal flexibilities, in the gears and bearings, have a major influence in the global dynamics of the turbine. As expected, the flexible multibody technique is the most suited for gearbox dynamics simulation. The major disadvantage with this technique is the computational cost. In addition to the detailed modeling, the author validates the models with experimental data obtained by Hansen Transmissions 13.2 MW test-rig. In this validation, it is demonstrated that including the off-diagonal terms in the bearing stiffness matrix has a significant effect in the gearbox global behavior. Moreover, through the calculation of the modal participation factors, it was identified that it is necessary to include the varying gear-mesh stiffness in the modeling process.

The previous summary of contributions by other authors highlights the state-of-the-art in gearbox modeling and simulation related to wind energy. The previous studies focused heavily in finding the possible causes for gearbox failure through modeling, experiments and field data; the models analysed the dynamics of the gearbox in a stand-alone configuration. Now that it seems that the answers about the level of complexity of models and the possible causes of failure have been solved, it is necessary to broaden the scope. In this case, it is important to include additional dynamic systems such as the generator, to study the impact of the internal loads of the gearbox. This introduces the need for an approach that accounts for the overall electromechanical interaction between the mechanical systems such as the gearbox (including its internal components), the tower structure, and the wind turbine rotor.

Next, some recent work is presented in where the electromechanical component of the whole drivetrain is considered. The most recent studies had different objectives, but the common denominator was the use of torsional models to represent the gearbox. In [39], the authors present a control strategy to reduce the torsional oscillations in the High-Speed Shaft (HSS) of the gearbox. The gearbox is represented by a torsional model that considers each stage of the gearbox as an inertia and with connecting torsional springs between stage, representing the shafts torsional flexibility. This model was validated measurements from the GRC 750 kW test gearbox. The contribution was a reduction in the torque oscillations, which can help to reduce the fatigue in the gears used in the HSS. In [40], the authors present a strategy to study and simulate the electrical grid aspects with a coupled simulation between Simulink and the aeroelastic code FAST. The contribution is the possibility of using these two tools to study the impact of the electric grid in the wind turbine. Similar work has been done before in this area in order to study the impact of the grid dynamics in the wind turbine structure, where HAWC2 has been used as the aeroelastic tool and Simulink is used for controls and power system simulation [18, 41]. In another study, more relevant to this dissertation, is the work by Girsang et. al [42] where a gearbox was implemented in Simulink's SIMSCAPE toolbox. The mesh stiffness of the planetary gears and the parallel stage was included, along with

the torsional stiffness of the intermediate shafts. This model is coupled with FAST and with SimPower Systems in Simulink, to simulate the entire system and get the response of the gears inside the gearbox. The modeling approach is different than the rest, since it is done by the pre-defined gear train modules that SIMSCAPE contains, however, it is possible to find the system natural frequencies, which are validates against the model presented by Lin and Parker in 1999. The most relevant contribution is the effects of the variations of the electromagnetic torque in a voltage dip. As it is known, this drastic oscillations can have a negative effect in the fatigue of the HSS gears. The main goal of this work was to present a framework to study the electromechanical interaction in the drivetrain. One disadvantage is that since it was modeled using the block diagrams from SIMSCAPE, there is no EOM available and it is a black box, which limits the model scalability in terms of expansion of DOF, non-linearities, or further development.

From the previous literature review, further considerations are needed in order to advance the research on reliability of wind turbine gearboxes:

1. Computer simulation cost (time) is a big issue in system simulation. Specifically in the wind energy sector, where large quantities of load cases need to be simulated for certification of wind turbines. One of the conclusions of the previous survey, is that fully flexible models are needed to gather an important amount of information about the internal gearbox dynamics and loading. However, it is known that these type of simulations have a high computational cost, even when the gearbox is considered as a stand-alone system, with certain torque patterns as input to the system. If it is required to carry out DLC simulations using the entire wind turbine, including the drivetrain as a flexible component, the computational cost would be very high. This is why there is the need for a good compromise between detailed models and the information they can provide in order to make decisions about the gearbox reliability, given different load cases when the entire wind turbine is considered. This requires a framework in where the electromechanical interaction in the drivetrain is implemented, along with the turbine and grid dynamics. Such a method can provide a tool for large amounts of DLC simulation for fatigue and extreme load studies of the drivetrain loads.

2. It has been shown that torque oscillations in the HSS have a negative impact on the fatigue of the gears, and therefore better controllers need to be implemented in order to reduce such oscillations. The source of this oscillations is related to the grid dynamics, where grid faults create different scenarios in the excitation voltage of the generator, which in turn, cause oscillations in the electromagnetic torque. One load case that needs more studies with respect to gearbox reliability, is the LVRT capability of the wind turbine and its effects on the gearbox components. This characteristic is required by modern grid codes (it varies per country), which is the ability of a wind turbine to remain connected (or ride through) during a voltage sag [43]. The specifications of how much time the turbine must remain connected varies depending on the grid code requirements.

3. Since the gearbox modeling techniques have already been defined extensively, it is

necessary to perform parametric studies in the type of internal components used currently in the gearbox. For instance, instead of spherical roller bearings, which are commonly used in the planet gears, it would also be relevant to perform the standard dynamic analysis using another type of bearings, e.g. cylindrical or tapered roller bearings.

Based on the previous information, the next section provides the research objectives of this dissertation and presents the framework in which it takes place.

1.3 Research objectives

The principal objective of the project is to study the electromechanical interactions between the rotor and the drivetrain loads. In this context, the drivetrain is defined from the main bearing to the terminals of the generator. Thus, these models should include the effect of aerodynamics, controls and the dynamics in the electrical grid. Moreover, the models developed in this project include the gearbox and the dynamics of the generator. The latter is the interface from the electrical grid dynamics to the mechanical loading of the gearbox in the HSS via the electromagnetic torque variations. From this, it is clear that the drivetrain is exposed to changes in the conditions from both dimensions, mechanical and electrical, and therefore, the gearbox is highly affected by this complex dynamic behavior, making it the center of this study. The diagram in Figure 1-2 depicts the framework in which the project takes place.

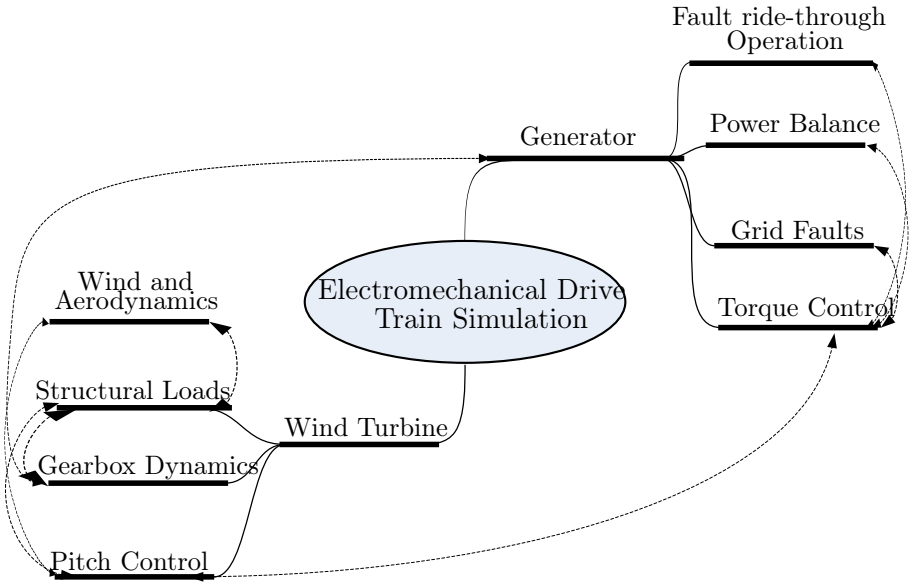

Figure 1-2: Framework of the project. Most of the components and external forces used in wind turbine simulation are interconnected through the electromechanical drivetrain simulation implementation.

From the diagram in Figure 1-2 it is possible to get a global perspective of the project. On the left side, the wind, aerodynamics and structural loads affect the gearbox directly given the physical connection among the components. On the right side, the generator dynamics are affected by a set of grid dynamics (FRT, power balance and grid faults), which in consequence, create additional dynamics given by the torque control. These dynamics in the "electrical domain" have effects on the gearbox and structural dynamics of the turbine.

Given the framework of the project, it is possible to describe a set of general objectives; in addition, a set of specific objectives are laid out in order to fulfill the higher level objectives.

1.3.1 Specific Objectives

The specific objectives described in this section are used as milestones in order to tackle the general objectives. These milestones are related to the implementation of the necessary models needed to study the electromechanical drivetrain loads.

1. To define a method (such as in [44]) which can be used to model a gearbox given the specifications of the wind turbine. This method should contain modules that make it easy to define different configurations of the gearbox, i.e high speed and medium-speed, by implementing multiple stages, and combining planetary and parallel gearboxes. These models should include bearing and gear teeth flexibilities.

2. To define two generator models: a DFIG and a PMSG. These models need to be consistent with the requirements of the wind turbine such as variable-speed and torque control. Therefore, the models should be accompanied by a control strategy for the generator torque, in order to comply with the torque balance requirements of the wind turbine model.

3. To define a reference wind turbine to be used as "working turbine". In addition to the structural parameters, it is necessary to define suitable, and realistic, gearbox and generator models using the previous objectives.

4. To validate the dynamic models of the gearbox and generator with experimental testing.

1.3.2 General Objectives

The general objectives described in this section are directly related to the contributions of the dissertation. These objectives stem mainly from the problem introduced previously in Section 1.1 and the state-of-the-art described later. In addition, the deliverables of this dissertation are aligned to those belonging to WP-5 from the project REWIND[2]. It is expected that the results from this PhD will be used along the results from other work packages for the benefit of REWIND project.

[2]Knowledge based engineering for improved reliability of critical wind turbine components

1. To develop a tool for electromechanical drivetrain simulation in the context of wind energy. This method should account for each subsystem described in Figure 1-2. Not only the dynamic behavior of the whole wind turbine as a system will be studied, but also the performance of the simulation when all the components are considered (computational time).

2. To study the fatigue of bearing loads under normal operation as specified in the IEC standard 61400-4 [44].

3. An insight of extreme loads of the components is to be presented from relevant load cases. For instance, a LVRT, DLC 2.3 (extreme operational wind gust plus the occurrence of a fault) and DLC 5.1 (emergency stop). There is no formal LVRT load case, so an electric fault will be simulated under normal turbulence wind conditions (DLC 1.1) to show the FRT effects.

4. To implement a suitable method that quantifies the reliability of the drivetrain throughout its life time using time domain simulations, where the wind turbine structure is coupled with the gearbox and generator dynamics.

5. Given the new generation of wind turbines, onshore and offshore, with increasing size and different configurations, the last objective focuses on finding the best solution between medium-speed and high-speed drivetrains. This is done from the context of reliability and system simulation.

1.4 Overview of the thesis

In the first chapter, the thesis is formulated by describing the current problem and laying out the contributions from past researchers to present the state-of-the-art. From the definition of the problem, several research objectives are presented to define the expected contributions from the dissertation.

Chapter 2 is dedicated to describe the necessary concepts used in this dissertation. It is not the intention to repeat existing knowledge, but to present the definitions of the components used here. It also serves as an explanation of terminologies for the subsequent chapters. A description of the different subsystems and components of the drivetrain is presented, along with the different configurations available. Later, the two generator systems used in the dissertation are briefly described. Since the concept of fatigue is used in the results part of the dissertation, a fatigue analysis section has been included in order to describe the main topics used for the analysis. Last, the wind turbine model used for the simulations is briefly described, given that it is a popular research turbine model that has been widely used.

The different models and methods used in this thesis are described in **Chapter 3**. The basis of these models have been presented by previous studies, therefore, the information in the chapter serves as a description of the general concepts, how are they used in this dissertation and their validation. First, a gearbox model is described from the

formulation of its constraints using the multi-body dynamics code implemented during the first year of the Ph.D. The limitations of this formulation are highlighted in relation to the research objectives from Section 1.3. Later, the gearbox models based on lumped-parameters used for the core of this dissertation are described, from the choice of reference frames, coordinate transformation, component forces to the solution to the EOM. The control system for a PMSG that is coupled with the gearbox is presented, along with the results showing its response. From here, the electromechanical simulation interface and the methodology for coupling with the wind turbine is presented. This sets the core of the dissertation by establishing the connection between the mechanical and electrical domain. And last, the system's model is validated using experimental data from the GRC project. The results show that the formulation chosen here is a good approximation of the test system used at NREL. The bearing forces and response of the overall system are validated at different power levels. Moreover, the electromechanical coupling between the different components is presented. Furthermore, the modeling and control strategy of two generator configurations is explained. The lumped-parameter models and the electromechanical drivetrain interface presented in this chapter are used to obtain the results in the subsequent chapters. In addition, they make part of the publications [45, 46]

In **Chapter 4** the wind turbine structure is coupled with the developed simulation tool to compute the drivetrain loads a normal operation load case (DLC 1.1). This load case requires a minimum number of simulations in order to be in line with the IEC standard recommendations. The entire system, i.e. wind turbine, gearbox and generator, are simulated in the validated co-simulation interface. Simulations over the entire wind speed range of the turbine provide with sufficient data to analyze the fatigue of the components, and different modes that contribute to the damage of the planet bearings are identified. In addition, a study of the wind turbine loads show that its dynamics are not affected by the introduction of an externally defined drivetrain. Hence, the co-simulation approach including the detailed gearbox is proven adequate. The results presented in this chapter correspond to work given in [46].

Different extreme load cases are simulated in **Chapter 5**, i.e. DLC 1.1/LVRT, DLC 2.3 and DLC 5.1. For the sake of clarity, there is no specific LVRT case defined in the IEC standard, therefore, a normal operation case (DLC 1.1) is simulated with a voltage fault occurring at different points in time. The LVRT is carried out following the recommendations form four different grid codes, in terms of considering the worst case scenario where the wind turbine must stay connected to the grid. A DFIG is used given its direct connection to the grid, which makes it more vulnerable to events in the grid voltage. The simulation time-series of the three load cases are used to compute the extreme loads and maximum contact stresses experienced by the planet bearings. Result show that the emergency brake is the case with the most negative impact on the bearings, followed by the LVRT for a specific grid code. Several recommendations to reduce the impact on the bearings are given based on analysis of the results, and the difference among the cases.

In **Chapter 6**, two types of bearings are modeled using the bearing model pre-processor described in Chapter 3. The purpose of the two representation is to obtain

two different bearing stiffness matrix and to compare the associated reliability (using the First-Order Reliability Method (FORM)) with respect to the expected life of each bearing. The results are obtained using the electromechanical interface and two different drivetrains are simulated. The results given insight in the different damage achieve by each type of bearing and the importance of the dynamic rating parameter as far of the probability of failure of each type of bearing. The work in this chapter is part of [47].

The summary of the contributions from the thesis, the limitations of the models and recommendations for future work are given in **Chapter 7**.

2

Theoretical Background

2.1 Introduction

This chapter presents the necessary background to analyze the components in the electromechanical drivetrain. The starting point is a definition of the different drivetrain constituents, along with their advantages and disadvantages. Then, the most important drivetrain constituents such as bearings, gears and generators are explained in detail. There is extensive literature about these concepts, but special attention is given to the relevant information related to the wind energy context. Furthermore, the fatigue of components is studied and foundations are given for the analysis of the bearing loads in the later chapters. Finally, a brief description of the wind turbine model used in this dissertation is presented.

2.2 Drive Train Subsystems and Configurations

The drivetrain of a wind turbine is defined from the main bearing to the generator, which in simple terms is usually represented as an equivalent inertia or shaft in conventional aeroelastic codes [17, 19, 21]. However, in this dissertation the drivetrain is defined externally and it includes the dynamics of the gearbox and generator. That is, the drivetrain system studied here, ends at the excitation terminals of the generator in order to account for the effects of the electrical system in the generator dynamics.

The drawing in Figure 2-1 shows the main parts of the drivetrain: main bearing, main shaft or LSS, gearbox, brake, HSS and generator. The different drivetrain configurations are defined based on the dimension and layout of the entire system. It is related to the number of suspension points, size of the gearbox and generator, or as in the case of a direct drive, without a gearbox.

The drivetrain configuration can be divided into three main categories: high-speed, medium-speed and direct drives. These types of drivetrains will be discussed in this section from a qualitative approach and to introduce the reader the different options available in wind energy industry. It is out of the scope of this dissertation to analyze in detail every possible configuration. Instead, the main topic of the dissertation is to

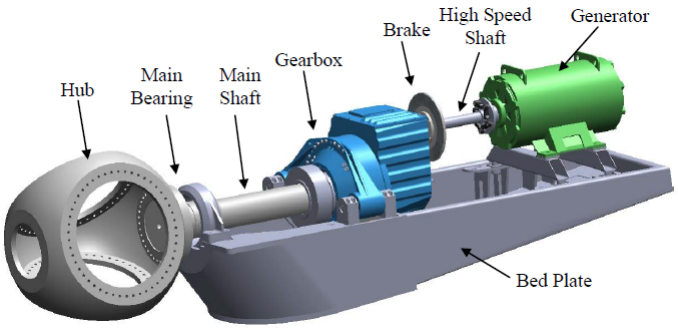

Figure 2-1: Drawing of the components inside a nacelle. In here, the most relevant parts of the drivetrain are depicted (reproduced from [2]).

study those configurations that contain a gearbox, whether is part of a high-speed or a medium-speed drivetrain.

In here, the configuration refers mainly to the operational speed of the generator. This rating depends on the type of turbine. Some operate at a higher speed, such as the case of the NREL 5MW reference turbine and therefore their rated torque is considerably low. In other cases, as medium-speed or direct-drives, permanent magnets synchronous generators are used and they operates at a much lower speed than the induction option. However, the rated torque is higher, and in the case of direct-drives, it is equal to the main shaft torque.

The definitions in this section have been denominated subsystems since they contain more elements that play a role in the wind turbine operation. It is the intention of the author to present the main concepts and characteristics of these subsystems, in order to navigate the reader from the big picture into the smaller elements of the system.

2.2.1 Main bearing and shaft

The low-speed section of the wind turbine's drivetrain is composed by the main bearing and shaft, whose main purpose is to the transfer the rotor torque to the gearbox. The main bearing, specially, is subject to the high bending moments in the different directions due to the wind fluctuations and to the blades loads transferred through the hub. In addition to transferring the drive torque through the gearbox, the main shaft and bearing, need to transfer the additional loading to the nacelle structure via their support points [48].

2.2.2 Gearbox

The main purpose of the gearbox is to increase the speed from the low speed in the rotor, to a higher speed for the generator operation. The rate of change depends on the gear ratio which is defined based on the type of turbine and generator. For instance, the NREL 5MW reference wind turbine [49] has a gear ratio of 1:97 but it is possible to find turbines with gear ratios of 1:37 [50], or in the case of direct-drive turbines [51]

the gearbox is non-existent. Another purpose of the gearbox is to decrease the driving torque also by a factor equal to the gear ratio. In this dissertation, the gearbox is given special attention in the modeling process in order to capture the internal dynamics of its components. The design of different sizes of gearbox is a trade-off between the reliability of its components and the cost. The gearbox will be discussed in more detail in the later sections.

Bearings

In wind energy, bearings play an important role in the operation of the turbine due to the constant operation and the different loading of its rotating parts. Specially, because wind turbine manufactures design for a 20 years lifetime of the entire wind turbine. However, the gearbox is the subsystem in the wind turbine with the most recorded downtime [2], furthermore, the bearings were identified as the component with the most failures [14]. Therefore, it is important to understand the different failure modes and to implement appropriate models to describe their behavior within wind turbine DLC simulations. This section provides conceptual information on the type of bearings used in wind turbines.

Bearings in general can be divided in three major categories: roller bearings, fluid film bearings and magnetic bearings. In drivetrains, the roller bearings are the most popular, and therefore, the present work only focuses on this type. This category can be further divided into different types of bearings: spherical, cylindrical, and tapered roller bearings. Figure 2-2 shows the types of roller bearings discussed here. As it is shown, roller bearings consist of two different size rings, with rolling elements in between them. The type of rolling elements dictate the shape of the rings and consequently the type of bearing [52].

1. **Cylindrical Roller Bearings**
   Mostly used in applications related to power transmission due to their low friction, this type of bearings are suitable for high operational speeds. It is common to find the rollers linked by a cage as shown in Figure 2-2. The main purpose of the cage is to make the bearing more suitable to withstand high radial loads and fast accelerations. These type of roller bearings are commonly used in planetary stage gearboxes, to support the planets and allow their rotation [11].

2. **Spherical Roller Bearings**
   In a spherical roller bearing, the roller components have their outer raceway with an spherical shape. Also, each bearing contains two rows of rollers whose axis are inclined to the axis of rotation of the bearing. This is a main advantage in case of shaft misalignment or deflection, the rollers are capable to adjust the outer raceway [52]. In addition, of all the roller bearing types, spherical roller bearings show the highest load capacity. Therefore, their location on a wind turbine is usually at the main shaft acting as the main bearing and gearbox support bearing (on a three support points drivetrain), in order to sustain the changing loading conditions on the rotor side.

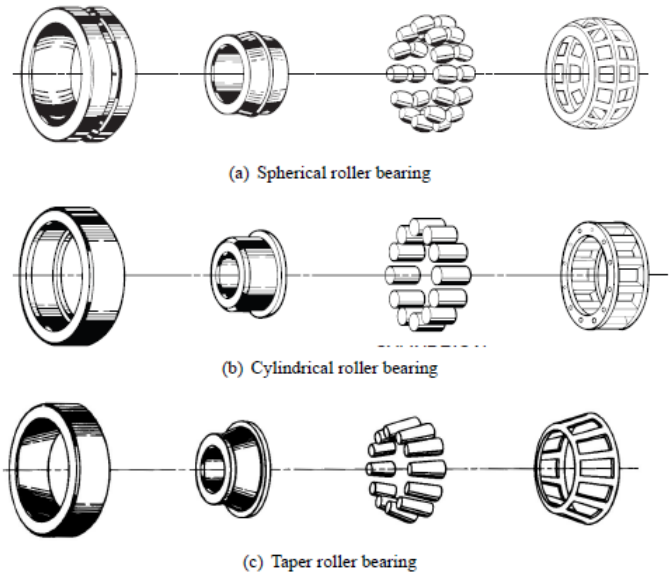

Figure 2-2: Types of roller bearings used in wind turbines drivetrain. The major parts are displayed (from left to right): outer ring, inner ring, roller component and roller cage (reproduced and modified from [3]).

3. **Tapered Roller Bearings**
   As seen in Figure 2-2, the rollers have a shape of truncated cones. Because of the position of the raceways, the tapered roller can take axial and radial loads in a single direction. However, it is very common to find a combination of two or four tapered roller bearings in back-to-back configuration, in order to support axial loads in either direction, and to take advantage of their high load carrying capacity.

Gears

The main objective of the gears is to transfer the load from the input to the output. In terms of kinematics, this is done by transferring the rotational motion using the contact in the gear teeth. This section introduces relevant concepts of gear transmission in wind energy. A detailed list of gear terminology is given in Appendix B.

Kinematics

The most basic expression that describes a gear pair operation is the gear ratio and is given as:

$$\frac{\omega_{out}}{\omega_{in}} = \frac{r_{b_{out}}}{r_{b_{in}}} = \frac{N_{out}}{N_{in}} \tag{2.1}$$

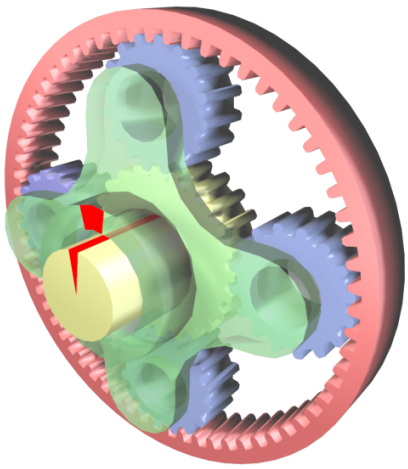

Figure 2-3: Planetary gearbox example (reproduced from [4]).

Equation (2.1) shows that the rotational motion of the gear pair will result in a change on speed in the output that depends on the geometry of the gears.

However, in geared wind turbine drivetrains, different gearbox configurations are used for either high or medium-speed operation. In both cases, it is common to find at least one planetary stage gearbox. The advantage of this type of gearbox stage is the high gear ratio achieved in a compact system. A planetary stage consists of a ring gear, a carrier and a set of planets. An example of a generic planetary stage gearbox is presented in Figure 2-3. In wind turbine drivetrains, the input torque is applied to the carrier, which produces a rotation of the planets around the sun gear. The ring gear is fixed, while the output is in the sun gear. In addition, the planets rotate around their rotational axis which is placed in the pins attached to the carrier.

The total gear ratio in a planetary gearbox is defined as the ratio of the sun speed to the speed of the carrier:

$$\frac{\omega_s}{\omega_c} = 1 + \frac{Z_r}{Z_s} \tag{2.2}$$

where Z_r and Z_s are the number of teeth of the ring and sun gear, respectively. This is a positive gear ratio given that the sun and carrier rotate in the same direction. Similarly, the ratio of the planet to the carrier is given by:

$$\frac{\omega_p}{\omega_c} = 1 - \frac{Z_r}{Z_p} \tag{2.3}$$

where Z_p is the number of teeth in one planet gear. This is a negative gear ratio because the planets rotate in opposite direction of the carrier. Finally, the ratio of the

sun to planet is given by:

$$\frac{\omega_s}{\omega_p} = \frac{1 + \frac{Z_r}{Z_s}}{1 - \frac{Z_r}{Z_p}} \tag{2.4}$$

This is also a negative gear ratio because of the opposite direction of rotation of the planets with respect to the sun.

Notice that the total gear ratio does not depend directly on the number of planets used. Instead, the major drivers are the number of teeth in the ring and sun gear. Moreover, the choice of the number of planets is rooted in the design loads at which the planetary stage is subject to. The choice of the design is related to cost savings because more planets mean a higher distribution of the load, which results in lower loading on the components, but also higher costs given the increase in number of components used. In contrast, the choice of a reduced number of planets means that more material needs to be used in order to maintain the gear ratio requirements.

The use of a gearbox is not only related to a change of speed. In larger turbines, the rotor speed tends to be in the order of 1-2 rad/s, while the induction generators, for example, operate at above 100 rad/s. Moreover, the input torque from the rotor is very high in comparison to the one needed in the generator. Therefore, the gearbox reduces the torque by a factor equal to the gear ration. As in any system, the energy transferred by a gear pair must be conserved as shown by:

$$T_{in}\omega_{in} = T_{out}\omega_{out}\eta_{gb} \tag{2.5}$$

where η_{gb} denotes the gearbox efficiency. In reality, some of the energy is loss in the load transfer due to friction losses in the transmission.

2.2.3 Generators

It is the case for most wind turbines, that the generator is located at the rear end of the drivetrain and it is coupled to the gearbox via the HSS. There are different types of generators used in the wind energy industry today. The most popular are the induction and synchronous generators. Their main purpose is to transform the mechanical power produced by the wind turbine's rotor into electric power. Nowadays, the generators reach efficiencies with values ranging from 94 % to 99%, thanks to advances in electrical machine design. For instance, thanks to progress in ferromagnetic materials, high temperature superconductors, high temperature insulation materials, and power electronics control techniques, to name a few [53]. This section is intended to highlight the advantages of the types of generators used within wind energy, and the main concepts related to their operation. Considering the advances in generator technology, the main focus of the concepts presented here are related to variable-speed configurations only. A comprehensive description of the advantages of variable-speed operation wind turbines and the type of generators used is given by [54].

The concept of variable-speed wind turbines

The main purpose of using variable-speed turbines is to increase the power capture by operating the wind turbine over a wide range of speeds. This means that the wind turbine needs to operate at the maximum aerodynamic efficiency over the range of speeds. To do so, the machine controller, governing the power electronics, must control the generator speed to adjust to the fluctuations in the wind field in the variable speed domain. This controller must operate in conjunction with the wind turbine controller governor so after the turbine reaches rated speed, the power production is maintained at the rated power level. Another advantage of variable-speed operation is the optimal power production that can be achieved at lower than rated wind speeds. As it is well known, the mechanical power a wind turbine can extract from the wind is proportional to the cube of the rotor speed:

$$P_m^{max} = K_{opt}\omega_r^3 \tag{2.6}$$

where

$$K_{opt} = \frac{1}{2}\rho\pi R^5 \frac{C_p^{max}}{\lambda_{opt}^3} \tag{2.7}$$

where ρ is the air density, R is the rotor radius, C_p is the power coefficient and λ is the tip-speed ratio. The latter depends on the rotational speed ω_r, R and mean wind speed u as shown:

$$\lambda = \frac{\omega_r R}{u} \tag{2.8}$$

Therefore, the maximum power produced by a given wind speed is achieved when the optimal λ is maintained. In addition, the variable-speed operation also reduces the mechanical stresses in the gearbox and shafts since the large rotor inertia absorbs the power fluctuations [54].

Doubly-Fed Induction Generator

A DFIG is wound rotor induction generator and the term "Doubly-Fed" reefers to the configuration of the connection to the grid. The power production of the wind turbine is provided to the grid through both, the stator and the rotor of the machine. Hence, the stator is directly connected to the grid, while the rotor voltage is controlled by a partial power converter. Unlike in the PMSG system, where the converter is fully-scaled, in a DFIG, the converter handles part of the power produced. This is an advantage over the PMSG configuration because of the reduction on the size of the power system, which translates into cost savings. The configuration of a DFIG and its power electronics is presented in Figure 2-4.

A detail description of the model, along with the controls implemented was previously presented by [18].

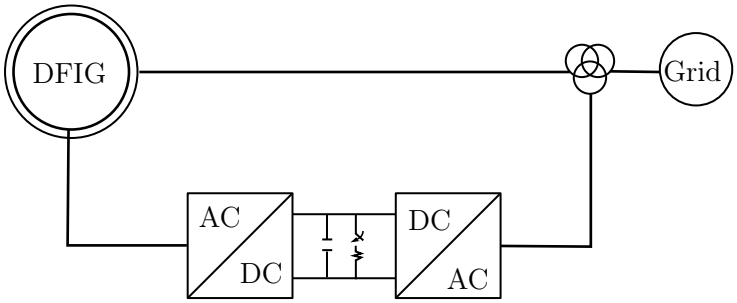

Figure 2-4: Diagram of the DFIG power system.

Permanent Magnet Synchronous Generator

The main advantage of using PMSG over DFIG, is the type of configuration used to connect the turbine to the grid. With a PMSG, the power system uses a full back-to-back converter. A full converter decouples the generator from the grid because it uses to independents converters connected by a DC link. The DC link consists of a capacitor in parallel to a chopper resistor. During short grid faults, a power unbalanced is created in the power system because of the difference in potential in the two converters. In such situation, the unbalance is handled by a chopper resistance. That said, for longer faults such a grid loss, this system will have to respond by shutting down the generator. The diagram in Figure 2-5 shows the configuration of the system. The control system is not included in this diagram because it will be explained later in Section 3.4.

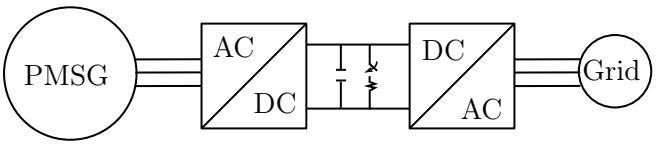

Figure 2-5: Diagram of the PMSG power system.

A description of the dynamic model of the PMSG implemented in this dissertation is included in the Appendix E.

2.3 Bearing life

This section is intended to summarize the important concepts related to bearing life analysis. It is not possible herein to delve into the analysis of bearing life from material fatigue theory. Instead, the concepts of bearing life, cycle counting techniques and material fatigue are used to analyze the resulting loads from the time domain simulation of the models presented in Chapter 3. The main concepts presented next, are based on the widely known theory of rolling bearings analysis [55, 56, 52, 57], mechanical components design [58] and its application in the wind energy industry [59, 11].

2.3.1 The S-N curve

Material fatigue is an effect of cycling loading situations where the component is subject to different levels of loading during a certain number of cycles. For this reason, the structural performance is assessed in fatigue tests and a characteristic curve is obtained for the magnitude of stress cycles to failure at different load levels. The test is carried out by applying a sinusoidal stress to a test specimen of the material, while counting the number of cycles to failure. A rough example of the S-N curve is presented in Figure 2-6. The equation that approximates the middle region in Figure 2-6 is given as:

$$N = KS^{-m} \tag{2.9}$$

where S is the load level that leads to failure during N cycles. The constant K is a material constant that varies from specimen to specimen, and m is a deterministic value that depends on the material under test [7]. The slope in the middle section of the plots of Figure 2-6 corresponds to m, and it is known as the Wöhler exponent.

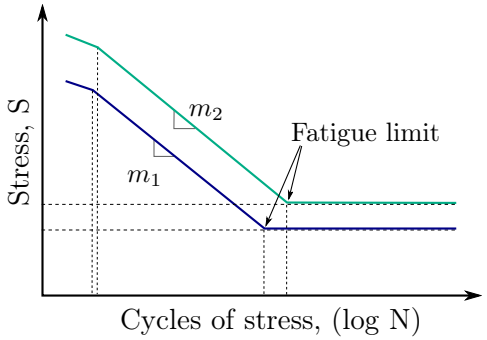

Figure 2-6: Example of S-N curve.

Several concepts that are important to understand the basis of the fatigue of materials can be derived from a qualitative analysis of figure 2-6. The two plot represent the results of fatigue testing of two materials. These could be the same kind of material, e. g. steel, but with different properties or environmental conditions that modify its fatigue limit. Thus, the fatigue limit (or endurance limit) is defined as the stress level at which the material can "last" indefinitely without experiencing fatigue damage. During the first section of the line, the material is subject to high level of stress, resulting in failure at a low number of cycles. This region is commonly known as Low Cycle Fatigue (LCF) and it is usual to be in the range $1 \leq N \leq 100$ [7]. In contrast, in the second region the material is subject lower levels of stress, but with a higher number of cycles until failure. This region is known as the High Cycle Fatigue (HCF) region with common values of $N > 100$.

The previous theory served as an introduction to the concept of fatigue analysis using the results of fatigue testing and the corresponding S-N curve. Next, this concept is extended to the analysis of the strength of the materials used in bearing manufacture.

Part of the focus of the analysis of the strength of the materials, used in the manufac-

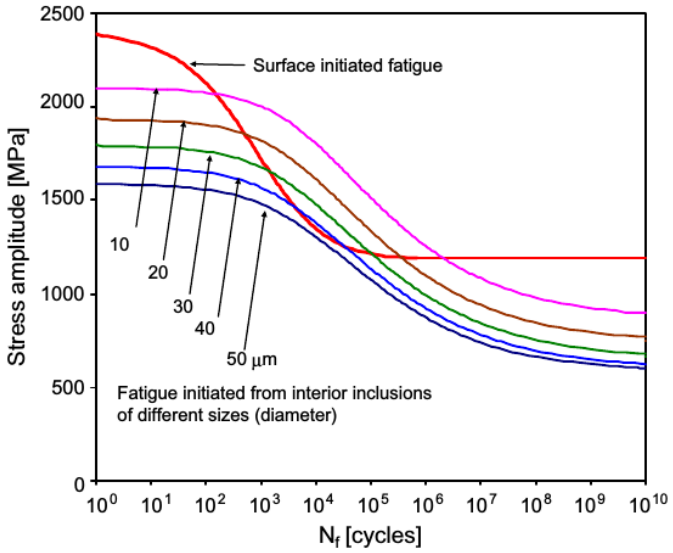

Figure 2-7: The plot shows an example of the effect that different inclusions size have in the fatigue limit of bearing steel 100Cr6 martensite. The results correspond to a prediction of surface failure using the model given in [5]. This plot is a reproduction from [5].

ture of bearings, is to identify the possible failure modes that a bearing might experience throughout its lifetime. For example, it has been identified that the failure of high strength steels in the HCF regime starts from the interior inclusions in the specimen. This is a source of crack initiation and growth, which is refereed to as "fish-eye", due to its shape, with fatigue strength at 10^7 cycles [5]. In addition to the classical regimens of fatigue testing, i.e. LCF and HCF, advances on high frequency fatigue testing equipment have allowed testing of specimens in the Very High Cyclic Fatigue (VHCF) regime beyond 10^7 cycles. For instance, the work by [60] carried out tests of bearing steels SUJ2 using Bending Rotating Fatigue (BRF) techniques. In their research, they found that different size of inclusions in the material will produce "duplex" S-N data. One set of the data corresponds to surface initiated failure at cycles $< 10^5$, while the second set of data corresponds to subsurface initiated failure in the high cyclic region above 10^7 cycles. The authors in [5] developed a model capable of estimating the fatigue crack growth from imperfections in the material, namely the inclusions. An example of their results is given in Figure 2-7. The results pertaining the surface initiated fatigue (red line) show that the fatigue limit is at a higher stress level, and lower cycles, than the second-step S-N curve corresponding to the subsurface initiated failure. Different sizes of inclusions were used in the model predictions, starting at a diameter of 10μm. Even though there is a "two-step" process for the material failure, the subsurface initiated fatigue is irrelevant due to the failure dictated by the lower stress cycles corresponding to the surface failure S-N data. This is specially true for larger sizes of inclusions, e. g. 50μm in Figure 2-7.

The preceding paragraphs attempted to illustrate a portion of the study of the fatigue

failure of materials used in the bearing manufacturing industry. Though these concepts are not explored in detail in the results section, it is relevant to include them, since ultimately, the external loading in the drivetrain components could lead to such phenomena. The next sections explore the methods used to analyze the impact of the external loading on the components from a higher level than the one presented previously.

2.3.2 Implications of fluctuating loads

The fatigue testing is done by applying constant loading, i. e. same stress levels, for a number of cycles to failure. However, in reality, the components in the systems studied in this dissertation are subject to time-varying loading. An example is given in Figure 2-8.

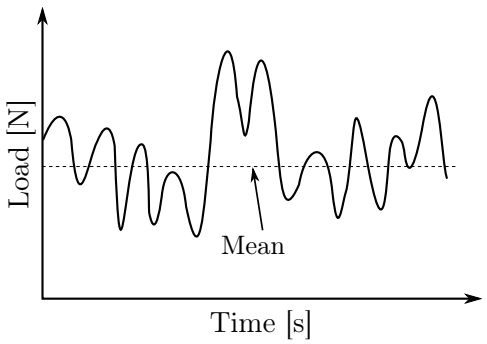

Figure 2-8: A time-varying load with different load cycles.

In the case of wind turbines, the loading in the components experience different levels of stress cycles due to fluctuations in the wind field, therefore, the stress distribution cannot be obtained directly and it is necessary to use cycle counting methods. There are several cycle counting methods such as level crossing, range-mean, range-counting and rainflow counting. For detailed descriptions on the first three methods, the reader is referred to [61, 7]. The rainflow counting algorithm is one of the most popular since it has proven to show accurate results when compared to experimental data. For instance, the range-mean method defines half cycles based on the adjacent peaks and valleys used as boundaries. This results on a series of half cycle values, with out information on the number of cycles associated to those ranges. In contrast, the rainflow counting method divides the time history of the load in a set number of bins k depending on the varying levels. Then, it counts the number of cycles of each load level. The result, is a set of N_i and S_i pairs that represent each range of loading at a determined number of cycles. This poses an advantage when analysing loads in wind turbine components, due to the many different cycle level produced by turbulent wind. The rainflow counting method is used in this dissertation in Chapter 4. For details on the complete procedure for the implementation, one can refer to [7].

The set of N_i and S_i pairs given by the rainflow counting method is used to determine

the accumulated damage D:

$$D = \frac{n_1}{N_1} + \frac{n_2}{N_2} + \cdots + \frac{n_k}{N_k} = \sum_i^k \frac{n_i}{N_i} \tag{2.10}$$

where k is the number of bins, n_i is the number of cycles at the stress range S_i, and N_i is the average number of cycles to failure at the ith stress obtained from the S-N curve of the material. The accumulated damage D denotes a percentage of life consumed by the component due to the exposure at the different stress levels. When D reaches 1, it means that failure has occurred. This relationship is commonly known as Miner's rule and it was introduced by M. A. Miner in 1945 [62].

2.3.3 Assessing bearing life

Different types of bearing failure modes common to the wind energy industry are presented in detail in [14]. Most of the failures are due to lubricant starvation, which in turn produces wear, abrasion, scuffing and cracks in the bearing rollers and rings. A starting point to analyze bearing life is to use known empirical equations which provide information on the dynamic loading and maximum contact stresses that the bearing experience, based on time domain simulations. The bearing life is related to the fatigue experienced by the components due to external loading and number of cycles. Therefore, the period of time required to observe the first signs of fatigue depends on the load magnitude and the number of revolutions experienced by the bearing. Thus, the life of a rolling bearing can be defined by the time in hours the bearing operates or the number of revolutions, before sings of flanking are detected in its races or rolling elements.

The main method to calculate the bearing rating life is the L_{h10} and is an fatigue life indicator of which 10% of the bearings would not survive. There are several versions of this formula, since it was first introduced by Lundberg and Palmgren [56]. Note that this measure is used for preliminary bearing selection according to the IEC standard for design requirements in wind turbine gearboxes [44] and it is given as:

$$L_{h10} = \frac{10^6}{60n} \left(\frac{C}{P}\right)^p \tag{2.11}$$

where n corresponds to the rotational speed, C is the dynamic bearing rating, P is an equivalent load and p is the life exponent: 3 for ball bearings and $10/3$ for roller bearings.

2.4 Wind Turbine Model

The wind turbine used throughout the dissertation is the NREL Reference 5MW wind turbine [49]. This is a variable-speed wind turbine with a rotor diameter of 126 m. The details of the wind turbine are presented in the previous reference. Table 2.1 shows the system parameters used in the dissertation.

Table 2.1: Summary of relevant parameters of the 5 MW reference wind turbine from NREL.

Parameter	Value
Rated Power	5 MW
Control	Collective pitch
Drive-train	High-speed, multi-stage gearbox
Hub height	90 m
Cut-in, rated, cut-out wind speed	3 m/s, 11.4 m/s, 25 m/s
Cut-in, rated	6.9 rpm, 12.1 rpm

The wind turbine has been implemented in HAWC2 in the past, and this model is used to obtain the results presented in Chapters 4, 5 and 6.

3

Drivetrain Dynamics

"The art of simplicity is a puzzle of complexity."

– Douglas Horton

3.1 Introduction

The drivetrain of a wind turbine is composed of two major subsystems: the mechanical and the electrical. The generator is seen as an electrical component. Given the characteristics of the generator, it is the bridge between the mechanical and electrical domains via the electromagnetic torque. The main objective of this chapter is to present the different techniques available to model the drivetrain dynamics, along with the advantages and disadvantages of each formulation. First, a general purpose implementation of a multibody dynamics code using the Newton-Euler formulation, with Lagrange multipliers and constraint equations (see the detailed formulation in Appendix C) is used to model a planetary gearbox. Thanks to the general purpose of the implementation, it is possible to describe different mechanisms composed by kinematic joints such as revolute, translational, fixed and gear constraints. With this formulation, results concerning the planetary gearbox kinematics are presented, along with an analysis on the performance of the implementation. It was observed that given the limited performance in terms of computational time and numerical stability, this approach was not appropriate for fulfilling the objectives of the thesis. The description of the constraint equations and the derivation of the EOM, along with results showing the performance, is presented in Section 3.2. Based on the initial analysis, a more efficient modeling technique known as lumped-parameter models was used as the main modeling approach to describe the gearbox. Two types of models, in increasing complexity in terms of the DOF involved are given. Moreover, the technique is used to derive the generic EOM of the planetary and parallel stages of a conventional wind turbine gearbox. Since the main focus of the thesis is on the planet bearings, the loading of this component is validated with experimental data provided by the GRC project. In addition, the response of the electromechanical interface is validated with a transient case, also with data provided by the GRC project.

The generator model is complete by the appropriate controls in order to ensure the torque balance in the drivetrain.

3.2 The spatial dynamics of a planetary gearbox

In the spatial multibody dynamics approach, the bodies are considered rigid and the interaction in between each body is by means of constraint equations. This section explains the theoretical basis to formulate a gearbox using multibody dynamics and the numerical approach to solve its EOMs with the multibody dynamics code implemented in this dissertation. The theory is based on the formulations presented by Nikravesh [63]. The details concerning the general theory, coordinate selection, basic constraint equations, numerical integration, examples and implementation are presented in the Appendix C. The information contained in this section relates to the formulation used to model gearboxes using this approach. Furthermore, the limitations are exposed based on the experiences of this thesis, but also with respect to findings from other authors.

The system of EOM of a constrained system of bodies for this formulation is defined in eq. (C.37). Two essential components of the EOM are the Jacobian Φ_q and the matrix γ, which represent the velocity and acceleration components of the constraint equations. In this section, the content presented in Appendix C is expanded to include the gear constraints necessary to formulate a planetary gearbox.

3.2.1 Planetary gear kinematic formulation

A common wind turbine planetary stage gearbox is composed by $N + 3$ bodies. Where, N is the number of planets. In the following sections, a value of $N = 3$ is used as an example since it is the most common configuration.

3.2.2 Constraint equations

First, let us consider the most general form of the unconstrained EOM of a system S:

$$\mathbf{M}(\mathbf{q}, t)\ddot{\mathbf{q}}(t) = \mathbf{Q}(\mathbf{q}, \dot{\mathbf{q}}, t) \tag{3.1}$$

where $\mathbf{q} = [q_1, q_2, ..., q_n]^T$ is a $n-$vector of generalized coordinates, $\mathbf{M}$ is the semi-positive definite mass matrix, and $\mathbf{Q}$ is the vector of total generalized forces exerted in the system. What if the unconstrained system is subject to a constraint in one or more of its generalized coordinates? It will result in a set of m holonomic constraint equations given by:

$$\mathbf{\Phi}(\mathbf{q}, t) = 0 \tag{3.2}$$

Note that the holonomic constraints depend only in the position coordinates of a particle or body. In simple terms, the effect that this constraints have in the system S

is described by:

$$\mathbf{M}(q,t)\ddot{\mathbf{q}}(t) = \mathbf{Q} + \mathbf{Q}^c(\mathbf{q}, \dot{\mathbf{q}}, t) \tag{3.3}$$

where $\mathbf{Q}^c$ is the constraint force, which is the additional force needed to satisfy the imposed constraints. Therefore, an interpretation of the constraint conditions is that the system is forced to maintain certain position, velocity and acceleration, in order to satisfy the 2nd law of motion.

The previous description was given with the purpose of introducing the concept of constrained motion of a system of particles. This concept can be extended to a system of bodies, as it is the case in the formulations presented next.

In the case of a gearbox, the gear constraints are defined by kinematic joints that impose conditions in the relative motion between the two gears. An advantage of this, is that the constraint formulation can be used for different types of configuration as long as the gear teeth interaction is consistent with the formulation. Hence, two types of kinematic joints are used to define the interaction of a gear pair. These are denominated spur gear joint and concave-convex gear joint. The first kind is used for modeling parallel stages, and the sun-planet interaction in the case of a planetary stage gearbox. The latter, is used for modeling the ring-planet interaction. The formulation presented here corresponds to the spatial kinematics of gears in absolute coordinates presented by [64]. Moreover, the Jacobian components to these gear constraints are presented. As described before, it is necessary to consider the effects of the acceleration of the bodies in the constrained motion. In mathematical terms, it is essential to include the second derivative of the constraint equations with respect to the generalized coordinates, in order to account for the acceleration. In this dissertation, this components is denoted as γ. For the case of the gear constraints, this component is derived in the following sections. The same notation as the reference [64] is used here and it is intended to show the most relevant equations for the implementation of this formulation in the multi-body code presented in Appendix C.

Spur gear joint

The diagram representing a spur gear joint is presented in Figure 3-1. The main assumption is that the gears are constrained in all the DOF except for the rotational one. Therefore, they are only allowed to rotate. Point p represents the point of contact where the teeth mate, and points p_0^i and p_0^j be the initial points of contact in gears i and j. In addition, ϕ^i and ϕ^j represent the angles between point p and p_0^i of gear i, and p and p_0^j of gear j. Since the gears rotate relative to each other and without slip, the constraint is formulated in terms of the arc length formed by the distances pp_0^i and pp_0^j:

$$\mathbf{\Phi}^{(sg)} \equiv \phi^j r_j + \phi^i r_i = 0 \tag{3.4}$$

where r_i and r_j represent the radii of gears i and j, respectively. The challenge in this formulation is to represent the values of the components of eq. (3.4) in terms of

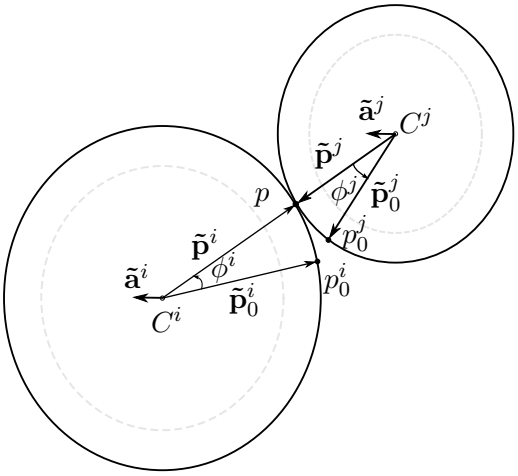

Figure 3-1: The kinematic joint of a spur gear. Vectors $\tilde{\mathbf{a}}^i$ and $\tilde{\mathbf{a}}^j$ are pointing out of the plane.

body coordinates. The values of r^i and r^j are computed as:

$$\begin{array}{rclcl} r^i & = & \|\tilde{\mathbf{p}}_0^i\| & = & \frac{1}{1+k}\|\mathbf{l}\| \\ r^j & = & \|\tilde{\mathbf{p}}_0^j\| & = & \frac{1}{1+k}\|\mathbf{l}\| \end{array} \tag{3.5}$$

where $k = r_j/r_i$ is the gear ratio and $\|\mathbf{l}\|$ is the magnitude of vector $\mathbf{l}$ with constant length between C^i and C^j (the center of the gears i and j). In addition, the angles ϕ^i and ϕ^j are computed as:

$$\phi^l = \arcsin\left[\mathbf{a}^{l'} \cdot \left(\mathbf{e}_0^l \times \mathbf{e}^l\right)\right] \tag{3.6}$$

where the superscript l represents either i or j, and the vectors $\mathbf{e}_0^l$ and $\mathbf{e}^l$ are unit vectors along $\tilde{\mathbf{p}}_0^l$ and $\tilde{\mathbf{p}}^l$.

Concave-convex gear joint

The concave-convex gear joint allows the inner gear j to roll without losing contact with the bigger gear i. A diagram showing the coordinates is shown in Figure 3-2.

The formulation is similar to the spur gear joint since the purpose is the same. The main difference is the change in direction of the vectors on which the constraint is dependent on. The constraint equation is defined as:

$$\mathbf{\Phi}^{(cc)} \equiv \phi^j r_j - \phi^i r_i = 0 \tag{3.7}$$

Since the direction of vectors $\tilde{\mathbf{p}}^i$ and $\tilde{\mathbf{p}}^j$ is the same, vectors $\mathbf{e}^i$ and $\mathbf{e}^j$ are equivalent (following the definition given in the spur gear joint).

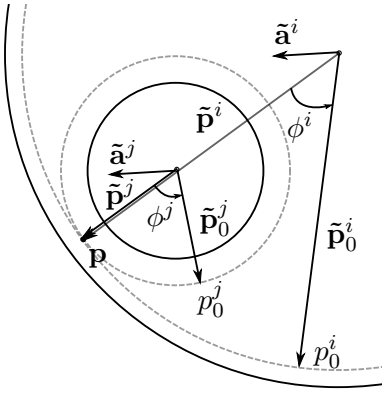

Figure 3-2: The kinematic joint of a concave-convex gear. This type of constraint is useful to represent the kinematic interaction between a ring and planet gear in a planetary gearbox. Vectors $\tilde{\mathbf{a}}^i$ and $\tilde{\mathbf{a}}^j$ are pointing out of the plane.

Velocity and acceleration of the constraint equations

This section presents the velocity and acceleration components of the constraint equations in (3.4) and (3.7). The velocity component is found by differentiating the constraint equations with respect to time and the result is:

$$\begin{aligned} \dot{\mathbf{\Phi}}^{(sg)} &\equiv \dot{\phi}^j r_j + \dot{\phi}^i r_i = 0 \\ \dot{\mathbf{\Phi}}^{(cc)} &\equiv \dot{\phi}^j r_j - \dot{\phi}^i r_i = 0 \end{aligned} \tag{3.8}$$

For the purpose of brevity the entire derivation of the Jacobian components are not shown here since the details are presented in [64], instead the result is given in Table 3.1:

Table 3.1: Jacobian matrix for the gear constraints

$\mathbf{\Phi}$	$\Phi_{\mathbf{r_i}}$	$\Phi_{\boldsymbol{\omega}_i}$	$\Phi_{\mathbf{r_j}}$	$\Phi_{\boldsymbol{\omega}_j}$
$\Phi_{\mathbf{q}}^{(sg,1)}$	$\mathbf{s}$	$-\mathbf{s} \times (\mathbf{c}^i + \mathbf{p}^i)$	$-\mathbf{s}$	$\mathbf{s} \times (\mathbf{c}^j + \mathbf{p}^j)$
$\Phi_{\mathbf{q}}^{(cc,1)}$	$-\mathbf{s}$	$\mathbf{s} \times (\mathbf{c}^i + \mathbf{p}^i)$	$\mathbf{s}$	$-\mathbf{s} \times (\mathbf{c}^j + \mathbf{p}^j)$

where $\mathbf{c}^i$ and $\mathbf{c}^j$ are vectors from the fixed reference frame to the centers of gears i and j, respectively; $\mathbf{s} = \mathbf{a}^i \times \mathbf{e}^i$ is perpendicular to the axis of rotation a of gear i. Physically, the terms of the Jacobian can be used to find information about the position, velocity and acceleration the generalized coordinates.

Let the second derivative with respect to time of the Jacobian matrix Φ_q be:

$$\mathbf{\Phi_q}\ddot{\mathbf{q}} = \boldsymbol{\gamma} \tag{3.9}$$

where γ is commonly referred to as the *right-hand side of the kinematic acceleration equations*. The use of γ becomes evident when looking at the overall system of equations

of a constraint system in eq. (C.34):

$$\begin{bmatrix} \mathbf{M} & \mathbf{\Phi_q}^T \\ \mathbf{\Phi_q}^T & 0 \end{bmatrix} \begin{bmatrix} \ddot{\mathbf{q}} \\ -\boldsymbol{\lambda} \end{bmatrix} = \begin{bmatrix} \mathbf{g} \\ \boldsymbol{\gamma} \end{bmatrix} \tag{3.10}$$

where $\mathbf{M}$ is a $6x6$ matrix, λ are the Lagrange multipliers and $\mathbf{g}$ is a vector of external forces. The mass matrix is defined herein:

$$\mathbf{M} = diag\left(m_i, m_i, m_i, J_x, J_y, J_z\right) \tag{3.11}$$

where m_i is the mass of body i and J_x, J_y and J_z are the moments of inertia in the x, y and z directions. The details of the procedure to define the system of equations in eq. (C.34) are presented in Appendix C.

Now, to find the corresponding $\boldsymbol{\gamma}$ of the gear constraints, the Jacobians in Table 3.1 is differentiated with respect to time as shown in eq. 3.9. The process is similar for both constraint equations since their components are the same but with differences in the signs, as shown in Table 3.1. Therefore, the following derivation is shown for one of the constraints only. A cautionary note: in the following derivation the terms (in **bold**) $\mathbf{r}_i$ and $\mathbf{r}_j$ correspond to the position coordinates of gears i and j. These are not to be confused with r_i and r_j, which correspond to the radii of gears.

For the sake of simplicity and organization in the following derivation, let us define the vector:

$$\mathbf{v}_l = \mathbf{s} \times (\mathbf{c}^l + \mathbf{p}^l) \tag{3.12}$$

where l refers to either gear i or j. Using the definition in (3.12) into the spur gear Jacobian from Table 3.1:

$$\Phi_{\mathbf{q}}^{(sg,1)} \equiv \mathbf{s}\dot{\mathbf{r}}_i - \mathbf{v}_i\boldsymbol{\omega}_i - \mathbf{s}\dot{\mathbf{r}}_j + \mathbf{v}_j\boldsymbol{\omega}_j = 0 \tag{3.13}$$

The differentiation with respect to time of eq. (3.13) gives:

$$\mathbf{s}^T\ddot{\mathbf{r}}_i - \mathbf{v}_i^T\dot{\boldsymbol{\omega}}_i - \mathbf{s}^T\ddot{\mathbf{r}}_j + \mathbf{v}_j\dot{\boldsymbol{\omega}}_j + \dot{\mathbf{s}}\ddot{\mathbf{r}}_i - \dot{\mathbf{v}}_j\boldsymbol{\omega}_i - \dot{\mathbf{s}}^T\ddot{\mathbf{r}}_j + \dot{\mathbf{v}}_j^T\boldsymbol{\omega}_j = 0 \tag{3.14}$$

where

$$\begin{array}{rcl} \dot{\mathbf{s}} & = & \dot{\mathbf{a}}^i \times \mathbf{e}^i + \mathbf{a}^j \times \dot{\mathbf{e}}^j \\ \dot{\mathbf{v}}_l & = & \mathbf{s} \times (\tilde{\boldsymbol{\omega}}\mathbf{c}^l + \dot{\mathbf{p}}^l) + \dot{\mathbf{s}} \times (\mathbf{c}^l + \dot{\mathbf{p}}^l) \end{array} \tag{3.15}$$

and the definition of $\tilde{\boldsymbol{\omega}}$ is presented in Section C.2. Re-arranging eq. (3.14):

$$\mathbf{s}^T\ddot{\mathbf{r}}_i - \mathbf{v}_i^T\dot{\boldsymbol{\omega}}_i - \mathbf{s}^T\ddot{\mathbf{r}}_j + \mathbf{v}_j\dot{\boldsymbol{\omega}}_j = -\dot{\mathbf{s}}\ddot{\mathbf{r}}_i + \dot{\mathbf{v}}_j\boldsymbol{\omega}_i + \dot{\mathbf{s}}^T\ddot{\mathbf{r}}_j - \dot{\mathbf{v}}_j^T\boldsymbol{\omega}_j \tag{3.16}$$

and the resulting $\boldsymbol{\gamma}$ is:

$$\boldsymbol{\gamma} = -\dot{\mathbf{s}}\ddot{\mathbf{r}}_i + \dot{\mathbf{v}}_j\boldsymbol{\omega}_i + \dot{\mathbf{s}}^T\ddot{\mathbf{r}}_j - \dot{\mathbf{v}}_j^T\boldsymbol{\omega}_j \tag{3.17}$$

The information on Table 3.2 shows the right hand side of the acceleration equation

of the kinematic constraints ($\boldsymbol{\gamma}$).

Table 3.2: Gamma (right-hand side of the acceleration equations) entries for the gear constraints

$\boldsymbol{\Phi}$	$\boldsymbol{\gamma}$
$\Phi_{\mathbf{q}}^{(sg,1)}$	$-\dot{\mathbf{s}}\ddot{\mathbf{r}}_i + \dot{\mathbf{v}}_j\boldsymbol{\omega}_i + \dot{\mathbf{s}}^T\ddot{\mathbf{r}}_j - \dot{\mathbf{v}}_j^T\boldsymbol{\omega}_j$
$\Phi_{\mathbf{q}}^{(cc,1)}$	$\dot{\mathbf{s}}\ddot{\mathbf{r}}_i - \dot{\mathbf{v}}_j\boldsymbol{\omega}_i - \dot{\mathbf{s}}^T\ddot{\mathbf{r}}_j + \dot{\mathbf{v}}_j^T\boldsymbol{\omega}_j$

The previous derivation is implemented in the Multibody Dynamics Code presented in Appendix C. The results of the simulation of a planetary stage gearbox are presented in the following section.

3.2.3 Planetary gearbox example

The previous two types of gear constraints are used in conjunction with revolute constraints defined in Appendix C to build the planetary gearbox model shown in Figure 3-3.

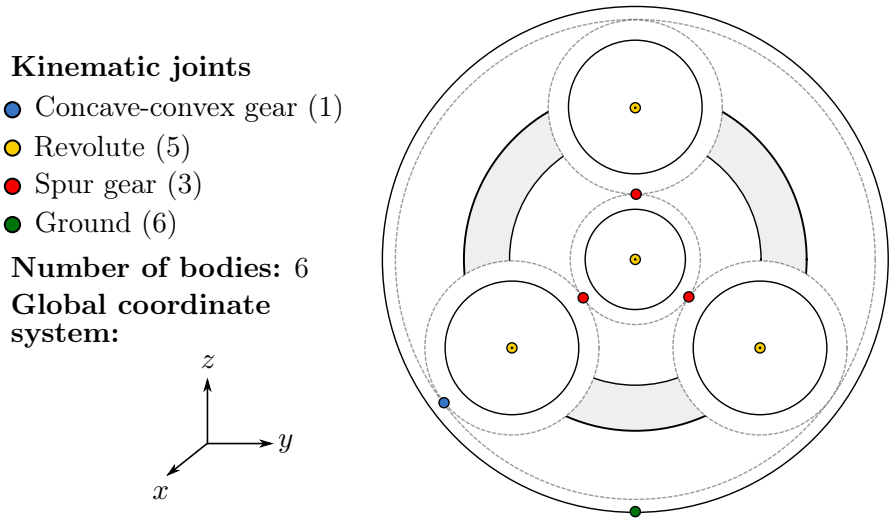

Figure 3-3: Planetary gearbox model using multi-body constraints and rigid bodies.

As seen in the figure, there is only one concave-convex joint being used, while three spur joints are used. In reality, all the movement of all the planets is constraint to the ring gear and sun to transfer the load torque. Though the approach presented here is not realistic, it is necessary to be implemented this way since using additional concave-convex joints will lead to redundant constraints. A small check on the number of coordinates and the number of independent constraints equations explains the reasoning behind limiting the use of concave-convex to just one. In the mechanical system of Figure 3-3 there are

6 moving bodies ($b = 6$), each with six coordinates defining its location and orientation. Therefore, the total number of coordinates in the system is $n = 6 \times 6 = 36$. Also, there are constraint equations that restrict the system to operate only in one rotational coordinate. The information in Table 3.3 shows the summary of the constraint equations, along with the coordinates that are restricted. For instance, a revolute joint constraints the three position and two rotation coordinates in order to ensure rotation in one direction only. Hence, it requires five constraint equations. Similarly, a ground constraint restricts the motion of a body by fixing its six coordinates. Therefore, six constraint equations are required to describe this kinematic joint.

Table 3.3: Total number of constrained coordinates in the planetary gearbox of Figure 3-3.

Type of joint	No. of constraint equations	Total coordinates
Revolute	5	25
Ground	6	6
Spur gear	1	3
Concave-convex gear	1	1
Total		35

Let $m = 35$ be the number of position coordinates on the mechanical system that are constrained due to the kinematic joints. Then, $k = n - m = 1$, where k is the number of DOF of the system. This means that the motion of the planetary gearbox can be described only by one coordinate and it corresponds to the rotation around the axis of the plane.

The unforced response of the system is simulated using as initial conditions the position due to the physical dimensions of the rigid bodies and an initial angular velocity around the axis of rotation x. The initial angular velocities where obtained from the kinematic analysis of a planetary stage presented previously in Chapter 2. For the example presented here, the initial angular velocities of the carrier, planets, sun and ring are as follow: $\omega_c = 1.2$ rad/s, $\omega_p = -1.429$ rad/s, $\omega_s = 6.217$ rad/s, and $\omega_r = 0$ rad/s. The planetary gearbox has a total gear ratio equal to 5.18.

The results in Figure 3-4 show the rotation of the bodies due to the initial conditions. Notice that the carrier rotates in the same direction as the sun, as it is expected, while the planet rotates in the opposite direction. Moreover, the sun displays more cycles of rotation, which is consistent with the concept of the speed multiplication from carrier to sun.

A critical component in the implementation of the gear constraints is to make sure the angles ϕ^i and ϕ^j do not grow out of control. This is a possibility given that their value is associated with the location of points $\tilde{\mathbf{p}}_0^l$, which are attached to the gear bodies, and as the gears rotate, the points move away from the contact point $\tilde{\mathbf{p}}$. Accordingly, lets analyze the expression in eq. (3.6). The value of the angles ϕ^i and ϕ^j is dependent on the result of (3.6). Since the inverse trigonometric function arcsin is restricted for

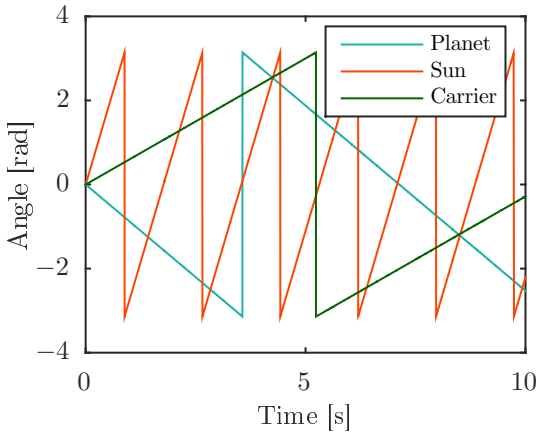

Figure 3-4: The rotation angle of the carrier, one of the planets and the sun. The saw-tooth like look is due the variation between $-\pi$ to π.

the interval $-\pi/2 \leq \phi \leq \pi/2$, a special condition in the implementation is needed. The previous restriction is achieved by moving the points $\tilde{\mathbf{p}}_0^l$ to a predetermined location once they cross a threshold. In the case of Figure 3-5, the threshold for both constraints implementation was set to 0.005. The word critical was used previously because if this consideration is not accounted for, there is a risk of reaching convergence problems in the gear constraints. Thus, even with this consideration in place, it was observed that the tendency of the simulation is to lose consistency in the result of the constraint equations, i.e. diverging from zero. This effect is shown in figures 3-6 where the result of the gear constraint tends to "drift" away from zero as the simulation time goes by.

One solution to the violation of the constraint equations, is the implementation of the Constraint Violation Stabilization Method [63]. In here, feedback control theory is used in order to minimize the inherit error produced by the numerical integration. For example, consider the system

$$\ddot{y} = 0 \tag{3.18}$$

where y is a 2nd order differential equation of the state y. A system as this is unstable when is subject to disturbances or noise. However, when it is placed in a closed loop system, the equation describing the complete system is:

$$\ddot{y} + 2\zeta\dot{y} + \beta^2 y = 0 \tag{3.19}$$

For 3.19 to be stable, the terms 2ζ and β^2 must be positive. As a note of caution, the term ζ is not necessarily the damping ratio present in engineering systems. Now, lets defined the violation of the constraints as:

$$\mathbf{\Phi} \equiv \mathbf{\Phi}(\mathbf{q}^*) = \boldsymbol{\varepsilon} \tag{3.20}$$

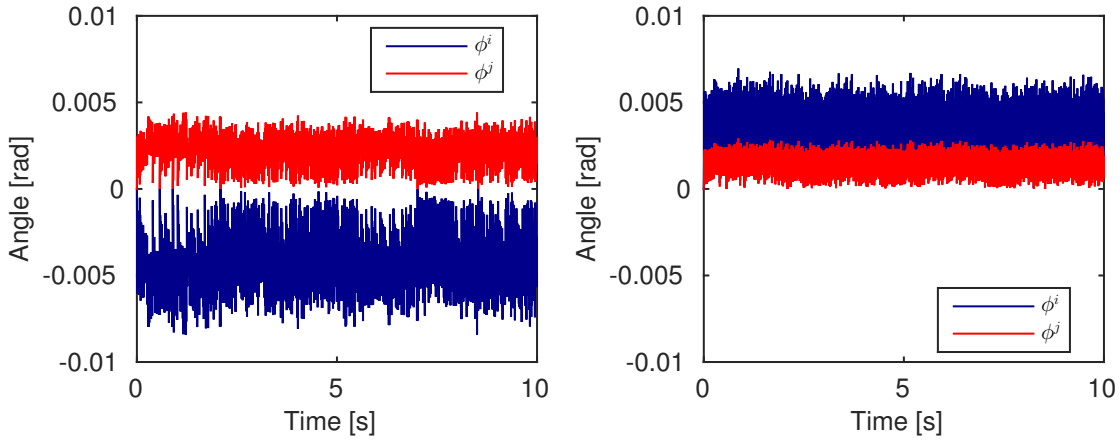

Figure 3-5: The angles ϕ^i and ϕ^j during the simulation for the spur (**left**) and concave-convex (**right**) gear constraints.

and it's first derivative with respect to time:

$$\dot{\mathbf{\Phi}} \equiv \mathbf{\Phi}_{\mathbf{q}}(\dot{\mathbf{q}}^*) = \boldsymbol{\sigma} \tag{3.21}$$

where $\mathbf{q}^*$ and $\dot{\mathbf{q}}^*$ are the computed values of $\mathbf{q}$ and $\ddot{\mathbf{q}}$. From eq. (C.34) and the known values $\mathbf{q}^*$ and $\dot{\mathbf{q}}^*$, it is possible to compute the acceleration vector:

$$\ddot{\mathbf{\Phi}} \equiv \mathbf{\Phi}_{\mathbf{q}}(\ddot{\mathbf{q}}^*) - \boldsymbol{\gamma}^* = 0 \tag{3.22}$$

The error in the vectors are defined as:

$$\begin{array}{rcl} \mathbf{q}^* - \mathbf{q} & = & \Delta\mathbf{q} \\ \dot{\mathbf{q}}^* - \dot{\mathbf{q}} & = & \Delta\dot{\mathbf{q}} \\ \ddot{\mathbf{q}}^* - \ddot{\mathbf{q}} & = & \Delta\ddot{\mathbf{q}} \end{array} \tag{3.23}$$

Since $\dot{\mathbf{q}}^*$ is obtained from integration of $\ddot{\mathbf{q}}^*$, it is necessary to guarantee that $\Delta\ddot{\mathbf{q}} = 0$. This will ensure that any errors in $\Delta\ddot{\mathbf{q}} = 0$ will not be carried forward during the integration process. For integration purposes, the open-loop $\Phi_q(\ddot{\mathbf{q}}) - \gamma = 0$ is replaced by the closed-loop in (3.24):

$$\Delta\ddot{\mathbf{q}} + 2\zeta\Delta\dot{\mathbf{q}} + \beta^2\Delta\mathbf{q} = 0 \tag{3.24}$$

Equations 3.20 and 3.21 are expanded about the generalized coordinates $\mathbf{q}$ to find:

$$\mathbf{\Phi}_q\Delta\mathbf{q} = \boldsymbol{\varepsilon} \tag{3.25}$$

$$\mathbf{\Phi}_q\Delta\dot{\mathbf{q}} = \boldsymbol{\sigma} \tag{3.26}$$

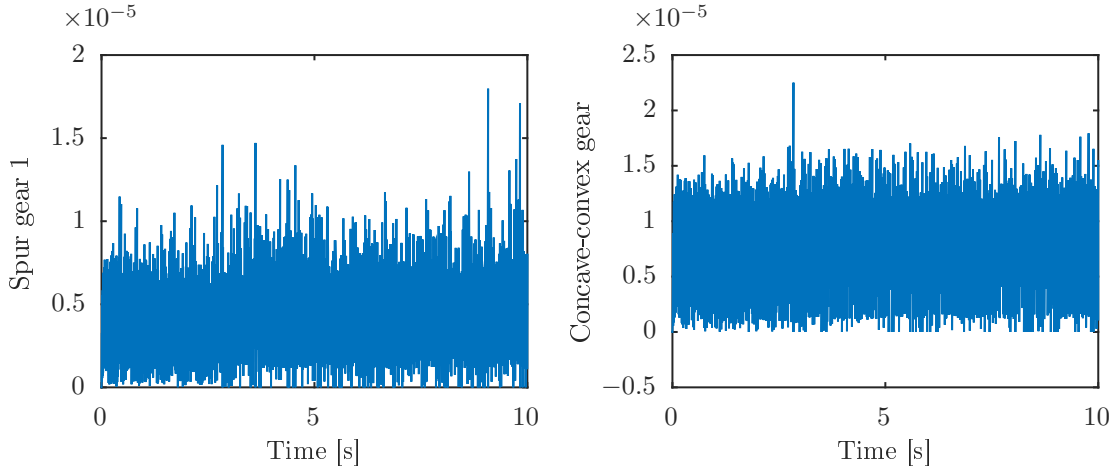

Figure 3-6: The magnitude of the gear constraint across the simulation time for the spur gear joint of planet 1 and the sun (**left**), and the concave-convex joint (**right**) between planet 1 and the ring. The Y-axis corresponds to the value of the constraint equations in (3.4) and (3.7).

Including eq. (3.25) and (3.25) in (3.24), and pre-multiplying by Φ_q yields:

$$\mathbf{\Phi}_q(\ddot{\mathbf{q}}^* - \ddot{\mathbf{q}}) + +2\zeta\mathbf{\Phi}_q\Delta\dot{\mathbf{q}} + \beta^2\Delta\mathbf{\Phi}_q\mathbf{q} = 0 \tag{3.27}$$

From the definition in (3.9), and the relations in (3.20) and (3.21):

$$\mathbf{\Phi}_q\ddot{\mathbf{q}}^* - \gamma + 2\zeta\boldsymbol{\varepsilon} + \beta^2\boldsymbol{\sigma} = 0 \tag{3.28}$$

and from the equivalences in eq. (3.20), (3.21) and (3.22):

$$\boldsymbol{\gamma}^* = \boldsymbol{\gamma} - 2\zeta\boldsymbol{\varepsilon} - \beta^2\boldsymbol{\sigma} = 0 \tag{3.29}$$

The result in eq. (3.29) is included in the equivalence of eq. (3.22) and appended to the system of equations in (C.34) in order to achieve stabilization.

$$\begin{bmatrix} \mathbf{M} & \mathbf{\Phi_q}^T \\ \mathbf{\Phi_q}^T & 0 \end{bmatrix} \begin{bmatrix} \ddot{\mathbf{q}} \\ -\boldsymbol{\lambda} \end{bmatrix} = \begin{bmatrix} \mathbf{g} \\ \boldsymbol{\gamma} - 2\zeta\dot{\mathbf{\Phi}} - \beta^2\mathbf{\Phi_q} \end{bmatrix} \tag{3.30}$$

The stabilization method is implemented in the code presented in Appendix C. There is no real "recipe" to find the values of ζ and β, and there is no physical meaning behind them. They are merely an addition to the EOM in order to ensure stability in the numerical integration. Different tests showed that there is a compromise between computation time and the values of these parameters, along with stability in the simulation. This was specially true for the gear constraints, since a violation meant to lose contact between the two bodies. The results showing the behavior in time of both constraints for different values of ζ and β is shown in Figure 3-7.

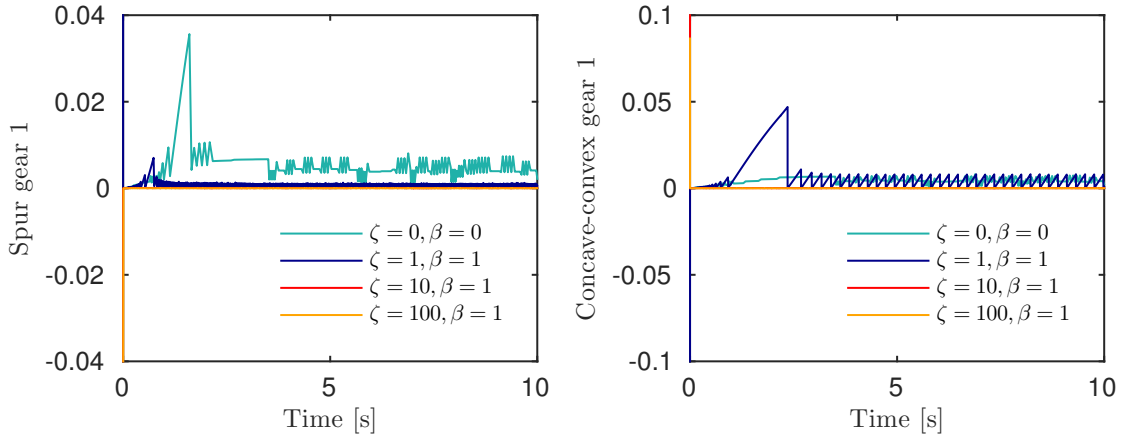

Figure 3-7: The magnitude of the gear constraints for different parameters of Baumgart stabilization. The Y-axis corresponds to the value of the constraint equations in (3.4) and (3.7).

Notice that from the beginning of the simulation, without using stabilization ($\zeta, \beta = 0$), results in a immediate violation of the constraints. An example is shown in Figure 3-8 where the violation of the constraint causes the gear bodies to stop rotating, hence the tendency to zero in the angular speed. This is consistent with the results in Figure 3-7 where there is a peak around 2 s, which causes loss of contact in the gears. Thus, without contact there is no load transfer, and hence, the gears will slow down. Certainly, this is not the case when a large value of ζ is used, as the constraint result is very close to zero in the order of 10^{-5}. It was observed that the value of ζ is more dominant, therefore the examples were using the same value of β. A summary of the implications as far of computational time are presented in Table 3.4.

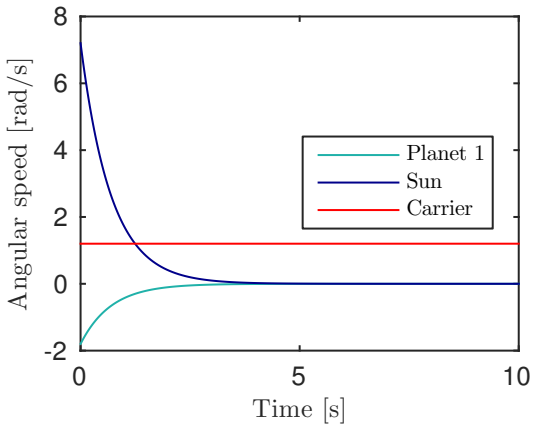

Figure 3-8: The angular speed in the x direction for the case when no stabilization is used ($\zeta, \beta = 0$).

Table 3.4: Impact of the stabilization implementation in the computational expense of the planetary gearbox simulation.

ζ	β	Com. Time [min]	Sim. Time [s]
0	0	0.5155	10
1	1	5.2688	10
10	1	14.6400	10
100	1	284.9525	100

In addition to the convergence issues with the gear constraints, the revolute joints presented more the same kind of issues in the results of its constraint equations. The definition of the revolute constraint in Appendix C indicates that there is only one relative DOF between the two bodies connected by the joint, in this case, the planet and the carrier. This means that there are five constraint equations associated to the revolute joint formulation. Three of these equations are associated with the position coordinates x, y and z of both bodies, imposing a fixed point defined by these three coordinates (see eq. C.21). Therefore, the result of the constraint equation associated to this condition must be equal to zero. This is not the case in the results shown in Figures 3-9 and 3-10. Even though the variation is small, there is an obvious growing tendency for the result of the constraints in the x and z coordinates. For longer simulation times, the system tended to violate the restrictions imposed by the constraints. This was also the case when higher speeds were reached under forced conditions. In addition to the convergence issues, the computational time is high with times of up to 20 min with a sampling frequency of 10 Hz. Similar issues were identify by [65]. In their study, the authors used a more advanced version of the implementation presented here. The main difference is that the varying gear teeth stiffness was included in the simulations. Also, the input torque contained turbulent wind obtained form the code FLEX5. Consequently, they report that a simulation with 30 s of simulation time takes between 10-15 hours.

In conclusion, given the issues associated with the example presented in this section, this approach is not convenient for the ultimate purpose of simulating the entire wind turbine system. Moreover, this example showed that to obtain an accurate and stable solution, it was required to include additional computations, which increase the computational expense dramatically. It might not be evident in the simple example, but when dealing with a co-simulation approach it is necessary to guarantee stability in the numerical integration. This is specially true for demanding simulations, as it is the case for wind turbines, where large amounts of load cases with significant simulation times (at least 600 s) are needed in order to comply with the certification standards.

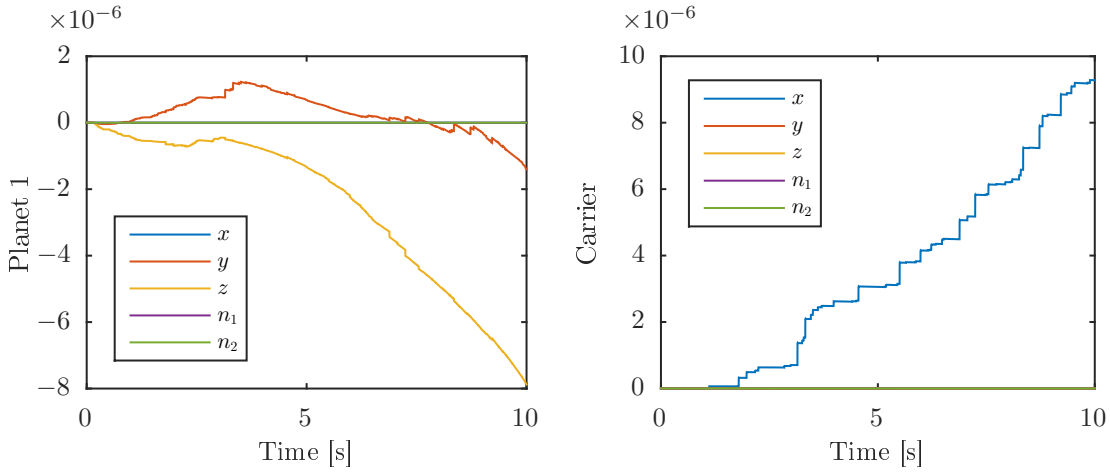

Figure 3-9: The magnitude of the revolute constraint coordinates across the simulation time for the carrier and 1st planet.

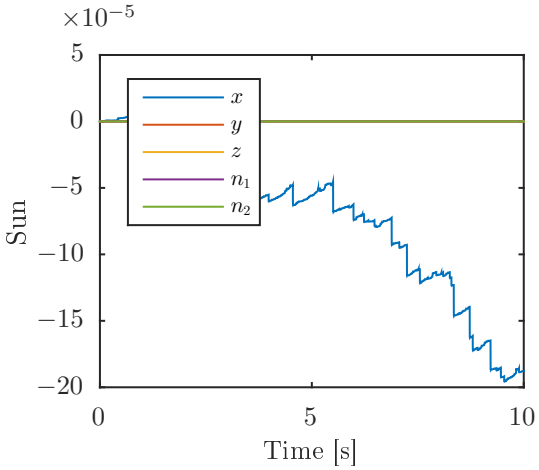

Figure 3-10: The magnitude of the revolute constraint coordinates across the simulation time for the sun.

3.3 Lumped-parameter models

The main characteristic of a lumped-parameter model over a multi-body model is the simplification of the physical system into a topology consisting of rigid bodies, and their interaction takes place in the form of springs and dampers. This technique simplifies the system of equations, but it poses higher computational advantages. With respect to gearboxes, the lumped-parameter models have been developed over the last 20 years by researchers in different applications such as automotive and helicopter industry. The models presented in this section have been derived mainly using the concepts presented by [66, 67, 68].

3.3.1 Rotational - 1D

The first step was to develop a simple model that can transfer the main torque from the wind turbine rotor to the generator. Therefore, a rotational model with only one DOF in the torsional direction was implemented. In this model, the load transfer between the gears is achieved by the gear mesh forces. The transmission between each stage is done through torsional springs representing the shafts. Each gear wheel is represented by a lumped-inertia and the interaction between bodies is represented by linear springs.

Parallel Stage

A representation of the parallel stage is shown in Figure 3-11. The vector $\mathbf{e_1}$ is an unit vector along the line of action and the subscripts g and p refer to the gear and pinion respectively. The dashed circle enclosing each gear wheel corresponds to the pitch circle and the intersection denotes the point of contact of the gear teeth in the real physical system. The linear spring that represents the gear mesh (not shown) lays along the line of action from point A to B. The distances r_g and r_p denote the base radii of the gears. The rotation coordinate for body are θ_g and θ_p. The subscripts g and p denote the gear and pinion, respectively.

At standstill, the uncompressed spring is positioned between the points A and B. When rotating, the mesh spring compresses and the new position is between points A_1 and B_1. In order to find the gear mesh force upon compression, one must find the gear mesh deflection defined by:

$$\delta_{gp} = \overline{AB} - \overline{A_2B_2} \tag{3.31}$$

where $\overline{A_2B_2}$ is the projection of line $\overline{A_1B_1}$ into the line of action. As it is shown, there is a displacement of points A and B due to the compression of the gear mesh spring. Thus, these displacements can be defined in terms of the unit vector $\mathbf{e_1}$. Then, $\overline{AA_2} = \delta A\mathbf{e_1}$ and $\overline{BB_2} = -\delta B\mathbf{e_1}$. In general, the magnitude of the vibration modes of the gears (excluding the rigid body) is very small which means that the lines $\overline{A_1A_2}$ and $\overline{B_1B_2}$ can be approximated by the arc displacement in each gear wheel as $\delta_{gp} = \delta A - \delta B$.

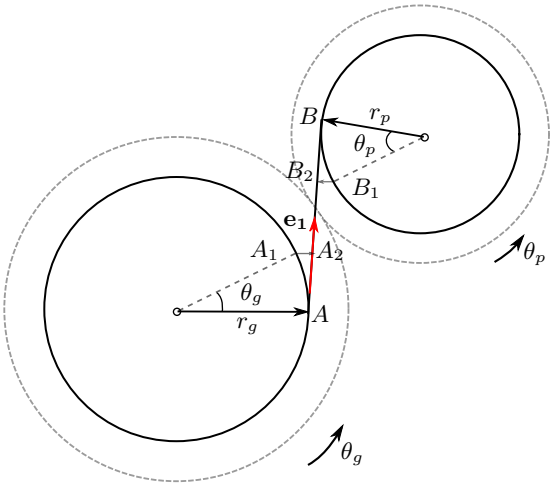

Figure 3-11: Torsional model of a gear pair. The direction of rotation is to establish rotational coordinate system.

Therefore, the gear mesh displacement in terms of the gear coordinates is:

$$\delta_{gp} = r_g\theta_g + r_p\theta_p \tag{3.32}$$

Using eq. (3.32) and Hooke's law, the gear mesh force of the gear pair is defined as:

$$F_{gp} = K_g\delta_{gp}\cos\phi \tag{3.33}$$

where K_g represents the gear mesh stiffness in the gear pair and ϕ is the pressure angle. This angle is the resulting angle between the pitch point and the point where the line of action is tangent to the gear's pitch circle. The pressure angle also characterizes the direction of the normal force F_n between the conjugated teeth as shown in Figure 3-12. The normal force generated at the contact point has a radial (F_r) and a tangential component (F_t). A force decomposition exercise of the normal force F_n yields:

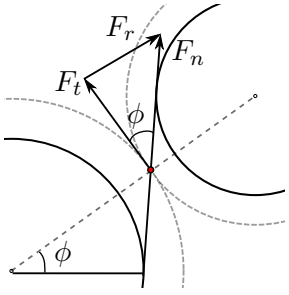

Figure 3-12: Force component in a gear mesh interaction for a gear pair.

$$\begin{aligned} F_t &= F_n \cos\phi \\ F_r &= F_n \sin\phi \end{aligned} \tag{3.34}$$

The value of ϕ is usually small, therefore, the tangential component is of greater magnitude in the overall normal force. Hence, the $\cos\phi$ term in eq. (3.33). From here, the EOM represented in matrix form are found to be:

$$\mathbf{J_{gp}} = \begin{bmatrix} J_g & 0 \\ 0 & J_{pi} \end{bmatrix} \tag{3.35}$$

$$\mathbf{K_{gp}} = \begin{bmatrix} K_g r_g^2 \cos\phi & K_g r_g r_p \cos\phi \\ K_g r_g r_p \cos\phi & K_g r_p^2 \cos\phi \end{bmatrix} \tag{3.36}$$

where J_g and J_p are the inertias of the gear and pinion, respectively.

Planetary Stage

This section presents generic inertia and stiffness matrices that describe a torsional planetary stage gearbox. The model has 6 torsional DOF: carrier, ring, 3 planets and the sun; moreover, it accounts for the gear mesh stiffness of the planet-ring and planet-sun interaction. The diagram of the system is shown in Figure 3-13.

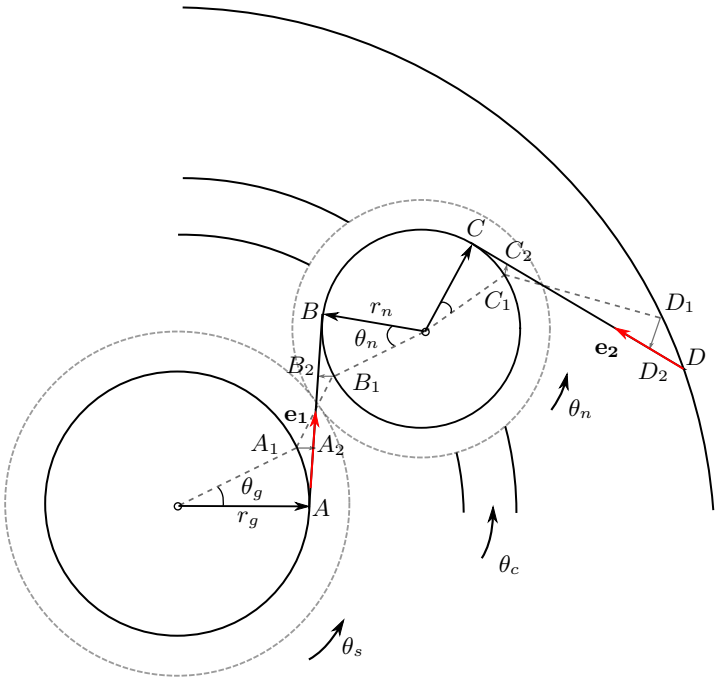

Figure 3-13: Torsional model of a planetary stage. The direction of rotation is to establish rotational coordinate system.

where the subscripts c, n, s and r denote the carrier, planet, sun and ring respectively.

The gear mesh displacements are derived using the same method presented previously in the parallel stage. In the planetary stage gearbox used in wind turbines, the carrier is used as the input and the sun is the output. This is done with the purpose of step-up the angular speed, while stepping-down the torque; in other applications the direction of the load transfer is the opposite. The planet is attached to the carrier planet pins, and rotates along with it in two ways: the body moves along with the carrier and it rotates in its own axis. Therefore, the absolute rotation of the coordinate θ_n is affected by the relative carrier rotation. Let us define the sun-planet gear mesh displacement as:

$$\delta_{sn} = \delta A - \delta B \tag{3.37}$$

where $\delta A \approx r_s\theta_s$ and denotes the displacement of point A; and, $\delta B \approx r_c\theta_c - r_n\theta_n$ denotes the displacement of point B. Using the definition in eq. (3.37), the sun-planet gear mesh displacement found to be:

$$\delta_{sn} = r_s\theta_s - r_c\theta_c + r_n\theta_n \tag{3.38}$$

Notice that the carrier rotation is accounted for in the overall displacement due to the planet's relative rotation with respect to θ_c. Similarly, the ring-planet gear mesh displacement is defined as:

$$\delta_{rn} = \delta C - \delta D \tag{3.39}$$

where $\delta C \approx r_c\theta_c + r_n\theta_n$ and denotes the displacement of point C; in wind energy applications, the ring gear is fixed so $\theta_r = 0$ and $\delta D = r_r\theta_r$ (because $\overline{DD_2} = 0$) and it denotes the displacement of point D.

$$\delta_{rn} = r_c\theta_c + r_n\theta_n - r_r\theta_r \tag{3.40}$$

This stiffness matrix was derived using the displacements eq. (3.38) and (3.40). The energy method using the Lagrange equation is used to derive the EOM [69]. The system matrices for a three planet stage ($n = 3$) are:

$$\mathbf{J_{pl}} = diag([J_c + 3m_n r_c^2 \quad J_r \quad J_n \quad J_n \quad J_n \quad J_s]) \tag{3.41}$$

$$\mathbf{K_{pl}} = \begin{bmatrix} 3(K_{rn}+K_{sn})(r_c cs)^2 & & & & & \\ -3K_{rn}r_r r_c cs & (K_h+K_{rn})r_r^2 & & & \text{symmetric} & \\ (K_{rn}-K_{sn})r_n r_c cs & -K_{rn}r_r r_n & (K_{rn}+K_{sn})r_n^2 & & & \\ (K_{rn}-K_{sn})r_n r_c cs & -K_{rn}r_r r_n & 0 & (K_{rn}+K_{sn})r_n^2 & & \\ (K_{rn}-K_{sn})r_n r_c cs & -K_{rn}r_r r_n & 0 & 0 & (K_{rn}+K_{sn})r_n^2 & \\ -3K_{sn}r_c r_s cs & K_{sn}r_n r_s & K_{sn}r_n r_s & K_{sn}r_n r_s & 0 & 3K_{sn}r_s^2 \end{bmatrix} \tag{3.42}$$

where m and J denote the mass and inertia of the associated body; K_{sn} and K_{rn} are the sun-planet and ring-planet gear mesh stiffness; *alpha* is the pressure angle; and cs is used as an abbreviation for $\cos\alpha$.

For purposes of verification, the model is subject to an eigenvalue analysis to find the

Table 3.5: Validation of the eigenvalues of the planetary gearbox torsional model. The units of the results are in Hz

Mode	DTU	Peeters	Dev[%]
1	0	0	0
2	2399	2217	8.23
3	5683	6159	7.72
4	6459	6444	0.24
5	6459	6444	0.24
6	11241.8	11205	0.33

natural frequencies of the system and it is compared to the results of a model proposed by Peeters in [3]. In this verification, the parameters provided in the reference are used to compute the natural frequencies with the model proposed here. The results are shown in Table 3.5. Notice that for higher modes, the accuracy of the results is very high with less than 0.5% difference. However, in modes two and three, there is low accuracy but the differences are still below 10%. The first mode corresponds to the rigid body mode, which is a nature of the free-free configuration of the system.

3.3.2 Translational/Rotational - 2D

The model presented here is based on the previous work by [70] where a translational and rotational model has been developed. In previous publications [30], the modeling of a planetary stage was presented along with an analytical modal analysis in where the different modes were described. Based on this work, the authors in [71] expanded the model to include additional stages (planetary and parallel) to model a complete wind turbine gearbox. A dynamic analysis showing the natural frequencies was presented, but no discussion was done regarding the loading on the internal components of the gearbox due to external excitations such as changing wind field, and generator torque dynamics. Later, [26] improved the lumped-parameter model by defining a detailed model with clearance non-linearity in the planet and carrier bearings. In addition, it was considered the effect of tooth wedging which is an effect of gravity and bearing clearance. The consequence is a change in the loading of the teeth in the sun-planet and ring-planet mesh.

In this thesis, the model is expanded to include additional stages and the interaction with the generator and wind turbine. The following considerations explain the model assumptions and the factors that need to be addressed in order to properly extend the model:

- The original model was defined with respect to a fixed coordinate system. The main difference with this formulation and the one presented in [30] is that the carrier rotational coordinate is coupled with those from the planets and sun. This

is particularly useful when going from the 2D to the 1D model by removing the translational DOF.

- Since the stages are connected with shafts, the coupling is made through the rotational DOF, similar to the approach used with the 1D model.

- The drivetrain is coupled with the wind turbine through the rotation DOF of the carrier. Therefore, this DOF is the only one considered for the carrier body.

- The gear mesh is assumed to be linear. It is well known that the non-linear nature of the gear mesh stiffness variation affects the dynamic response of the system, but no method is available to estimate the variations in this application using the lumped-parameter model under variable speed and without predetermined speed signals. It is possible to use large FEM formulations, but it defeats the purpose of having an implementation which is computationally simple, yet complex enough to capture the loading of internal components of the gearbox.

- The bearings are represented by linear supports and are modeled as a diagonal matrix using the common approach presented by previous authors. However, the bearing stiffness matrix is not limited to this. It is possible, as it will be shown later, to include the off-diagonal terms if desired.

- The gears are considered rigid bodies, hence the flexibilities in the overall system correspond to the gear mesh stiffness, bearings and shafts connecting the stages.

- The EOM are obtained using Lagrange's equation and are arranged in a LTI state space formulation (3.43), where the states correspond to the displacements and velocities of each DOF in the system (the coordinates that describe the translational motion and the rotation). The numerical solution is found by using the ode23tb solver from Matlab/Simulink.

- The inputs to the model are the LSS and HSS torques. One of the requirements to reach equilibrium is to provide the system with the exact torque values. Therefore, it is recommended to use a dynamic coupling between the wind turbine rotor and the low-speed stage of the gearbox, in order to adjust the inputs to the changes on speed. This concept is expanded in Section 3.5.

$$\begin{aligned} \dot{\mathbf{x}} &= \mathbf{A}\mathbf{x} + \mathbf{B}\mathbf{u} \\ \mathbf{y} &= \mathbf{C}\mathbf{x} + \mathbf{E}\mathbf{u} \end{aligned} \tag{3.43}$$

The displacement coordinates for a parallel and planetary gearbox, respectively, are: $q_{pa} = \{x_g, y_g, \theta_g, x_p, y_p, \theta_p\}$ and $q_{pl} = \{x_c, y_c, \theta_c, x_i, y_i, \theta_i, ..., x_N, y_N, \theta_N, x_s, y_s, \theta_s\}$. The subscripts g, p, c, i, s denote the gear, pinion, carrier, planets and sun respectively (N is

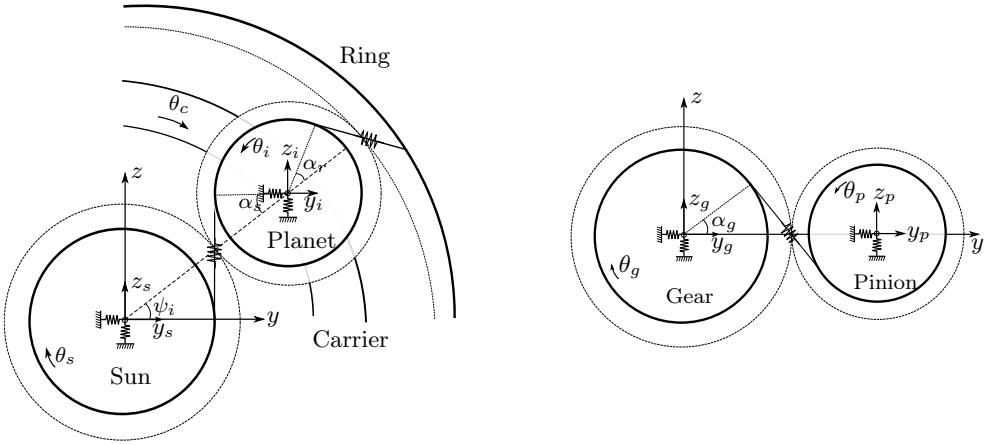

Figure 3-14: Model of planetary and parallel stages. The figure shows the coordinates used for the formulation. Each gear is represented by a rigid body with its own set of coordinates. In the formulation, the displacements of each gear due to the vibrations are projected into the line of action in order to obtain the gear mesh displacements of equation (3.44).

equal to the total of planets). Both stages are depicted in Figure 3-14. From here, the formulation for the gear mesh displacements are defined as:

$$\begin{aligned}
\delta_{si} &= -y_s \sin\psi_{si} - y_i \sin\psi_{si} + z_s \cos\psi_{si} - z_i \cos\psi_{si} + r_s\theta_s + r_i\theta_i - r_c\theta_c \cos\alpha_s, \\
\delta_{ri} &= y_i \sin\psi_{ri} - z_i \cos\psi_{ri} + r_r\theta_r - r_i\theta_i - r_c\theta_c \cos\alpha_r, \\
\delta_{gp} &= y_g \sin\alpha_g - y_p \sin\alpha_g + z_g \sin\alpha_g - z_p \sin\alpha_g + r_g\theta_g + r_p\theta_p
\end{aligned} \tag{3.44}$$

where $\psi_{si} = \psi_i - \alpha_s$, $\psi_{ri} = \psi_i - \alpha_r$, ψ_i is the location angle of the planet with respect to the y coordinate in the fixed reference system, which is concentric with the sun and carrier frames; α_s, α_r and α_g are the pressure angles of the sun, ring and gear, respectively. The expressions from equation (3.44) correspond to the gear mesh deflection of the sun-planet, ring-planet and gear-pinion pairs, respectively. The components of the gear mesh deflections in eq 3.44 have a physical meaning. They represent the projections of the displacements of each coordinate into the line of action between two given gear bodies. For example, the component $y_s \sin\psi_{si}$ in δ_{si}, is the contribution of the sun gear displacement in the y direction. Likewise, the term $r_c\theta_c \cos\alpha_s$ is the contribution of the relative rotation of the carrier as a part of the mesh deflection. This is a recurrent component if compared with the formulation presented in the previous section for the 1D case.

The energy methods are used to derive the EOM. Let us define the potential energy

based on the gear mesh displacements for the planetary and parallel stage:

$$U_{gm}^{pl} = \frac{1}{2}\sum_{i=1}^{N} K_{ri}\delta_{si}^2 + \frac{1}{2}\sum_{i=1}^{N} K_{si}\delta_{ri}^2 \tag{3.45}$$

$$U_{gm}^{pa} = \frac{1}{2}K_{gp}\delta_{gp}^2 \tag{3.46}$$

and the generalized contribution from the bearings:

$$U_B = \frac{1}{2}\sum_{i=1}^{N_b} K_b^h(y_n^2 + z_n^2) \tag{3.47}$$

where N is equal to the total number of planets, N_b is equal to the total number of bearings and K_b^h is the bearing stiffness supporting gear h.

Assuming that $\alpha_s = \alpha_r = \alpha$, and using the definitions in eq. 3.44 and 3.45, the stiffness matrix for a planetary stage gearbox with three planets is derived and presented in eq. 3.56. The sub-matrices that compose $\mathbf{K}_m$ are presented in eq. 3.48 to 3.55.

$$\mathbf{K}_c^i = r_c\cos\alpha^2\begin{bmatrix}0 & 0 & 0\\ 0 & 0 & 0\\ 0 & 0 & K_{ri}+K_{si}\end{bmatrix} \tag{3.48}$$

$$\mathbf{K}_{cp}^i = r_c\cos\alpha\begin{bmatrix}0 & 0 & 0\\ 0 & 0 & 0\\ K_{si}\sin\psi_{si} - K_{ri}\sin\psi_{ri} & K_{si}\cos\psi_{si} + K_{ri}\cos\psi_{ri} & (K_{ri}-K_{si})r_i\end{bmatrix} \tag{3.49}$$

$$\mathbf{K}_{cs}^i = K_{si}r_c\cos\alpha\begin{bmatrix}0 & 0 & 0\\ 0 & 0 & 0\\ \sin\psi_{si} & -\cos\psi_{si} & -r_s\end{bmatrix} \tag{3.50}$$

$$\mathbf{K}_s^i = K_{si}\begin{bmatrix}\sin\psi_{s1}^2 & -\sin\psi_{s1}\cos\psi_{s1} & -r_s\sin\psi_{s1}\\ -\sin\psi_{s1}\cos\psi_{s1} & \cos\psi_{s1}^2 & r_s\cos\psi_{s1}\\ -r_s\sin\psi_{s1} & r_s\cos\psi_{s1} & r_s^2\end{bmatrix} \tag{3.51}$$

$$\mathbf{K}_{sp}^i = K_{si}\begin{bmatrix}\sin\psi_{s1}^2 & -\sin\psi_{s1}\cos\psi_{s1} & r_s\sin\psi_{s1}\\ \sin\psi_{s1}\cos\psi_{s1} & -\cos\psi_{s1}^2 & r_s\cos\psi_{s1}\\ -r_i\sin\psi_{s1} & r_i\cos\psi_{s1} & r_ir_s];\end{bmatrix} \tag{3.52}$$

$$\mathbf{K}_{\tilde{ps}}^i = K_{si}\begin{bmatrix}\sin\psi_{si}^2 & \sin\psi_{si}\cos\psi_{si} & -r_i\sin\psi_{si}\\ \sin\psi_{si}\cos\psi_{si} & \cos\psi_{si}^2 & -r_i\cos\psi_{si}\\ -r_i\sin\psi_{si} & -r_i\cos\psi_{si} & r_i^2\end{bmatrix} \tag{3.53}$$

$$\mathbf{K}^i_{\tilde{pr}} = K_{ri} \begin{bmatrix} \sin\psi_{ri}^2 & -\sin\psi_{ri}\cos\psi_{ri} & -r_i\sin\psi_{ri} \\ -\sin\psi_{ri}\cos\psi_{ri} & \cos\psi_{ri}^2 & r_i\cos\psi_{ri} \\ -r_i\sin\psi_{ri} & r_i\cos\psi_{ri} & r_i^2 \end{bmatrix} \tag{3.54}$$

$$\mathbf{K}^i_p = \mathbf{K}^i_{\tilde{ps}} + \mathbf{K}^i_{\tilde{pr}} \tag{3.55}$$

$$\mathbf{K}^{pl}_m = \begin{bmatrix} \sum \mathbf{K}^i_c & \mathbf{K}^1_{cp} & \mathbf{K}^2_{cp} & \mathbf{K}^3_{cp} & \sum \mathbf{K}^i_{cs} \\ & \mathbf{K}^1_p & \mathbf{0} & \mathbf{0} & \mathbf{K}^1_{sp} \\ & & \mathbf{K}^2_p & \mathbf{0} & \mathbf{K}^2_{sp} \\ & & & \mathbf{K}^3_p & \mathbf{K}^3_{sp} \\ & & & & \sum \mathbf{K}^i_s \end{bmatrix} \tag{3.56}$$

Similarly, the mesh stiffness matrix for a 2D parallel stage is derived and presented in eq. 3.61. The sub-matrices that lead to the result are presented in eq. 3.57 to 3.60.

$$\mathbf{K}_g = K_{gp} \begin{bmatrix} \sin\alpha^2 & \sin\alpha\cos\alpha & r_g\sin\alpha \\ \sin\alpha\cos\alpha & \cos\alpha^2 & r_g\cos\alpha \\ r_g\sin\alpha & r_g\cos\alpha & r_g^2 \end{bmatrix} \tag{3.57}$$

$$\mathbf{K}_{gp} = K_{gp} \begin{bmatrix} -\sin\alpha^2 & -\sin\alpha\cos\alpha & r_p\sin\alpha \\ -\sin\alpha\cos\alpha & -\cos\alpha^2 & r_p\cos\alpha \\ -r_g\sin\alpha & -r_g\cos\alpha & r_g r_p \end{bmatrix} \tag{3.58}$$

$$\mathbf{K}_{pg} = K_{gp} \begin{bmatrix} -\sin\alpha^2 & -\sin\alpha\cos\alpha & -r_g\sin\alpha \\ -\sin\alpha\cos\alpha & -\cos\alpha^2 & -r_g\cos\alpha \\ r_p\sin\alpha & r_p\cos\alpha & r_g r_p \end{bmatrix} \tag{3.59}$$

$$\mathbf{K}_p = K_{gp} \begin{bmatrix} \sin\alpha^2 & \sin\alpha\cos\alpha & -r_p\sin\alpha \\ \sin\alpha\cos\alpha & \cos\alpha^2 & -r_p\cos\alpha \\ -r_p\sin\alpha & -r_p\cos\alpha & r_p^2 \end{bmatrix} \tag{3.60}$$

$$\mathbf{K}^{pa}_m = K_{gp} \begin{bmatrix} \mathbf{K}_g & \mathbf{K}_{gp} \\ \mathbf{K}_{pg} & \mathbf{K}_p \end{bmatrix} \tag{3.61}$$

Moreover, the bearing stiffness matrix in the planetary and parallel stages are defined as:

$$\mathbf{K}^{pl}_b = diag(\mathbf{0}, \mathbf{K^b_i}, \mathbf{K^b_i}, \mathbf{K^b_i}, \mathbf{K^b_s}) \tag{3.62}$$

note that the first term in equation 3.62 is $\mathbf{0}$, i.e. the only DOF of the carrier that is considered in the formulation is the torsion. Likewise, the bearing stiffness matrix for the parallel stage is found to be:

$$\mathbf{K}^{pa}_b = diag(\mathbf{K^b_g}, \mathbf{K^b_p}) \tag{3.63}$$

where the matrices $\mathbf{K^b_c}$, $\mathbf{K^b_i}$, $\mathbf{K^b_s}$, $\mathbf{K^b_g}$ and $\mathbf{K^b_p}$ are 3×3 matrices of the form $K^h_b =$

$diag(k_b, k_b, 0)$. Then, the final stiffness matrix of the planetary stage gearbox is given as:

$$\mathbf{K}^{pl} = \mathbf{K}^{pl}_m + \mathbf{K}^{pl}_b \tag{3.64}$$

Likewise, the total stiffness matrix of a parallel stage is composed of the mesh and bearing stiffness matrices:

$$\mathbf{K}^{pa} = \mathbf{K}^{pa}_m + \mathbf{K}^{pa}_b \tag{3.65}$$

Furthermore, the mass matrices for both stages are defined as:

$$\mathbf{M}^{pl} = diag(\mathbf{M}_c, \mathbf{M}_i, \mathbf{M}_i, \mathbf{M}_i, \mathbf{M}_s) \tag{3.66}$$

and

$$\mathbf{M}^{pa} = diag(\mathbf{M}_g, \mathbf{M}_p) \tag{3.67}$$

where

$$\mathbf{M}_h = diag(m_h, m_h, J_h) \tag{3.68}$$

where m_h and J_h are the mass and moment of inertia of gear h in the coordinates x, y and θ.

With the definitions in place for each gearbox type system matrix, let us define the torsional coupling between stages. For instance, the coupling of a planetary and a parallel stage, in matrix form, can be defined as:

$$\mathbf{K}_{gl} = \begin{bmatrix} \begin{bmatrix} \ddots & \vdots \\ \cdots & K_{si} r_s^2 + K_c \end{bmatrix} & \begin{matrix} \ddots & \vdots \\ \cdots & -K_c \end{matrix} \\ \begin{matrix} \ddots & \vdots \\ \cdots & -K_c \end{matrix} & \begin{bmatrix} \ddots & \vdots \\ \cdots & K_{gp} \sin\alpha^2 + K_c \end{bmatrix} \end{bmatrix}$$

where $\mathbf{K}_{gl}$ represents the global stiffness matrix of the planetary+parallel gearbox, and K_c is the shaft coupling torsional stiffness in Nm/rad.

The formulations presented in the previous paragraphs are used to implement a modular simulation code in order to combine freely different gearbox stages with the ultimate purpose to model an entire gearbox. More technical details on the implementation of the code are presented in Appendix D.

3.3.3 Bearing models

In the previous section, the gearbox models were presented. Special attention was given to the formulation in 2D since with this approach, it is possible to obtain the bearing loads from different excitations. In the formulation, the bearing matrices associated to each gear were defined as $K^h_b = diag(k_b, k_b, 0)$. This representation is useful for general analysis of the dynamics of the system [72, 73] and to study the lateral vibrations

of a rotor system. According to the findings of [38], this representation is no longer valid when a more accurate study of the internal dynamics of a wind turbine gearbox is desired. The theory of bearing design [52], and dynamic modelling of bearing elements is well documented in literature, where several authors propose different methods to find the stiffness matrices and the bearing loads. These models are function of the bearing geometry, contact deformation, and the effective axial and radial displacements of the bearing's center of gravity, according to Hertzian contact theory. In [74], the authors present a method computational efficient to calculate the stiffness matrix of a spherical roller bearing and it is validated using commercial software. In [75], the authors present the models for ball and cylindrical roller bearings with special attention to the bearing stiffness matrix which shows the effects of the cross-coupling components in the overall dynamic response. Their main contribution is a model that can be used to study the vibration transmission through rolling element bearings in rotor dynamics.

This section presents the method implemented in order to find the cross-terms of the bearing stiffness matrices and the bearing forces acting on the shaft and gear bodies. The main objective is to study the impact on the bearing loads under different conditions of wind turbine operation. The method is the same as presented by [75] but it is documented in this section as background information to illustrate the effect on the bearing loads given the mean bearing displacements and radial clearance for a roller bearing. Notice that the nomenclature is maintained with that of the references, in order to keep consistency with the literature.

The elastic deformation of a roller bearing is determined by

$$\delta_R(\psi_j) = \begin{cases} (\delta)_{rj}\cos\alpha_0 + (\delta)_{zj}\sin\alpha_0, & \delta_R > 0 \\ 0, & \delta_R \leq 0 \end{cases} \tag{3.69}$$

where $(\delta)_{rj}$ and $(\delta)_{zj}$ correspond to the effective radial and axial displacements of the jth rolling element, respectively and are defined in equations (3.70) and (3.71); and α_0 is the unloaded contact angle. For the rolling bearing type α_0 is constant because it is not affected by the loading and the elastic deformation of the rolling elements. In this paper, cylindrical roller bearings are treated with $\alpha_0 = 0^0$ and tapered roller bearings $\alpha_0 = 14^0$.

$$(\delta)_{rj} = \delta_x \cos\psi_j + \delta_y \sin\psi_j - r_L \tag{3.70}$$

$$(\delta)_{zj} = \delta_z + r_j\left[\beta_x \sin\psi_j - \beta_y \cos\psi_j\right] \tag{3.71}$$

where δ_x, δ_y, δ_z, β_x, β_y are the inner raceway displacements in the x, y and z directions, and the tilting motion in the x and y directions, respectively as seen in Figure 3-15; and ψ_j is the jth rolling element position.

The elastic deformations for each roller are used to calculate the bearing stiffness terms [75], and consequently the bearing matrix (equation 3.72) for specific displacements and tilting in the x, y and z directions. These deflections correspond to the lateral vibrations of the shaft in the inner raceway of the bearing. Notice that the terms cor-

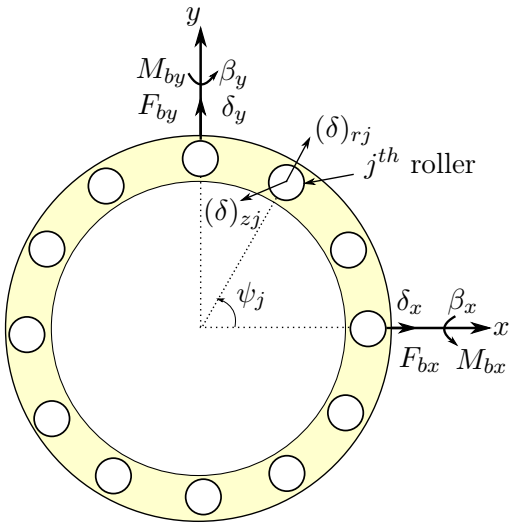

Figure 3-15: Roller bearing (cylindrical or tapered) coordinate system and kinematics. The forces and moments are included for illustration purposes and to define their direction. The z direction goes out of the plane.

responding to the torsion in the β_z direction are zero because the bearing allows free rotation around this direction, i.e. is the rotational degree of freedom of the shaft.

$$\mathbf{K_b} = \begin{bmatrix} K_{xx} & K_{xy} & K_{xz} & K_{x\theta_x} & K_{x\theta_y} & 0 \\ K_{xy} & K_{yy} & K_{yz} & K_{y\theta_x} & K_{y\theta_y} & 0 \\ K_{xz} & K_{yz} & K_{zz} & K_{z\theta_x} & K_{z\theta_y} & 0 \\ K_{x\theta_x} & K_{y\theta_x} & K_{z\theta_x} & K_{\theta_x\theta_x} & K_{\theta_x\theta_y} & 0 \\ K_{x\theta_y} & K_{y\theta_y} & K_{z\theta_y} & K_{\theta_x\theta_y} & K_{\theta_y\theta_y} & 0 \\ 0 & 0 & 0 & 0 & 0 & 0 \end{bmatrix} \tag{3.72}$$

In addition to compute the bearing matrix for dynamic analysis, it is possible to compute the bearing loads using the following expressions:

$$\begin{Bmatrix} M_{bx} \\ M_{by} \\ M_{bz} \end{Bmatrix} = K_n \sin\alpha_0 \sum_{j=1}^{Z} r_j \left\{ (\delta)_{rj} \cos\alpha_0 + (\delta)_{zj} \sin\alpha_0 \right\}^n \begin{Bmatrix} \sin\psi_j \\ -\cos\psi_j \\ 0 \end{Bmatrix} \tag{3.73}$$

$$\begin{Bmatrix} F_{bx} \\ F_{by} \\ F_{bz} \end{Bmatrix} = K_n \sin\alpha_0 \sum_{j=1}^{Z} r_j \left\{ (\delta)_{rj} \cos\alpha_0 + (\delta)_{zj} \sin\alpha_0 \right\}^n \begin{Bmatrix} \cos\alpha_0 \cos\psi_j \\ \cos\alpha_0 \sin\psi_j \\ \sin\alpha_0 \end{Bmatrix} \tag{3.74}$$

where K_n is the rolling element load-deflection constant. It is know from literature [52] that cylindrical roller bearings can take only radial loads and tapered roller bearings

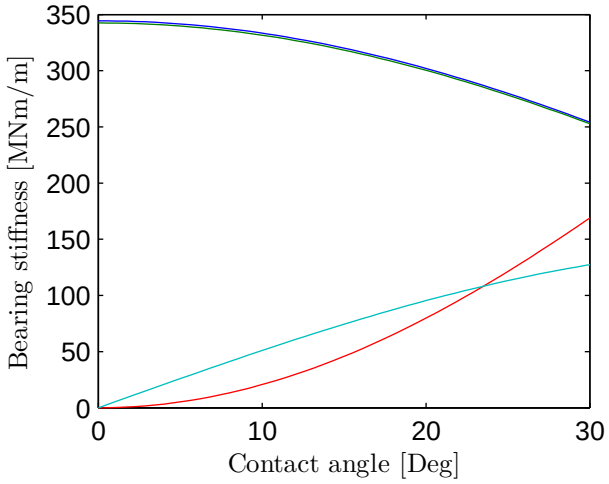

Figure 3-16: Bearing stiffness matrix terms with variation of contact angle: K_{xx} (-), K_{yy} (-), K_{zz} (-) and K_{xz} (-).

can take radial and some axial loads. This is demonstrated with the model described earlier. It was observed that for a contact angle of zero (cylindrical rollers), the affected stiffness terms correspond to those in the radial directions, i.e. K_{xx}, K_{xy}, K_{yx} and K_{yy}. In addition, when higher values of contact angle were used (tapered rollers), not only the radial components were affected but also the axial components, along with those matrix components corresponding to the rotational degrees-of-freedom. Figures 3-16 to 3-18 show the effect of the change in contact angle on the most dominant components of the bearing stiffness matrix. These results were computed with initial bearing displacements of 0.025 mm in the x, y and z directions; $K_n = 300$ MN/m^n, where n is the load-deflection exponent and it is equal to 10/9 for roller bearings; radial clearance $r_L = 0.00175$mm.

Currently, is common to find planetary stage gearboxes with cylindrical roller bearings in their planets [76]. However, the rotor of the turbine is exposed to a thrust force, which results in non-torque loads that are propagated into the gearbox and have a negative effect on the components, such as the bearings [35]. From this premise, it is seen as feasible to study the bearing loading using the tapered roller bearing model given its capability to take axial loading.

3.4 Generator control

When the reference wind turbine controller is used (in aeroelastic) simulations, the reference generator torque computed by this controller is used as an input to a 2nd order system that represents the generator. Hence, its response is a torque that is used to maintain a torque balance in the drivetrain. This is possible because the drivetrain is considered as ideal. However, when the drivetrain dynamics are accounted in a fully-coupled simulation, it is necessary to provide the turbine with the appropriate torque to

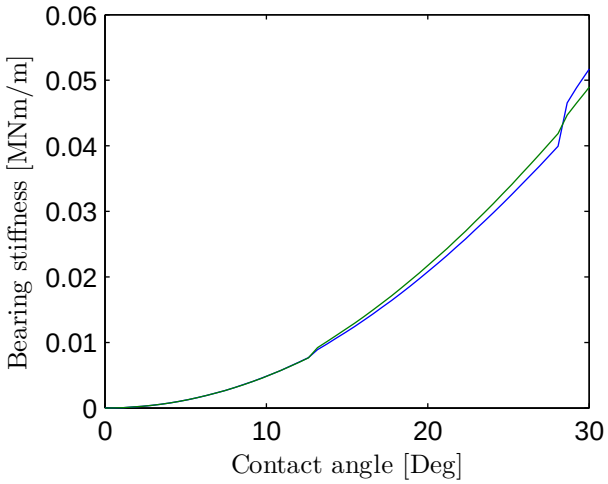

Figure 3-17: Bearing stiffness matrix terms with variation of contact angle: $K_{\theta_y\theta_y}$ (-) and $K_{\theta_x\theta_x}$ (-).

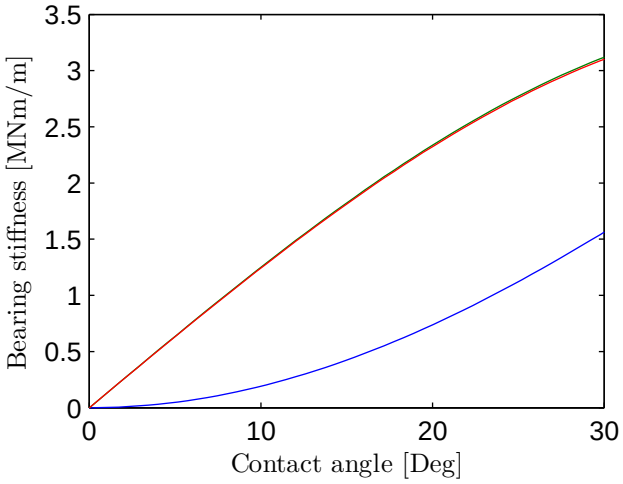

Figure 3-18: Bearing stiffness matrix terms with variation of contact angle: $K_{z\theta_y}$ (-), $K_{x\theta_y}$ (-) and $K_{y\theta_x}$ (-).

ensure stability. That is, it is necessary to include a controller for the generator torque given the torque demand from the reference controller. In this section, the controller design is described and results are shown to verify its operation. The controller described in this section is meant to be used with the PMSG described in the Appendix E. There has been different studies in the control of PMSG for wind turbine's operation such as [77, 54, 78, 79]. In all of these, the power electronics are included in the control algorithm and different coordinates transformation have to take place such as dq to abc [77], dq to $\alpha\beta$ and $\alpha\beta$ to abc [78]. However, the scope of this implementation is limited to the dynamic models of the gearbox and generator, therefore, the power electronics are not included in the models and the control algorithm. The reason for this is that with the approach taken here, it is possible to define a set of voltage profiles for studies related to the performance of the turbine under different conditions on the grid. In addition, for the studies intended here which are related to the estimation of loads and reliability of the gearbox, this is unnecessary.

The controller was designed using a linear state-space model version of the model presented previously in Equations (E.1, E.2, E.3). It was linearized at the machine's operating point, i.e. the rated values found from the results of the dynamic models after the transient period: u_{sd}^0, u_{sq}^0, i_{sd}^0, i_{sq}^0 and P_m^0.

$$\begin{bmatrix} \dot{\psi_{sd}} \\ \dot{\psi_{sq}} \end{bmatrix} = \begin{bmatrix} -\frac{R_s}{L_d} & \omega_e \\ -\omega_e & \frac{R_s}{L_q} \end{bmatrix} \begin{bmatrix} \psi_{sd} \\ \psi_{sq} \end{bmatrix} + \begin{bmatrix} 1 & 0 \\ 0 & 1 \end{bmatrix} \begin{bmatrix} \Delta u_{sd} \\ \Delta u_{sq} \end{bmatrix} \tag{3.75}$$

$$\begin{bmatrix} \Delta i_{sd} \\ \Delta i_{sq} \\ \Delta P_m \end{bmatrix} = \begin{bmatrix} \frac{1}{L_d} & 0 \\ 0 & \frac{1}{L_q} \\ 0 & \frac{3}{2}\omega_r p \psi_{pm} L_q^{-1} \end{bmatrix} \begin{bmatrix} \psi_{sd} \\ \psi_{sq} \end{bmatrix} \tag{3.76}$$

where the variables preceded by a Δ correspond to the changes around the operating setpoint. Therefore, it is possible to operate the machine at different points that are close to those defined earlier from the steady-state results.

The linear model was validated by applying a step input to the to voltage in the in the q-axis of the machine. The results shown in Figure 3-19 demonstrate the response of the linear and non-linear models. In these results is possible to see that the linear model is a good approximation and therefore can be used for the design of the controller.

The controller implemented here follows a similar structure than the one presented in [77] with the following assumptions and characteristics:

1. The power electronics are not included. Instead, it is assumed that the controller's control signals u_{sd} and u_{sq} are the output from the power electronics. That is, the controller electronics are bypassed in this study.

2. The reference variable is the torque demand from the reference controller, which is at a higher level of hierarchy in the wind turbine system. Unlike aeroelastic simulations with HAWC2, where the input to the reference controller is the low-speed shaft speed, the input here is the actual speed of the generator. It was

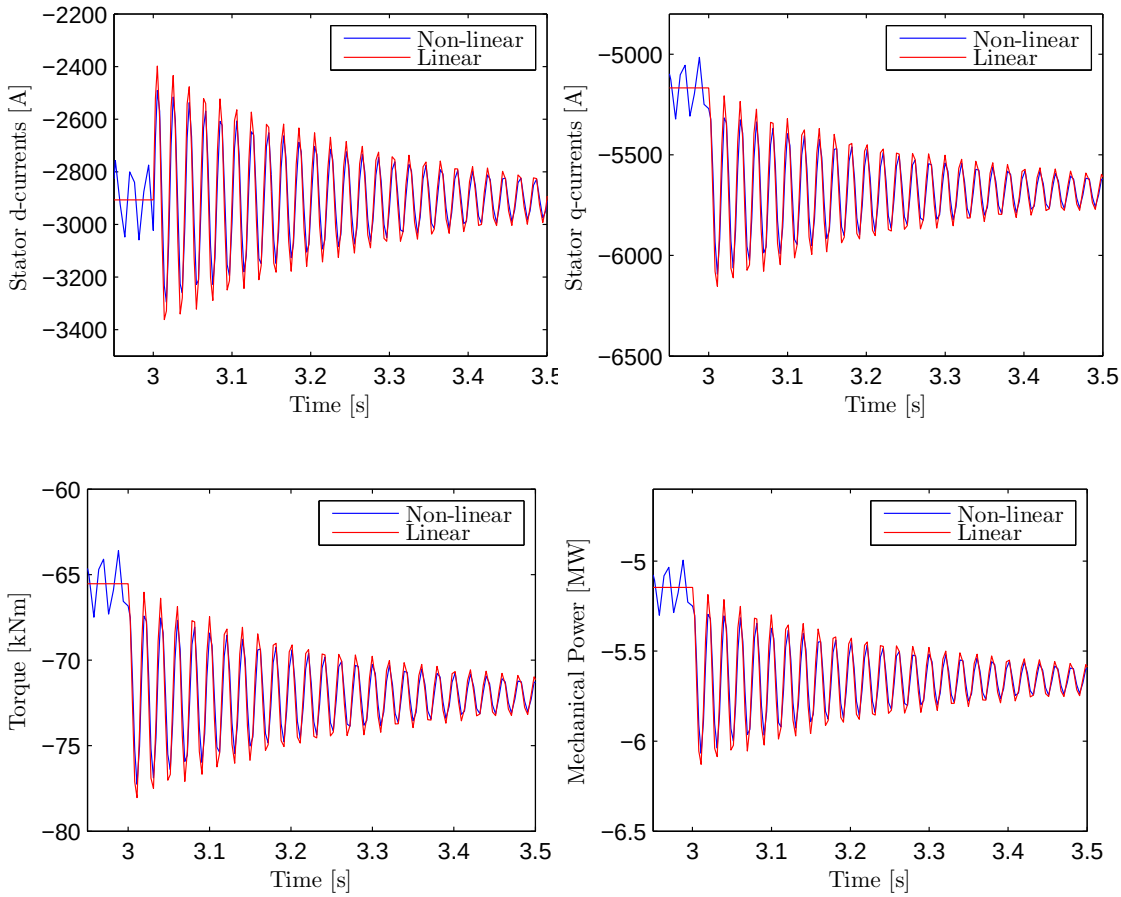

Figure 3-19: Validation of the linear model of the PMSG with respect to the dynamic model presented in Appendix E.

observed that using the conventional approach, would induce a phase-lag between the reference torque and the machine torque.

3. The different levels of the controller (Figure 3-20) are needed in order to obtain the correct reference values for the stator currents i_{sd} and i_{sq}, which are used to control the stator voltages u_{sd} and u_{sq}. These reference values must be obtained from the reference torque demand from the reference controller.

   The controller levels work on hierarchy where the higher level provides the reference values for the current level:

   - **Level 1:** It is the lower level in the hierarchy and it works as a damper of the current i_{sq}. The control signal is Δu_{sq}, which is a variation required in the voltage in the q-axis.
   - **Level 2:** Controls the voltage in the q-axis using the i_{sq}^{Ref} value.

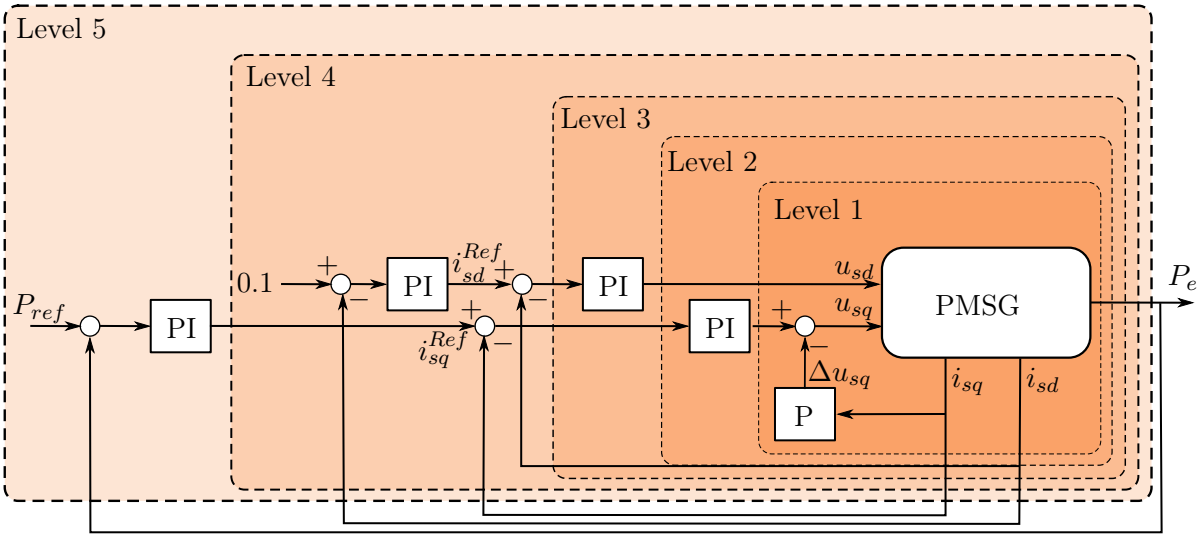

Figure 3-20: PMSG system block diagram. The controller is set-up as a hierarchy with the outer loop corresponding to the reference power. This value is obtained from the torque demand of the reference controller and the high-speed stage rotational speed.

- **Level 3:** Controls the voltage in the d-axis using the i_{sd}^{Ref} value.
- **Level 4:** It is meant to generate the correct i_{sq}^{Ref} signal, from the P_e^{Ref} value computed from the torque demand coming from the reference controller.
- **Level 5:** From the dynamic equations of the PMSG (E.3,E.4) it is possible to identify that the real power and torque of the machine are directly related to changes in the current i_{sq}. Therefore, the entire control strategy revolves around controlling this current. Moreover, the controller in Level 5 is designed to keep the i_{sd} current at a low value of 0.1.

The controller gains for each level in the hierarchy are presented in Table 3.6.

The controller is validated by applying a step equal to 80% of the rated torque. The response of the machine torque is seen in Figure 3-21, along with the resulting mechanical power. From the results, the operation of the controller is appropriate given that there is no overshoot and the settling time continues to be of around 1 s. The low overshoot characteristic is important because high variations of the machine torque could have negative effects in the loads of the gearbox, specially on realistic conditions where there are high dynamic events such as turbulent wind, wind gusts, and possible electric faults. Moreover, it has been observed that large overshoots in the dynamic system might compromise the stability of the time domain simulations in the co-simulation environment used here.

Table 3.6: Controller gains for each level in the hierarchy

Level	K_p	K_i
1	0.22400	0
2	0.02500	7.2765
3	0.04044	11.844
4	0.00043181	0.026125
5	0.15309	19.596

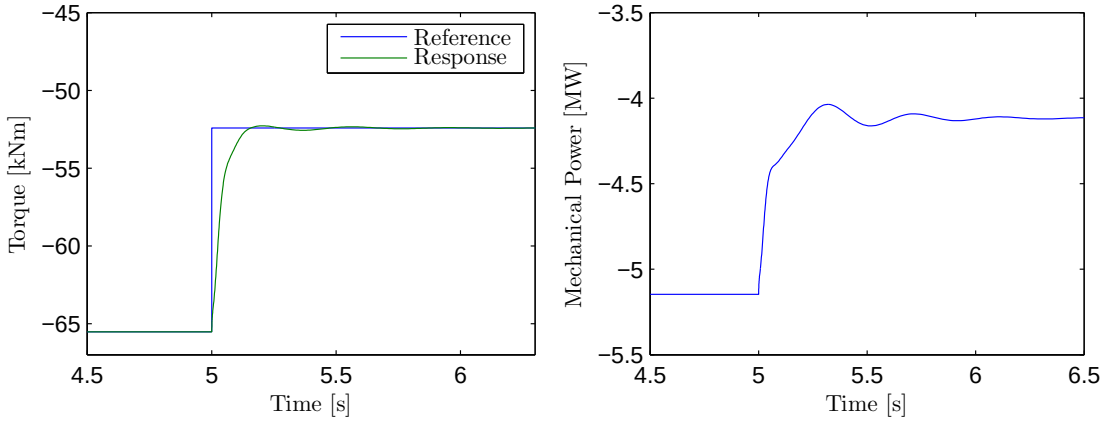

Figure 3-21: Validation of the torque controller

3.5 Electromechanical simulation interface

HAWC2 is an aeroelastic simulation and load calculation code for wind turbines. The code is based on a multi-body dynamics formulation to model the structure of the wind turbine and includes the effects of wind and waves (in the case of offshore wind turbines) on the structure. The controls are defined externally throughout dynamic-linked libraries (DLL) and it is possible to connect the model to externally defined systems, or forces, by means of DLL.

The interface between HAWC2 and MATLAB/Simulink allows for an integrated design where the generator dynamics, and/or controller can be included in the simulations. This work extends the previous approach by including a more detailed gearbox model and by using the standard wind turbine controllers.

The block diagram shown in Figure 3-22 represents the structure of the overall co-simulation system and the interaction between the tools. The wind turbine structure and wind field conditions are modeled in HAWC2, whereas the gearbox, generator and machine control are defined in MATLAB/Simulink. As shown in the diagram, there is a bidirectional communication between the two tools: *a*) HAWC2 sends to MATLAB

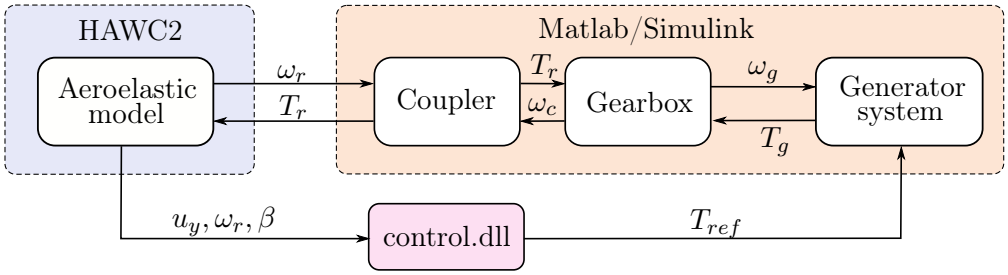

Figure 3-22: Co-simulation interface for the electromechanical models.

the rotor speed which is used by the coupler to calculate the rotor torsion at the input of the drivetrain; *b*) the calculated torsion is the input to the gearbox, but is also the reaction force seen in the shaft of the wind turbine and tower-top (Figure 2); and, *c*) the entire system is simulated using a co-simulation approach. That is, each tool models and simulates a different subsystem by defining the EOM and finding their solution independently so that their boundary constraints are satisfied. In HAWC2, the EOM are arranged in the form of Newton-Euler equations and are solved using the Newmark-beta method. The time-step is usually in the order of 0.02 s since the dynamic range of interest is usually within 0-10 Hz. In contrast, the EOMs in MATLAB/Simulink are solved using an implicit Runge-Kutta variable-step solver, which is part of the standard solver suit from MATLAB. This value is usually small in the range of 0.1 - 0.5 ms . The coupler equation (3.77) estimates the torsion at the carrier side. It is derived from the simplified version of a drivetrain, where the rotor and gearbox inertia interact via a torsional spring, e.g. a two mass model in free-free condition, where the reaction forces on each mass are equivalent in magnitude but opposite directions.

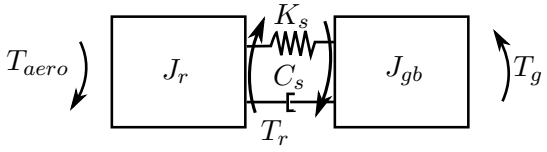

$$T_r = K_s \int (\omega_r - \omega_c)\, dt + C_s\, (\omega_r - \omega_c) \tag{3.77}$$

where T_r is the reaction moment; K_s is the main shaft stiffness; ω_r and ω_c are the rotor and carrier speed, respectively; and C_s is the main shaft damping coefficient.

When using the aeroelastic tool alone, the torque balance is achieved through the wind turbine controller which produces a torque demand that is applied to the rotor as a reaction moment. In this context, where an actual drivetrain is implemented, it is paramount to keep the torque balance in order to maintain the proper wind turbine dynamics and power production. The block `control.dll` in Figure 3-22 corresponds to a generic wind turbine controller with two main functions: *a*) to control the rotor speed with a pitch controller, and *b*) to compute the torque demand which is to be

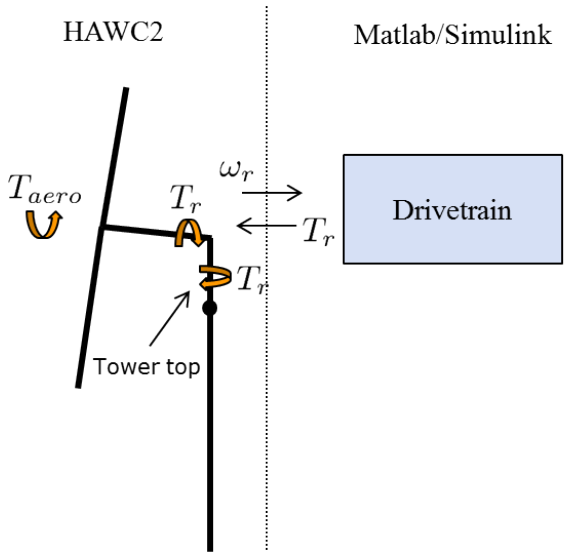

Figure 3-23: Interaction of reaction moments between the wind turbine and the externally defined drivetrain.

applied to the main shaft and tower-top as a reaction moment. When interacting with the externally defined drivetrain, the torque demand computed by the `control.dll` is used as a reference for the machine controller, and therefore, the torque balance in the wind turbine is maintained through the reaction moment computed by the coupler in (3.77) and through the gearbox.

An important aspect of the dynamic system simulation is the damping. It is known that the gearbox has very low damping in reality and due to it's free-free configuration in a wind turbine drivetrain it is prone to instability. The pole-zero map in Figure 3-24 shows the location of the poles of the state-space model for an example gearbox. The system has 52 poles in total, and several of them are located on the right-hand side, which leads to instability (Figure 3-25). Note that there is a low-frequency component that corresponds to the rotor torsion mode (free-free), along with higher harmonics due to the gearbox flexibilities. From this, some artificial damping is necessary in order to avoid numerical instabilities in the simulations. In this work, this is achieved using three different damping sources in the overall drive-train: *a*) the main shaft, in HAWC2, is damped using al Rayleigh damping $\beta_s K_s$; *b*) the gearbox is damped as well using a Rayleigh β parameter, and therefore, the damping matrix is proportional to the stiffness matrix by a factor of β_{gb}; and, *c*) the machine controller adds additional damping and it was designed taking into account a known structure for generator control in wind turbines presented in [77].

The main shaft in HAWC2 is tuned to 5% of critical damping as per the NREL reference wind turbine [49]. This value is tuned to the original drivetrain free-free frequency of 2.19 Hz. Thus, the same values for the shaft stiffness is used in the coupler equation. In addition, an eigenvalue analysis of the complete drivetrain, including the rotor inertia

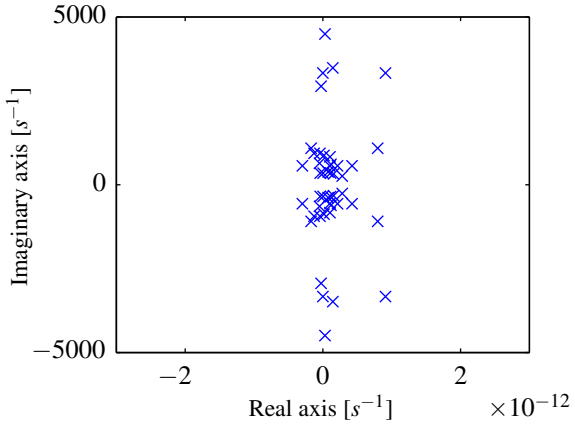

Figure 3-24: Pole-zero map for the drivetrain dynamic system before applying artificial damping.

and gearbox, results in a low-shaft mode equal to 2.48 Hz. This mode is damped in the gearbox in DUDE with $\beta_{gb} = 6.41 \times 10^{-3}$ in order to maintain the 5% critical damping ratio in the entire drivetrain.

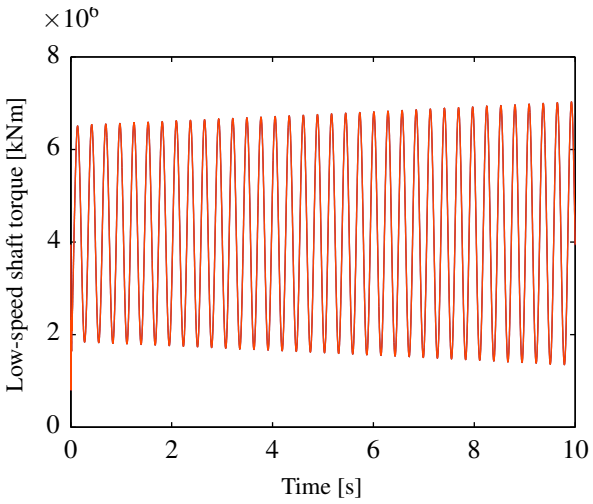

Figure 3-25: Time response of the low-speed shaft torque with zero damping.

$$f_{free-free} = \frac{1}{2\pi}\sqrt{K_s\left(\frac{1}{J_{rotor}} + \frac{1}{n^2 J_{gen}}\right)} \tag{3.78}$$

3.6 Model validation

3.6.1 Test article

The model validation (details in Section 3.6) was done using the available data from the GRC project [76]. The testing is carried on a 750 kW drivetrain (test article) with a multiple stage gearbox and an asynchronous generator. The gearbox layout is shown in Figure 3-26, where the arrangement of the gears and bearings presented here is an approximation of the configuration of the real system. There are three stages in total and are arranged in the following order: *a*) planetary stage with three equally spaced planets supported by two CRB on each planet, and with the carrier supported by two Full-Complement Cylindrical Roller Bearings (fnCRB); *b*) a parallel stage with its gear and pinion supported by two TRB on each component; and, *c*) a final parallel stage supported in the upwind side by two CRB and two TRB supporting the HSS in the downwind side.

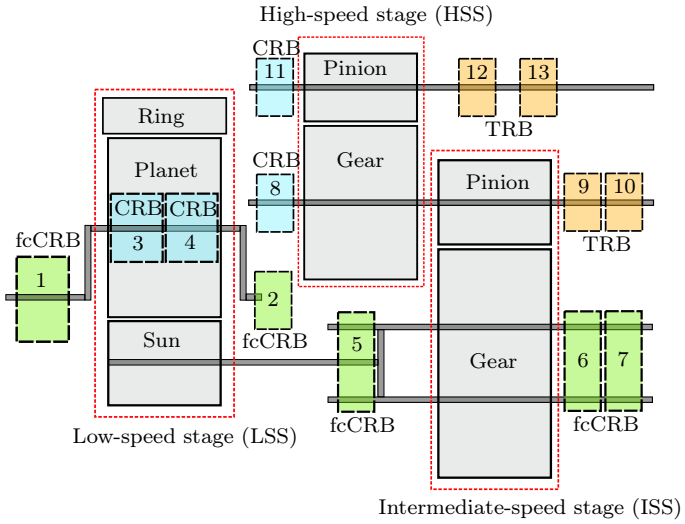

Figure 3-26: GRC gearbox configuration.

Table 3.7: Planetary stage physical parameters - GRC gearbox

Parameter	Planet	Sun	Carrier	Ring
Inertia [kg·m^2]	0.4	1.02	116.72	891
Number of teeth	39	21	-	99
Base diameter [mm]	369.46	198.83	-	937.36
Pressure angle [Deg]	20	20	-	20
Helix angle [Deg]	7.49	7.49	-	7.49
Gear ratio	5.143			
Mesh stiffness [kNm/m]	$k_{sp} = 3.5 \times 10^9$, $k_{sp} = 4.55 \times 10^9$			

Table 3.8: Parallel stages physical parameters - GRC gearbox

Parameter	Gear 1	Pinion 1	Gear 2	Pinion 2
Inertia [kg·m^2]	31.72	0.4	3.42	0.08
Number of teeth	82	23	88	22
Base diameter [mm]	652.79	183.10	424.58	106.14
Pressure angle [Deg]	20	20	20	20
Helix angle [Deg]	14	14	14	14
Gear ratio	-3.5652		-4	
Mesh stiffness [kNm/m]	$k_{pg^1} = 2.69 \times 10^9$		$k_{pg^2} = 1.89 \times 10^9$	

The generator is a fixed-speed induction machine with two synchronous speeds: 1200 rpm and 1800 rpm, which correspond to 200 kW and 750 kW power production, respectively. The machine operates at a 5% slip, which translates into operating speeds of 1206 rpm and 1809 rpm.

3.6.2 Emergency stop

The overall system is validated using the GRC 750 kW test setup during a shut-down at 25% of rated power. This process is necessary when problems arise during operation, such a grid loss or storm conditions. The process starts by disconnecting the generator from the grid. At the same time, the speed of the rotor is reduced in a controlled manner in order to reduce the impact on the structural loads. With the experimental data as an input to the drivetrain model, the shut-down case is recreated. The purpose with the next validation is to show the approach with the coupler is a valid approximation when considering torsional loading in the drivetrain.

First, from the experimental torque signal, it is identified that there is approximately 6% damping ratio in the shaft. This value includes the material damping along with the controls in the drive-system of the test rig. From the frequency domain, two main frequencies are identified (Figure 3-27). The first frequency is used as a reference for finding the damping value in the coupler equation, using Rayleigh damping as explained in the previous section.

The results shown in Figures 3-28 and 3-29 exhibit several important aspects regarding the functionality of the tool:

1. The LSS speed follows correctly the reference. This is due to the coupler equation that estimates the required torque so that the carrier in the gearbox can achieve the reference speed, and therefore, produce an adequate load transfer across the gearbox connected to the generator. It is important to highlight that the carrier speed shown in Figure 3-28 corresponds to the solution of the state assigned to the carrier after the EOMs are solved at each time-step (i.e. it is the dynamic response of the carrier).

2. The machine controller used for this test follows the reference and compensates accordingly to the step change in power.

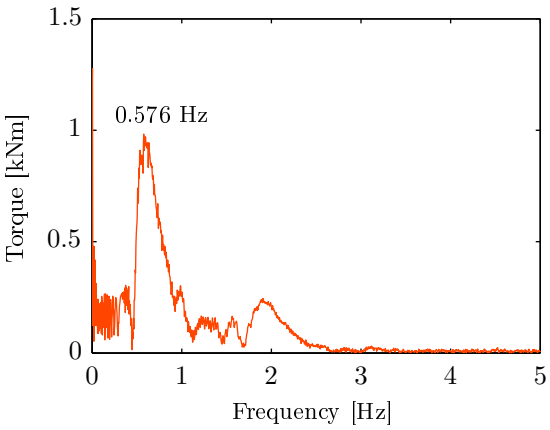

Figure 3-27: Frequency domain of the LSS torque signal in the shut-down.

3. Damping in the overall system plays an important role during transient events. Although the steady state value in the speed agree, it is observed that the steady state of the torque is not as accurate. This is due to the difference in the control parameters from the simulation and the real system. In addition, the torque displays a peak around 110 s, which corresponds to a small change in the speed (Figure 3-28). This reaction is due to a change in the error value between the reference and the carrier speed in the coupler equation. However, it is concluded that the assumed damping in these simulations is appropriate given the level of agreement between the experimental data and the simulations.

It is shown then, that the methods used to simulate the drivetrain are an appropriate approximation of the general dynamic behavior of the drivetrain test setup. With reasonable accuracy in the load transfer throughout the drivetrain, it is possible to say that this model is suitable to represent the physics of wind turbine drivetrain dynamics without incurring into expensive computations. It is also possible to extend the model to the complete test-rig, considering the external loading in the wind turbine structure, which can be improved further for testing using hardware in the loop techniques.

3.6.3 Normal operation

In addition, the validation of the calculated planet bearing loads by the tool is presented. In this test, the dynamo-meter is ran at steady conditions under three power levels: 25, 50 and 100% of rated power. No non-torque loads or steps in torque, or speed, are applied. The results are presented in Figure 3-30.

The results show a good agreement between the two models and the experiment. The variation of low-frequency vibrations in both, corresponds to the mode associated with the shaft torsion. The simulation is carried out by using the speed signal as reference. The speed data from the experiments is used as a reference and the machine controller

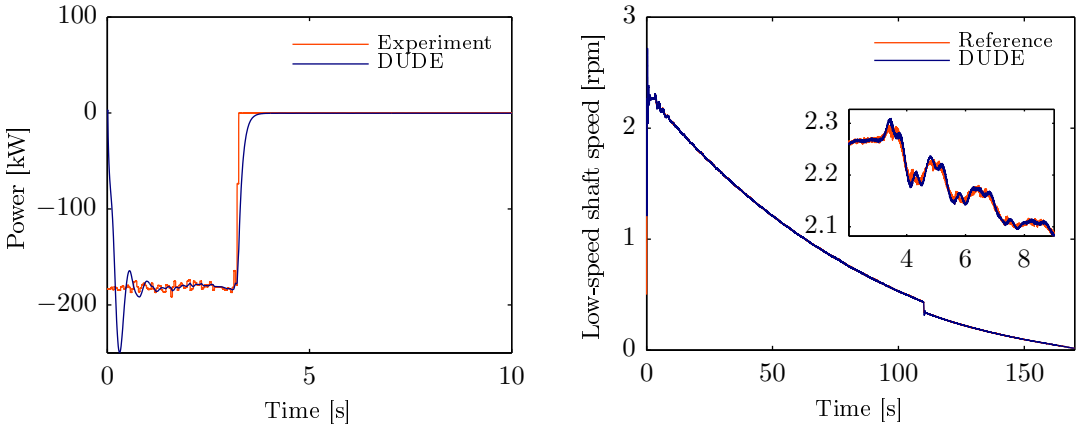

Figure 3-28: Validation of the dynamic response of the drivetrain model. The figure shows the generator electric power and speed in the low-speed shaft.

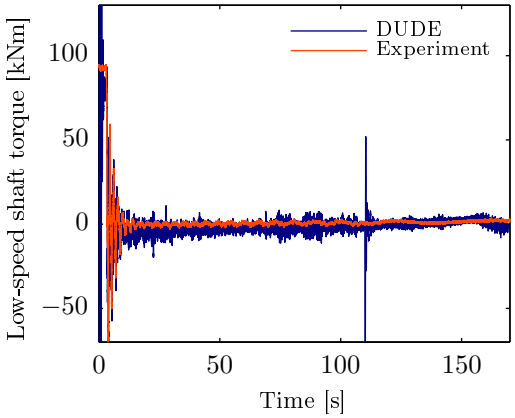

Figure 3-29: The response of the coupler equation to an experimental reference of the low-speed shaft speed.

reference is set to each power level.

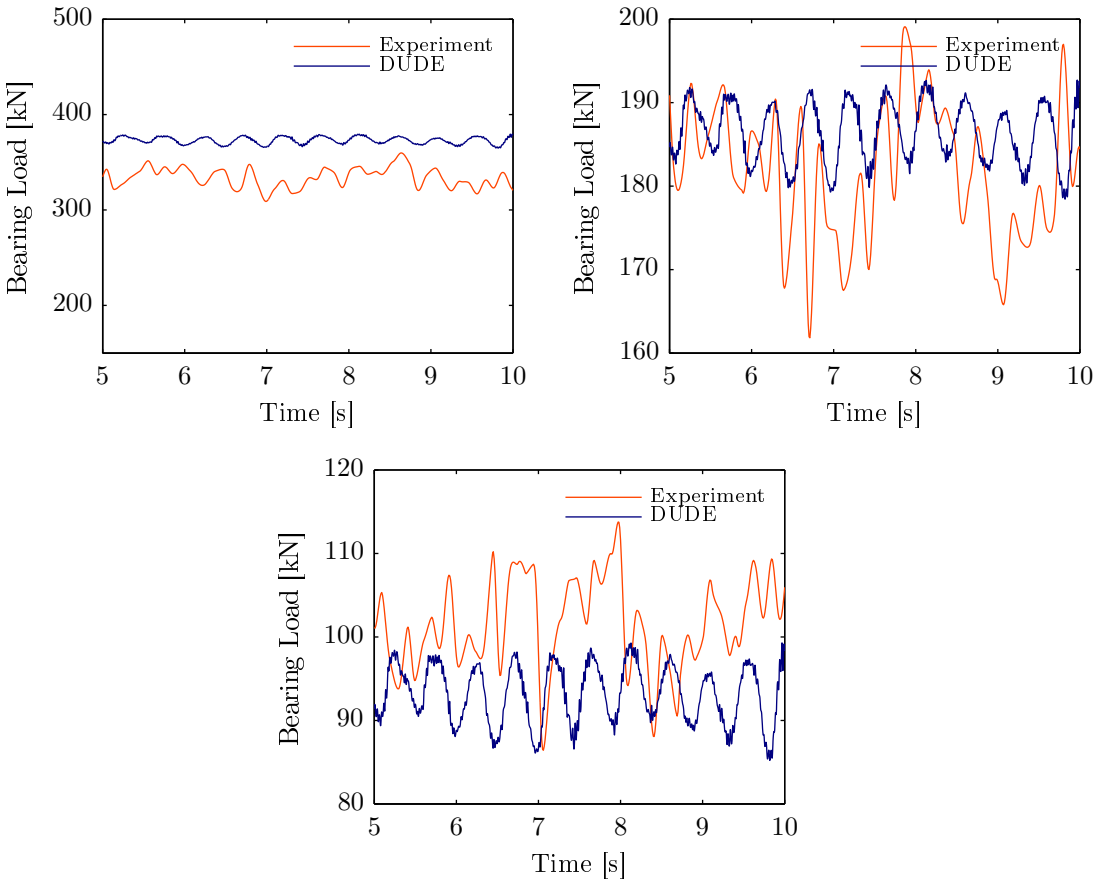

Figure 3-30: Bearing force comparison for three different power levels. From left to right: 100%, 50% and 25% (bottom).

3.7 Conclusions

This chapter presented a series of models developed throughout the length of this dissertation. First, a multibody dynamics implementation was done in order to model the gearbox using the gear constraints and the Newton-Euler formulation. The model of the planetary gearbox was used as an example to show the capabilities of the tool and its limitations. It was concluded, that the high computational time needed to perform a simulation that complies with the certification load cases in the IEC standard for wind turbine design, is a major drawback. The result was consistent to those found by other researches and the limitations in computational time were identified, along with issues in the constraint violation, unless stabilization techniques were used. It was shown that for a simple planetary gearbox example, with a small simulation time (10 s), the performance of the code won't be successful for a load case simulation (600 s, plus additional 100 s to pass the transient phase) given the high computational time and issues found with the gear constraints.

From this, it was decided to seek other alternatives to model the gearbox. A simple, yet accurate model was implemented based on the theory of lumped-parameters. In this approach, the topology of the gearbox is simplified and the load transfer between gears and gearbox stages was achieved through linear flexible components defined as springs. It is important to highlight that the models needed for the success of this thesis not only rely on a gearbox model, but also to the coupling with an electrical component as the generator. This adds states into the solution of the overall EOM, along with the necessary controls that maintain the system in equilibrium. Hence, the electromechanical interface presented here showed a method where the gearbox is coupled to a generator model and an aeroelastic tool, i. e. HAWC2. With this approach, the wind turbine reference model and controller are used in full in order to maintain the fundamental dynamics specified in the wind turbine design.

The gearbox model, it's coupling with the generator and the overall response of the system was validated using experimental data from the GRC project at NREL. The validation case was a shutdown exercise where the transient behavior of the drivetrain test-rig was matched by the model. It was shown that the system stabilizes at the reference points dictated by the nature of the system. That is, being in a free-free condition in which the input torque and generator torque based on the power requirements are highly important for the stable operation of the entire drivetrain. Moreover, the bearing radial loads obtained by the model were validated under normal operation conditions at three different power levels.

Using the results from this chapter as a basis to gain confidence in the functionality of the tools developed here, the studies presented in the rest of the dissertation use the same approach with variations in the drivetrain configuration, i.e. using either a PMSG or a DFIG. With this, it is possible to run different types of load cases following the guidelines in the IEC standard 61400-1 [10], and assess their impact in the drivetrain bearings.

4

Loading under normal operation

This chapter establishes validated models that can accurately account for the dynamics of the gearbox, along with the external dynamics that excite the system. A drivetrain model implementation is used where the gearbox and generator are coupled to the wind turbine structure in the dynamic simulation environment presented in Section 3.5. The wind turbine is modeled using HAWC2 and the gearbox is described using lumped parameters in MATLAB/Simulink. Each component in the gearbox model includes rotational and translational DOFs, which allows the computation of the bearing and gear-mesh loads. However, emphasis is made to the planet bearings. The drivetrain model is configured for a 5 MW power capacity and coupled to the corresponding wind turbine and load simulations are carried out under turbulent wind following the guidelines from the IEC 61400-1 standard [10]. Fatigue analysis shows the effect in the bearing damage equivalent loads, when including a detailed drivetrain model in the overall wind turbine simulation for a 20 year period. Results show a higher level of damage (up to 180%) when the detailed model is used in comparison to a simplified approach for load calculation. It is found that some of the wind turbine modes can have negative consequences on the life-time of the planetary bearings.

4.1 Introduction

One of the biggest challenges today is to design reliable wind turbines, especially with the expansion of offshore wind farms, where repair and maintenance can be very costly. Today, most of the downtime of wind turbines are accredited to the gearbox [14], along with the generator, making the drivetrain one of the most critical sub-systems in terms of reliability. Several major studies over the last decade have been dedicated to investigate the gearbox dynamics and its subcomponents within the wind turbine context [3, 80, 26, 28].

Gearbox dynamics have been studied for several years and the literature is extensive. Lin and Parker [30] and Kahraman [32] developed linear and non-linear lumped-parameters models for the helicopter and automotive industry. However, these investigations were made from a generic point of view, i.e. on the generic model of planetary

gears. From here, Peeters [3] applied different types of modeling techniques in increasing complexity, focusing on linear time invariant (LTI) systems and extended the models to helical gears. He also presented a study on a complete gearbox from a wind turbine. First, he verified the different vibration modes present on a planetary gearbox such as rotational, translational and planet. Second, he extended the current modeling techniques to the use of *flexible multibody models*, where additional DOF are included to represent the body deformation. Helsen [38] continued Peeters work by analysing the dynamics of a full wind turbine gearbox in different levels of complexity. Although the more detailed models provide a good insight regarding the loads experienced by the drive train, the author calls for models that describe the dynamics at the component level using flexible multibody dynamics. The major disadvantage with theses modeling techniques is the computational cost, and the lack of publicly available models tailored to the prediction of fatigue design loads on wind turbine gearbox bearings. While the models need to be simple enough for fast computation, they should adequately represent the system such as possess off-diagonal terms in the bearing stiffness matrix, which can have a significant effect in the gearbox global behavior. The studies presented in [81, 36] are a comprehensive investigation of the effects of non-torque loads, gravity, bearing clearance, nonlinear mesh stiffness, and input torque in the planetary gear loads. It was demonstrated by simulation, and experimental verification, that the bending moments caused by non-torque loads such as tower shadow, rotor weight, wind induced moments, thrust and the tilting of the nacelle, can produce external excitations in the carrier frame leading to an increment in the gearbox internal loads and the uneven distribution of the load share among the planets. Further, several variations of lumped-parameter models are available in the literature within the context of wind energy. For instance, the work in [71] implemented a multi-stage gearbox model based on the work of [30] and investigated the torsional and radial vibrations of the gears, specially in the planetary stage. Similarly, the work in [82] implemented a variation of the existing lumped-parameters model and used a torque signal caused by random wind speed to study the dynamic behavior of the gears inside a planetary stage. The work on [83] coupled a planetary stage gearbox with an aeroelastic wind turbine model implemented in HAWC2 [17]. The results showed the effect of the gear teeth loads when including double-contact in the gear model, and considering the dynamics of the complete wind turbine. However, the bearings are considered rigid, the gearbox was represented by a planetary stage only, the gears where allowed only to rotate and the generator was modeled ideally.

Some other studies have implemented the drivetrain dynamics, along with an aerolastic model of the wind turbine, but they use very high fidelity models (FEM), followed by a condensation of the DOF using super-elements. Even though the super-element approach reduces computational time, it can be quite demanding to run a full load case simulation for certification and fatigue studies. As pointed out by [84], during the design of wind turbine components it is paramount to test the model through several load cases. In addition, it is recommended to include the drivetrain dynamics in order to simulate LVRT of wind turbines, since this allows simulation conforming to national grid codes [6]. These requirements call for an approach which provides accurate loading time-series

at the internal components of the drivetrain within a stipulated computation time. In this chapter, an integrated approach [18] is extended to include a detailed model of the drivetrain (gearbox and generator), along with the wind turbine structure. The code developed here focuses on the bearings loads, which are obtained by a dynamic model that accounts for the translational and torsional degrees-of-freedom. Compared to a HAWC2 simulation without drivetrain dynamics, the proposed tool takes approximately 1.6 times more to solve the EOM, depending on the platform used.

4.2 Wind turbine loads validation

4.2.1 Methods

First, let me describe the simulation setup used. The wind turbine corresponds to the 5MW NREL Reference Wind Turbine [49] and it is simulated in HAWC2. It is a variable-speed, collective pitch turbine. For the coupled simulation using the Wind Turbine and Drivetrain Under Dynamic Excitation code (WTDUDE), the configuration shown in Figure 3-22 is used with the Risø controller [85]. The controller used here is a reference controller that ensures the wind turbine dynamics of the baseline system are not changed.

The drivetrain is composed of a multi-stage gearbox (same configuration as the one presented in Section 3.6.1) and a PMSG (see Appendix E). The purpose of these studies is not to design a gearbox, and therefore, the geometric parameters are not conforming to a manufacturer's design. The physical parameters available from the previous design of the 5MW PMSG presented in [12] and the gearbox presented in [71], it is possible to obtain a complete drivetrain by scaling the parameters to meet the gear ratio and inertia requirements. The mass and inertia properties were scaled using the power scaling laws:

$$k_m^{up} = \left(\frac{P_2}{P_1}\right)^{3/2} \tag{4.1}$$

$$k_i^{up} = \left(\frac{P_2}{P_1}\right) \tag{4.2}$$

where k_m^{up} and k_i^{up} are the upscaling factors of the mass and inertia, respectively. The values used here are: $P_2 = 5$ MW and $P_1 = 1.5$ MW, for the planetary stage; and $P_2 = 5$ MW and $P_1 = 750$ kW for the parallel stages. The physical parameters of the gearbox stages are presented in Tables 4.1 and 4.2.

The content of the rest of the section is meant to serve two purposes:

- basic validation of the wind turbine loads from WTDUDE using HAWC2 as a reference, and
- long-term fatigue analysis of the loads in the planetary stage bearings.

Table 4.1: Planetary stage physical parameters - 5MW gearbox

Parameter	Planet	Sun	Carrier	Ring
Inertia [kg·m^2]	120	23.33	1960	2970
Number of teeth	45	30	-	117
Base radii [mm]	630	430.4	-	1638
Pressure angle [Deg]	22.5	22.5	-	22.5
Gear ratio	4.90			
Mesh stiffness [kNm/m]	$k_{sp} = 2.3 \times 10^9$, $k_{sp} = 1 \times 10^9$			

Table 4.2: Parallel stages physical parameters - 5MW gearbox

Parameter	Gear 1	Pinion 1	Gear 2	Pinion 2
Inertia [kg·m^2]	220	1.3	140.04	15.446
Number of teeth	94	22	64	22
Base radii [mm]	752	180	600	199.3
Pressure angle [Deg]	20	20	20	20
Gear ratio	-4.17		-3.04	
Mesh stiffness [kNm/m]	$k_{pg^1} = 3.20 \times 10^9$		$k_{pg^2} = 3.20 \times 10^9$	

4.2.2 Validation of the coupled analysis

The main purpose of this section is to study the effect in the wind turbine response of including an external drivetrain using the method presented here. As shown previously in Figure 3-23, the components that are more affected by the drivetrain are the main shaft and tower of the wind turbine. Therefore, the results presented here focus on the loading of these components.

The wind turbine is simulated using the guidelines for the power production Design Load Case 1.2 from the IEC 61400-1 standard [10]. This corresponds to the operation of the wind turbine across a range of wind speeds 5 m/s-25 m/s under NTM (Normal Turbulence wind Model) with 10 min duration, for each simulation. The simulations are performed on increments of 2 m/s bins and 6 random turbulence seeds are used for each wind speed. The purpose of these simulations is to validate the performance of the wind turbine when using the detailed drivetrain proposed in this work (WTDUDE), and to estimate the fatigue damage equivalent loads on the internal components of the gearbox. The results of the detailed wind turbine model results are compared to those from a simulation using an ideal drivetrain (HAWC2). (Note: even though 6 seeds were used for the simulation, only one representative seed is shown in the validation results).

First, the time series of the rotor speed and torsion in the main shaft for a wind speed of 7 m/s are presented in Figure 4-1. It correspond to the wind turbine's operation below rated wind speed. Due to the higher wind turbulence intensity and no control action in the pitch, it is more valuable to show the operation of the wind turbine with WTDUDE in order to show the capabilities of the coupling and the controls. From the results it is observed that in the time domain the simulation with WTDUDE performs as expected.

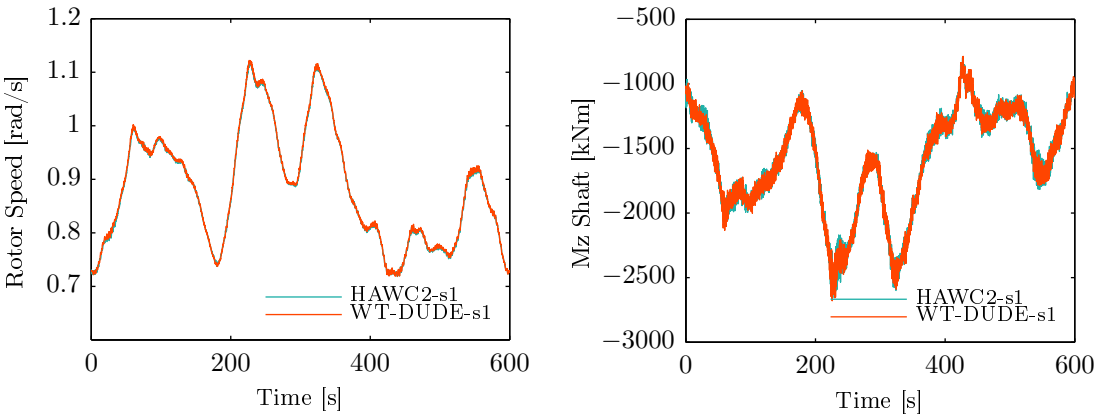

Figure 4-1: Time series of rotor speed and main shaft torsion for seed No. 1 at 7 m/s.

In addition, the frequency domain analysis (Figure 4-2) shows that the differences in the loads are not significant. There is, however, a small difference in the frequency concerning the drivetrain torsion mode. In HAWC2, this frequency corresponds to the free-free drivetrain mode with the turbine under normal operation. The value of this mode depends on the torsional stiffness of the main shaft and the drivetrain and effective rotor inertia. When using WTDUDE, the effective torsional stiffness is slightly different since the internal flexibilities of the detailed drivetrain come into the picture. This results in a frequency shift of the drivetrain torsion. The difference is small in the range of 4%.

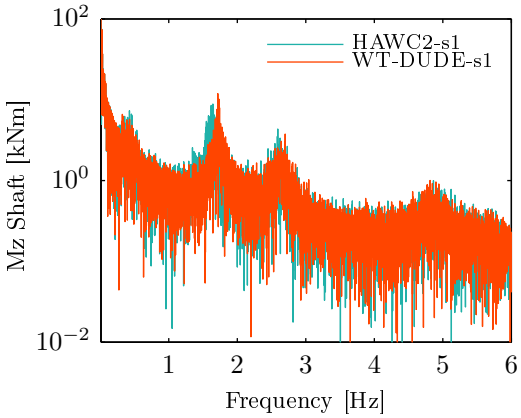

Figure 4-2: Torsional loads of the shaft in the frequency domain.

An additional verification is done by comparing the mean and standard deviation at every wind speed for one of the seeds with the purpose of verifying the mean loads and variations for both methods. The standard deviation corresponds to the variation of the load, with respect to the mean level,and it is due mainly to the wind turbulence intensity.

The mean value is achieved by means of controller action after rated wind speed. The sensors studied are the rotor speed, electric power, the tower-top moments, torsion in the shaft, and side-to-side tower base moments. The results show a good agreement across the wind speed spectrum. However, it is observed that the torsional moment in the shaft (Mz shaft) has small differences in the standard deviation for wind speeds higher than rated in HAWC2 simulations. The reason behind the difference is explained in the next section.

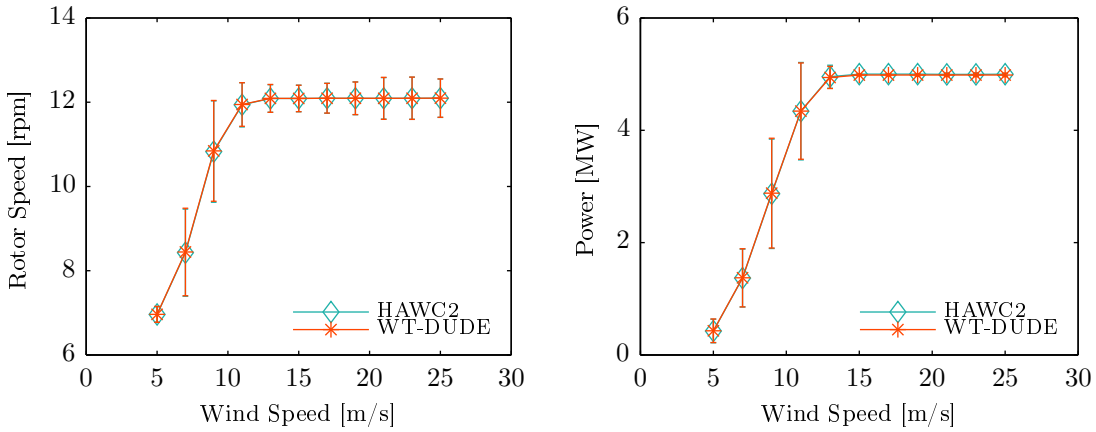

Figure 4-3: Mean and standard deviation of the rotor speed and power produced by the generator model.

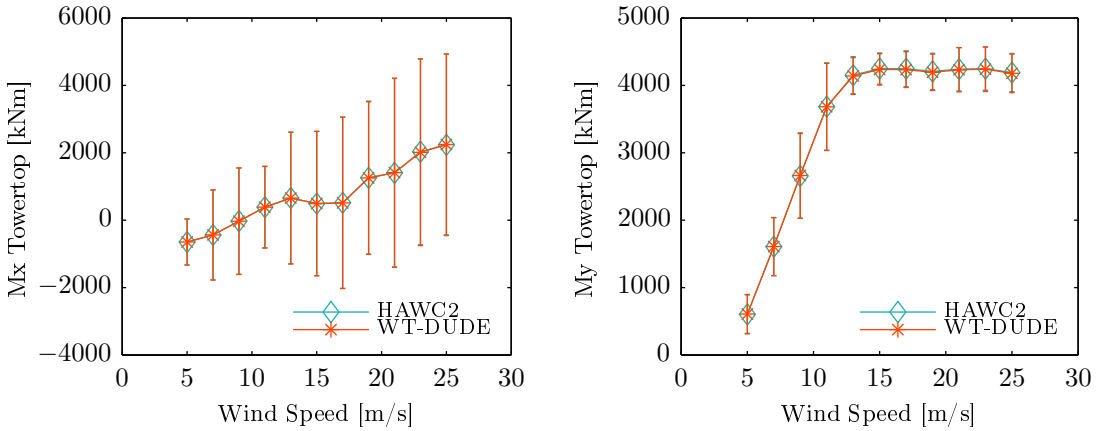

Figure 4-4: Mean and standard deviation of the tower-top fore-aft (**left**) and side-to-side (**right**) moments.

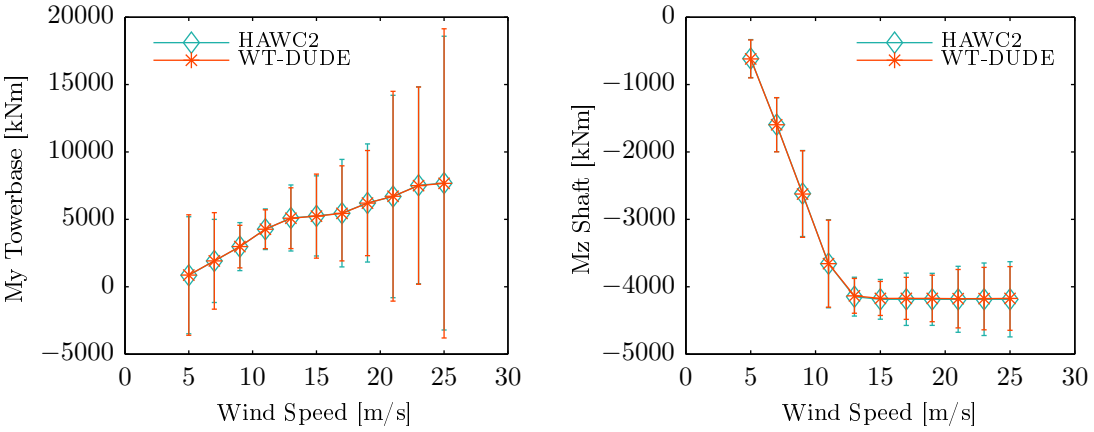

Figure 4-5: Mean and standard deviation of the tower-base side-to-side and shaft torsional moment.

4.3 Fatigue analysis

The previous results show the capabilities of the tool to estimate the loads in the drivetrain internal components and in the wind turbine. This section is intended to show the impact of including a detailed drivetrain in wind turbine DLC simulations by presenting results concerning the Damage Equivalent Load (DEL) for the radial loads in the planet bearings; the turbine's main shaft torsion and bending; tower top side-to-side moment; and tower base side-to-side moment. These elements from the wind turbine structure are chosen for the study since they are directly directly connected to the gearbox, and therefore, it is expected to be affected by the introduced model.

The fatigue DEL (S_{eq}) corresponds to a constant load amplitude value that represents the loading the component will experience during its lifetime (reference load cycles, N_{eq}), with respect to a load level (S_i) at a number of cycles (n_i). In addition to the load range and cycles, this value depends on the material, which it is specified using the Wohler exponent m. DEL is calculated using equation (4.3):

$$S_{eq} = \left(\frac{1}{N_{eq}} \sum_{i=1}^{n_b} n_i S_i^m \right)^{\frac{1}{m}} \tag{4.3}$$

The values of n_i and S_i are obtained using the Rainflow counting algorithm, and N_{eq} is related to the expected lifetime of the component. In this work, 6 seeds where used and each seed corresponds to 10 min operation of the wind turbine. It is expected the wind turbine lifetime to be 20 years, therefore, the sample simulation results for one hour are scaled to 20 years. In addition, a more realistic approach would include the annual mean wind speed distribution. For the 5MW NREL Reference Turbine, a class II wind turbine, the wind distribution is assumed to follow a Weibull distribution with and exponent equal to 2. The results for the DEL computation for a 20 year period are

obtained using equation (4.3) and the Cumulative Density Function (CDF) of the wind distribution.

Planet Bearings Long-term Damage Assessment

The bearing loads are analysed using two approaches. First, with the detailed gearbox model the bearing loads are calculated using the translational displacement of the planet bodies and bearing stiffness. Since it is a dynamic simulation, the displacement time-series is a result of the reactions from the gear body in the bearings due to the interaction through the gear mesh forces in the teeth. Changes in the velocity and torque coming from the wind turbine, and generator, affect the overall dynamic response of the bearings. For comparison purposes, the second approach is to estimate the bearing loads with a kinematic formulation based on the input torque of the gearbox and the planet carrier dimensions. This approach is similar to the one presented in [86], where it was used to find the gear teeth forces. This relation is defined as:

$$S_b = \frac{1}{N}\frac{T_{in}}{r_c} \tag{4.4}$$

The ratio $1/N$ relates to the load distribution from the carrier to the planets, where N is the number of planets. The time-series of the bearing loads using both approaches are used to calculate the DEL for the life-time of the wind turbine. The results are presented in Figure 4-6.

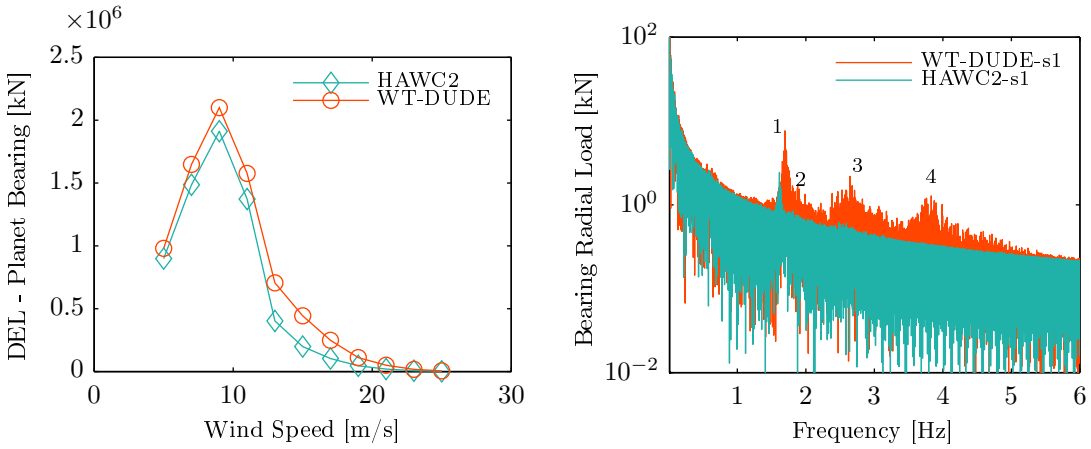

Figure 4-6: **Left:**Damage equivalent loads corresponding to the planet bearing radial loads. **Right:** frequency response of the the planet bearing radial load at 13 m/s. The numbers 1–4 are labels representing four different modes explained at the end of this section.

Notice the large difference in the damage equivalent load results between HAWC2 and WTDUDE. This is due to a number of reasons:

- When using the kinematic approach using the input torque to the ideal drivetrain, the higher dynamic content that appears due to the gearbox internal flexibilities in the bearings, gear mesh and connecting shafts, along with the interaction with the generator dynamics, is omitted as in the original HAWC2 simulation.
- WTDUDE calculates the bearing loads for every time step of the simulation in MATLAB. Hence, any reaction due to changes in the wind conditions and gearbox dynamics are accounted in the bearing loads. This is an appropriate approach since the bearings experience many dynamic events such as changes in torque directions, acceleration and deceleration, in addition to possible emergency stops.
- From the computational dynamics point of view, when using WTDUDE, MATLAB/Simulink solves the EOMs at a smaller time-step which translates into a higher content of dynamics in the bearing loads. Incidentally, there are more load cycles present in the final time-series and this produces a higher fidelity result in the damage load calculation.

The frequency analysis of the radial bearing loads show the presence of modes with higher energy content when computed with WTDUDE, which explains the higher long-term damage results. In contrast, these modes have very low energy content in the computation of the loads using as in traditional aeroelastic software (4.4). The following list provides a description of these modes:

1. **Frequency** ≈ 1.6 – Drive-train torsion. It was explained, and justified, before the frequency shift on this mode when using WTDUDE. In contrast with the previous results, it is seen that this mode has more energy content in WTDUDE when compared to HAWC2.
2. **Frequency** ≈ 1.8 – 2nd symmetric rotor edge.
3. **Frequency** ≈ 2.67 – 2nd symmetric rotor flap.
4. **Frequency** ≈ 3.8 – From a modal analysis of the entire system, which includes the rotor inertia, gearbox and generator it is found that this mode is a combination of the torsion in the intermediate and high speed gear stages, and the generator.

The previous analysis shows the benefits of including the wind turbine structure in the analysis of the internal components of the drivetrain.

Long-term Damage of Wind Turbine Structure

In addition, it has been observed that the wind turbine loads that are more affected when WTDUDE is used are the tower top and tower base side-to-side moments (Figure 4-7). The fatigue results indicate that the presence of a gearbox model in the overall system simulation has an effect in the long-term damage of the tower components studied here. This is especially true for the tower base side-to-side moment. Furthermore, the results

for the main shaft torsion are nearly the same using both software (Figure 4-8). This is due to the presence of additional controls, mitigating the dynamics of the drivetrain. Moreover, there is active damping associated with the generator control system that causes a reduction on the damage loads. The main shaft bending is not affected by the introduction of a detailed drivetrain because the coupling in the co-simulation approach is done only in the torsional DOF.

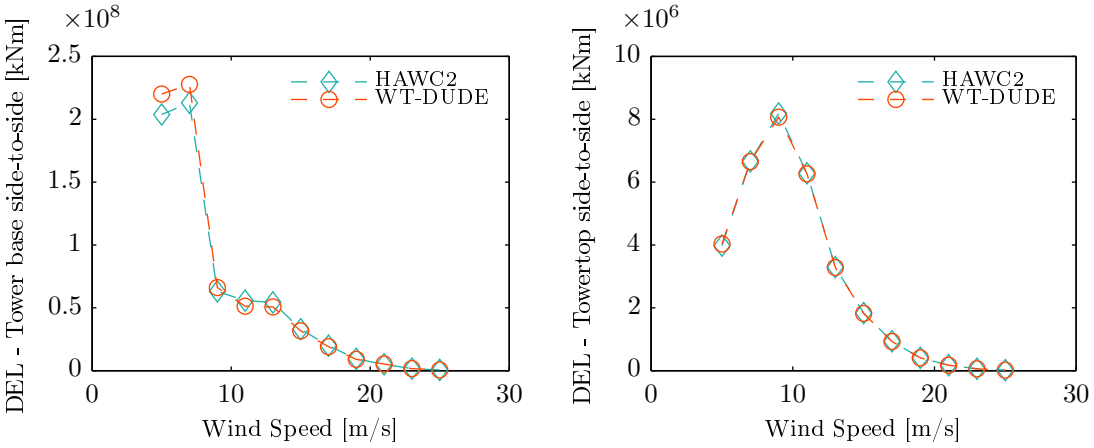

Figure 4-7: Damage equivalent loads results of the wind turbine structure in the tower components.

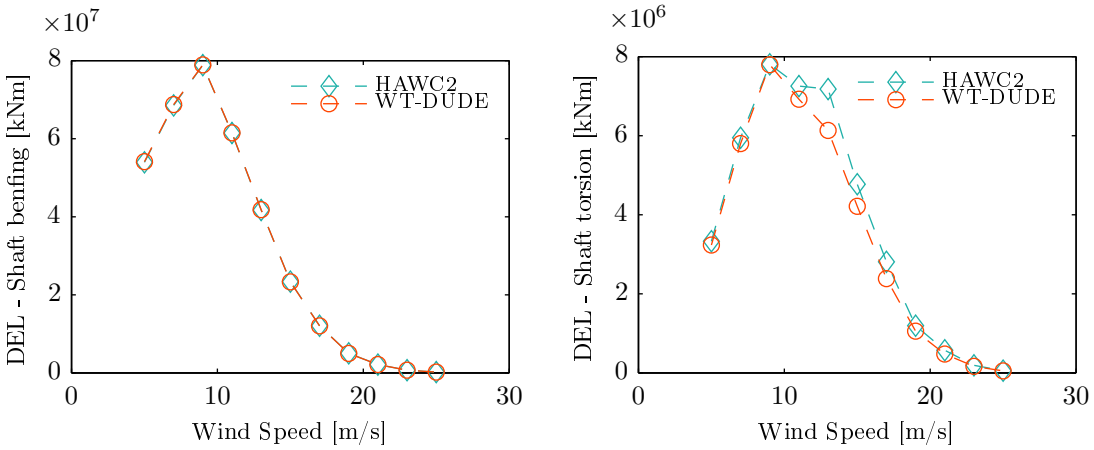

Figure 4-8: Damage equivalent loads results of the wind turbine structure in the main shaft.

4.4 Conclusions

This chapter describes the implementation of a computationally fast simulation tool that can be used to study the loading of the internal components of a drivetrain while dynamically coupled by torsion to a wind turbine structure. The assumptions for the gearbox model do not disregard the non-linearities that are inherent in the torsional dynamics. This setup was shown to perform complex studies for the bearing displacement and gear mesh interaction. In addition, when comparing wind turbine loads, the use of the tool together with HAWC2 showed that the dynamics of the wind turbine are not drastically affected, which provides confidence in the overall system simulation. The shift in the drivetrain torsion mode is interesting from the controller design point of view, since the results presented here allow for speculations in the wind turbine controller design with a detailed drivetrain model. The benefits are not constrained only to the purpose of a more robust controller, since the detailed approach can contribute to the drivetrain load reduction through controller design.

Here, it was chosen to present fatigue studies using the design load case 1.2, power production, of the IEC 61400-1 standard. It is important to highlight that the tool's computational time is very appropriate to such studies, given that it takes in average 30 min to obtain 10 min (600 s) simulation time. This is substantially an advantage compared to FEM models where the computation time can be hours for the same purposes.

Fatigue analysis showed the effects of including a dynamic model in the wind turbine simulation, especially for the long term damage load computation of the bearings in the planetary stage. The results showed that above rated wind speeds the difference in damage is up to 180% higher when the detailed model is used. This shows that there might be an underestimation of the fatigue in the planetary stage bearings when using simplified models, or even with de-coupled approaches. The higher damage found by WTDUDE is due to the presence of wind turbine modes in the bearing loads computation. This could be an explanation on the failure of these bearings and it justifies why it is important to consider the entire wind turbine system during the design stage. It was also shown how the addition of a drivetrain model affects the results in the wind turbine loads fatigue analysis in the tower top, tower base and main shaft.

5

Extreme loads in wind turbine drivetrain components

5.1 Introduction

It is common that every year, different regions set new goals for reducing the carbon emissions by minimizing the usage of fossil fuels in energy production. To accomplish these goals, it is necessary to increase the installation of renewable energy facilities. In Europe, wind energy plays a significant role with a goal of increasing energy production from renewable resources up to 27% by 2030. In Denmark, renewable energy accounts for up to 40% of the energy production in the country. With more installations of wind turbines and wind farms to come, it is necessary to assure a stable operation by increasing the reliability of the components in the system and by developing control strategies that ensure stability. These two premises apply to the operation of the turbine when wind conditions are appropriate, but there are certain events that may have an impact on the operation and life-time of the components. One example, is an electric fault in which the grid is disturbed with a short circuit or a voltage sage affecting the turbine operation. In the past, when the number of wind turbines connected to the power system was rather low, they were not required to contribute to the voltage recovery during and after a fault, hence disconnecting.

This chapter investigates the impact of different load cases that drive the damage of wind turbine components due to extreme loading. Along with the established cases in the IEC standard 61400-1 [10] such asDLC 2.3 and 5.1, the grid code requirements are considered by including a LVRT in the DLC 1.1 simulation. The study is carried out using an electromechanical approach where a detailed wind turbine structure (modeled with HAWC2), and a detailed drivetrain that includes the gearbox and the generator dynamics (modeled in Matlab/Simulink), are coupled in a co-simulation environment (see Section 3.5). The effect of the extreme events is quantified in the gearbox bearings in terms of their maximum loads under different wind conditions. Results show the impact of the different extreme cases and the LVRT requirements in the gearbox bearings.

5.2 Extreme events strategies

The load cases simulation strategies in this approach are carried out by combining actions in both tools: HAWC2 and Matlab/Simulink. The investigation presented here is done in the context of co-simulation where the different models are dynamically coupled, i.e. wind turbine structure, gearbox, generator, controls and power system (see Section 3.5). Therefore, there is a coordination between the wind turbine controller and the external drivetrain. This section presents in detail the interaction of the two tools for each extreme case, their implication in terms of the response of the drivetrain, and the simulation setup for each event.

5.2.1 Low-voltage ride through

The FRT requirements (also refereed to as LVRT in case of voltage sags) for wind turbines are common in almost every country's grid code. Nowadays, a considerable portion of the overall power production comes from wind energy, so it is considered mandatory to avoid the disconnection of the turbines from the grid during electric faults to ensure stability in the power system [87]. In addition, the wind turbines are required to provide reactive current to the grid during a FRT operation in order to support the grid voltage level recovery [6, 88] (summary in Table 5.1). Earlier studies have focused on the operation and control of different wind turbine generator systems during grid faults [89, 54, 77, 90]. These studies described different strategies to control the response and mitigate the impact on the power system and torsional vibrations of the main shaft, as a result of the FRT capability. However, it has been shown by [91] that considering a reduced two-mass model to represent the wind turbine rotor dynamics it is not necessary to asses the impact of a grid fault on fixed and variable speed wind turbines. From this, an offline complementary approach was implemented in [92] where the power system simulation tool PowerFactory [93] was coupled with the detailed aeroelastic code HAWC2 to study the dynamic response of the wind turbine to a grid fault, with and without FRT control. In here, the impact was quantified by computing 1 Hz damage eq. loads in the tower structure and blades. The conclusion was that the loads are not affected by the FRT requirement when compared to the turbine being disconnected from the grid. This approach was extended by [94] with an online co-simulation approach using HAWC2 and MATLAB/Simulink, while using a detailed DFIG model which provided realistic torque response. The effect on the structural loads was again studied with the 1 Hz damage eq. loads. In the study it was shown that it is possible to reduce the impact in some of the structural loads, in the case of asymmetric fault, by damping the 100 Hz frequency (twice the supply voltage frequency) by means of a resonant damp controller.

Some studies [42, 95, 96] present models that are capable of capturing the dynamic response of the gearbox to events in the electric grid, while being coupled to the wind turbine. Yet, some of these models account only for the gear mesh interactions computed by models with 1 DOF per body, and do not quantify in detail the impact on the gearbox loads. Therefore, there is a need for a more detailed insight on how the FRT response of the whole turbine, including the structure and power system, affects the internal

components in the gearbox. The importance of these studies can provide additional answers on how to mitigate the loads inside the gearbox and to extend the life-time of the components. Consequently, this investigation aims to provide the necessary methods to assess the impact on the internal drivetrain components, namely the bearings in the planetary stage planets and high-speed stage, when the wind turbine is simulated during a FRT requirement.

Table 5.1: Summary of FRT requirements for the countries of Denmark, Ireland, USA and the province of Quebec, CA.

Country	Voltage loss [%]	Fault duration [s]	Recovery time [s]
Quebec	100	0.15	0.18
Ireland	85	0.625	3
USA	85	0.625	2.3
Denmark	75	0.1	1

The normal operation case is simulated as it is specified for the DLC 1.1 in the IEC 61400-1 standard [10]. Thus, a symmetric fault initiated in the stator terminals of the generator is included, in order to simulate the ride-through capability of the system. In this case, the wind turbine controller is the main governor of the system. Even though there is a fault, the controller will continue to operate the wind turbine under the premise that the fault is short enough to ride-through. Moreover, the dynamics of the wind turbine are slower ($\sim$5 Hz) compared to the duration of the fault ($\sim$100-300 ms). Different grid codes define different requirements, which the wind turbines have to comply, for the worst case scenario during an electric fault. These requirements put constraints in the operation and control of the system, by defining voltage levels for which the turbine must be kept connected to the grid. Thus, the grid codes have been implemented taking into consideration the stable operation of the entire power system. On that account, this investigation also takes into consideration three different grid-codes to put through the wind turbine system. This is done under the premise that the torque oscillations in the generator caused by grid faults have a negative impact in the drivetrain. Moreover, the grid codes suggest different levels of voltage drop, fault duration and recovery to rated values. These aspects are considered here for four grid codes: Denmark, Ireland, United States and Quebec. The choice of the countries is done on the basis of different voltage levels, fault duration and recovery type. The voltage profiles used for the studies here are shown in Figure 5-1 in per. unit (p.u.). The base values for the conversion from the physical quantities to p.u. correspond to the rated value of the line-to-line voltage (Table 5.4).

Consequently, when the drivetrain is exposed to a voltage sag in the stator terminals, the generator will react by dropping the active power due to the loss of magnetization in its windings. This also causes a drop in the electromagnetic torque. Because of the free-free condition of the drivetrain, the loss on one of the input torques creates an unbalance in the system, and therefore, the gear bodies accelerate (and decelerate) as the system

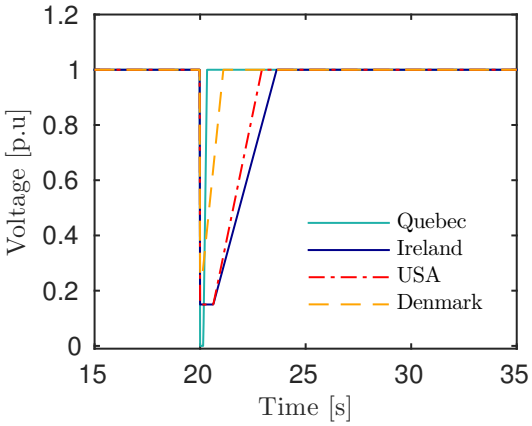

Figure 5-1: The voltage profiles of three national grid codes chosen for the study (the data was obtained from [6]).

oscillates and comes back to a balanced state after the fault is cleared.

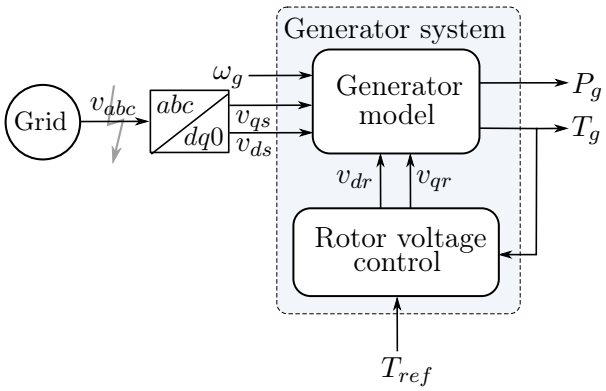

Figure 5-2: Generator system when using a DFIG, voltage rotor controller and simplified grid.

The generator model used in the studies is a typical 3rd order DFIG model. The block diagram of the system is depicted in Figure 5-2, with a gray arrow over the v_{abc} voltages that signifies the possible occurrence of a grid fault. The reference torque T_{ref} is obtained from the wind turbine controller. The full mathematical description is out of the scope of this investigation and it has been presented before by many researchers. However, the main concepts of the model are outlined here so it is easier to understand what happens when there is a change in the excitation voltage. The 3rd order model is a reduced version of the complete dynamic model with the assumption that only the rotor flux linkages vary with time. Hence, these are the states of the model, while the stator fluxes and the generator torque are computed with algebraic equations. A rough matrix

representation of the model in the dq-frame is presented in (5.1):

$$\begin{bmatrix} 0 \\ \dot{\lambda}_{dqr} \end{bmatrix} = \mathcal{M} \begin{bmatrix} \lambda_{dqs} \\ \lambda_{dqr} \end{bmatrix} + \begin{bmatrix} v_{dqs} \\ v_{dqr} \end{bmatrix} \tag{5.1}$$

where $\mathcal{M}$ is a matrix that depends on the windings' resistance and inductance defined in the dq-frame so it is time-invariant, and the input variables of the state-space system are the stator and rotor voltage in the dq-frame. Moreover, the generator torque is found by:

$$T_{em} = \frac{3}{2}\frac{p_f}{2}\frac{L_m}{D}(\lambda_{qs}\lambda'_{dr} - \lambda_{ds}\lambda'_{qr}) \tag{5.2}$$

For a detailed derivation of the complete dynamic model and control strategies of a DFIG, see [97, 98, 99, 100, 18]. The examples shown in Figure 5-3 show the response of the main shaft torsion during the imbalance in the grid, with the addition of the controller effort to overcome the drop in active power.

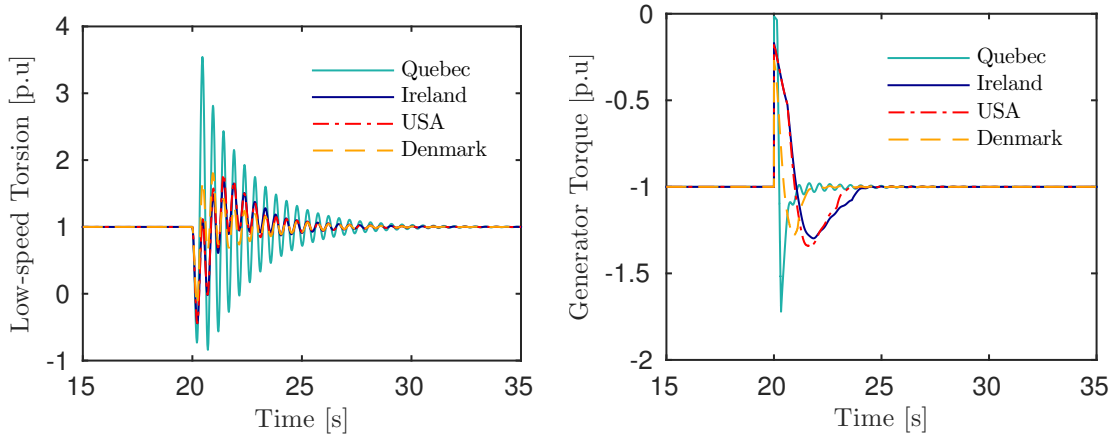

Figure 5-3: Drivetrain torques during the LVRT cases treated here. Notice the impact of the FRT requirements of each country in the transient period. The base values used for the conversion to p.u. are: $T_{lss}^{base} = 4.180$ MNm and $T_{hss}^{base} = 51.292$ kNm.

From Eq. (5.1) it is clear that a change in the stator voltages will disturb the steady-state conditions of the flux linkages. The response of the torques to the unbalance is highly affected by the percentage of voltage loss, fault duration and recovery time specified in the FRT requirements in Table 5.1. For instance, from Figure 5-1 it is seen that the requirements for Quebec are more demanding given the torque oscillations that result from the voltage drop (Figure 5-3). Even though the low-speed side transient period is similar for all the cases, the low-speed shaft torsion increases more than three times the rated value, compared to almost two times in the rest of the cases. Not only, does the torsion increases significantly, but a reversal is also seen in the initial part of the transient. In contrast, the effect is not as significant on the generator side, but this

is due to the controller action to maintain the reference power at rated conditions. For that reason, after the fault occurs, an effort is seen in the torque signal to recover from the fault. This control effort is changed when the fault is cleared and the recovery starts.

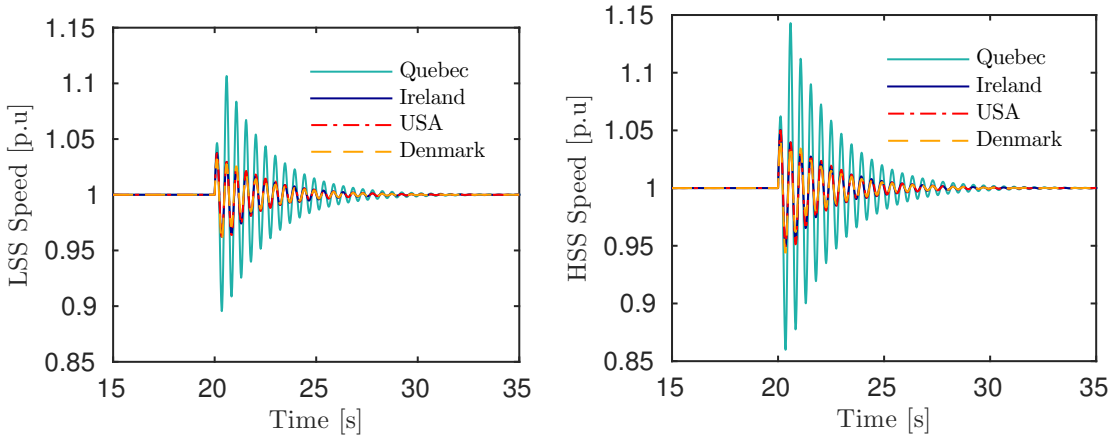

Figure 5-4: Drivetrain rotational speed at the input of the gearbox (**left**) and generator side (**right**). The base values used for the conversion to p.u. are: $\omega_{lss}^{base} = 1.2671$ rad/s and $\omega_{hss}^{base} = 122.9$ rad/s.

The LVRT requirements also have an impact on the rotational speed of the system as seen in Figure 5-4.

The examples on this section were obtained with a simple simulation case using only the drivetrain defined in MATLAB/Simulink with the purpose to illustrate the consequences of the FRT requirements. Later, these requirements will be used to simulate a normal production load case, where the drivetrain is coupled with the wind turbine. To that end, the entire system will be subject to turbulent wind, which will add more dynamic and stochastic content to the simulation. The system will endure the wind conditions, in addition to a LVRT for the cases in Table 5.1. It is expected that the chain of events will produce extreme loads in the drivetrain components which might affect the expected 20 year life-time.

5.2.2 Power production plus occurrence of fault

The purpose of the power production plus occurrence of a fault load case, or DLC 2.3, is to expose the turbine to a wind gust, with the occurrence of a grid fault during the gust. A previous study [101] investigated optimal control strategies to mitigate the tower-base and blade-root loads for different DLCs, including DLC 2.3. Even though no results regarding the gearbox where presented, it is of interest since it presents a control strategy that can ultimately have positive consequences on the gearbox loads. In the study, a load reduction in the tower base was presented and given the nature of the reaction forces due to the drivetrain, it could benefit the drivetrain response. Another study [102] showed the damage in the bearings induced by normal and emergency stops. His conclusion

was that the emergency stop produces more severe damage at the planet bearings from the low-speed planetary stage. This is due to the presence of higher loading in the low-speed shaft as a consequence of the emergency stop. The author uses a sophisticated commercial model that includes the 6 DOF in the drivetrain components. However, the study was carried out by an uncoupled approach.

In the present study, an electromechanical simulation tool is used to asses the extreme loads caused by an Extreme Operating Gust (EOG) as specified by the IEC 61400-1 standard [10]. A loss of the network is simulated at different points in time during the gust by disconnecting the generator terminals, in addition to a shut-down command from the wind turbine governor. These points are chosen so they occur at zero acceleration and low wind; highest acceleration; and, zero acceleration at the peak wind speed. An example of the EOG is shown in Figure 5-5, along with the time of occurrence of the fault.

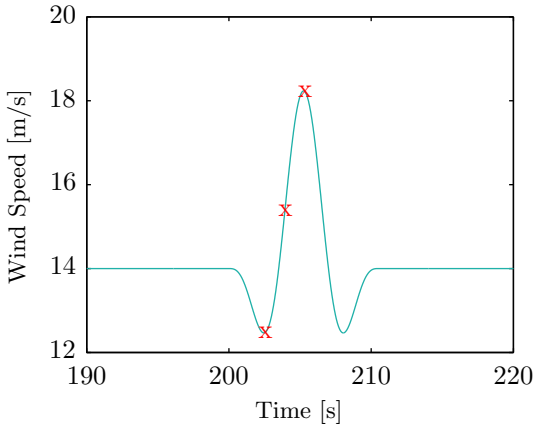

Figure 5-5: Wind speed for the DLC 2.3. The loss of electrical network occurs at the points with x.

Following the guidelines of the IEC standard, the event is simulated at 11.4 m/s (rated wind speed), 9.4 m/s, 13.4 m/s and 25 m/s (cut-out). In addition, the starting azimuth of the wind turbine rotor is changed for each set of simulations. That is, the initial orientation of the blades is changed by 60 degrees. This is done so at the gust occurrence, several states of the rotor position are considered adding randomness to the process. The rotor positions considered here are presented in Figure 5-6 and the numeric data specifying the detail positions are presented in Table 5.2. In summary, a total of 48 simulations will be used to study the extreme loads in the gearbox bearings.

5.2.3 Emergency shut-down: DLC 5.1

Certain situations such as, excessive tower-top vibrations or when human safety is at jeopardy, require the stop of the wind turbine abruptly using an emergency stop procedure. In this case, it is a decision taken by the turbine operator or a pre-defined safety

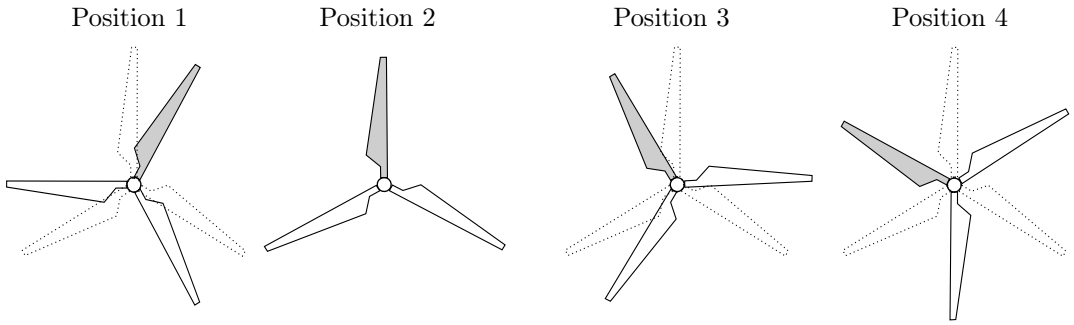

Figure 5-6: The four rotor positions that represent each set of DLC 2.3 simulations. The dotted figure represents a reference position and it is plotted for illustration purposes only. The gray blade is to ease the visualization of the rotation.

Table 5.2: Angles (in Deg.) of the blades in the different rotor positions, where θ_2 is the gray shadowed blade in Figure 5-6. The phase angle between each position is 30^0.

Case	θ_1	θ_2	θ_3
Position 1	180	60	-60
Position 2	210	90	-30
Position 3	240	120	360
Position 4	270	150	30

feature of the wind turbine controller. With the push of a button, the following sequence takes place:

1. A mechanical brake is applied to a disk placed either at the low-speed or high-speed shaft of the turbine. The position of the brake disc depends on the turbine's design. In the example presented here, the NREL 5MW reference turbine has the brake in the HSS [49]. There are advantages and disadvantages associated to the location of the brake. A high-speed brake is more likely to have negative impacts in the gearbox loading, whereas a low-speed shaft brake will cost more given the need for higher braking torque.

2. Once the brake is activated, the controller starts pitching the blades at the maximum rate (Example: 9 Deg/s). This is to bring near zero the aerodynamic torque.

3. Coincident with the brake application, the generator is shut-down so the electromagnetic torque is equal to zero.

The system implemented to simulate an emergency shut-down is presented in Figure 5-7. The general idea is the same as the electromechanical simulation tool explained

before, but the diagram in Figure 5-7 shows in detail the interaction of the relevant signals during the shut-down. The brake is defined as a DLL and it is synchronized with the wind turbine's controller. To start the stop sequence, it is necessary to specify the cut-out time. At the time of the stop, the controller triggers the brake flag f_b to indicate the beginning of the braking sequence. The brake DLL will compute the braking torque T_b using Eq. (5.3). At the same time, the torque demand T_{ref} will be set to zero and the resulting torque applied into the HSS of the gearbox will be equivalent to T_b. Furthermore, the controller sends a pitch angle demand β_d to the servo DLL. The slope demand signal corresponds to the maximum allowed pitch rate, which is defined in the controller parameters.

$$T_b = T_{b_{max}} \tanh(\alpha \omega_r) \tag{5.3}$$

In Eq. (5.3) $T_{b_{max}}$ is the maximum brake torque; depending on the type of turbine, this value could be equivalent to the rated torque or it could be up to two times rated torque. Moreover, α is the "reaction slope" of the brake torque. A higher value will produce a more sensitive brake torque response to the changes in the rotor speed (ω_r). The fundamental requirement of the emergency stop sequence is to halt the turbine's operation within 5-10 sec, therefore, the torque required should be at least equivalent to rated torque. A similar approach was taken by [102]. In this case $T_{b_{max}} = 8.6$ MNm and $\alpha = 10$.

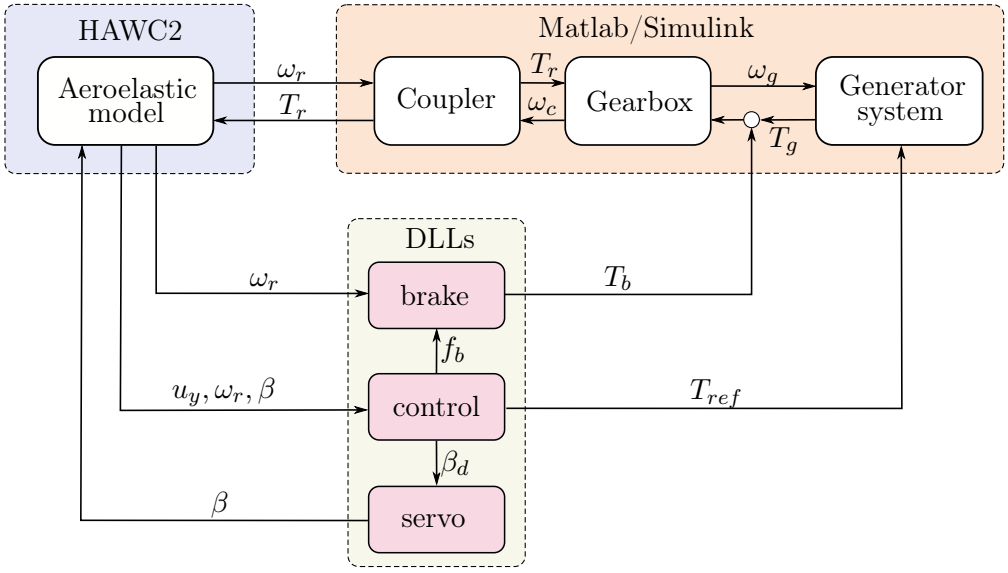

Figure 5-7: The system's block diagram used for the emergency brake load case.

As an example, the illustrative plots in Figure 5-8 show the response of the turbine during an emergency brake sequence. The brake is engaged at $t = 50s$ and the wind turbine is exposed to a turbulent wind, with mean wind speed equal to 25 m/s.

The results show that the big impact on the LSS with up to three times the rated values. The sequence, however, operates as expected since the turbine stops after 10 s.

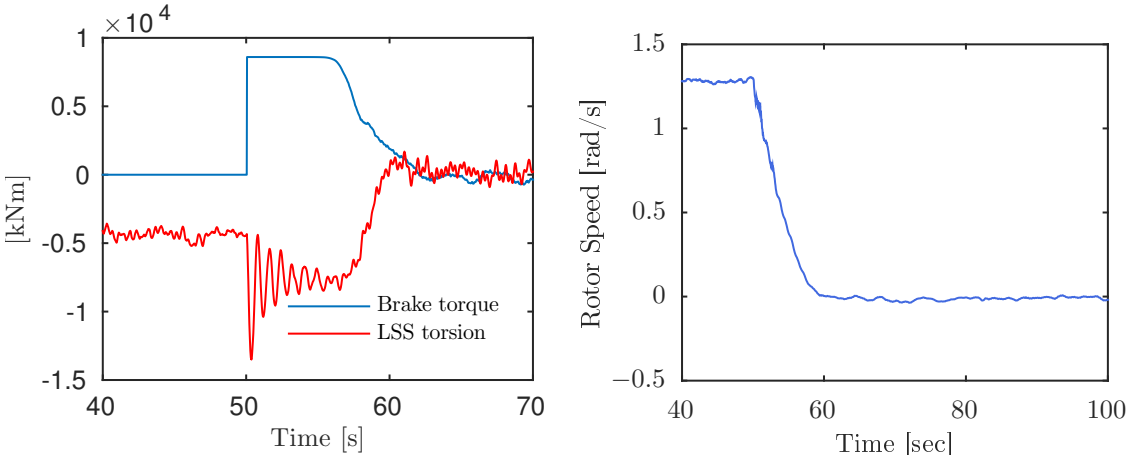

Figure 5-8: Left: Brake torque and the torsion seen at the input of the gearbox. **Right:** The rotor's angular speed.

Notice the comparison of the brake and aerodynamic torque. After the turbine stops, there is still torque present in turbine rotor, which means that the turbine will idle very slowly (the rotor speed is in the order of 10^{-1}). Thus, the reaction of the brake torque to this low speed is seen.

5.3 Simulation setup

A summary of the load cases used to obtain the results in Section 5.4 are presented in Table 5.3. The "Special" column specifies the cases considered here, as an addition to the traditional load cases. For example, the special cases concerning DLC 2.3 are denoted R_i and t_j, which corresponds to the possible combinations of rotor positions ($i = 1, 2, 3, 4$) and time of occurrence of the fault (t_1, t_2, t_3). The "Total" column corresponds to the total number of simulations that are carried out for each case. A total of 10 seeds are used for the cases LVRT and DLC 5.1, that combined with four wind speeds (9.4, 11.4, 13.4 and 25 m/s), it leads to 40 simulations per case. In the case of DLC 2.3, we have four wind speeds, three times of occurrence of the fault and four rotor positions, which leads to a total of 48 simulations.

For the current investigation, the reference NREL 5MW Wind Turbine [49] is used in HAWC2. A recently developed 5MW gearbox presented by [103] is used with some minor modifications. The reference gearbox was upscaled from a 750 kW gearbox presented previously by NREL. Therefore, the gear ratio is equal to 81. The DFIG generator used here is a 5MW that operates at 1200 rpm synchronous speed, with the parameters presented in Table 5.4, previously used in different variable-speed wind turbine operation studies presented in [104, 40, 90]. Hence, a gear ratio of 97 is needed for the gearbox, which was obtained by modifying the last parallel stage from 4 to 4.7618. The modifications

Table 5.3: Summary of the load cases used to calculate the extreme loads of the drive-train [10].

Design Situation	DLC	Wind Condition	Special	Total
Power production/LVRT	NA	NTM $V_{hub} = V_r \pm 2$ and V_{out}	QB	40
			IR	40
			US	40
			DK	40
Power production plus fault	2.3	EOG $V_{hub} = V_r \pm 2$ and V_{out}	R_i,t_j	48
Emergency stop	5.1	NTM $V_{hub} = V_r \pm 2$ and V_{out}	NA	40

were made to the pinion base radii, since in the lumped-parameter model this parameter drives the load transmission, and therefore, the gear ratio.

Table 5.4: 5MW DFIG parameters

Parameter	Value
Rated Output Power	5 MW
Line-to-line voltage	480 Vrms
Line frequency	60 Hz
Stator resistance, R_s	$2.55 \times 10^{-4}\Omega$
Rotor resistance, R_r	$4.35 \times 10^{-4}\Omega$
Stator reactance, X_s	$4.5 \times 10^{-3}\Omega$
Rotor reactance, X_r	$6 \times 10^{-3}\Omega$
Synchronous Speed	1200 rpm
Number of poles	6
Efficiency	94%

The machine controller topology used here is the same as the one presented in [94], but different gain parameters were tuned in order to meet the 5MW power requirements and to follow the reference torque from the wind turbine controller with an acceptable time constant and stabilization time. These are important requirements since under turbulent wind operation, the speed of the turbine changes constantly, and hence, the torque, in order to maintain constant power production.

5.4 Results

The effect of the extreme events are assessed based on their impact in the planet and pinion bearings of the low-speed planetary and high-speed parallel stages, respectively. The analysis of the former components is important because, overall, they present the most damage during the life-time of the wind turbine. The latter is accounted because it is close to the generator and due to the low value in terms of reliability (see [105]).

The general expression to compute the radial bearing loads in any given gear is given

as:

$$F_b = \sqrt{F_x^2 + F_y^2} \tag{5.4}$$

where F_x and F_y are the bearing force components in the x and y directions respectively and are computed as:

$$\begin{bmatrix} F_x \\ F_y \end{bmatrix} = \begin{bmatrix} K_{xx}^b & K_{xy}^b \\ K_{yx}^b & K_{yy}^b \end{bmatrix} \begin{bmatrix} x \\ y \end{bmatrix} \tag{5.5}$$

where K_{ij}^b are the bearing stiffness components. This representation is generalized in case the cross-diagonal terms are available. In this study, these components are assumed to be equal to zero and only the main diagonal is considered, as it was presented previously in Section 3.3. The force components will be analysed with respect to the planetary bearings that, as the planets vibrate and rotate with the carrier, the local value of these components change. However, the total radial force is stationary around a value that makes sense kinematically. Perhaps, at this point, it is not of too much relevance to know the value of each individual component, but it helps to understand how the load on the bearings is developed in time with the addition of transient events such as those studied here.

An example of the variation of both force components for one of the planets in the planetary stage is presented in Figure 5-9. The radii of the circle created by the variation of the force components corresponds to the magnitude of the force given in eq. (5.4). In addition, a second example in the same figure shows what happens when a fault occurs. It is shown how the progression of the components is affected. Moreover, the location of the planet and the magnitude of each component is related. However, in terms of the magnitude of the radial load experience by the bearing, this is not too relevant since it will have the same value regardless of the location. This might change when gravity is included, but that is not the case in this model.

The rest of the section is focused on presenting the simulation results of the cases in Table 5.3. Since we are dealing with extreme events, the results will focus on finding the maximum loads achieved by each of these cases. The recommendations given in [10] for ultimate limit state analysis are used to find the worst case scenario loads, which are computed from the time-series and with the safety factors as:

$$F_d = \gamma_f F_k \tag{5.6}$$

where F_d is the design load, γ_f is the safety factor and F_k is the characteristic value of the load. The latter is computed differently depending on the case, which will be explained in detail in each subsection concerning the results for each load case. The safety factors are included so the uncertainties that are inherent in the analysis and methods used in wind turbine certification, are accounted for in the calculation of design loads. Furthermore, there are safety factors concerning the *"importance of structural components with respect to the consequence of failure"*, but those are not included here since the current study focuses only in finding the ultimate loads.

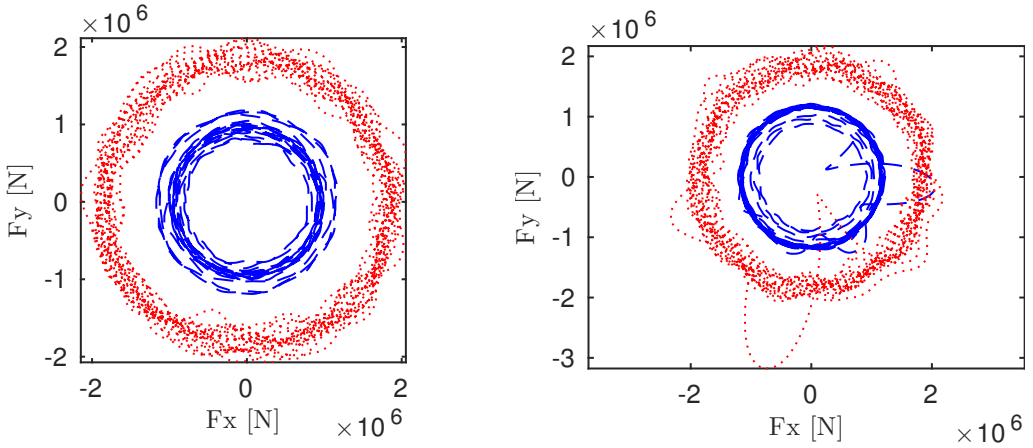

Figure 5-9: The force components of the planet bearing at 9.4 m/s (blue –) and 25 m/s (red :).

5.4.1 LVRT

In the normal operation DLC 1.1 the turbine operates with turbulent wind defined by the NTM at different intensities, which depend on the mean wind speed. Here, the impact on the planet bearings of the planetary stage and the pinion of the parallel stage is assessed by means of the maximum load achieved. This is done for the four grid codes treated here. But first, let us present an example of the time history for both bearings in Figures 5-10 and 5-11. The time history of one of the seeds is plotted to visualize the effect of the LVRT. Qualitatively, both bearings, in the planetary stage and HSS stage, experience the same impact in terms of load amplification with respect to their mean, and recovery time. This is consistent to the concept of a gearbox, where the load path is transferred between the input and the output in order to maintain equilibrium. Therefore, the foregoing analysis is done on the impact of the LVRT in general for both components.

As it was expected from the torque signals in Figure 5-3, the case of Quebec seems to be worst. In contrast, the short recovery period of Quebec's grid code does not have a positive effect since the generator controller will generate a control effort by increasing the reactive current in order to support the fault. This produces the high spikes in the torque signal (as it was shown in 5-3). Consequently, higher oscillations translate into longer recovery time, as it is the case for $U_y = 25$ m/s. But, why is it higher at this mean wind speed? A detailed observation into the wind speed time series, and in comparison to another seed, shows that during the fault, the wind speed of seed 4 was 14% lower than the mean of $U_y = 25$ m/s. In contrast, the wind speed on seed 7 at the time of the fault was only 6%. This produces difference in the main shaft rotational speed. For instance, at the moment of the fault, the speed corresponding to seed 4 was 1.5% higher than rated. On the contrary, the rotational speed that corresponds to seed 7 was 2% higher than rated. That is to say, that at higher speed the lower is the torsional moment

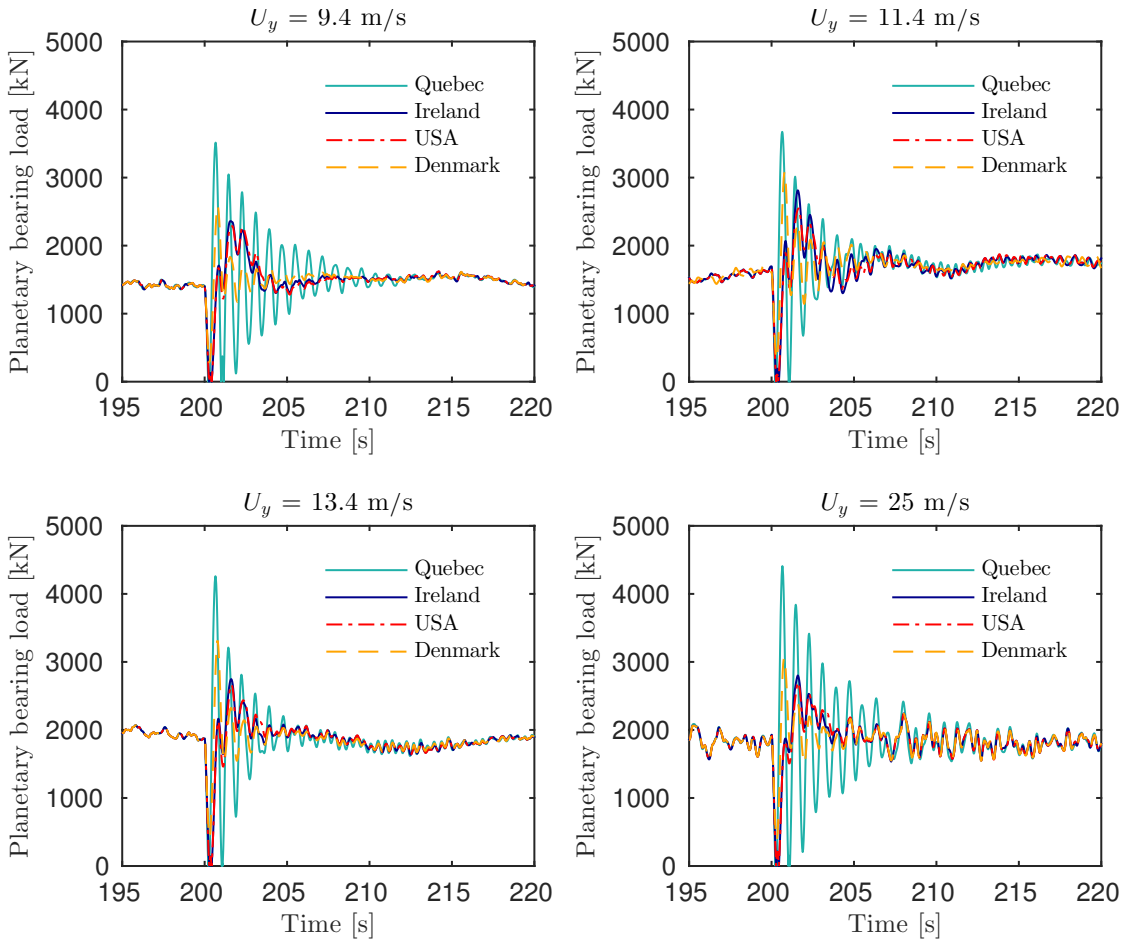

Figure 5-10: Sample result of the LVRT under the NTM for one of the planets in the low-speed planetary stage. The four wind speeds are shown for one of the seeds.

in the main shaft, which transfers the loading into the gearbox. A comparison of the two loads is presented in Figure 5-12, along with the rotor speed, where the difference in mean rotational speed is obvious at the moment of the fault. To ease the visualization, the results from seed 7 were shifted -150 s so the fault seems to "occur" at the same time. In reality, in this seed the fault was scheduled at 550 s.

An extreme value analysis of the entire set of simulations (160 in total) shows that the effects are worst for the cut-out speed (25 m/s) and for the Quebec grid code. The numerical results that represent the mean value of the maximum loads for each wind speed are presented in Table 5.5 and a graphical representation is shown in Figure 5-13. Observe that the Quebec case is consistent throughout the wind speed range by causing maximum loads, compared to the other cases. In contrast, the cases of Ireland and United States are similar, as it is for their recovery strategy. The grid code that

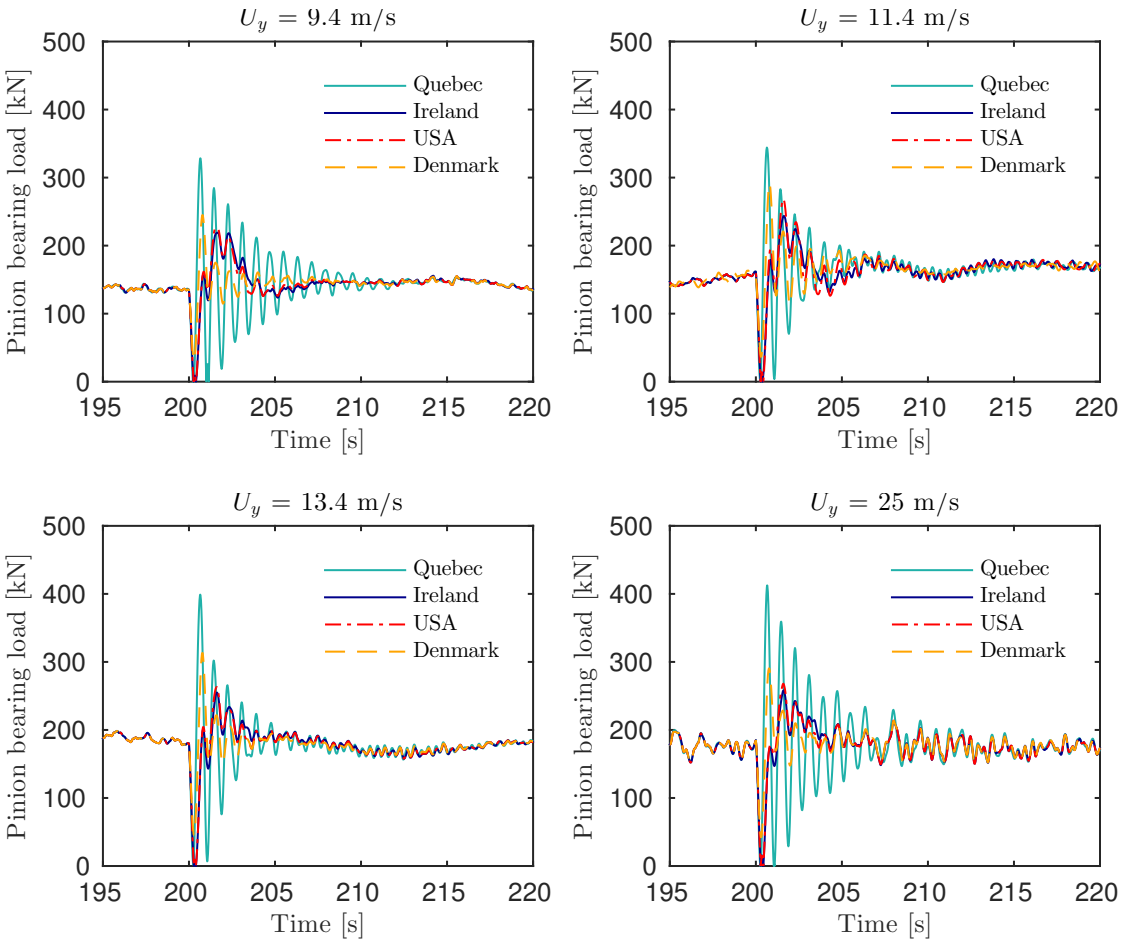

Figure 5-11: Sample result of the LVRT under the NTM for the pinion in the high-speed stage. The four wind speeds are shown for one of the seeds.

produces less impact on the bearing loads is Ireland, which consequently has a longer recovery time. Moreover, it's requirement for percentage of voltage loss is the same as the US, but nevertheless, the recovery time seems to be the driver for reduced bearings loads.

If we compute the area "over" the curve of the voltage profile during the fault times, and normalize the loads from Table 5.5 with respect to the mean value of the load during the fault, we obtain the results shown in Figure 5-14. Each data point corresponds to each country in the following order from the highest to the lowest load: Quebec, Denmark, United States and Ireland. This result is very important since it accounts for the parameters that drive the type of voltage profile and it compares them with a "perceived" impact in terms of average maximum loads in the bearings. From this, it can be concluded that there is a compromise in the voltage profile in terms of the percentage loss, fault duration and recovery time, that could potentially reduce the impact in the

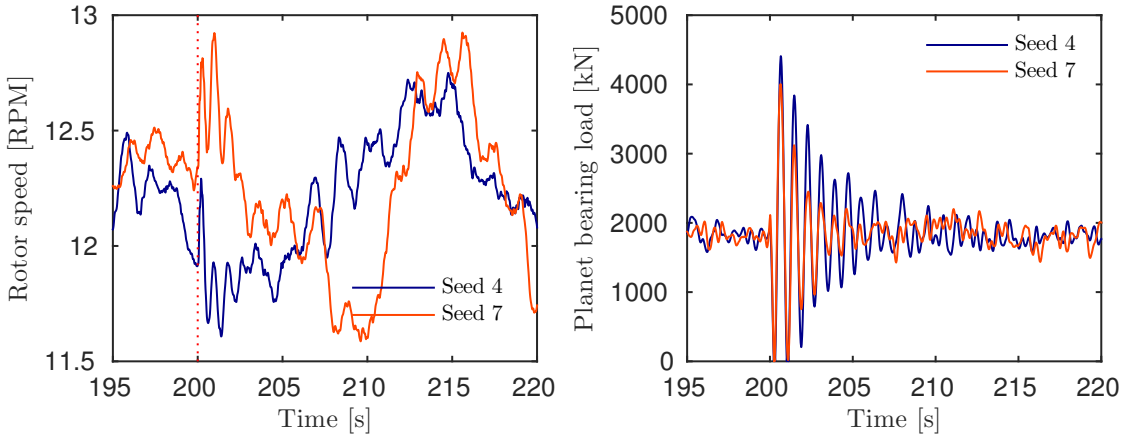

Figure 5-12: Sample result of the LVRT for seeds 4 and 7 at 25 m/s. The vertical dotted line in the left plot indicates the occurrence of a fault.

Table 5.5: DLC 1.1 with LVRT results: the mean maximum values of the bearing radial loads (in MN) for each wind speed (in m/s), grid code case and gearbox stage.

Stage	Wind Speed	QB	US	IR	DK
Planetary	9.4	3.2822	2.3449	2.3558	2.5684
	11.4	4.0890	2.7888	2.6959	3.2368
	13.4	4.6231	2.9957	2.9268	3.6251
	25	4.6640	3.0899	2.9928	3.5525
Parallel	9.4	0.3072	0.2251	0.2259	0.2438
	11.4	0.3830	0.2671	0.2581	0.3067
	13.4	0.4329	0.2866	0.2797	0.3429
	25	0.4369	0.2954	0.2859	0.3365

bearing loading.

So far, it was observed that two parameters might be driving the high loads due to an LVRT. The first, and obvious one, is the FRT requirement that the grid code of each country recommends. Another possibility is a stochastic event such as a gust within the simulation seed, which either accelerates or decelerates the turbine, producing a different mean rotational speed before, and during the fault. In reality, the loads at a given component whether in a wind turbine or an engineer structure, are driven by the contribution of the vibration modes of such a structure. For rotating machinery, it is the first rotational frequency that appears as a source of excitation. In 3-bladed wind turbines, one of the excitation modes comes from the rotational speed and it is known as 1P (1×the rotational speed). In addition, the rotor passing frequency also excites the system with a frequency equal to 3P [106]. Consequently, the studies in this section deal with the occurrence of a short transient event within a long simulation time. From this, a waterfall plot was obtained for the ongoing example of seed 4 at a mean wind speed

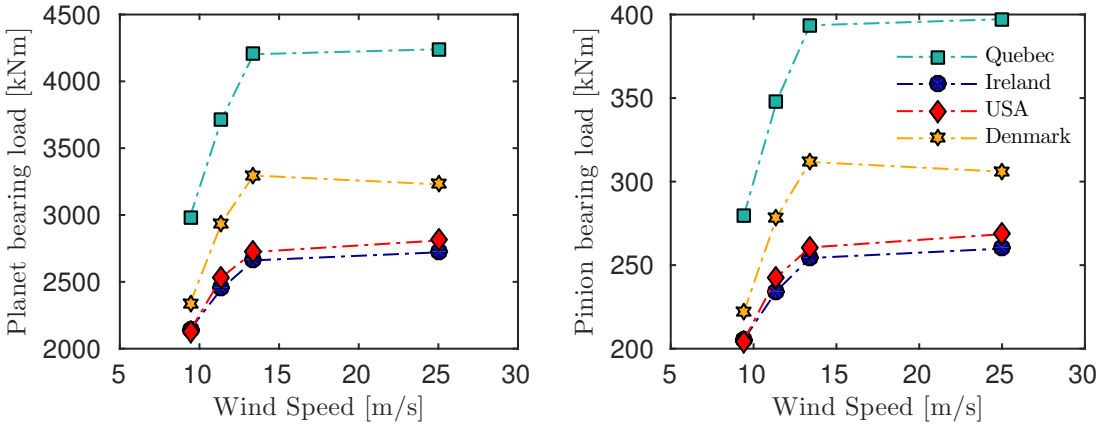

Figure 5-13: The mean of the maximum radial loads (among all seeds) in the bearings of one of the planets in the planetary stage (**left**) and the high-speed pinion bearing (**right**).

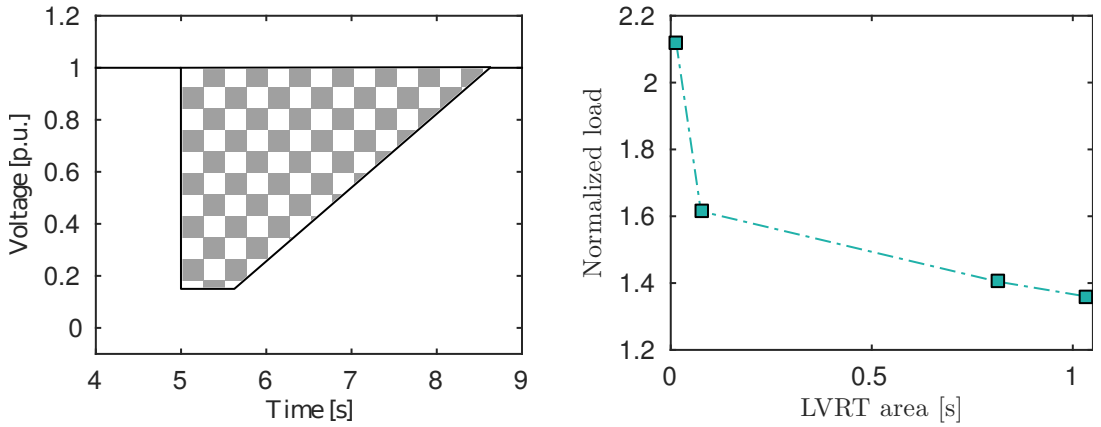

Figure 5-14: The area "over" the curve used for the analysis is shaded with checkers (**left**). A graphical representation of the impact on the bearing maximum loads due to FRT requirements (**right**). An area equal to zero means that no fault occurs.

of 25 m/s. This result sheds some light in what could be driving the maximum loads during this event. The result is shown in Figure 5-15. The square box corresponds to the highest amplitude in the frequency domain, which occurs in the bin around 200 s. From intuition, one might think that the drivetrain torsional mode is contributing to the high load, which is accurate (and is consistent with the findings on Chapter 4). However, the mode that contributes the most is 3P and is the frequency of the peak marked with the red box.

In the wind turbine model used here, a 3P frequency corresponds to roughly 0.6 Hz. A closer look into the generator torque response due to the Quebec type fault, shows

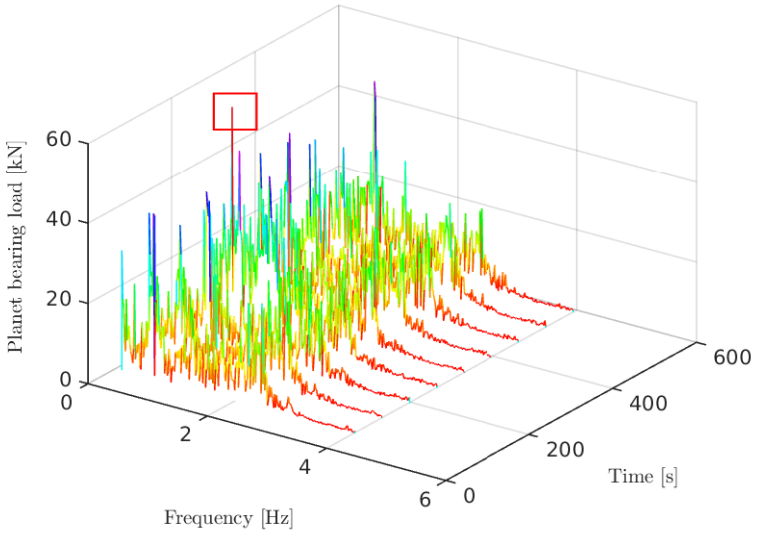

Figure 5-15: The waterfall spectrum of the planet bearing load for seed 4 at 25 m/s (see Figure 5-10). The square box denotes the maximum point in the spectrum.

that the total recovery time, including the transients after the fault is cleared, is roughly 1.6 s. This period corresponds to ≈ 0.6 Hz, which is believed to excite the system at this frequency, which causes 3P to have a higher contribution to the loads during the transient period.

5.4.2 Power production plus fault

In a DLC 2.3 with failure of the electrical network, the generator torque is set to zero at different points during a wind gust, as it was shown previously in Figure 5-5. From a total of 48 simulations, four sets of results are categorized depending on the wind speed. Each set contains 12 seeds, which is the result of a combination of three rotor positions R_i and time of occurrence of the fault t_i. The different rotor position cases add randomness to the simulations, but it was observed that the rotor position has little effect on the bearing loads. However, the time of the fault has a big impact as seen in Figure 5-16 and in the results in Table 5.6.

The results are consistent with the previous results for the LVRT cases, where the maximum loads were achieved at the cut-out wind speed. In the case of DLC 2.3, this makes sense since the wind gust magnitude is computed as a function of the mean wind speed, among other parameters [10].

Table 5.6: DLC 2.3 Results: the mean maximum values of the bearing radial loads (in MN) for each wind speed (in m/s), time of occurrence of a case fault and gearbox stage.

Stage	Wind Speed	t_1	t_2	t_3
Planetary	9.4	1.5355	1.5997	1.7084
	11.4	2.1436	2.1878	2.1891
	13.4	2.2417	2.2852	2.2841
	25	2.4154	2.4772	2.4802
Parallel	9.4	0.1473	0.1532	0.1639
	11.4	0.2056	0.2096	0.2097
	13.4	0.2147	0.2186	0.2185
	25	0.2303	0.2359	0.2362

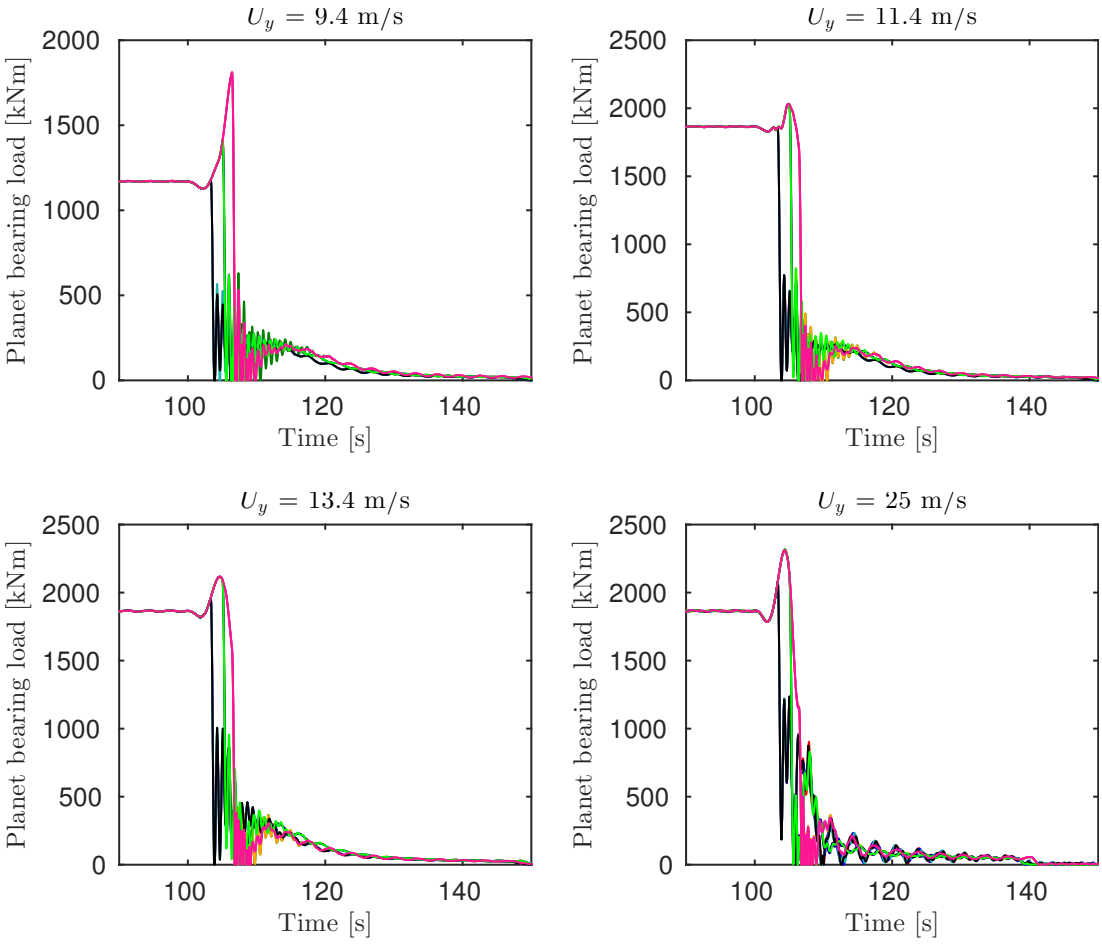

Figure 5-16: Planetary bearing loads due to a normal stop. All seeds are shown.

5.4.3 Emergency stop

An emergency brake was represented by a higher than rated torque in the high-speed shaft, as shown in diagram 5-7. There is no real directive that recommends a specific value for the brake torque, so a value of two times rated torque was used. Examples of the bearing loads in the planetary stage is shown in Figure 5-17. All the seeds are shown and the brake was activated at the same time, i.e. 150 s.

A glance at the time-series shows that the loads reach around three times their rated value, with the maximum point being two times the overall torque reached while the brake is activated.

Table 5.7: DLC 5.1 results: the mean maximum values of the bearing radial loads (in MN) for all the seeds at each wind speed (in m/s).

Wind Speed	Parallel	Planetary
9.4	0.6103	6.4523
11.4	0.6187	6.5335
13.4	0.6196	6.5404
25	0.6194	6.5952

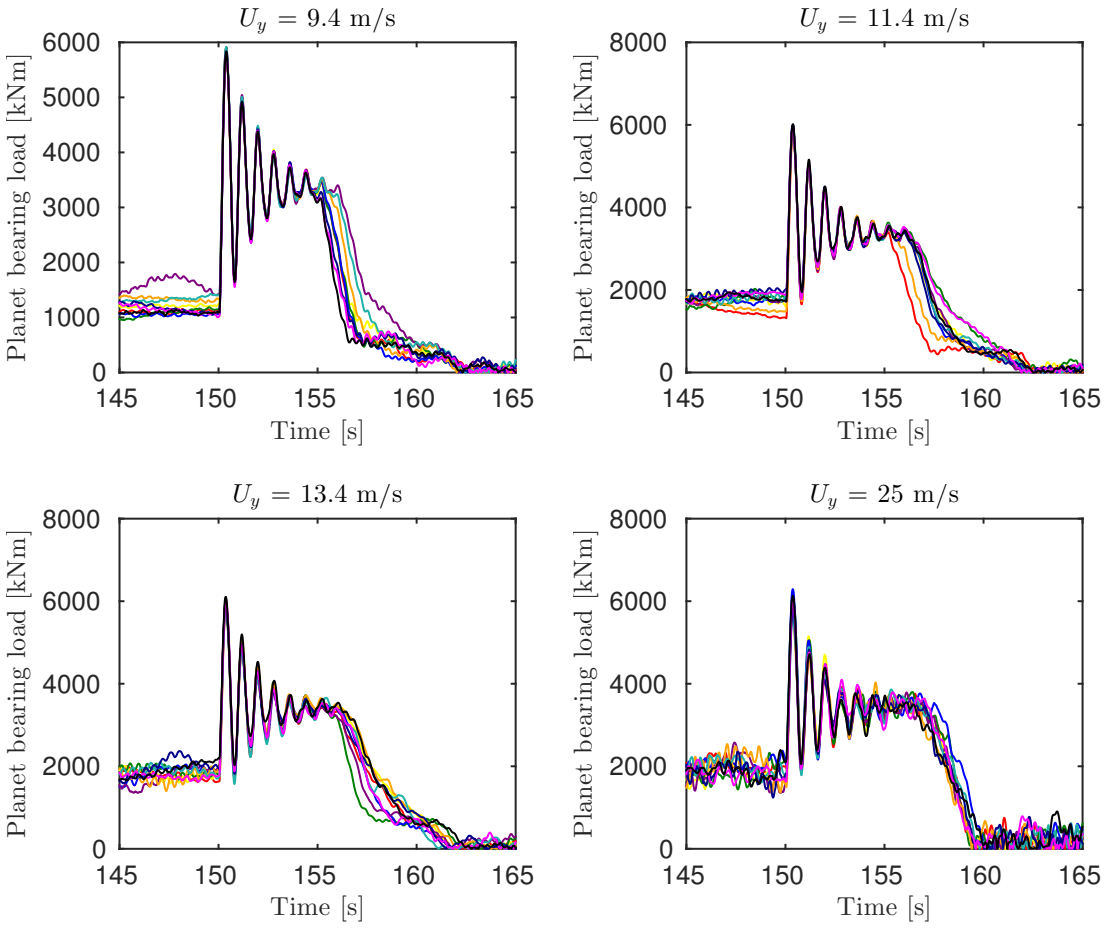

Figure 5-17: Planetary bearing loads due to a emergency stop. All seeds are shown.

5.5 Maximum contact stress

The contact stresses computation is important for the design of bearings since it gives an idea of the possible impact, due to extreme loads, that the bearing will experience. Even though the bearings are designed for moderate loading, the rollers can experience high stresses due to the small surface in contact with the race. This contact surface is usually modeled as a point contact for ball bearings and a line contact for roller bearings [57]. In the investigation presented in this chapter, it is assumed the bearings are of the roller bearing type, therefore the following calculation is based on line contact.

The IEC 61400-4 standard for wind turbine gearbox design [44] recommends different methods to compute the maximum roller contact stresses. It is not an intention to repeat step by step the method in the standard, but to highlight the most relevant concepts and to present the results based on the load computation in the preceding section.

The starting point is to calculate the equivalent bearing load by:

$$P_0 = X_0 F_r + Y_0 F_a \tag{5.7}$$

where X_0 and Y_0 are static radial and axial load factors, respectively; F_r is the maximum radial load in N; and F_a is the maximum axial load in N. In the models used here, only the translation in the x and y direction are considered. Therefore, only the radial loads are calculated and $F_a = 0$ N. According to the standard, $X_0 = 0.5$ for double-row bearings, which is the case in the model used here. Then, P_0 will be equal to the values found in the previous section. In reality, this load is distributed among the rolling elements. The load distribution can be estimated based on the number of rollers and the load sharing factor k, which depends on the initial bearing clearance.

$$Q = \frac{P_0}{Z \cos \alpha_0} k \tag{5.8}$$

where Q represents the single roller maximum load, Z is the total number of rolling elements in a bearing row and α_0 is the nominal contact angle (in this case is equal to zero). The maximum contact pressure p_{line} is calculated by:

$$p_{line} = 270 \sqrt{\frac{1}{2} \frac{Q}{L_{we}} \sum \rho_{line}} \tag{5.9}$$

where L_{we} denotes the effective roller length in mm, and $\sum \rho_{line}$ is the contact pressure factor for a line contact and it is an indicator of the curvature and it is used to *"describe the contact between two mating surfaces in revolution"* [57]. The contact pressure factor is computed by:

$$\sum \rho_{line} = \frac{2}{D_w} + \frac{2}{\frac{D_{pw}}{\cos \alpha_0} - D_w} \tag{5.10}$$

Table 5.8: The parameters used to represent one set of planet bearings in the low-speed planetary stage [11]. A cylindrical roller bearing type was chosen.

Parameter	Value
Inner diameter, b [mm]	200
Outer diameter, D [mm]	420
Basic dynamic load, C [kN]	1980
Pressure angle, α_0 [Deg]	0
Roller length, L_{we} [mm]	138
Roller diameter, D_w [mm]	37.5
Bearing pitch diameter, D_{pw} [mm]	310

Moreover, the maximum contact stress is given as:

$$p_{max} = K_{lc} K_m p_{line} \tag{5.11}$$

where K_m and K_{lc} are the misalignment and the ratio to maximum nominal line contact pressure factors, respectively.

Next, the preceding method is used to compute the maximum contact stresses of the planet bearings with the results from the previous section in Tables 5.5, 5.6 and 5.7. The bearing parameters in Table were used for the computation

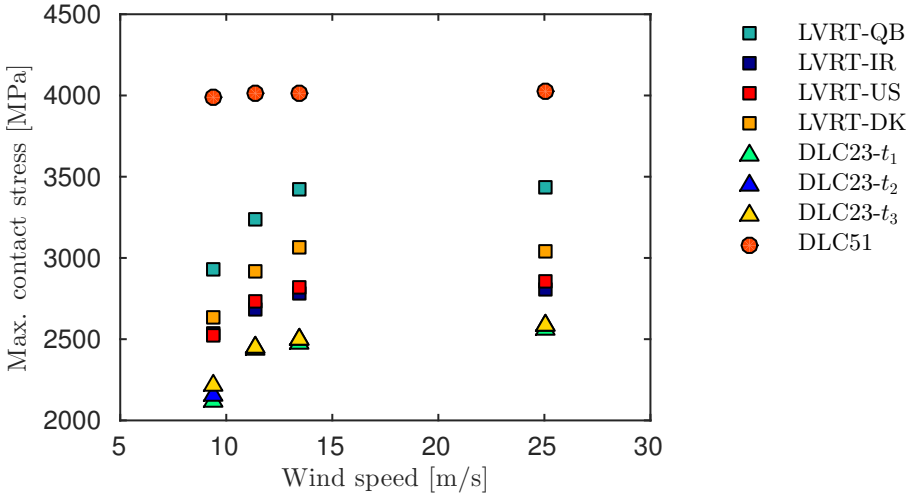

Figure 5-18: The maximum contact stresses from the bearing radial loads in one of the low-speed planetary stage planets. According to the IEC 61400 standard, there is risk of damage above 2000 MPa.

Without doubt, the emergency brake is the event that imposes the highest stresses in the bearing components, followed by the LVRT events. As seen before, the strategy for recovery affects the severity of the impact, now in terms of contact stresses. Moreover,

the normal stop operation is the most benign case in terms of bearings stresses. However, for wind speeds below rated, there is no major effect in the bearing contact stresses.

5.6 Conclusions

It was the purpose of this chapter to document the capabilities of the methods developed here in terms of transient events that affect the wind turbine such as LVRT, normal and emergency stop. Moreover, the effect on the bearing loads of these transient events was investigated, putting emphasis in the planet bearings in the low-speed planetary gearbox. That being said, three major conclusions can be deducted:

LVRT In the event of an electric fault at the DFIG's excitation voltage, the fault does not greatly affect the turbine, hence, it is possible to ensure the continuous operation, in addition to following the grid codes. However, with the voltage profiles treated here it was shown that the amount of excitation lost, the duration of the fault and the recovery time have an important effect on the bearing loads. The cases chosen for the study, i.e. Quebec, Ireland, USA and Denmark, were carefully considered in order to have different levels in the parameters that define the voltage profile, so the impact on the loads was easily assessed. A major finding from the LVRT simulations is that if we considered the area "over" the curve of the voltage profiles, it is easy to realize the maximum loads that can be obtained in the bearings, mostly due to the percentage of voltage loss and the recovery time of the fault. This opens the door for future research on the importance of considering an integrated design. There is no data available, to the knowledge of the author, that shows a higher percentage of failure of the bearings in wind turbines located in Quebec, for instance. But regardless of this, the findings show that by re-considering the worst case in where a turbine must stay connected it is possible to mitigate the negative effects on the drivetrain components, when an electric fault occurs. Moreover, the frequency around 3P was identified to be the most excited during a LVRT event.

DLC 2.3 The normal stop operation was the event that with the least negative effect on the bearing loads. Accordingly, there is no major event driving the bearing loads to a maximum point out of the ordinary. The maximum values obtained were due to the wind gust at 25 m/s where the peak wind speed reach 32 m/s, and the turbine was stopped. However, the load magnitude is due merely to the response of the turbine and not the stop. The modification in the rotor position showed no effect on the loads. The major driver was the time of occurrence of the fault, in this case, at t_3 which corresponds to the highest wind speed during the gust.

DLC 5.1 From the overall results, it was observed that the emergency stop case presented the highest impact on the bearings for all wind speeds. With almost twice the allowed maximum contact stress, this case is the one that seems more likely to accelerate damage in the bearings. However, the high load produced at the time

of breaking is directly proportional to the brake torque. In the case treated here, the brake torque was equivalent to two times rated torque, hence, the maximum load reached approximately three times its value before the brake was activated. Although the loads were very high compared to the other cases, it is possible to reduce them by implementing better braking techniques that use a lower brake torque and bring the turbine to stop within a reasonable amount of time (<10 s). It is out of the scope of this thesis to explore braking methods, but it is believed that this is a relevant topic for future research.

Previous research has shown that the bearing failure starts with cracks under the surface, due to normal fatigue. However, the extreme events studied here can accelerate this process due to the special cases where the load is doubled or tripled. Consequently, cases like this will most likely result in premature failure of the bearings, as it is the case nowadays. Therefore, the methods presented here showed the impact on the bearings maximum loading, which can be accounted for in the early stages of design. In order to reduce the effects, it is important to include this type of simulations in the design stage so methods to mitigate the high loads can be investigated. In addition, the rating of the bearings can be adjusted to the findings so a compromise is reached in terms of reliability and cost reduction.

6

Reliability of wind turbine drivetrains

6.1 Introduction

One of the main focuses of the wind energy research community is to design systems based, not only on dynamical models representing the behavior of the system, but also, on models that include additional stochastic information. The latter approach allows an estimation of the expected lifetime (or expected failure frequency) of the components based on previous knowledge of the wind conditions, strength of the material and uncertainties, just to name a few. An important element of this approach, is to make reliability based decisions in order to minimize costs in repair and maintenance of wind turbine components. In the context of wind turbine drivetrains, it is of high relevance to study the planetary stage bearings due to the recurrent failures that reduce the lifetime of the components. Therefore, it is important to consider different configurations in the design stage of the gearbox. For instance, different types of bearings are designed to withstand different loading distributions among the rollers. In this chapter, the bearing models presented in Section 3.3.3 are included into the electromechanical simulation model of the drivetrain (Section 3.5). The bearing model pre-processor is used to estimate the bearing stiffness matrix components in the radial directions, based on the bearing physical parameters such as race dimensions, number of rollers and roller contact angle. In the past, other studies have focused on the fatigue of the planetary bearings. For example, Nejad et al. [105] presented results for the entire gearbox components in terms of the cumulative damage and produced a "vulnerability map" where it is possible to identify the components more prone to failure. Another study found, from field data, that failure due to bearing fatigue is feasible even at rated conditions given their observations of the bearing loads in the planetary stage [81]. According to the study, some events that produce torques above 150% of rated could induce higher damage in the components. This is the case in extreme events such as emergency brakes or electric faults. However, these are cases that do not occur that often, and are related to the ultimate load analysis presented in Chapter 5. Therefore, when the focus is on

fatigue and reliability, it is necessary to analyze the response of the components under normal operation conditions. The chapter is structured as: first, the theory of reliability analysis and the method implemented for the investigation is presented. Second, the method used to obtain the simulation results is given. It includes the bearing models, CRB and TRB, and a description of the system. The difference in the model lies in the contact angle of the rollers and the effect it has on the stiffness matrix. Later, the reliability analysis is done in conjunction to the bearing life and the requirements of the IEC 61400-1 standard for wind turbine design [44]. Finally, the results are explained and conclusions are drawn from the difference in terms of reliability found between the two bearing models.

6.2 First-order reliability method

Structural integrity is perhaps one of the major focus during the lifetime of a component. In theory, there are multiple modes of failure which the structure is vulnerable to. However, it is impossible to analyze all the possible failure modes due to the complexity of certain structures. Therefore, attention is given to a subset of relevant failure modes [7]. In the early stages of the design, the structure's response to external loading is analysed using models that intend to describe its behavior. Without doubt, uncertainty in the models contribute to differences in the response, specially when considering degradation in the material properties over time. This is one of the factors that contribute to a small probability that the system under study will not perform as desired in terms of longevity [107]. No system can perform as designed forever, meaning unlimited life. Therefor, there is always a probability of failure associated to the system, and it is influenced by the design of the components, material properties, loading, extreme events, etc.

The main purpose of reliability analysis is to find the probability of failure of a given structure, or system, subjected to external loading. For the computation of reliability it is necessary to specify the resistance of the structure, along with different uncertainties related to the models and the assumptions during the design. The basic problem formulation in reliability analysis is to define the so-called limit state equation, which describes the state of the structure by a quantitative index [7]. Let $g(\mathbf{x})$ be defined as the limit state function, which describes the state of the structure for a given set of $\mathbf{x}$. The failure domain is defined for the condition $g(\mathbf{x}) \leq 0$ and $g(\mathbf{x}) = 0$ is the failure surface. Calculating the probability of failure amounts to evaluating the integral of the joint distribution of the set of random variables over the failure domain:

$$p_f = \int\limits_{g(\mathbf{x}) \leq 0} f_{\mathbf{x}}(\mathbf{x})\, d\mathbf{x} \tag{6.1}$$

where is the joint probability density function of the random variables $\mathbf{x}$. These variables are representative of the loading in the structure, the resistance and the associated uncertainties, and $g(\mathbf{x}) \leq 0$ is a zero-one indicator function which equals 1 when failure occurs.

A straightforward interpretation of the limit state equation is to define it as a combination of the capacity of the structure and the demand which it is subject to. For example:

$$g(\mathbf{x}) = R(\mathbf{x}) - S(\mathbf{x}) \tag{6.2}$$

It is clear from eq. 6.2 that if the demand $S(\mathbf{x})$ is equal to the resistance $R(\mathbf{x})$, the structure will fail. Later in the chapter, this concept will be used to derive a limit state equation that relates the required bearing life in hours, to the failure of the bearings.

There is no trivial solution to the integral in eq. 6.1 and a numerical solution is time consuming [7], specially for larger dimensions of the vector $\mathbf{x}$. However, for the case of normal distributed variables and a linear limit state function, the probability of failure found by:

$$p_f = \Phi(-\beta) \tag{6.3}$$

where β is the reliability index and it is defined as:

$$\beta = \frac{\mu_g}{\sigma_g} \tag{6.4}$$

where μ_g and σ_g are the mean and standard deviation of $g(\mathbf{x})$, respectively.

However, in the reliability analysis of complex structures, the limit state equation is generally a non-linear function of the random variables related to the structure, in addition, to the associated uncertainties. In such cases, the vector of random variables $\mathbf{x}$ and the uncertainties are defined in terms of probability distributions. This type of analysis falls into the category of **Level III** reliability methods [107, 7]. Hence, the reliability index is to be defined as the *first-order reliability index* and it is found by applying FORM.

In FORM, the variables in vector $\mathbf{x}$ are assumed to be correlated and normally distributed. Therefore, the initial step is to transform the variables from the $x-$space to the normal space ($u-$space), so they become statistically independent and identically distributed. This transformation is made by:

$$u_i = \Phi^{-1}(F(x_i)) \tag{6.5}$$

where $F(x_i)$ is the cumulative distribution of the random variable x_i. With this, it is possible to compute the value of the limit state function $g(\mathbf{u})$ in the normal space.

From the transformation to the normal space it is possible to define the Hasofer-Lind reliability index, β, as the minimum distance between the origin and the failure surface. Since in general the limit state equation is of non-linear nature, it is necessary to find the design point, and hence the reliability index, by solving the optimization problem in

eq. 6.6. The iteration procedure is given in Algorithm 1.

$$\beta = \min_{g(\mathbf{u})=0} \sqrt{\sum_{i=1}^{n} u_i^2} = \mathbf{u}^{*T}\mathbf{u}^* \tag{6.6}$$

where $\mathbf{u}^*$ is denoted as the design point and is located on the failure surface at a location with the smallest distance to the origin.

Figure 6-1 shows the geometrical interpretation of β for an example of a reliability problem with two random variables. The vector $\boldsymbol{\alpha}$ is an unit vector normal to the design point and is commonly known as the important factor defined as:

$$\boldsymbol{\alpha} = -\frac{\nabla g(\mathbf{u}^*}{|\nabla g(\mathbf{u}^*)|} \tag{6.7}$$

From eq. 6.7 it is seen that this vector represents the sensitivities of the inaccuracies in the random variables used for the reliability index calculation. Later, in the results section, it will be seen that importance factor is associated to the uncertainties that are included in the definition of the limit state equation. This is an important relationship, since the uncertainties are a measure of the accuracy of the statistical data and the models used to obtain the bearing loads.

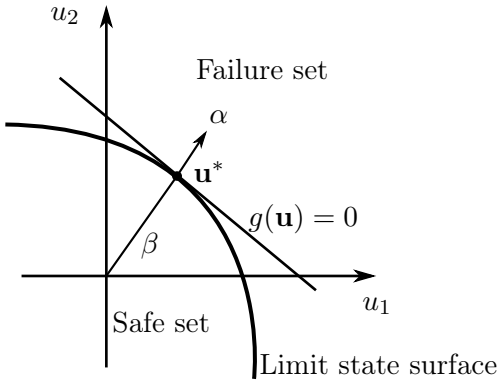

Figure 6-1: Illustration of the probability of failure in the normal space for two random variables (inspired from [7, 8]).

This concludes the description of the FORM implemented in this chapter to analyze the impact that different bearing configurations have in the overall drivetrain reliability. The next section describes the methods used to model the bearing types for the calculation of the loads in the planet bearings of the planetary stage.

Algorithm 1: Iterative procedure to find β and $\mathbf{u}^*$ [8]

Data: Mean and standard deviation of the random variables in the limit state function

Result: Reliability index β

Define the initial point $\mathbf{u}^0$, and set the iteration $i = 0$;

Compute the value of $g(\mathbf{u_i})$;

Compute the gradient $\nabla g(\mathbf{u}_i)$;

Estimate an updated value of $\mathbf{u}^{i+1}$:

$$\mathbf{u}^{i+1} = \frac{\nabla g(\mathbf{u}_i)^T \mathbf{u}_i - g(\mathbf{u}_i)}{\nabla g(\mathbf{u}_i)^T \nabla g(\mathbf{u}_i)} \nabla g(\mathbf{u}_i)$$

Update the reliability index: $\beta^{i+1} = \sqrt{(\mathbf{u}^{i+1})^T \mathbf{u}^{i+1}}$;

Stop if $|\beta^{i+1} - \beta^i| < \varepsilon$;

6.3 Methods

The models discussed in Section 3.3 are used to describe a multi-stage gearbox for the investigation in this chapter. Initially, the bearing matrix was given as a main diagonal equal to the bearing stiffness values, and with zero value cross-diagonal components. The detailed bearing models presented in Section 3.3.3 are used here in order to find all the bearing matrix components based on the hypothesis that a contact angle equal to zero will produce a CRB, while a value lager than zero produces a TRB. The main difference will be the overall bearing stiffness matrix of the planet bearings in the low-speed planetary stage gearbox.

Let us define the bearing matrix corresponding to the flexible supports a translational/rotational gear model as:

$$K_b = \begin{bmatrix} K_{xx} & K_{xy} & 0 \\ K_{yx} & K_{yy} & 0 \\ 0 & 0 & 0 \end{bmatrix} \tag{6.8}$$

where $K_{xx} = K_{yy}$ and $K_{xy} = K_{yx}$. The zero entries correspond to the rotational DOF. The non-zero entries are found with the bearing model discussed before for different contact angles and a pre-defined displacement in the x and y direction. Form previous simulations, an average of this values was found and it was used to compute the final bearing cross-diagonal components. A variation of the stiffness given different contact angles and displacements is shown in Figure 6-2.

From the figure it is seen that the major drivers of the variation in the stiffness is the contact angle of the roller and the initial displacement in one of the radial directions, in this case, in x. The stiffness values used in the simulations are presented in Table 6.1.

Since grid events are not considered in this investigation and a normal operation load case is considered, the electromechanical model used here is the same as the one used

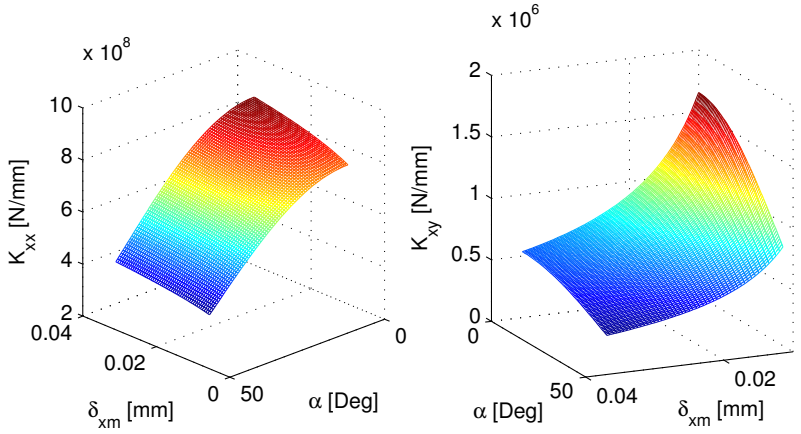

Figure 6-2: Bearing stiffness component variation due to different values of displacement in the x direction and contact angle.

Table 6.1: Bearing stiffness parameters for the CRB and TRB.

Type of Bearing	K_{xx} [N/m]	K_{xy} [N/m]
Cylindrical Roller Bearing	5.2×10^8	4.969×10^6
Tapered Roller Bearing	6.907×10^8	1.346×10^7

in Chapter 4. That is, a multi-stage gearbox composed of a low-speed planetary stage, followed by two parallel stages. The generator is a PMSG and its model is given in Appendix E. The overall system follows the block diagram in Figure 3-22.

6.4 Results

The entire wind turbine system is simulated using the co-simulation approach presented in the previous section. Two sets of simulations are done, each with a different bearing stiffness matrix representing the difference in bearing configuration. The DLC 1.1 normal operation case from the IEC 61400-1 ed. 3 standard [4] is chosen in order to perform fatigue computations and reliability analysis from both configurations. In total, six random turbulence seeds using the Normal Turbulence Model (NTM) are simulated at mean wind speeds ranging from 5 m/s to 25 m/s in increments of 2 m/s bins.

6.4.1 Bearing life

The time-series is analysed to compute the bearing fatigue damage resulting from variations in the torsional loads due to turbulent wind. Furthermore, the reactions due to the gear mesh forces also have an effect in the bearing response. The analysis in this section uses the loads in units of Newton opposed to stresses which are commonly used in this type of analysis. The damage equivalent load due to the bearing radial forces is found

by eq. 4.3. From here, the results are fitted to a normal distribution and it is shown in Figure 6-3. As expected, the mean value of the TRB is higher than the CRB.

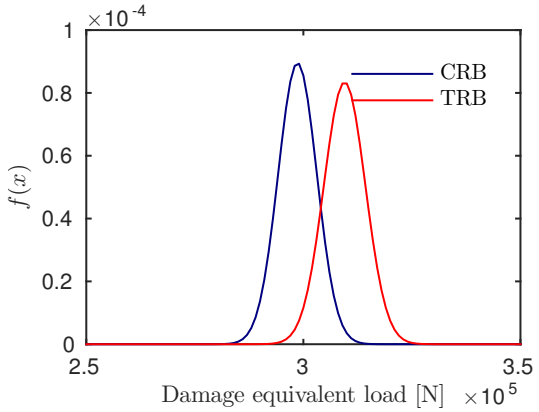

Figure 6-3: Fit to a normal distribution of the damage equivalent loads for both types of bearings.

The results in Figure 6-4 shows the damage equivalent load computed from one of the seeds and for each wind speed from the bulk of simulations (consistent to the results shown in Figure 6-3). Before reaching rated speed the difference on the equivalent loads between the two sets is small. However, as the wind turbine reaches rated-speed (9 and 11 m/s), and after (>11 m/s), the damage equivalent load in both sets increase with a similar trend with the TRB having higher damage than the CRB. The higher load is due to a higher stiffness component in the stiffness matrix (see Table 1).

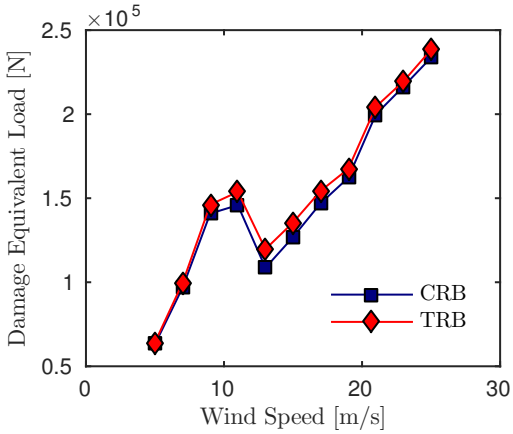

Figure 6-4: 1-h Damage equivalent load of one of the seeds for both sets of simulation.

The main focus is to determine whether a CRB or a TRB configuration is more beneficial for the planetary gearbox reliability. Hence, the minimum requirements for a wind turbine bearing life given by [19] are used for the analysis of these configurations.

Table 6.2: Bearing parameters [11]

Parameter	CRB	TRB
Inner diameter, b [mm]	200	200
Outer diameter, D [mm]	400	360
Basic dynamic load, C [kN]	1980	2090

The basic rating life can be computed using:

$$L_{h10} = \frac{10^6}{60n}\left(\frac{C}{P}\right)^p \tag{6.9}$$

where n is the operational speed, C is the bearing dynamic load rating (given by the manufacturer), P is the equivalent load and p is the life exponent (10/3 for roller bearings). According to the IEC 61400-4 standard [44], the recommended basic rating life for a bearing in the low-speed planetary stage should be of 10^5 hours for a 20 year design life.

6.4.2 Reliability

Because the analysis of the bearing life is of interest in this study, the limit state function is formulated as:

$$g(\mathbf{x}) = \frac{10^6}{60n}\left(\frac{C}{P(\mathbf{x}_r)\chi_s\chi_{aero}\chi_{dyn}\chi_{stat}}\right)^p - 10^5 \tag{6.10}$$

where χ_{aero}, χ_{dyn}, and χ_{stat} are stochastic variables representing the uncertainties in: aerodynamic load calculation, dynamic response of the turbine, and statistical uncertainty due to the reduced number of simulations. The uncertainty models presented in [105] are used since the approach is similar. Last, $\mathbf{x}_r$ denotes the random variable related to the radial load in the bearing which has a stochastic effect in the equivalent load calculation. In equation (6.10), the value of 105 hours is the condition for a bearing to survive the 20 year requirement. The results presented in Figure 6-5 show the values for the reliability index and the probability of failure for different values of C. It is seen that the CRB configuration more reliable than TRB when the reliability analysis is done for the same value of dynamic rating. However, the zoomed section shows that for the corresponding dynamic rating of the bearing parameters used in the simulations (see Table 6.2) the TRB is slightly more reliable than the CRB. According to the results, there seems to be a relation between the dynamic rating, the damage equivalent load and the stiffness of the bearing.

For instance, even though a higher damage equivalent load is observed for the TRB throughout the wind speeds, it is still more reliable than the CRB when considering a 5% higher dynamic rating. This therefore portrays the significance in ascertaining an accurate dynamic rating of the bearing from the manufacturer. A summary of the results

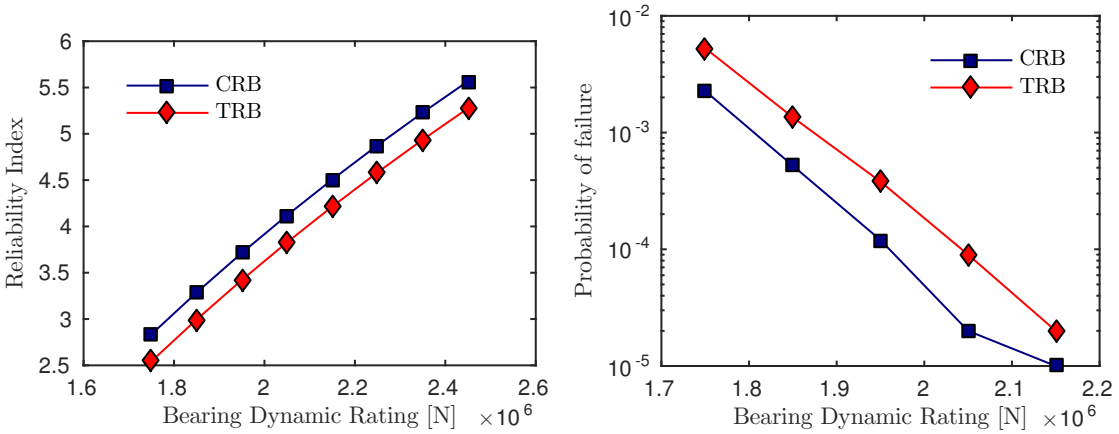

Figure 6-5: Effect of the dynamic load rating (C) in the reliability index (**left**) and the probability of failure **right**.

Table 6.3: Reliability analysis results

Bearing type	β	p_f	Importance factors, α			
			χ_s	χ_{aero}	χ_{dyn}	χ_{stat}
Cylindrical Roller bearing	3.83	9.0×10^{-5}	0.121	0.809	0.405	0.405
Tapered Roller bearing	3.97	6.0×10^{-5}	0.121	0.809	0.405	0.405

including the reliability index, probability of failure and importance factors is presented in Table 6.3. Note the high impact of the uncertainty related to the aerodynamic calculation. This is consistent with the findings from previous work [105] where this value was also higher than other factors. The higher stiffness associated with a higher contact angle than zero will result in higher stresses in the bearing rollers. Even though the stresses are not calculated explicitly, the theory behind the bearing life in equation (6.9) is based on Hertzian stress contact theory for line contacts, as proposed by Lundberg and Palmgren in [56]. Therefore, it is expected that a higher probability of failure is to be observed for same values of dynamic rating. These values have been computed with an implementation of FORM [7].

Note the high impact of the uncertainty related to the aerodynamic calculation. This is consistent with the findings from previous work [105] where this value was also higher than other factors. The higher stiffness associated with a higher contact angle than zero will result in higher stresses in the bearing rollers. Even though the stresses are not calculated explicitly, the theory behind the bearing life in equation (6.9) is based on Hertzian stress contact theory for line contacts, as proposed by Lundberg and Palmgren in [56]. Therefore, it is expected that a higher probability of failure is to be observed for same values of dynamic rating.

6.5 Conclusions

This chapter presented a method that can be used in bearing selection stages during the preliminary design of a planetary gearbox for use in wind turbines. First, an approach for a dynamic coupling between two tools, based on previous work, is extended to include a detailed gearbox model based on lumped-parameters. The coupled analysis allows for complete system simulation of the electromechanical and structural components of the wind turbine. A model of this kind provides added information in early design stages since it is relatively fast to run, compared to high-fidelity FEM models, in addition to the possibility of defining different gearbox and generator combinations. From this, a simulation of normal power production is carried out in order to perform fatigue analysis in the bearings. The results showed the differences in bearing fatigue and it was found that the TRB accumulates more damage across the wind speed range due to the higher stiffness in the model. However, there is no big difference between the two models in terms of reliability due to the significant effect of the dynamic bearing capacities. This chapter demonstrates the capabilities of the simulation tool and the potential results in terms of bearing reliability when a parametric analysis is made. Additional work, in the future, should include the axial loads generated by non-torque loads in the wind turbine rotor such thrust and bending moments.

7

Conclusions

"In soloing - as in other activities - it is far easier to start something than it is to finish it."

– Amelia Earhart

This dissertation has shown progress in the methods for integrated analysis of wind turbines. Special attention was given to the gearbox, where a translational/rotational model was included in the dynamic simulations. The translational degrees-of-freedom are relevant for the analysis of the bearing loads. The method used for the modeling of the gearbox was the lumped-parameter method, a simplification of the topology of the system, yet accurate enough as it was shown by the experimental validation. Furthermore, the model is more efficient in terms of computational time when compared to an early implementation of a multi-body dynamics code that showed to be slow and unstable, given the chosen constraint formulations. The turning point, meaning the change of modeling approach, was backed up by the results from other researchers, where complex gear mesh stiffness models were implemented, along with very long computational times (14 h - 15 h) to obtain 30 s of simulation time. Consequently, the low amount of data obtained with results of this kind, will reduce the confidence for future probabilistic analysis, where large amount of data is needed in order to reduce uncertainties in the results. The method presented here is capable to provide the requirements to carry out future probabilistic analysis of the response of the drivetrain components, in terms of probability of failure, fatigue, extreme value analysis and reliability.

The main focus of the analysis in this dissertation was to quantify the impact that certain events have on the planetary bearings. Hence, most of the results from the preceding chapters make emphasis on this component. Accordingly, several studies were carried out where the bearing loads were analysed in terms of fatigue, maximum contact stresses and reliability.

First, the electromechanical drivetrain simulation tool was tested with DLC 1.1 simulations, while dynamically coupled by torsion to HAWC2. An additional validation of the tool was made in order to confirm the correct operation in the co-simulation mode. That is, the wind turbine dynamics were not affected by the addition of an external system

and reaction forces. The most critical mode that must be considered in this approach is the drivetrain torsion, which depends heavily on the equivalent inertia and stiffness of the drivetrain components when referred to the low-speed shaft. The inertias were matched but it was found that the mode was shifted due to the added flexibilities of the internal components. This finding sheds light into the importance of an integrated analysis. In addition, the fatigue analysis of the planet bearings showed that the contribution to the damage source is a combination of some wind turbine modes and the 2nd drivetrain mode, which is a combination of the high-speed stage and generator. Thus, this a conclusion that cannot be reached when using only an aeroelastic code.

An additional study looked into the effects of extreme loads have on the bearings. The major contribution was to carry out LVRT simulations where the bearing response is considered and quantified. Personally, one of the most important conclusions from this dissertation comes from the analysis of different grid codes requirements in the system simulation. It was found that the FRT requirements are relevant in terms of the maximum loads the bearings experience when subject to a low voltage grid event. In addition, the requirements for the wind turbine operation during such events contribute to the negative impact on the components. The emergency brake situation was shown to be the one with the highest impact on the bearing loads. However, the impact of these cases can be mitigated by making modifications on the way the turbine handles such events.

A reliability method was used to assess the probability of failure of two different kind of bearings under normal operation. The importance of the dynamic rating factor was studied for the two kinds of bearings. The method used to define the types of bearings is a pre-processor where the stiffness matrix is estimated depending on geometry parameters and operational speed. The results showed that different equivalent loads are achieved when using a different kind of bearing, which is consistent with the different reliability indexes found by the FORM analysis.

7.1 Limitations

As it is with any simulation tool, the models presented here have certain limitations, that may or may not, affect the results greatly.

1. The coupling with HAWC2 is done by torsion only. It has been shown by different researchers that the non-torque loads contribute negatively to the loading in the planetary stage bearings.

2. The nature of a translational/rotational model neglects the axial component of the gear bodies. However, since only torsion was being considered, it was not paramount to include the axial component in the model.

3. The bedplate of the nacelle is not included in the drivetrain model. This component is relevant, because in reality, the combined load with the tower-top is transferred through the couplings of the gearbox. The effects become more clear when more

detail studies in the tower-top loads are carried out. It is believed, however, that this limitation would not affect the results of the bearing loads found with the proposed models.

7.2 Future work

Perhaps, the element that was over-looked in the implementation of the electromechanical drivetrain simulation tool was the generator. Mainly because of existing models that provide an accurate representation of the electromagnetic torque due to changes in the load, operational speed or excitation voltage. Moreover, the coupling with HAWC2 was done through torsion only, as well as the coupling of the generator with the HSS of the gearbox. However, it is known that misalignment in the high-speed stage can lead to early failure of the bearings and gear teeth. Therefore, the model development of generators should be targeted to be able to re-produce the misalignment together with the high-speed stage of the gearbox. A possibility is to represent the magnetic forces in the air gap of the generator as flexible elements, and hence, obtain the forces acting on the high-speed shaft. This is a simplification of complex FEM models in order to maintain the low-computational times as a requirement, in addition to considering the co-simulation with an aeroelastic code. A model of this kind can be put through a LVRT case, for example, and it will be possible to study the reaction of the system in the high-speed shaft with additional degrees-of-freedom. A design consideration is that the different high-speed bearings are put in place along the high-speed shaft in order to absorb the off-axis loading from the generator, but what about the location? How is this determined? These kind of questions can be answered with a model of this kind, thanks to optimization techniques where the entire system is put through a series of numerical tests with some constraints in order to full-fill an objective function. In this case, the function could describe the minimization of the loading in the high-speed bearings given their location.

The modeling environment where DUDE was developed has many advantages for describing electrical systems, that were not completely exploited during the PhD study. A possible future study, could be to include the power system in the simulations. Perhaps, a more detailed control model of the power electronics can mitigate the loads in the drivetrain? This has been investigated in the past, but not with a model that includes the bearings, for example. Moreover, a more realistic response of the generator to grid events can be obtained. Hence, improving the response of the internal components of the drivetrain.

A very relevant addition to the current implementation will be the non-torque loading coming from the main shaft. This can be achieved by defining a coupling with HAWC2 that includes the other moments and forcing components. At the same time, this coupling becomes more relevant when considering axial loading in the planet bearings. As seen in Chapter 5 and 6, the axial component was ignored, therefore, the axial loading in the bearings was not considered in the analysis. This loading becomes more interesting when working with TRB, which can take axial loads in addition to the radial loads.

The previous considerations are relevant because:

1. It will advance the development of DUDE so more relevant results can be used to aid in the integrated design of wind turbine drivetrains.

2. In system simulation, it is important to consider as many parameters and subsystems, as possible, without compromising accuracy and computational time. Advances in DUDE can show what is to be considered relevant depending on the type of studies being carried. For example, is it really needed to run full FEM models of gearboxes to estimate the fatigue of the components? Are the cycle counting techniques going to ignore some of this frequency content, and therefore, obtain results that could have been obtained with a simplified model?

Dissemination

Journal articles

J. Gallego-Calderon, A. Natarajan, and N. A. Cutululis, "Ultimate design loads analysis of gearbox bearings under extreme loading," Submitted to *Wind Energy*, March 2015.

J. Gallego-Calderon and A. Natarajan, "Assessment of Wind Turbine Drive-train Fatigue Loads under Torsional Excitation," Under Review. *Engineering Structures*, November 2014.

Peer-reviewed conference proceedings

J. Gallego-Calderon, A. Natarajan, and N. K. Dimitrov, "Effects of bearing configuration in wind turbine gearbox reliability," Under Review. *Energy Procedia*, February 2015.

Conference proceedings

J. Gallego-Calderon, K. Branner, A. Natarajan, N. Cutululis, and J. Hansen, "Electromechanical drivetrain simulation," in Proceedings of the *9th PhD Seminar on Wind Energy in Europe*, European Academy of Wind Energy (EAWE), Visby, Sweden, September 2013.

Poster and oral presentations

J. Gallego-Calderon, A. Natarajan, and N. K. Dimitrov, "Effects of bearing configuration in wind turbine gearbox reliability," Poster presented at *EERA DeepWind'2015 Deep Sea Offshore Wind R&D Conference*, Trondheim, 4 - 6 February 2015.

J. Gallego-Calderon, "Advances on Electromechanical Drive-train Simulation tool," Oral presentation at the *Paper club*, National Wind Technology Center, NREL, Boulder, CO, May 2014.

J. Gallego-Calderon, K. Branner, A. Natarajan, N. Cutululis, and J. Hansen, "Electromechanical drivetrain simulation," Oral presentation presented at the *9th PhD Seminar on Wind Energy in Europe*, European Academy of Wind Energy (EAWE), Visby, Sweden, September 2013.

J. Gallego-Calderon, Anders M. Hansen, John M. Hansen, Braulio Barahona, Kim Branner, Nicolaos A.Cutululis, "Towards a more detailed drivetrain model with Matlab and HAWC2," Oral presentation presented at the *ECCOMAS Thematic Conference on Multibody Dynamics*, Zagreb, Croatia, July 2013.

J. Gallego-Calderon, K. Branner, J. Hansen and N. Cutululis, "Electromechanical drivetrain simulation," Oral presentation presented at the *DCAMM the 14th Internal Symposium*, Nyborg, Denmark, March 2013.

Appendix A

HAWC2's external system interface

A.1 Introduction

One of the most important things in system simulation is flexibility. Thus, being able to choose between different options in order to achieve the desired results is an important factor of the flexibility given in a simulation software. These options could be toolboxes within a software, or the possibility to integrate different simulations environments. Most of the time, when using commercial software, there are certain limitations such as high costs, or simply compatibility issues, which compromise flexibility. In the case of HAWC2, it is possible to connect an external system and to simulate the dynamics of such coupling. So far, this capability has been used by [83] to simulate the reaction forces in the teeth of a planetary gearbox. The gearbox was defined as an external system DLL and constrained to a wind turbine. Thanks to this interface, it was possible to study the dynamics of the complete structure given variations in the wind field. However, the interface was programmed using Fortran90. Although this language has been used for years in different areas of research, another options for research tools have arise, such as Matlab. An advantage with Matlab is the easy programming paradigm and ready to use mathematical functions. Thus, later developments allow the user to generate C/C++ code directly from Matlab algorithms. The generated code can be used as stand-alone implementation, or as a Dynamic Link Library (DLL).

The purpose of this report is to explore the definition of external systems, to be connected with HAWC2, and to generate a DLL interface using Matlab. In the first section, the purpose of the interface is described in general terms. Also, the solution to the EOM inside HAWC2 is presented in order to introduce the formulation of the external system together with HAWC2. The formulation of the external system is explained, along with specifics of the state vectors which are used as DOF in the solution to the EOM together with those from HAWC2. Then, the two relevant constraints that are used to "attach" external system to HAWC2 are explained. In the following section, the details of the necessary subroutines are explained with specifics of the parameters that are passed by reference by HAWC2. This explanation is used as a basis of understanding the program flow, which is presented later on. Also, the initial limitations with Matlab

are discussed and a solution is presented. Finally, two simple examples are given to show the solution of their corresponding un-constrained EOM solved with HAWC2 and using the formulation that is discussed in section A.2.

A.2 Interface Description

In theory, it is possible to define any external system outside HAWC2 by using a DLL. It is also possible to define multiple external systems so they interact in two ways: 1) constraint a body in the external system with one body from HAWC2, or 2) create a series of constraint equations that allow interaction between all the external systems and bodies inside HAWC2. Using any of these two options depends only in the application, where the requirements dictate the type of interaction needed for doing the simulations. A diagram showing this generalization is presented in Figure A-1. Here, a generalized structure is defined in HAWC2 and it interacts with two external systems, which are connected via generalized constraints. An important feature is that the external systems are defined with respect to the global coordinate system inside HAWC2. This means that when the systems are defined, special considerations need to be taken so the location and orientation of the external bodies are defined with respect to the global coordinate system.

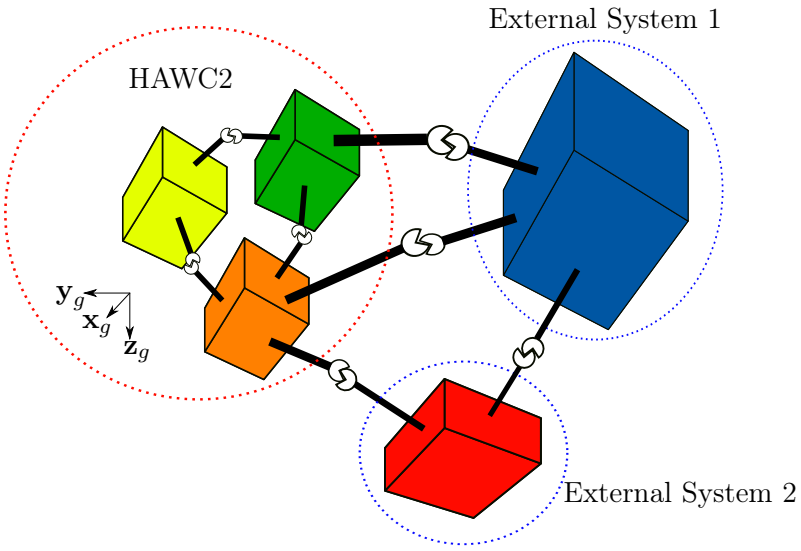

Figure A-1: General representation of interaction between HAWC2 bodies with external systems. The interaction is possible thanks to the external system interface using constraint equations

In [83], the method for solving external systems DOF with those from HAWC2 is presented in detail. However, it is also explained here to create a context in where the interface can be explained clearly. First, the concept of external system and how

it relates to HAWC2 is presented. Then, the formulation used by HAWC2 to solve the whole system (external and the one defined by HAWC2) is explained. Later, the formulation used to describe the external system and how it interacts with HAWC2 is presented, along with a process description to generate the DLL.

A.2.1 How does HAWC2 solves the EOMs?

The underlying motivation of an interface that allows an external system to interact with HAWC2 is to add flexibility in the integrated simulation process. This way, the user is not constrained to those systems defined in HAWC2's structure definition file (*.htc), and to the method used inside the software to define new structures. Therefore, the user can define any external system and connect it to HAWC2 by means of constraint equations. This process allows to define how the external DOFs are related to those from HAWC2.

The combined solution is based on the Virtual Work Principle, more specifically, D'Alembert's principle that states that:

> *"a system of rigid bodies is in dynamic equilibrium when the virtual work of the sum of the applied forces and the inertial forces is zero for any virtual displacement of the system"*

An important remark to the previous statement, is that the virtual displacement δq_j applied to the particle will lead to a virtual work of zero only if the movement is consistent with the constraints. This is an important characteristic of the formulation since the all the bodies within the HAWC2 environment interact with each other via constraint equations. The D'Alambert's principle can be state in mathematical terms as

$$\delta W \;=\; \sum_{j=1}^{n} (F_j - m_j a_j) \cdot \delta q_j \;=\; 0 \tag{A.1}$$

where a_j is the acceleration and F_j are the forces acting on particle j. The force term F_j can be generalized so it is a combination of external forces and internal forces, such as:

$$F_{k_j} \;=\; k_j q_j \quad , \quad F_{c_j} \;=\; c_j \dot{q}_j \tag{A.2}$$

where k_j and c_j are the stiffness and damping, respectively, associated particle j. In a system of rigid bodies, these forces are expressed in terms of the stiffness and damping matrices $\mathbf{K}$ and $\mathbf{C}$ in the generalized equation of motion:

$$\mathbf{M} \cdot \ddot{\mathbf{q}} \;+\; \mathbf{C} \cdot \dot{\mathbf{q}} + \mathbf{K} \cdot \mathbf{q} \;=\; \mathbf{F} \tag{A.3}$$

where F represents the external forces acting on the system, such as gravity for example.

When different systems are being considered (i.e HAWC and a external system), the total solution must contain the EOMs for both and the virtual work done must be equal

to 0.

$$\delta W = \delta W_i + \delta W_e = \delta \mathbf{q_i} \cdot \mathbf{B_i} + \mathbf{q_e} \cdot \mathbf{B_e} = 0 \tag{A.4}$$

where the subscripts i and e refer to the internal and external systems, respectively; vectors $\mathbf{B_i}$ and $\mathbf{B_e}$ represent the un-constrained EOM of the internal and external system, respectively; and the virtual work for both, the internal and external system, is expressed as a function of the virtual DOFs, $\delta \mathbf{q_i}$ and $\delta \mathbf{q_i}$.

$$\mathbf{B_e} = \mathbf{M} \cdot \ddot{\mathbf{q}}_\mathbf{e} + \mathbf{C} \cdot \dot{\mathbf{q}}_\mathbf{e} + \mathbf{K} \cdot \mathbf{q_e} - \mathbf{F} \tag{A.5}$$

The expression in equation (A.5) shows the generalized form of a system using the mass $\mathbf{M}$, damping $\mathbf{C}$, stiffness $\mathbf{K}$ and external forces $\mathbf{F}$, defined as the un-constrained EOM. The resulting vector $\mathbf{B_e}$ is used to calculate the virtual work done by the external system using equation (A.4). Thus, if only (A.5) is defined HAWC2 could be used as a solver to find the time response of the external system. However, the intention with the interface is to solve **together** the EOMs for both, the internal and external system. The way both system interact is by means of constraint equations which couple the DOFs of both systems.

It has been shown before in [63], that each constrain in the system adds an additional DOF to the system and it is known as the Lagrange multiplier λ. This additional DOFs represent the reaction forces created by the constraint equations and the dynamics of the related bodies by such constraint. Since new DOFs are introduced in the system, and new virtual energy is added, the virtual work calculation needs to be modified in order to account for the new DOFs.

$$\begin{aligned}
0 &= \delta W + \delta(\lambda \cdot \mathbf{g}) \\
0 &= \delta W + \delta\lambda \cdot \mathbf{g} + \delta\mathbf{g} \cdot \lambda \\
0 &= \delta \mathbf{q_i}(\mathbf{B_i} + (\bigtriangledown_{q_i} \mathbf{g_i})^T \cdot \lambda) + \delta \mathbf{q_e}(\mathbf{B_e} + (\bigtriangledown_{q_e} \mathbf{g_e})^T \cdot \lambda) + \delta\mathbf{g} \cdot \lambda \\
0 &= \delta \mathbf{q_i}(\mathbf{B_i} + \mathbf{G_i} \cdot \lambda) + \delta \mathbf{q_e}(\mathbf{B_e} + \mathbf{G_i} \cdot \lambda) + \delta\mathbf{g} \cdot \lambda
\end{aligned} \tag{A.6}$$

where $\mathbf{g}(\mathbf{q_i}, \mathbf{q_e}) = \mathbf{0}$ is the constraint vector and the matrices $\mathbf{G_i}$ and $\mathbf{G_e}$ represent the gradient, or Jacobian, of the internal and external system, respectively. Since the total virtual energy must be zero for all the virtual variations of the DOFs, the system of equations is reduced to:

$$\begin{aligned}
\mathbf{B_i} + \mathbf{G_i} \cdot \lambda &= 0 \\
\mathbf{B_e} + \mathbf{G_e} \cdot \lambda &= 0 \\
\mathbf{g} &= 0
\end{aligned} \tag{A.7}$$

From (A.7), it is clear that the DLL must provide the vector $\mathbf{B_e}$ representing the un-constrained EOMs of the external system, the constrain vector $\mathbf{g}$ and the Jacobian $\mathbf{G_e}$.

A.2.2 Defining the external system in Matlab

A Multibody Dynamics code was implemented last year using Matlab. In this code, the formulation for constrained systems and the properties of rotation of rigid bodies, was implemented using the information presented in [63]. The code is defined as a spatial system of constrained bodies, which are defined in the absolute coordinates system. The EOM are in the form of Newton-Euler equations (C.34) with three position coordinates $\mathbf{r} = [x, y, z]_i^T$ and four rotational coordinates $\mathbf{p} = [e_0, e_1, e_2, e_3]_i^T$. Therefore, the vector $\mathbf{q_i} = [x, y, z, e_0, e_1, e_2, e_3]_i^T$ represents the coordinates of body i

$$\begin{bmatrix} \mathbf{M} & \mathbf{G}^T \\ \mathbf{G} & \mathbf{0} \end{bmatrix} \begin{bmatrix} \dot{\mathbf{h}} \\ -\lambda \end{bmatrix} = \begin{bmatrix} \mathbf{fn} - \mathbf{b} \\ \boldsymbol{\gamma} \end{bmatrix} \tag{A.8}$$

where $\mathbf{M}$ is the mass and inertia matrix, $\mathbf{G}$ is the Jacobian matrix of the constraint equations in terms of the angular velocity $\boldsymbol{\omega}'$, $\dot{\mathbf{h}}_i = [\ddot{\mathbf{r}}, \dot{\boldsymbol{\omega}}']_i^T$ is the body velocity vector, $\mathbf{fn}_i = [f, n_i]_i^T$ is the external forces and moments vector, $\mathbf{b_i} = [0, \tilde{\boldsymbol{\omega}}' J' \boldsymbol{\omega}']_i^T$ is the quadratic velocity terms vector, and $\boldsymbol{\gamma}$ is the right-hand side of the acceleration found by calculating the second derivative of the constraint equations. Recall the expression in equation (A.5) using the stiffness and damping elements of the system? In the initial version of the Matlab formulation, these elements were treated as force elements and were included in the vector $\mathbf{fn}$ of equation (C.34), along with any external force affecting the system. In the new implementation, the force elements (i.e. springs and dampers) will be included in the stiffness and damping matrices. Any external forces (i.e gravity or moments) are included in the vector $\mathbf{F}$ of equation (A.5).

Although the same implementation cannot be used to build the external system directly, the concepts applied initially can be carried out in order to define an external system which is to be connected to HAWC2 via constraints. First, let us define the new vectors that describe the states of the system:

$$\mathbf{q}_i = \begin{bmatrix} \mathbf{r} \\ \boldsymbol{\theta} \\ \mathbf{p} \end{bmatrix}_i, \ \dot{\mathbf{q}}_i = \begin{bmatrix} \dot{\mathbf{r}} \\ \boldsymbol{\omega}' \\ \dot{\mathbf{p}} \end{bmatrix}_i, \ \ddot{\mathbf{q}}_i = \begin{bmatrix} \ddot{\mathbf{r}} \\ \dot{\boldsymbol{\omega}}' \\ \ddot{\mathbf{p}} \end{bmatrix}_i \tag{A.9}$$

where the vectors $\mathbf{r}$, $\boldsymbol{\omega}'$ and $\mathbf{p}$ have the same definition of those used in (C.34). A new set of DOFs are introduced by vector $\boldsymbol{\theta}$, and they represent the pseudo-rotations of body i. With this new coordinate representation, it is necessary to define the first derivative of the euler parameters, $\dot{\mathbf{p}}$, in terms of the angular velocity and depending explicitly in the rotational coordinates $\mathbf{p}$. This is necessary because the new formulation in Matlab needs to be compatible to the one with HAWC2 (A.5). Using the properties of the euler parameters and angular velocity presented in [63], the relationship between the angular velocity vector and $\dot{\mathbf{p}}$ can be defined as:

$$\dot{\mathbf{p}} = \frac{1}{2}\mathbf{H}(\omega')\mathbf{p} \tag{A.10}$$

where $\mathbf{H}(\omega')$ is a transformation matrix depending on the components of the angular

velocity vector and it is defined as:

$$\mathbf{H}(\omega') = \begin{bmatrix} 0 & -\omega'_x & -\omega'_y & -\omega'_z \\ \omega'_x & 0 & \omega'_z & -\omega'_y \\ \omega'_y & -\omega'_z & 0 & \omega'_x \\ \omega'_z & \omega'_y & -\omega'_x & 0 \end{bmatrix} \tag{A.11}$$

Equation (A.10) completes the un-constrained EOM used to calculated the residual **Be** needed by HAWC2. As an example, the system in (A.12) shows how the un-constrained EOM would look like for one un-constrained body implemented in Matlab as an external system, that will be solved later using HAWC2:

$$\begin{bmatrix} \mathbf{M}_{6\times6} & \mathbf{0}_{6\times4} \\ \mathbf{0}_{4\times6} & \mathbf{0}_{4\times4} \end{bmatrix} \ddot{\mathbf{q}} + \begin{bmatrix} \mathbf{0}_{6\times6} & \mathbf{0}_{6\times4} \\ \mathbf{0}_{4\times6} & \mathbf{I}_{4\times4} \end{bmatrix} \dot{\mathbf{q}} + \begin{bmatrix} \mathbf{0}_{6\times6} & \mathbf{0}_{6\times4} \\ \mathbf{0}_{4\times6} & -\mathbf{H}_{4\times4} \end{bmatrix} \mathbf{q} - \begin{bmatrix} \mathbf{fn}_{6\times1} \\ \mathbf{0}_{4\times1} \end{bmatrix} = \mathbf{B_e}$$

or

$$\mathbf{M} \cdot \ddot{\mathbf{q}} + \mathbf{C} \cdot \dot{\mathbf{q}} + \mathbf{K} \cdot \mathbf{q} - \mathbf{F} = \mathbf{B_e} \tag{A.12}$$

The system of equations from (A.12) can be implemented as an un-constrained external system and get its solution from HAWC2. This means that the interface can also work with only un-constrained systems and HAWC2 can be used as a solver for the EOM defined as (A.12). At the end of the report, in section A.4, two examples of the solution for un-constrained systems are presented: (1) 1 DOF spring-mass system, and (2) a 6 DOF system, where it is shown how the body rotates given an initial angular velocity.

A.2.3 Constraint formulation

As mentioned before, the external system can be formulated by itself and solved in HAWC2. But, what if the external system needs to interact with the system defined in HAWC2, i.e. a wind turbine? In order to have a fully coupled system the external system DOFs have to be related somehow to those from a body (or bodies) inside HAWC2. This is accomplished by means of constraint equations.

Given the nature of a drive train system in a wind turbine, the two most relevant constraints that will "attach" this system to the main shaft defined in HAWC2 are the position and rotational constraints. A diagram of the system is shown in Figure A-2. An ideal drive train has been defined as an external system and it is constrained to the main shaft in HAWC2 at point P. It is clear that the drive train needs to rotate along the main shaft. Thus, the moments and forces acting on the shaft are transferred to the drive train. This section details the formulation of such constraints and explains how they are implemented in Matlab.

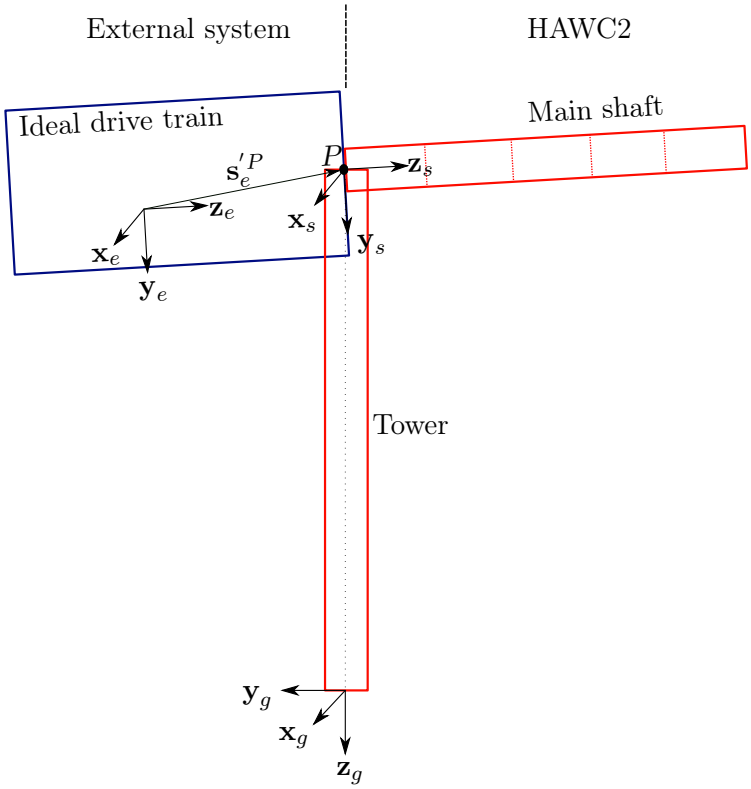

Figure A-2: A drive train defined as an external system and constrained to the main shaft inside HAWC2.

Position constraint

A *position constraint* between bodies e and s it is shown in Fig. A-2. The center of the joint is at point P, which has constant coordinates with respect to the local coordinate systems of bodies e and s. This constraint ensures the bodies are attached to point P at all times. The vector $\mathbf{s}_s^{'P}$ it is not shown in the figure because in this case is equal to zero, given that the coordinate system of the shaft coincides with point P. The constraint equation is defined as:

$$\Phi^{(p,3)} \equiv \mathbf{r}_e + \mathbf{A}_e \mathbf{s}_e^{'P} - \mathbf{r}_s - \mathbf{A}_s \mathbf{s}_s^{'P} = 0 \tag{A.13}$$

where vectors $\mathbf{r}_e$ and $\mathbf{r}_e$ correspond to the location of the local coordinate system of the external body and the shaft, respectively; matrices $\mathbf{A}_e$ and $\mathbf{A}_s$ represent the rotation matrices of external body and the shaft, respectively; and, vectors $\mathbf{s}_e^{'P}$ and $\mathbf{s}_s^{'P}$ represent the distance from the center of each coordinate system to point P.

Rotational constraint

The rotational constraint is composed of three single constraint equations. These single equations are usually referred to as perpendicular constraints n. They are formulated by defining perpendicular vectors on each body and ensuring that they maintain their orthogonality at all times. The purpose of this constraint is to fix the rotation of the external system to the rotation of the body inside HAWC2. For instance, if the shaft rotates 1 rad in the clockwise direction, then the drive train must rotate 1 rad in the clockwise direction. This constraint, together with the position constraint, ensures that all the DOFs from both bodies are fully coupled.

$$\begin{aligned} \Phi^{(n,1)} &\equiv \mathbf{u}_{ez}^T \mathbf{u}_{sy} = 0 \\ \Phi^{(n,1)} &\equiv \mathbf{u}_{ex}^T \mathbf{u}_{sx} = 0 \\ \Phi^{(n,1)} &\equiv \mathbf{u}_{ey}^T \mathbf{u}_{sz} = 0 \end{aligned} \tag{A.14}$$

where $\mathbf{u}_{ex}$, $\mathbf{u}_{ey}$ and $\mathbf{u}_{ez}$ are unitary vectors along the axis x_e, y_e and z_e of the external system; and, $\mathbf{u}_{sx}$, $\mathbf{u}_{sy}$ and $\mathbf{u}_{sz}$ are unitary vectors along the axis x_s, y_s and z_s of the main shaft inside HAWC2.

A.3 Program Structure

The formulation from the previous section is implemented in Matlab in a series of subroutines that are necessary so HAWC2 can build the state and constraint vectors, and seek a solution using the process described in section A.2.1. This section, explains how these subroutines are expected from HAWC2, how they are built in Matlab, and necessary considerations/limitations need it to build the interface with HAWC2 through a Dynamic Link Library (DLL). The information of the specifics of these subroutines is from the example DLL presented in [83].

A.3.1 Details of the subroutines

The process of defining an external system and to constrain it to HAWC2 can be visualized as two major tasks:

- Definition of the un-constrained EOM, as it was shown in equation (A.12).
- Formulation of the constraint equations used to constrain the external system to a HAWC2 body (equations (A.13) and (A.14)).

First, let us define the subroutines related to the definition of the external system. As an example, the module name used here is called "hawc2shell" and it refers to the module name that it is specified in the external system section of the htc file. This is the name that HAWC2 looks for inside the DLL in order to call the subroutines. For

example, here is a definition in the htc file of an external system named "DriveTrain" which is located in the DLL:

```
begin ext_sys;
 name DriveTrain;
 module hawc2shell;
 dll .\hawc2shell.dll;
 ndata 6;
 data 5025497.444         ; Generator inertia referred to the slow shaft.
 data 1                   ; Mass of the drivetrain [Kg]
 data  0.0 0.0 -89.56256   ; Position of the drivetrain (global)
 data 5.0                 ; Tilt angle (around global X)
 data 0.5                 ; Initial shaft rotation [rad/s]
 data 0.02                ; Time step
end ext_sys;
```

Initialize external system

The system is initialized by defining the dimensions given, preferebly, by the vector `sdata`. This vector contains the information specified in the htc file for the external system. In addition, the subroutine should specify the dimension of the time dependent and independent matrices. This subroutine is called **once**. The detailed information about each of the parameters is presented in Table A.1.

```
esys_init(pwrk,Nnr,Nnq,Nout,Nvis,Nheader,sdata)
```

Table A.1: Parameters of the initialization routine

`sdate`	[in] Data lines from the htc file. Each data line has a fixed length CHAR(256) so that the total length of "sdata" becomes (CHAR256*Number of data lines).
`pwrk`	[out] Pointer to the structure where the information of the external system is defined.
`nnr`	[out] Dimension (nnr*nnr) of the time dependent system matrices.
`nnq`	[out] Dimension (nnq*nnq) of the time independent system matrices. $DOF = nnr + nnq$
`nout`	[out] Number of states to be logged in the output file.
`nvis`	[out] Number of reals used to store variables used for visualization.
`nheader`	[out] Number of reals to store header variables for visualization.

Initial conditions of the external system

The system's initial conditions are specified by means of the state vectors `q`, `qdot` and `qdot2`. This subroutine is called **once**.

```
esys_update(pwrk,q,qdot,qdot2)
```

Table A.2: Parameters of the initial conditions routine

`pwrk`	[in] Pointer to the structure where the information of the external system is defined.
`q`	[in/out] Initial conditions for the states.
`qdot`	[in/out] Initial conditions for 1st time derivative of the states.
`qdot2`	[in/out] Initial conditions for 2nd time derivative of the states.

Update the external system

This subroutine is called during the iterations that HAWC2 makes to update the system matrices, such as rotation and external forces, and to return the mass, damping and stiffness matrices. The current state vectors are received as inputs in order to do the update.

```
esys_update(pwrk,time,q,qdot,qdot2,M,C,K)
```

Compute the residual vector

This subroutine is called at **every time step** to compute the residual vector $\mathbf{B_e}$ from equation (A.5). The current value of the states is passed so the residual is calculated.

```
esys_residual(pwrk,q,qdot,qdot2,be)
```

Table A.3: Parameters of the update routine

`pwrk`	[in] Pointer to the structure where the information of the external system is defined.
`time`	[in] Current simulation time.
`q`	[in] Current value of the states.
`qdot`	[in] Current value of the 1st time derivative of the states.
`qdot2`	[in] Current value of the 2nd time derivative of the states.
`M`	[out] Mass matrix.
`C`	[out] Damping matrix.
`K`	[out] Stiffness matrix.

Table A.4: Parameters of the routine that computes the residual vector

`pwrk`	[in] Pointer to the structure where the information of the external system is defined.
`q`	[in] Current value of the states.
`qdot`	[in] Current value of the 1st time derivative of the states.
`qdot2`	[in] Current value of the 2nd time derivative of the states.
`be`	[out] Residual vector

Output

This subroutine is called at the end of convergence to write the current states into the output vector. Therefore, the subroutine is called at **every time step**

```
esys_output(pwrk,out,q,qdot,qdot2)
```

Table A.5: Parameters of the routine to write in the output vector

`pwrk`	[in] Pointer to the structure where the information of the external system is defined.
`out`	[out] Output vector. The states must be written into this vector
`q`	[in] Initial conditions for the states.
`qdot`	[in] Initial conditions for 1st time derivative of the states.
`qdot2`	[in] Initial conditions for 2nd time derivative of the states.

Once the subroutines that define the un-constrained EOMs for the external system are completed, it is necessary to define the constraint subroutines. For each constraint there must be a set of two subroutines: initialization and update. For the system shown in Figure A-2 it is necessary to define two constraints: position and rotation. Therefore, there will be a total of 4 constraint subroutine. The parameters necessary, and the purpose of each subroutine is explained next.

Here, an example of the definition of the position constraint in HAWC2. This constrained as been named `constraint01`. Notice that the initialization constraint is defined in the HAWC2 code as `constraint01_init` and the update subroutine is `constraint01_update`. It is also necessary to define the number of equations in the constraint, the number of bodies in HAWC2 and the external system involved in the constraint. In addition, the node where the constraint occurs in HAWC2 and the external system is defined by the commands `mbdy_node` and `esys_node`, respectively.

```
begin dll;
 dll        .\hawc2shell.dll;
 init       constraint01_init;
```

```
 update     constraint01_update;
 neq        3;
 nbodies    1;
 nesys      1;
 mbdy_node  towertop last;
 esys_node  DriveTrain 0;
end dll;
```

Initialize constraint

This subroutine is called three times during initialization. At each call, the flag `itask` is changed to indicate what parameters are passed through the variables `var1`, `var2`, `var3`, `var4` and `var5`. The value of `pwrk` is also changed. The details of these values are specified in Table A.6.

```
constraint01_init(pwrk,itask,var1,var2,var3,var4,var5)
```

Table A.6: Parameters of constraint initialization routine

pwrk	`itask`= 0	The subroutine must return the address where the object type `constraint01` is located.
	`itask`> 0	Not used
	`itask`< 0	`pwrk` will contain the address of the location of the external system type object (the one created in the `esys_init`) subroutine. **It is important to save this address in one of the fields of the object type constraint01 because it would be used in the update routine**.
var1	`itask`= 0	Number of equations
	`itask`> 0	Total number of body DOFs
	`itask`< 0	Total number of esys DOF
var2	`itask`= 0	Number of bodies inside HAWC2 involved in the constraint
	`itask`> 0	Coordinates of the node in HAWC2 where the constraint takes place
	`itask`< 0	Coordinates of the node in the external system where the constraint takes place
var3	`itask`= 0	Number of bodies of the external system involved in the constraint
	`itask`> 0	Rotation matrix of the nbody inside HAWC2
	`itask`< 0	Index of the body involved in the external system
var4	`itask`= 0	Constraint vector
	`itask`> 0	Index of the body involved in HAWC2
	`itask`< 0	Gradient matrix of the external system
var5	`itask`= 0	Not used
	`itask`> 0	Gradient matrix of the body inside HAWC2
	`itask`< 0	Not used

Update constraint

This subroutine is called **every time step** to calculate the constraint vector. The calculation is stored in the field corresponding to the constraint vector inside the object type `constraint01`. The external system is found by taking the address from the corresponding field of the constraint object (see description of `pwrk` in Table A.6). In this subroutine, `pwrk` points to the subroutine type `constraint01`.

```
constraint01_update(pwrk,time)
```

This conclude the explanation of the purpose for each subroutine. Next, the previous information is put into the context of the simulation by describing the program flow.

A.3.2 Program Flow

The way HAWC2 calls each subroutine it is shown in Figure A-3. The simulation in HAWC2 has three major stages: initialization, run-time simulation, and closing the simulation and writing the outputs. In the initialization task, HAWC2 makes sure to get all the necessary information of the bodies defined in the htc file, along with those defined in the external system. That is, initial coordinates and initial conditions of the state vectors. In addition, it initializes the constraint equations. Then, in the run-time simulation, every time step seeks to update the state vector and system matrices after convergence has been achieved. After the simulation time is done, it writes the outputs in the respective file.

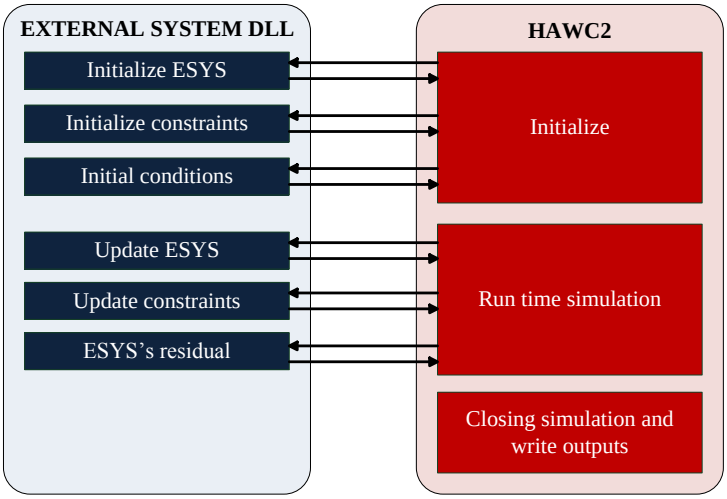

Figure A-3: Flowchart of the interface.

A.3.3 Final remarks about the interface

In the previous sections, the subroutines used to define, and solve, the external system together with HAWC2 were explained. Also, the flow of the program was described but no details about the interface were mentioned so far. Initially, it was intended to generate a DLL file directly from Matlab but it was not possible for the following reasons:

- To ensure a correct communication between HAWC2 and the DLL, it is necessary to define the subroutines prototypes correctly. Since the subroutines need to be defined as Matlab functions before the conversion, the variables will appear in different order depending if they are defined as output or input. After the conversion, it was noticed that the variables were not in the exact order.

- On the HAWC2 side, when a subroutine in the DLL is called, the parameters are passed by reference, i.e. pointers. However, they are not single pointers to a value but a pointer to a pointer. Therefore, once again, the prototypes from Matlab are defined in a way that is not compatible with what HAWC2 expects.

Given the previous reasons, it was decided to build a "shell" interface around the subroutines created in Matlab (Figure A-4). The shell takes care of building the right prototypes of the subroutines and to ensure that the pointers types are correct.

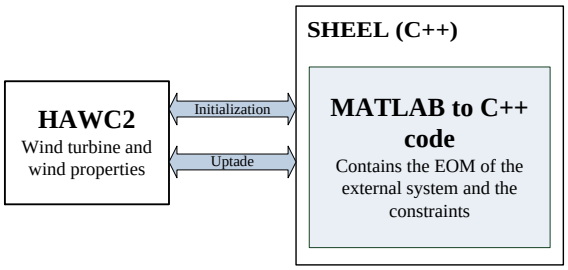

Figure A-4: Interface block diagram.

A recurring issue was to understand how were the pointers handled by HAWC2 and how they should been treated in the shell. Since they are pointers to pointers, it means that the value of `pwrk`, for example, contains the address in memory of the structure type external system. An representation of this is shown in Figure A-5, where `pESYS` represents the contents of the address at which `pwrk` is pointing at, and it corresponds to the address of the working structure type external system.

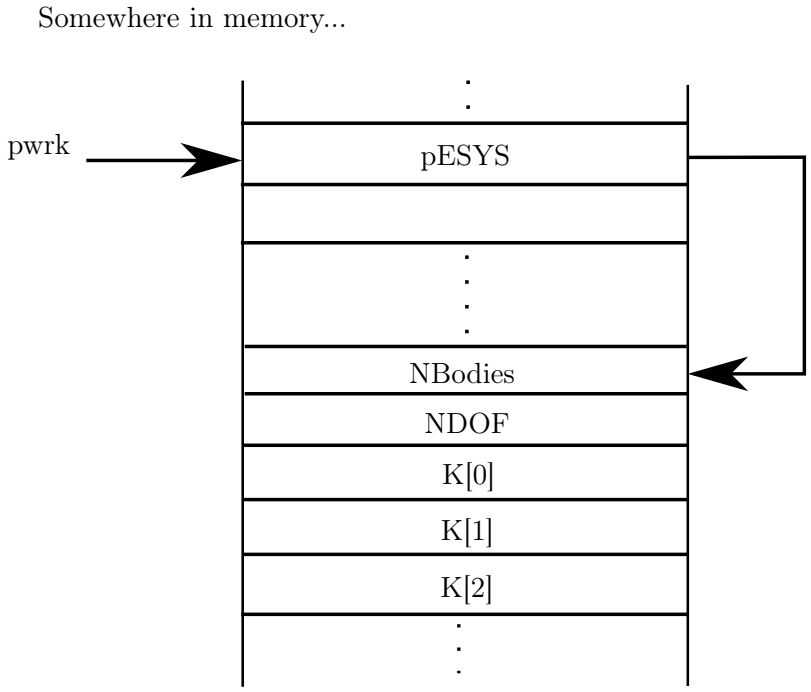

Figure A-5: Working with the pointers.

A.4 Examples

In this section, two examples of the solution to the un-constrained EOMS are presented. First, a 1-DOF system represented as a spring-mass is presented along with the displacement and velocity given the initial conditions. The second example involves all the DOF, or the states in vector **q**, and it shows the rotation of a body given an initial angular velocity. This is an important example since its simplicity helps in the validation of the formulation presented in equation A.12.

A.4.1 Spring-mass system

Since this is a 1 DOF system, the definition of the rotational coordinates don't apply and it is only necessary to define one-dimensional quantities for the mass, stiffness, damping, and state vectors. Therefore, the EOM of the system is given by

$$m\ddot{q} + c\dot{q} + kq \;=\; 0 \tag{A.15}$$

The external system is defined in the htc file, where the mass and stiffness are specified. Notice that the definition of a system with out constraints is simple, since there is no need to define additional bodies in the structure:

```
begin new_htc_structure;
```

```
   begin orientation;
   ;
   end orientation;
   ;
   begin ext_sys;
      name mass;
      dll .\hawc2shell_smm.dll;
      module hawc2shell;
      ndata 3;
      data 2       ; mass of mass [Kg]
      data 10      ; stiffness
      data 2       ; time step
   end ext_sys;
end new_htc_structure;
```

The initial conditions of the system were defined as $q = 1$ and $\dot{q} = 0$. The results of the simulation, displacement and velocity of mass m, are shown in Figure A-6. Based on the input information about the parameters of the system in the htc file, the system has the following natural frequency, which is verified by the spectrum plot in Figure A-7:

$$f_n = \frac{1}{2\pi}\sqrt{\frac{k}{m}} = 0.35588\text{Hz} \tag{A.16}$$

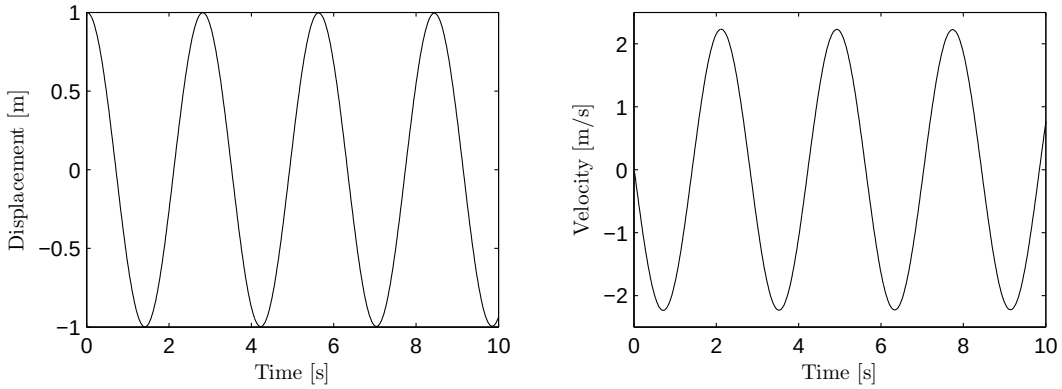

Figure A-6: (a) Displacement $x(t)$ as function of time t. (b) Velocity $\dot{x}(t)$ as function of time t.

A.4.2 Rotating body

This example explores the functionality of the formulation presented before. This is a single body with 6 DOF, that has initial angular velocity of $\boldsymbol{\omega}' = \{-0.2, 0.5, -0.5\}$ (Figure A-8). There are no external forces or moments acting on it. The results in Figures

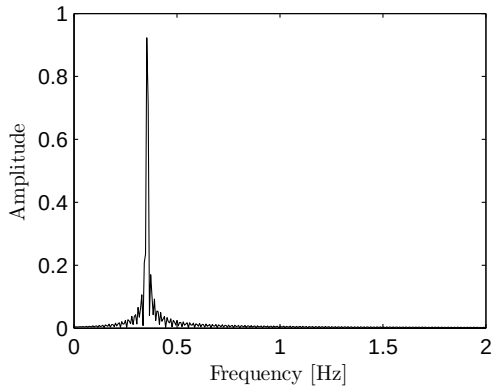

Figure A-7: Spectrum of the displacement of m.

A-9 and A-10 show the variations of the euler parameters, the value of the components of the vector $\boldsymbol{\omega}'$ and the rotating angles. The EOMs for this body are those presented in equation (A.12).

As specified in the initial conditions, the sign of rotation in the x and z components is the same. The result, the values of the angles θ_x and θ_z have the same sign. Also, notice the delay of θ_x compared to θ_z, given that the rotations in the z component go at a higher angular velocity than in x. In addition, there is a variation within each components and this is due that the body is not rotating around a fixed axis, because the initial conditions for the three components of $\boldsymbol{\omega}'$ contain non-zero values.

A.4.3 Drive train as a concentrated mass

This section presents the simulation results of a external system constrained to a body in HAWC2. The external system represents the drive train of a wind turbine as a concentrated mass. This is the model of the drive train that is commonly used in Aerolastic calculations and that HAWC2 uses in the *NREL 5MW Reference Wind Turbine*. The external drive train is formulated as a rigid body with 10 DOF following the formulation that was presented in Equation (A.12). The system is also attached to the wind turbine by means of a position and rotational constraints, which make sure that the shaft moments, forces and angular velocity are transferred into the external drive train.

The model is to be validated with the simulation results from the *NREL 5MW Reference Wind Turbine* using the internally defined drive train. It is expected a high degree of correlation between the results obtained using both models. This is an important preliminary study to validate the operation of the proposed interface, in order to move forward to more detailed models of the drive train.

The results presented here correspond to a 500 sec simulation with ramp up, ramp down and a wind gust. This is done with the purpose of observing the performance of the external DLL when transients occur in the simulation. As a starting point, the wind behaviour is presented in Figure A-11.

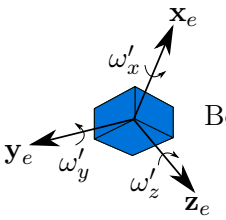

Body defined as an external system

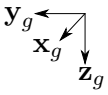

Global coordinate system in HAWC2

Figure A-8: One body rotating given initial values for the angular velocity components.

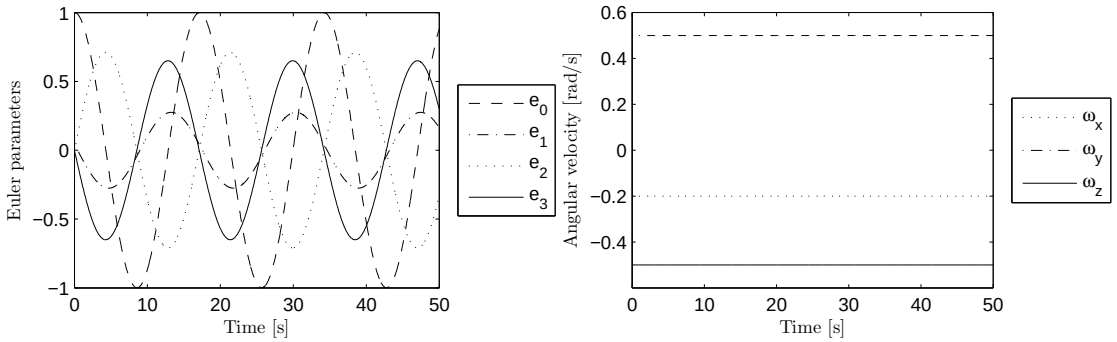

Figure A-9: (a) Components of vector $\mathbf{p}$ as function of time t. (b) Components of the angular velocity vector $\boldsymbol{\omega}'$ as function of time t.

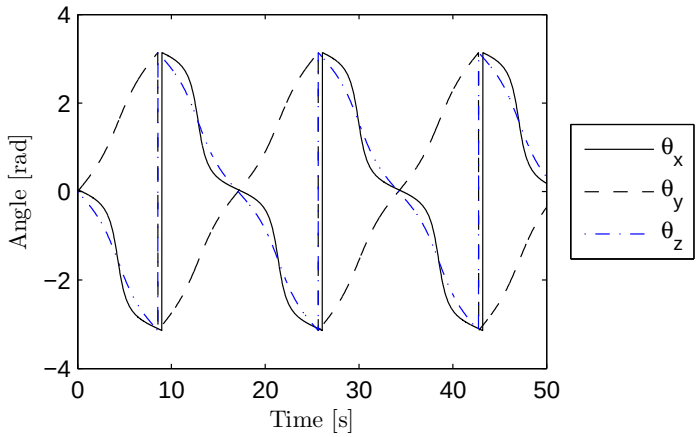

Figure A-10: Rotation angles.

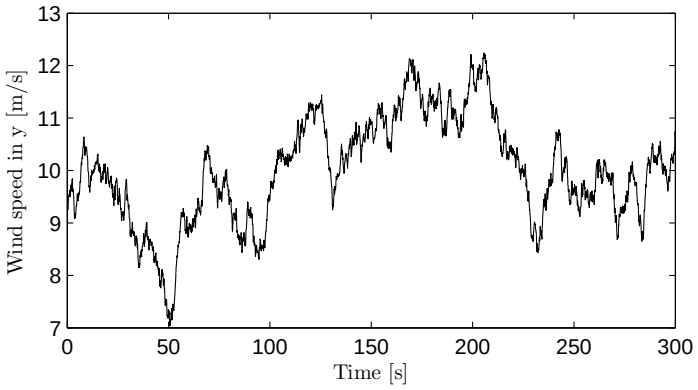

Figure A-11: Wind speed in y.

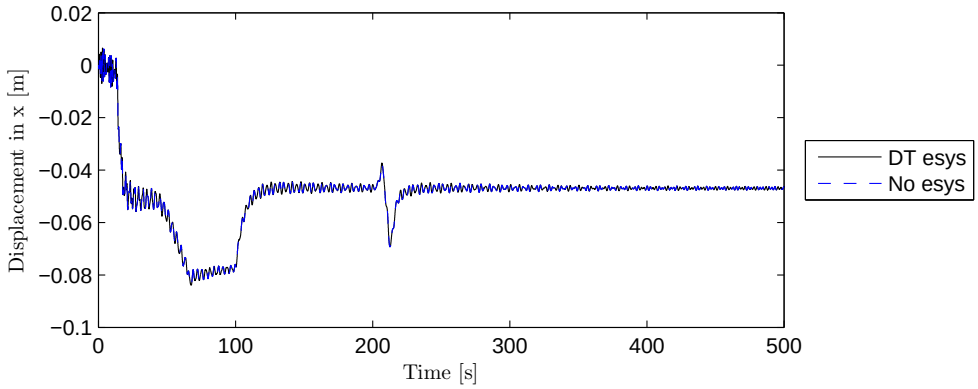

Figure A-12: Towertop displacement in the x direction.

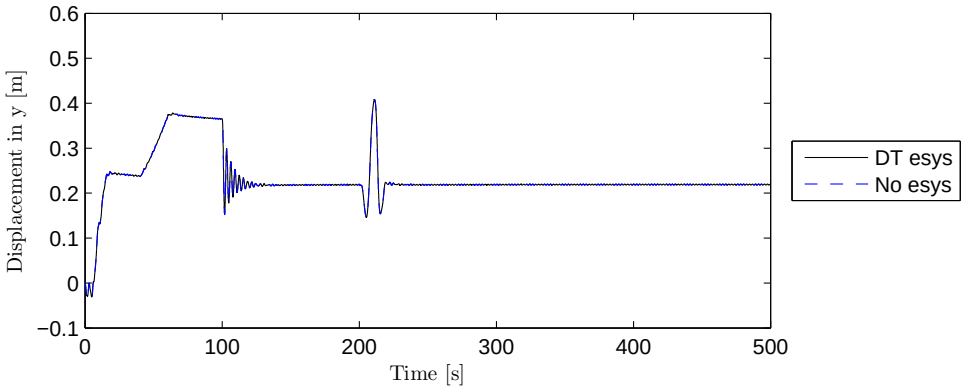

Figure A-13: Towertop displacement in the y direction.

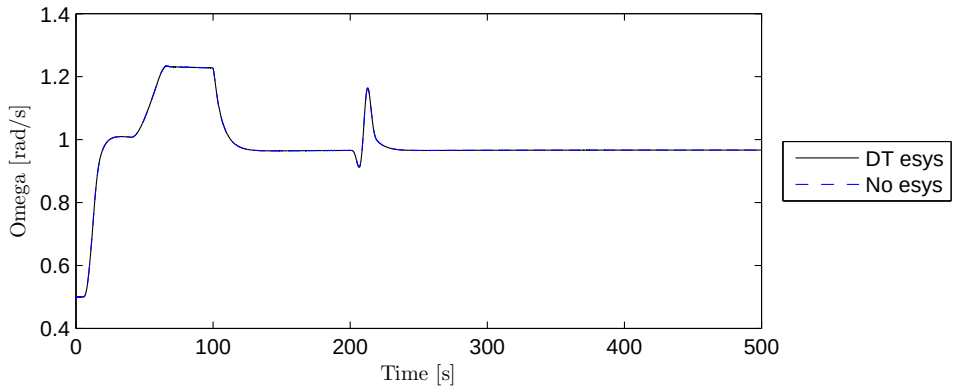

Figure A-14: Rotor angular velocity.

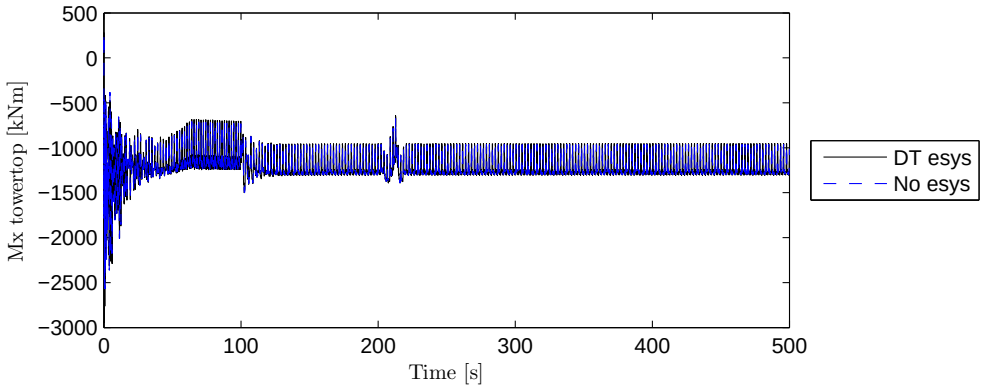

Figure A-15: Moment around the x axis in the towertop.

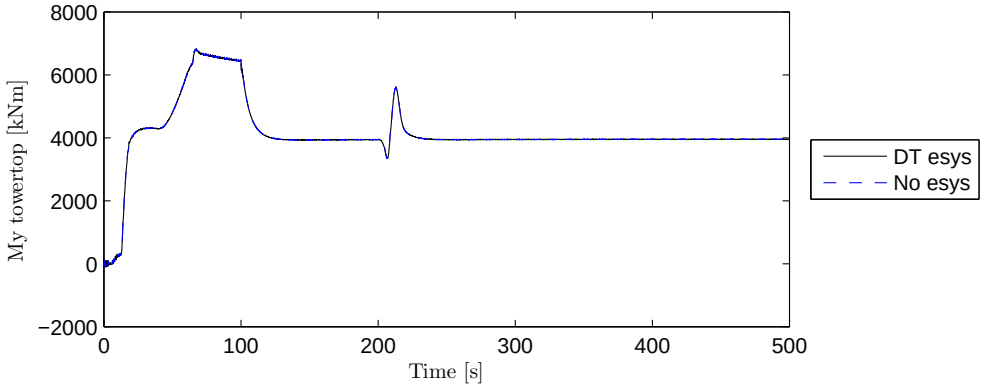

Figure A-16: Moment around the y axis in the towertop.

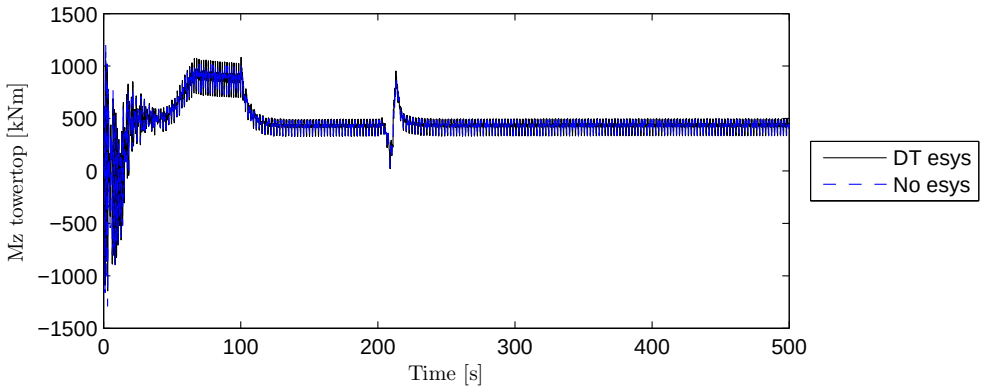

Figure A-17: Moment around the z axis in the towertop.

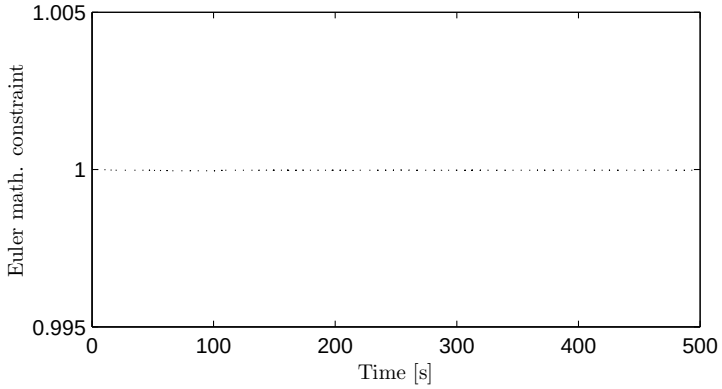

Figure A-18: Mathematical constraint of the Euler paramenteres $p = e_0^2 + e_1^2 + e_2^2 + e_3^2$.

Appendix B

Definitions in gear design

This section presents a glossary of terms related to gear design and that are used in this dissertation. To complement the glossary, Figures B-1 show the nomenclature on a pair of mating spur gears.

Addendum: Radial distance from the pitch circle to the outside diameter.

Backlash: The amount of clearance between mating components, in this case gear teeth. It is also defined as the lost of motion due to a clearance when movement is reversed and contact is re-established.

Base radii: Radial distance from the gear center to the base circle.

Base circle: It is the circle from which the involute tooth are originated from.

Dedendum: Radial distance between the pitch circle and the root diameter.

Mesh stiffness: The required load over 1 mm of face width along the line of action, to cause in line with the load a deformation of the tooth of 1μm [108].

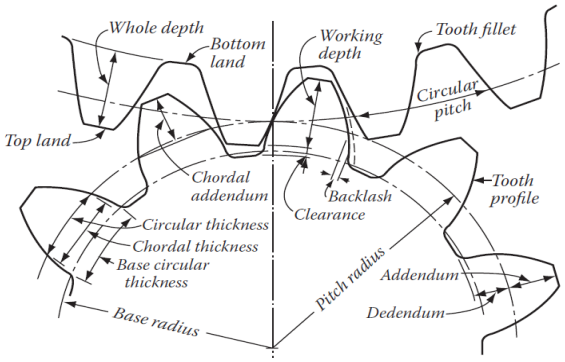

Figure B-1: Diagram showing the gear terminology [9].

Outside diameter: Diameter of the gear measured from the top of the teeth.

Pitch circle: It is the imaginary circle that is located on the contact point between two meshing teeth. and

Pressure angle: It is the angle at a pitch point between the line of contact which is normal to the tooth surface and the plane tangent to the pitch surface.

Transmission error: It is defined as the difference between the actual position of the driven gear and the theoretical angular position that the gear should occupy while running the driving gear at constant speed.

Module: A normalization parameter that describes the tooth thickness in order to ensure kinematic compatibility between the mating teeth of a gear pair. This compatibility is guaranteed by the ratio:

$$m = D/N \tag{B.1}$$

where D is the pitch diameter and N is the number of teeth.

Pitch radii: Distance from the gear center to the pitch point, which is the point in the line of action at which the gear teeth mate. This is also the distance from the center to the *pitch circle*.

Appendix C

Theory of multi-body dynamics

C.1 Basic Concepts

This chapter focuses in the definition of the basic concepts and terms commonly used in the analysis of multibody systems. Reference frames and vector coordinates are introduced, along with the description of planar and spatial coordinate systems.

C.1.1 Definitions

The study of multibody systems seeks to describe the dynamics of mechanical systems that are formed by several bodies (rigid or deformable), which are interconnected by kinematic constraints. These kinematic constraints are the result of different types of joints and it allows for each body to be subject to translation and rotational displacements.

This document focuses in rigid bodies and introduces the concept of deformable bodies. The main difference between *rigid* and *deformable* bodies is that the distance of the particles in rigid bodies remains constant. On the contrary, the particles of a deformable body move relative to each other.

A set of rigid bodies that are arranged to produce a specific motion is defined as *mechanism*, and the individual bodies are called *links*. The combination of two links in contact are defined as *kinematic pair* or *joint*. Kinematic analysis deals with the study of the motion of rigid bodies. This includes their displacement, velocity and acceleration, to determine the design geometry of the mechanical parts. In addition, it studies the motion of a system of rigid bodies (i.e. mechanism), resulting from applied forces.

It is always helpful to have a visual representation of the mechanism. Schematic diagrams are used to describe the bodies, kinematic joints and external forces acting in a multibody system (Fig. C-1). The shape of each body is trivial, since the importance of the schematic representation is to show the connectivity of the bodies, the type of joints and the physical characteristics of the external forces in the system. This representation will be use to identify the bodies and their respective coordinates in the global reference frame and in the system.

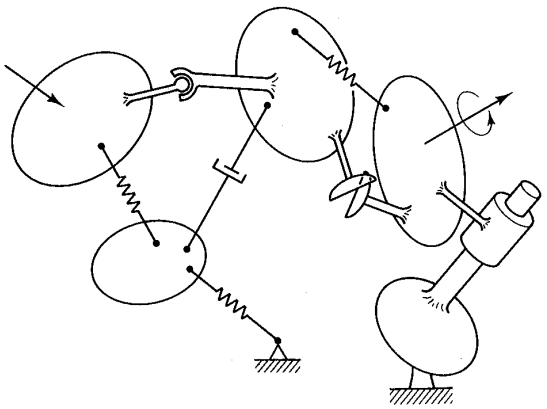

Figure C-1: Schematic representation of a multibody system.

C.1.2 Vector Coordinates

There are two sets of vector coordinates that can be used to describe the kinematic behavior of rigid bodies. The type of coordinates used depends on the level of complexity desired for the study of the mechanical system. These two modes of representation could be used, independently, to describe the motion of a rigid body or a mechanism. In the case of *planar motion* the multibody system is analysed in the xy plane. The translational coordinates of the body i can be represented by the vector $\vec{r_i} = [x, y]_i^T$, which are used to locate the body in the *global reference frame*. In addition to the global coordinates, $\vec{r_i}$, a *local* or *body-fixed reference frame* $\xi_i\eta_i$ is defined inside the body i; also, the angle ϕ_i is defined as the rotational angle of the body with respect to the global reference frame, and it is used to determine the orientation of the body in the xy plane. An example of the planar representation is shown in Fig. C-2.

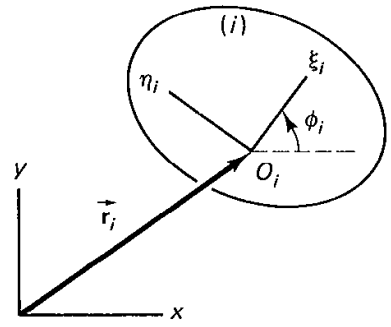

Figure C-2: Vector coordinates for planar motion.

The total number of coordinates required to describe the motion of a body in the planar system xy is three: two translational coordinates, x_i and y_i, and one rotational ϕ_i. These coordinates are arranged in vector form as: $\vec{q_i} = [x, y, \phi]_i^T$.

In the case of spatial analysis, the body is placed on a 3D global reference frame

xyz and it's translational coordinates are defined by the vector $\vec{r_i} = [x, y, z]_i^T$. These coordinates locate the body-fixed reference frame $\xi_i \eta_i \zeta$ in space, and it is relative to the global xyz axes. Unlike the planar motion representation, in spatial analysis it is necessary to define three rotational coordinates in order to specify the orientation of the body. Thus, the vector of coordinates of a multibody system is defined as: $\vec{q_i} = [x, y, z, \phi_1, \phi_2, \phi_3]_i^T$. An example of the planar representation is shown in Fig. C-3.

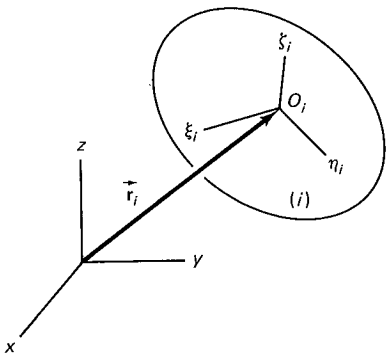

Figure C-3: Vector coordinates for spatial motion.

Although three rotational coordinates are defined here, the formulation presented in this report uses four rotational coordinates. These coordinates are known as *Euler parameters* and the advantage over the previous representation, is the avoidance of singularity issues in the numerical computation. In the next chapter, these concepts will be introduced when the formulation for spatial analysis is described.

As it was shown, the number of coordinates required to describe a system depends on the number of bodies and the type of coordinates used (planar or spatial). In general terms, a multibody system with b bodies can be described by $n = 3 \times b$ for planar systems, and $n = 6 \times b$ for spatial systems, only if three rotational coordinates are use. In the formulation presented in this report, four rotational coordinates are used, and therefore, $n = 7 \times b$ coordinates are needed. Also, the vector of coordinates of the system is defined as $\vec{q_i} = [q_1^T, q_2^T, ..., q_b^T]^T$.

As explained before, a mechanism is composed by links and kinematic joints, which connect two bodies (links). From the coordinates perspective, this means that not all the coordinates are independent because there are *constraint equations* that relate such coordinates.

C.2 Spatial Analysis of Multibody Systems

In this chapter, the concepts concerning planar kinematics introduced earlier are extended to spatial kinematics. Although the analysis is the same, the process of describing the orientation of the body with respect to a global coordinate system is not as straightforward. In the first part of this chapter, the rotational coordinates known as *Euler parameters* are explained. These parameters are used to specify the orientation of a body in space

with respect to a global coordinate system. Like it was shown before, a point can be located in space using:

$$s^P = As'^P \tag{C.1}$$

where s'^P corresponds to the local coordinates of point P and A is defined as the *direction cosines matrix*. This matrix depends on the Euler parameters, which will be explained in the following section.

C.2.1 Rotational Coordinates

First, the *Euler's theorem* states that:

The general displacement of a body with one point fixed is a rotation about some axis.

This means that a rotational coordinate transformation can be accomplished by only one rotation along an "imaginary axis", which is coincident with the global axes, see Fig. C-4. This means that the rotation of a body in space can be described with four coordinates: the three components of the rotation axis, u_1, u_2, u_3, and the rotation angle Φ.

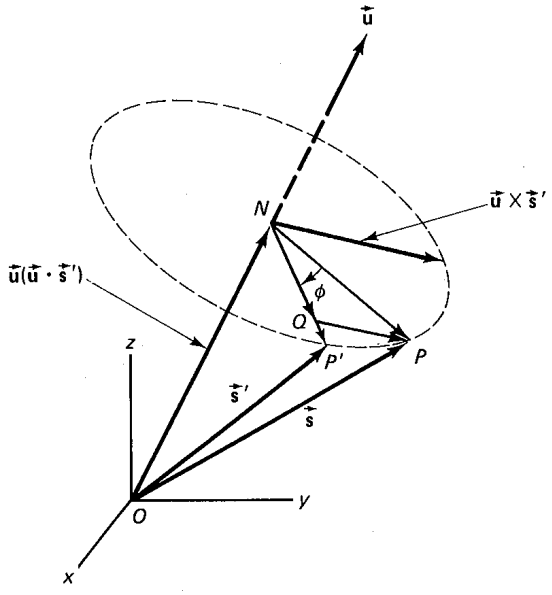

Figure C-4: Vector diagram for derivation of rotation formula.

Through geometric manipulation of the vectors in Fig. C-4, it is possible to find the *rotation formula*:

$$\vec{s} = \vec{s'}cos\phi + \vec{u}(\vec{u} \cdot \vec{s'})(1 - cos\phi) + \vec{u} \times \vec{s'}sin\phi \tag{C.2}$$

In addition, several trigonometric identities can be used to find the new quantities:

$$\begin{aligned} e_0 &= cos\frac{\phi}{2} \\ \vec{e} &= \vec{u}\, sin\frac{\phi}{2} \end{aligned} \tag{C.3}$$

Then,

$$\mathbf{s} = [(2e_0^2 - 1)\mathbf{I} + 2\mathbf{e}\mathbf{e}^T e^T + 2e_0\tilde{\mathbf{e}}]s' \tag{C.4}$$

where $\mathbf{e} = [e_1, e_2, e_3]^T$ and $\tilde{\mathbf{e}}$ is the skew-symmetric matrix of vector $\mathbf{e}$. If Eq. C.4 is compared with Eq. C.1 it becomes clear that:

$$A = [(2e_0^2 - 1)\mathbf{I} + 2\mathbf{e}\mathbf{e}^T e^T + 2e_0\tilde{\mathbf{e}}] \tag{C.5}$$

and expanding Eq. C.5,

$$A = 2\begin{bmatrix} e_0^2 + e_1^2 - \frac{1}{2} & e_1e_2 - e_0e_3 & e_1e_3 + e_0e_2 \\ e_1e_2 + e_0e_3 & e_0^2 + e_2^2 - \frac{1}{2} & e_2e_3 - e_0e_1 \\ e_1e_3 - e_0e_2 & e_2e_3 + e_0e_1 & e_0^2 + e_2^2 - \frac{1}{2} \end{bmatrix} \tag{C.6}$$

Euler parameters identities

This section introduces some important identities that are used in the numerical analysis of multibody systems, when the Euler parameters are used to specify the orientation of the body. First, the transformation matrices **G** and **L** are defined. These matrices are used extensively in transformations that deal with global and local vectors, respectively.

$$G = \begin{bmatrix} -e_1 & e_0 & -e_3 & e_2 \\ -e_2 & e_3 & e_0 & -e_1 \\ -e_3 & -e_2 & e_1 & e_0 \end{bmatrix} \tag{C.7}$$

and

$$L = \begin{bmatrix} -e_1 & e_0 & e_3 & -e_2 \\ -e_2 & -e_3 & e_0 & e_1 \\ -e_3 & e_2 & -e_1 & e_0 \end{bmatrix} \tag{C.8}$$

Another important aspect of matrices **G** and **L** is that they are linear transformations that occur before the **A** matrix. In other words "*the quadratic transformation matrix* **A** *can be treated as the result of two successive linear transformations*" (Nikravesh, 1988).

$$\mathbf{A} = \mathbf{G}\mathbf{L}^T \tag{C.9}$$

Angular velocity

The angular position is described by Eq. C.1 and it's derivative with respect to time is given by

$$\dot{s}^P = \dot{A}s'^P + A\dot{s}'^P \tag{C.10}$$

Since vector $\vec{s}^P$ is constant with respect to the local coordinate system, $\dot{s}'^P = 0$, and therefore

$$\dot{s}^P = \dot{A}s'^P \tag{C.11}$$

The term $\dot{\mathbf{A}}$ is the result of another transformation, e.g. (Nikravesh, 1988), given by

$$\dot{\mathbf{A}} = \tilde{\omega}\mathbf{A} \tag{C.12}$$

where $\tilde{\omega}$ is the Skew-symmetric matrix of vector $\omega = [\omega_{(x)}, \omega_{(y)}, \omega_{(z)}]^T$. The previous equation expresses $\dot{\mathbf{A}}$ in terms of the global coordinates of the angular velocity. Eq. C.12 can also be written in the local coordinates and it is defined by

$$\dot{\mathbf{A}} = \tilde{\omega}'\mathbf{A} \tag{C.13}$$

where $\omega' = [\omega_{(\xi)}, \omega_{(\eta)}, \omega_{(\zeta)}]^T$. More identities can be formulated by means of the previous equations. Comparing Eq. C.12 and Eq. C.13 can be demonstrated that

$$\begin{aligned} \tilde{\omega}\mathbf{A} &= \mathbf{A}\tilde{\omega}' \\ \tilde{\omega}\mathbf{A}\mathbf{A}^T &= \mathbf{A}\tilde{\omega}'\mathbf{A}^T \\ \tilde{\omega} &= \mathbf{A}\tilde{\omega}'\mathbf{A}^T \end{aligned} \tag{C.14}$$

Also, combining Eq. C.12 and Eq. C.10 produces

$$\dot{\mathbf{s}} = \tilde{\omega}\mathbf{s} \tag{C.15}$$

Another set of useful identities has to do with the time derivatives of the Euler parameters. These identities are used to relate the angular velocity, in global and local components, and the derivative of the Euler parameters.

$$\omega = 2\mathbf{G}\dot{\mathbf{p}} \tag{C.16}$$

$$\dot{\mathbf{p}} = \frac{1}{2}\mathbf{G}^T\omega \tag{C.17}$$

and in the local components of ω,

$$\omega' = 2\mathbf{L}\dot{\mathbf{p}} \tag{C.18}$$

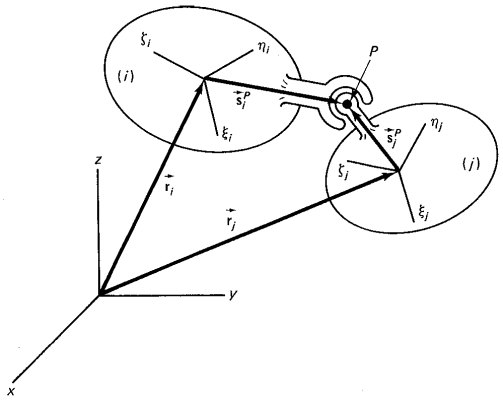

Figure C-5: Spherical Joint.

$$\dot{\mathbf{p}} = \frac{1}{2}\mathbf{L}^T\omega' \tag{C.19}$$

C.2.2 Kinematic Constraints

In this section, the constraint equations for the standard kinematic pairs(i. e. spherical, revolute and translational) are presented. It will be shown that by means of parallel and perpendicular vectors concepts, it is possible to derive the kinematic constraints of the pairs. Also, the Jacobian entries for each constraint type, along with the terms of the right hand side of the acceleration will be presented.

Spherical Joint

A *spherical joint* between bodies i and j is shown in Fig. C-5. The center of the joint is at point P, which has constant coordinates with respect to $\xi_i\eta_i\zeta_i$ and $\xi_j\eta_j\zeta_j$. The constraint equation is of the type spherical, (s), defined by:

$$\Phi^{(s,3)} \equiv \mathbf{r}_i + \mathbf{A}\mathbf{r}_i'^P - \mathbf{r}_j - \mathbf{A}\mathbf{r}_j'^P = 0 \tag{C.20}$$

The spherical joint has three DOF, from which two represent the direction and the third represents the rotation around the directional axis.

Revolute Joint

A *revolute joint* between bodies i and j is shown in Fig. C-6. This type of joint has similar motion properties as the spherical joint. However, it is constrained to a one degree of freedom because vectors $\vec{s_i}$ and $\vec{s_i}$ must remain parallel at all times. Therefore, two

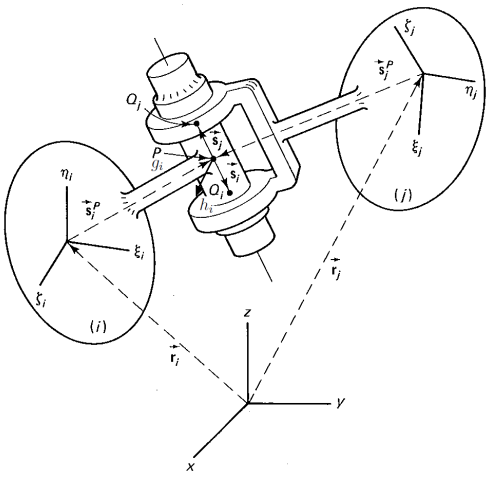

Figure C-6: Revolute Joint.

constraint equations can be defined, at first glance, by the following expression:

$$\begin{aligned} \Phi^{(s,3)} &= 0 \\ \Phi^{(p1,2)} &\equiv \tilde{s}_i s_j = 0 \end{aligned} \tag{C.21}$$

The parallel constraint can be simplified by creating two additional vectors, $\vec{h_i}$ and $\vec{g_i}$ perpendicular to each other and to $\vec{s_i}$. This condition will simplify the constraint formulation of the parallel type constraint. It is clear that the parallel constraint results in three equations, of which only two are independent. By using the two perpendicular constraints, the process of finding the independent equations is avoided. Therefore, the constraint equations for a revolute joint are:

$$\begin{aligned} \Phi^{(s,3)}(P_i, P_j) &= 0 \\ \Phi^{(n1,1)} &\equiv h_i^T s_j = 0 \\ \Phi^{(n1,1)} &\equiv g_i^T s_j = 0 \end{aligned} \tag{C.22}$$

The perpendicular constraint is defined as the scalar product between the two vectors, which result is zero.

Translational Joint

A *translational* or *prismatic joint* is shown in Fig. C-7. In this kind of joint, no rotation is allowed between the two bodies i and j, and there is only a translational movement along one axis. From this two premises, the following statements can be inferred :

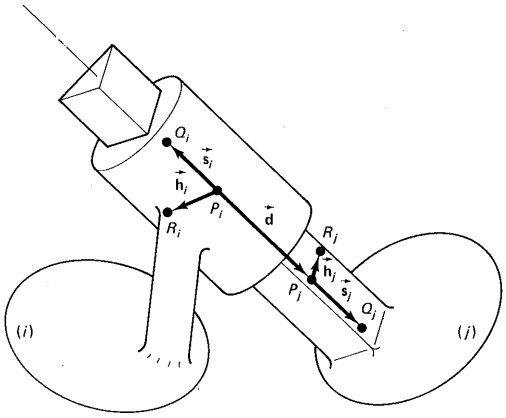

Figure C-7: Translational Joint.

- Vectors $\vec{s_i}$ and $\vec{s_j}$ must remain parallel to ensure only one axis of translation.
- Vectors $\vec{s_i}$ and $\vec{d}$ must remain parallel to ensure the translation along one axis. In this case, vector $\vec{d}$ is a variable magnitude vector.
- In order to prevent the rotation between the two bodies, vectors $\vec{h_i}$ and $\vec{h_j}$ must remain perpendicular.

Using the conditions above, the constraint equations are given by:

$$\begin{aligned} \Phi^{(p1,2)} &\equiv \tilde{s}_i s_j = 0 \\ \Phi^{(p2,2)} &\equiv \tilde{s}_i d_{ij} = 0 \\ \Phi^{(n1,1)} &\equiv h_i^T h_j = 0 \end{aligned} \tag{C.23}$$

Again, the parallel constraints can be modified by adding a perpendicular vector $\vec{g_i}$ to $\vec{s_i}$ at point P_i. Now, another option for the constraint equations is given by

$$\begin{aligned} \Phi^{(n1,1)} &\equiv h_i^T h_j = 0 \\ \Phi^{(n1,1)} &\equiv h_i^T s_j = 0 \\ \Phi^{(n1,1)} &\equiv g_i^T s_j = 0 \\ \Phi^{(n2,1)} &\equiv h_i^T d_{ij} = 0 \\ \Phi^{(n2,1)} &\equiv g_i^T d_{ij} = 0 \end{aligned} \tag{C.24}$$

Velocity and acceleration

Through the differentiation with respect to time of the constraint equations, it is possible to find the Jacobian matrix of a given system. Moreover, it is also possible to find the

right hand side of the acceleration expressions. This results are used in the dynamic analysis of a given multibody system. The results for the types of constraints used here (normal type 1, normal type 2 and spherical) are presented in Table C.1

$\mathbf{\Phi}$	Φ_{r_i}	$\Phi_{w_i'}$	Φ_{r_j}	$\Phi_{w_j'}$
$\Phi_q^{(s,3)}$	I	$-\tilde{s}_i^P A_i$	-I	$-\tilde{s}_j^P A_j$
$\Phi_q^{(n1,1)}$	0^T	$-s_j^T \tilde{s}_i A_i$	0^T	$-s_i^T \tilde{s}_j A_j$
$\Phi_q^{(n2,1)}$	s_i^T	$-(d_{ij}^T + s_i^{P^T})\tilde{s}_i A_i$	s_i^T	$-s_i^T s_j^P A_j$

Table C.1: Jacobian matrix for the basic constraints

where $\mathbf{I}$ is a 3×3 identity matrix and $\mathbf{0}$ is a 3×1 vector. The entries for the right-hand side of the acceleration equations are given in Table C.2.

$\mathbf{\Phi}$	γ
$\Phi_q^{(s,3)}$	$-\tilde{\omega}_i \dot{s}_i^P + \tilde{\omega}_j \dot{s}_j^P$
$\Phi_q^{(n1,1)}$	$\dot{s}_i^T \tilde{\omega}_i s_j^P - 2\dot{s}_i^T \dot{s}_j + \dot{s}_j^T \tilde{\omega}_j s_i^P$
$\Phi_q^{(n2,1)}$	$-d_{ij}^T \tilde{\omega}_i \dot{s}_i - 2\dot{s}_i^T \dot{d_{ij}} - s_i^T(\tilde{\omega}_j \dot{s}_j^P - \tilde{\omega}_i \dot{s}_i^P)$

Table C.2: Gamma (right-hand side of the acceleration equations) entries for the basic constraints

C.2.3 Newton-Euler Equations

In this section, a system of constrained EOM is presented. There are different types of formulations, but the one used here is in terms of the Euler parameters. Also, the angular velocity is formulated in terms of it's local coordinates in order to maintain the inertial tensor constant (Nikravesh, 1988). The formulation presented here provides a conceptual basis for the numerical analysis algorithm presented in chapter 3.

Newton's 2nd law of motion is used as starting point to express the translational part of the EOM and it is given by

$$\mathbf{N_i}\ddot{\mathbf{r}}_\mathbf{i} = \mathbf{f_i} \tag{C.25}$$

where $\mathbf{N_i} = diag[m, m, m]_i$. The rotational EOM are:

$$\mathbf{J_i'}\dot{\boldsymbol{\omega}}_\mathbf{i}' + \tilde{\boldsymbol{\omega}}_\mathbf{i}'\mathbf{J_i'}\boldsymbol{\omega}_\mathbf{i}' = \mathbf{n_i'} \tag{C.26}$$

Equations C.25 and C.26 can be combined to form:

$$\begin{bmatrix} m_i I & 0 \\ 0 & J_i' \end{bmatrix}_i \begin{Bmatrix} \ddot{\mathbf{r}} \\ \dot{\omega}' \end{Bmatrix}_i = \begin{Bmatrix} \mathbf{f} \\ \omega' \end{Bmatrix}_i - \begin{Bmatrix} 0 \\ \tilde{\omega}' J' \omega' \end{Bmatrix}_i \tag{C.27}$$

Where the subscript i means that the expressions correspond to body i. Equation C.27 can be written as:

$$M_i \dot{h}_i = g_i - b_i \tag{C.28}$$

where the mass matrix is defined as

$$M_i = \left[\begin{array}{cc} m_i I & 0 \\ 0 & J_i' \end{array} \right]_i \tag{C.29}$$

the body velocity vector:

$$\dot{\mathbf{h}}_i = \left\{ \begin{array}{c} \ddot{\mathbf{r}} \\ \dot{\omega}' \end{array} \right\}_i \tag{C.30}$$

the external forces:

$$g_i = \left\{ \begin{array}{c} \mathbf{f} \\ \omega' \end{array} \right\}_i \tag{C.31}$$

and the quadratic velocity terms vector

$$b_i = \left\{ \begin{array}{c} 0 \\ \tilde{\omega}' J' \omega' \end{array} \right\}_i \tag{C.32}$$

The previous set of equations can be used to represent the motion of an unconstrained body. This concept can be extended to a system of constrained bodies. In the preceding section, the entries for the Jacobian and the acceleration were defined, i.e Eq. C.33.

$$\Phi_q \ddot{\mathbf{q}} = \gamma \tag{C.33}$$

which is appended to the EOM, to result in the system of equations:

$$\left[\begin{array}{cc} \mathbf{M} & \mathbf{B}^T \\ \mathbf{B} & 0 \end{array} \right]_i \left[\begin{array}{c} \dot{\mathbf{h}} \\ -\lambda \end{array} \right] = \left[\begin{array}{c} \mathbf{g} - \mathbf{b} \\ \gamma \end{array} \right] \tag{C.34}$$

where $\mathbf{B} = [\Phi_{r_1}, \frac{1}{2}\Phi_{p_1} L_1^T, \ldots, \Phi_{r_b}, \frac{1}{2}\Phi_{p_b} L_1^T]$ which is written in terms of the local coordinates of the angular acceleration to be consistent with the formulation. The resulting formulation is a system of differential algebraic equations that can be solved using a numeric solver. In the next chapter, an algorithm to solve the system is presented, along with simulation results for the kinematic pairs discussed in this chapter.

C.3 Numerical Analysis of Multibody Systems

At the end of chapter 2 a formulation to find the dynamics of a kinematically constraint system was presented. In the end, the problems turns out to be an algebraic-differential equations (DAEs) problem. In this chapter, an algorithm used to solve this set of equations is presented. In addition, a set of examples showing simulation results for the standard kinematic pairs explained in section C.2.2 will be used to show the implemen-

tation of the algorithm. The chapter begins by explaining some of the basic programming concepts used for this implementation, then it moves to describe the algorithm, and last, the simulation results are presented.

C.3.1 Data structures

A multibody system can contain as much of b bodies and m kinematic pairs. The complexity of the program, in computational time and organization, grows proportional to the number of b and m. A way to keep the program organized in "categories" that are easy to understand, and to program, is by using *data structures*. The data structures are organized as the data is read from the input file and are operated as global structures, i.e. they can be modified in any part of the code. For the body type structure, the global coordinates, translational and rotational (i.e. Euler parameters), are given in the file. As for the kinematic pair structures, the fields contain the local and global coordinates of the points of interest for the constraint formulation. The global coordinates are calculated using the direction of cosines matrix at each time step.

C.3.2 Integration Array

In this section, the numerical integration process will be explained for the case of solving the DAEs of a spatial system. The solver used is ode45 from Matlab. Now, recall from Section C.2.3 the systems of equations given by Eq. C.34. This system is of the form:

$$\mathbf{AX} = \mathbf{B} \tag{C.35}$$

of which, the solution can be found by solving the system for $\mathbf{X}$. If the section corresponding to λ is discarded, for now, it can be said that vector $\dot{\mathbf{h}}$ contains the solution of interest which is:

$$\dot{\mathbf{h}}_i = \left\{ \begin{array}{c} \ddot{\mathbf{r}} \\ \dot{\omega}' \end{array} \right\} \tag{C.36}$$

This solution will lead to n second-order differential EOM. Moreover, these set of equations can be converted to a $2n$ first-order set of equations by defining two arrays y and $\dot{y}$.

$$y = \left[\begin{array}{c} q \\ \dot{q} \end{array} \right] \quad \dot{y} = \left[\begin{array}{c} \dot{q} \\ \ddot{q} \end{array} \right]$$

The two arrays can be arranged arbitrarily but they must be consistent in their order. For instance, if the ith element of y contains x_i, then the ith element of $\dot{y}$ must contain $\dot{x}_i$. For the case of planar analysis, this numerical integration will be straightforward since the vectors are in correct order and are consistent as far of their components. However, in spatial analysis this is not the case as shown in Eq. C.36. In order to execute the numerical integration it is necessary find $\dot{p}$ from ω' using Eq. C.19. In summary, the vector organization occurs as follows:

$$y = \begin{bmatrix} \mathbf{r} \\ \mathbf{p} \\ \dot{\mathbf{r}} \\ \omega' \end{bmatrix} \quad \rightarrow \quad \dot{\mathbf{p}} = \tfrac{1}{2}\mathbf{L}^T\omega' \quad \rightarrow \quad \dot{y} = \begin{bmatrix} \dot{\mathbf{r}} \\ \dot{\mathbf{p}} \\ \ddot{\mathbf{r}} \\ \ddot{\mathbf{p}} \end{bmatrix}$$

C.3.3 Algorithm

In generalized form, for planar and spatial systems, the set of equations for a kinematically constrained mechanical system is given by

$$\begin{aligned} \ddot{\mathbf{\Phi}} \equiv \mathbf{\Phi_q}\ddot{\mathbf{q}} - \gamma = 0 \\ \mathbf{M}\ddot{\mathbf{q}} - \mathbf{\Phi_q^T}\lambda = \mathbf{g} \end{aligned} \tag{C.37}$$

For Φ in Eq. C.37 it is assumed that it contains both the kinematic and mathematical constraints. Therefore, the matrix $\mathbf{B}$ of Eq. C.34 is already included in the formulation. In the following algorithm, the DAEs are solved to obtain the dynamic response of a system described by Eq. C.37. The numerical integration routine explained in the previous section it is then implemented.

C.3.4 Simulation Results

Spherical Joint

This example describes the motion of a classical pendulum, who's joint is made up of a spherical joint. The joint is centered at ground and the origin of the global reference frame. The center of gravity it is assumed to be in $\frac{l}{2}$ of the pendulum, where it's local reference frame is located and $l = 5$. There is no friction in the joint and the pendulum is dropped from $\theta = 45^o$ with the vertical, along the z axis. The results for the displacement and rotational coordinates are presented in Figures C-12, respectively.

The same pendulum was tested when $\theta = 0^o$, i.e. dropped from the horizontal. The results are shown in Fig. C-9. Notice how the value of Z stays constant for an instant. This happens when the pendulum reaches it's maximum value and the velocity is equal to zero. Again, there is no friction in the joint and therefore the movement is constant in time without any decay.

Revolute Joint

The revolute joint is very similar to the spherical joint, but there is a motion constraint and there is only one relative DOF between the two bodies. The system used for the simulation is the pendulum used in the previous section.

Notice that the parameter $e_0 = 0$ when the pendulum reaches the other side and it's local reference frame as a rotation of π rad. This is consistent with the literature

Algorithm 2: How to find the dynamics of a multibody system through numerical integration

Data: coordinates file
Result: Solution to the set of DAEs

1 Read data file (initial conditions) and construct data structures;
2 Initialize operation matrices;
3 Update the coordinates of the kinematic joints, and transformation matrices using the initial conditions;
4 Construct the initial conditions vector $\mathbf{y_0} \equiv [\mathbf{q_0}^T, \dot{\mathbf{q}}_\mathbf{0}^T]^T$;
5 Enter the numerical integration routine;

- Update the body coordinates;
- Update the coordinates of the kinematic joints, and transformation matrices using the previous update;
- Calculate $\dot{\mathbf{p}}$ from ω' using Eq. C.19;
- Calculate the forces present in the system;
- Calculate the Jacobian and γ entries for each constraint type;
- Build the system of equations in the form of Eq. C.34, which is of the form of Eq. C.35;
- Solve for $\mathbf{X}$;
- Construct vector $\dot{\mathbf{y}} \equiv [\dot{\mathbf{q}}^T, \ddot{\mathbf{q}}^T]^T$;
- Return;

6 Plot the results;

(see Nikravesh, 1988) where is expressed that *when the angle of rotation is* $\phi = k\pi, k = \pm 1, \pm 3, ...,$ *then* $e_0 = 0$.

Translational Joint

This joint was simulated as a slider that moves due to the presence of gravity. The slider is placed at $\theta = 45^o$ and it is expected to fall in the y and z negative direction. The result is presented in Fig. C-11.

Spring-damper mass system

This example, illustrates how the external forces, produced by a spring and a damper, affect the dynamic behavior of the system shown in Fig. C-13. The coordinates formulation was done in xy plane and the acting force of gravity produces the masses to fall

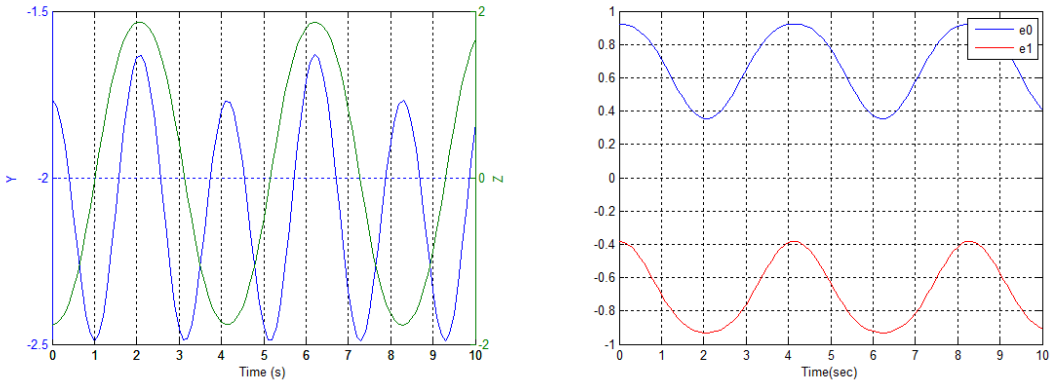

Figure C-8: Pendulum results when it is dropped from $\theta = 45^o$ - Spherical joint

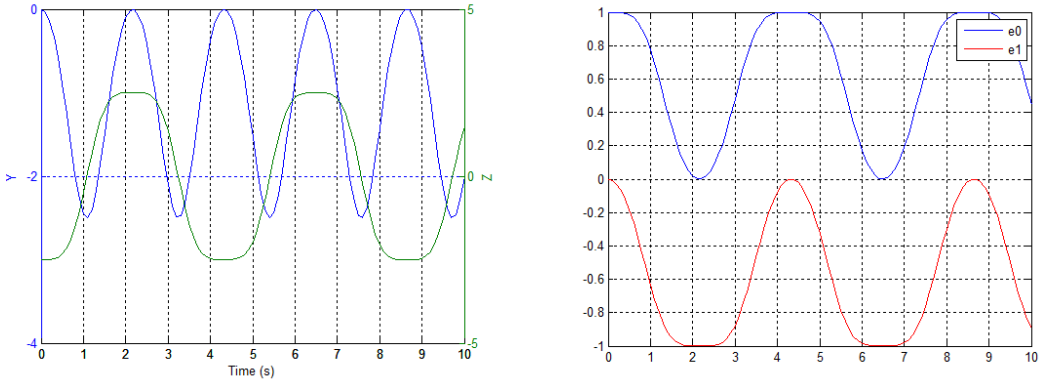

Figure C-9: Pendulum results when it is dropped from $\theta = 0^o$ - Spherical joint

into the negative y position.

Spatial Slider-crank

The mechanism presented in this section gathers some the basic kinematic joints explained in the previous sections (Fig. C-15). The model, composed by four bodies, is defined as follows:

The model presented in Table C.4 is a modified version because the original model had redundant constraints by having a revolute joint between the two cranks. Also, the slider was defined as a translational joint but the constraint that prevents it from rotating was already defined by the revolute joint 2. These types of issues are not explicitly identified by the program, but it was observed that the redundancy of constraints generated singularities in the Mass/Jacobian matrix.

The model is defined by the position, velocity, angular velocity and rotational coordinates of each body; and the points required to define each kinematic joint. Since the

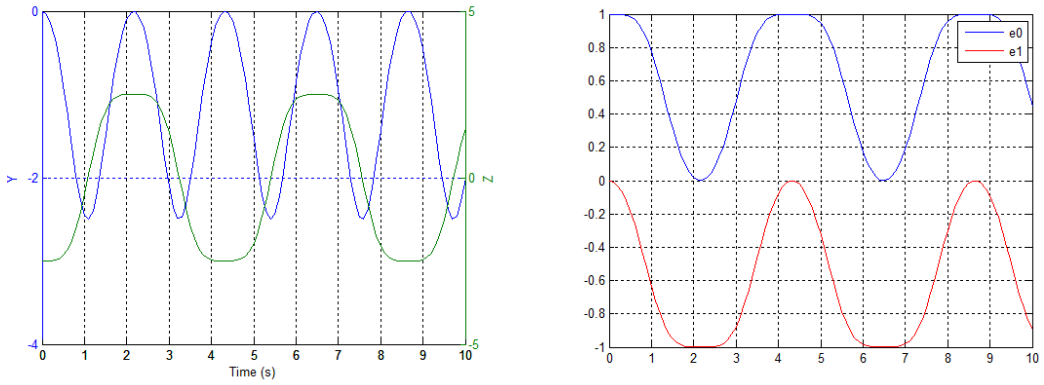

Figure C-10: Pendulum results when it is dropped from $\theta = 0^o$ - Revolute joint

system is at rest at $t = 0$, the velocity coordinates are equal to zero. The coordinates required for the model are defined as follow:

The mechanism is simulated as it was at rest at $t = 0$. No external forces, other than gravity, are acting in the system. It is expected that the slider will move in the positive y direction and the two cranks will fall. There is no restriction with respect to ground for the cranks, and therefore they will fall into the negative z direction (1). When the cranks fall below $z = 0$, the slider would have to move in the direction towards $y = 0$ (2). Once it reaches this position, the effects of inertia will generate moments in the cranks and these will move and make the system come back into the initial position (3). The process repeats periodically because friction is not accounted in the joints. The displacement of the two cranks and the slider are shown in Fig. C-15. The numbers in the figure are intended to show the positions where the previous three steps take place.

The rotational coordinates are shown in Fig. C-16. Notice the Euler parameters of the slider: since it is moving horizontally, there is no rotation and therefore are constant.

The algorithm and results presented in this chapter show the advantages of implementing a modular program to analyze Multibody Dynamics. The program was designed so it is possible to include additional constraints formulations for other types of joints.

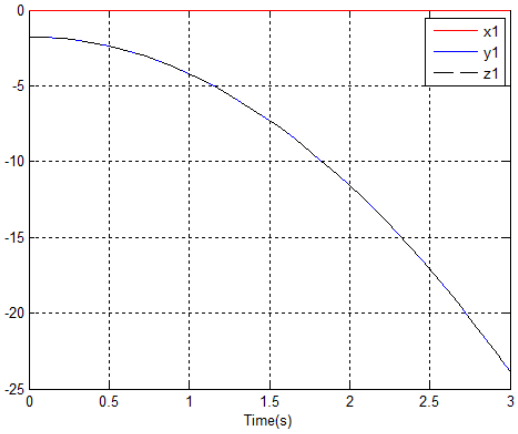

Figure C-11: Translational joint simulation.

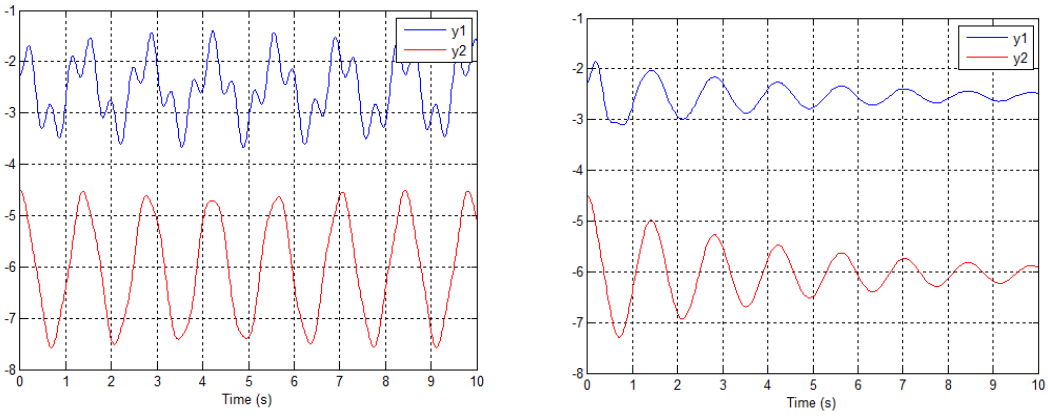

Figure C-12: Mass displacement when gravity acts in the system.

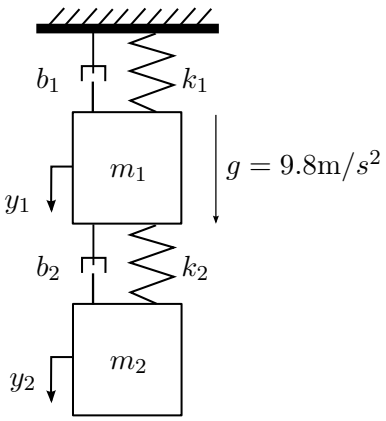

Figure C-13: Spring-damper mass system.

Slider-crank model	
Bodies	
Four Bodies	nc=24
Constraints	
Revolute joint (ground, crank 1)	5
Spherical joint (crank 1, crank 2)	3
Revolute joint (crank 2, slider)	5
Cylindrical joint (slider, ground)	4
Ground constraint	6
DOF = 24-23 = 1	nh=23

Table C.3: Slider-crank model description

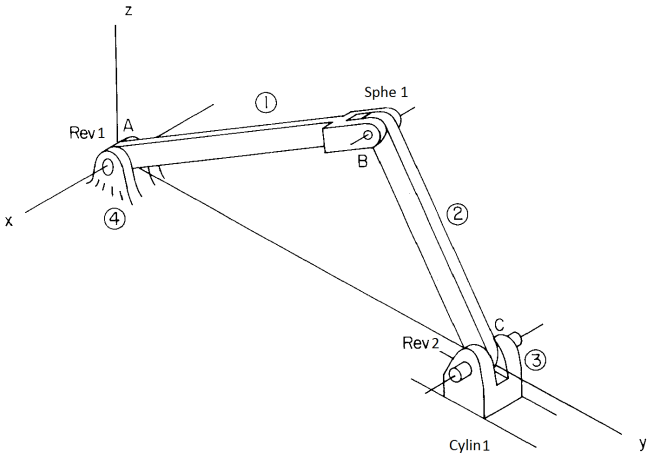

Figure C-14: Slider-crank Mechanism.

Body	x	y	z	e_0	e_1	e_2	e_3
1	0.0	0.3182	0.3182	0.9239	0.3827	0.0000	0.0000
2	0.0	0.9192	0.3536	0.9239	-0.3827	0.0000	0.0000
3	0.0	1.2021	0.0707	1.0000	0.0000	0.0000	0.0000
4	0.0	0.0000	0.0000	1.0000	0.0000	0.0000	0.0000

Table C.4: Slider-crank bodies' coordinates

Body	P			Q			R			S		
	ξ	η	ζ	ξ	η	ζ	ξ	η	ζ	ξ	η	ζ
Crank 1	0.00	-0.45	0.00	0.10	-0.45	0.00	0.00	-0.50	0.10	0.00	-0.45	0.10
Ground	0.00	0.00	0.00	-0.10	0.00	0.00	NA	NA	NA	NA	NA	NA
Crank 2	0.00	0.40	0.00	0.10	0.40	0.00	0.00	0.40	0.10	0.00	0.50	0.10
Slider	0.00	0.00	0.00	-0.10	0.00	0.00	NA	NA	NA	NA	NA	NA

Table C.5: Revolute joints' coordinates

Body	P		
	ξ	η	ζ
Crank 1	0.00	0.45	0.00
Crank 2	0.00	-0.40	0.00

Table C.6: Spherical joint coordinates

Body	P			Q			R			S		
	ξ	η	ζ	ξ	η	ζ	ξ	η	ζ	ξ	η	ζ
Crank 2	0.00	0.00	-0.07071	0.00	-0.10	-0.07071	0.10	0.00	-0.07071	0.00	0.00	0.00
Slider	0.00	1.30	0.00	0.00	1.50	0.00	0.00	1.30	0.10	NA	NA	NA

Table C.7: Cylindrical joint coordinates

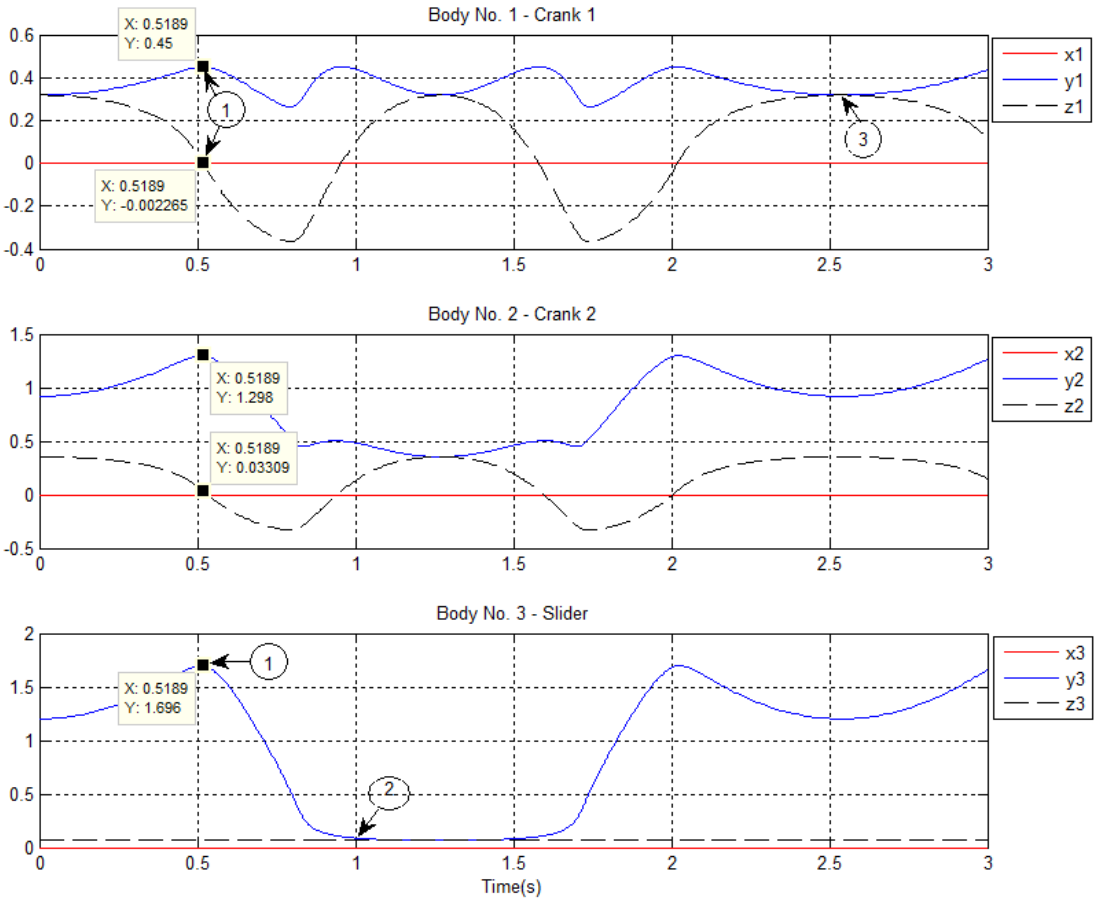

Figure C-15: Slider-crank displacement coordinates.

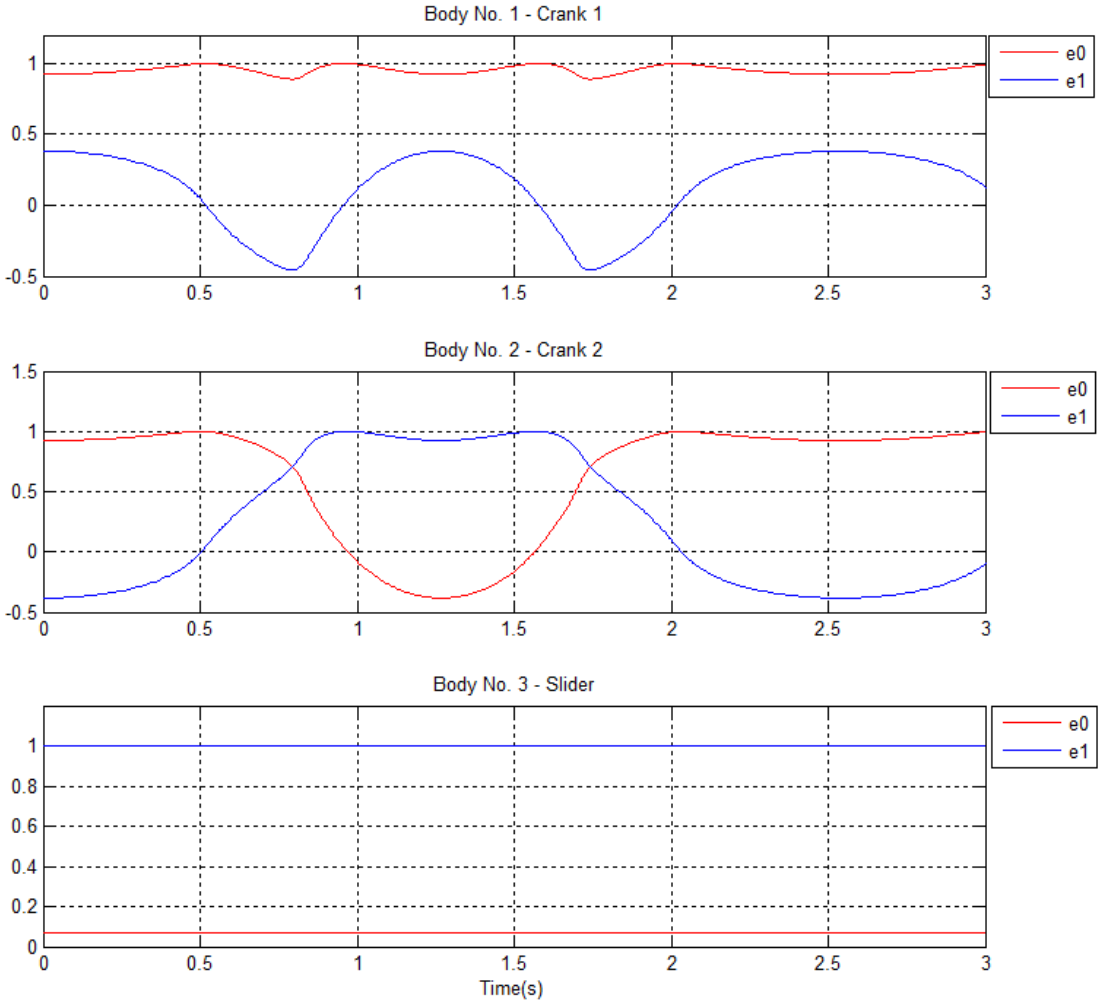

Figure C-16: Slider-crank rotational coordinates.

Appendix D

Notes on the implementation

D.1 Introduction

This appendix describes the implementation of the electrical and mechanical models of wind turbine generators and gearboxes, respectively. Combined, they are used to describe the electro-mechanical interaction that occurs inside a wind turbine's drive-train. These models are implemented in Matlab/Simulink and are coupled with the aeroelastic tool HAWC2 (Horizontal-axis Wind turbine simulation Code 2nd generation [17]). The literature on gearbox modeling is extensive [33, 32, 30, 109, 3, 26] and it is not the purpose of this report to present novel modeling techniques or the models in itself. These were presented previously in Chapter 3.

As a summary, here are the main features of the tool up-to-date:

1. *Modular approach:* the implementation of the tool is done is such a way that it is possible in theory to model any configuration of the existing drive-trains. This applies to multi-stage gearboxes consisting on a combination of planetary and parallel gearbox stages, and the corresponding generator.

2. *Complexity:* as of now, it is possible to model the drive-train with two different levels of complexity. This reefers to the number of DOF per body used to describe the gearbox. The first level correspond to torsional models (1D) and the second level is of translational/rotational models (2D). Depending on the desired results, it is possible to specify which level is to be used to describe the models.

3. *Generators:* the tool contains generic models of the two types of generators most used in the wind energy industry. A DFIG and a PMSG are available to be coupled with the gearbox. The generator modules contain generic control strategies, which parameters can be easily modified in the code.

4. *Electric fault simulation:* Depending on the generator system, there are two ways to simulate a grid fault. In the case of a PMSG, the power system "de-couples" the generator from the grid. Hence, short faults are unlikely to affect the generator since

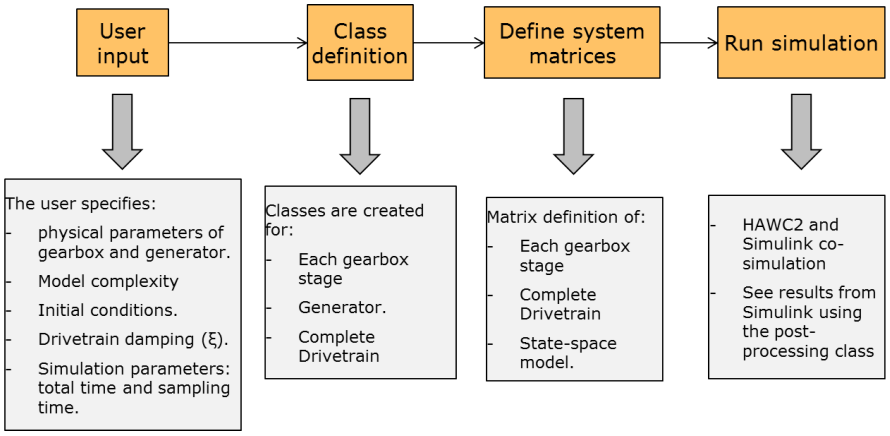

Figure D-1: Flow chart of the tool.

the chopper takes care of the power unbalance. Therefore, since the wind turbine controller is used to generate the reference, it is possible to specify the electric fault parameters such as start-time, duration and recovery type (this depends on the grid codes) in order to change the reference to simulate an electric fault in the generator terminals. This attempts to reproduce the change in electromagnetic torque of the generator that occurs when the excitation voltage is modified due to a grid fault or a voltage dip. In the case of a DFIG system, the voltage in the stator is changed according to a specified grid code. This is done under the premise that a DFIG's stator is directly connected to the grid and a grid fault will affect it immediately.

5. *Input:* example files with the required parameters for the system is available. Notice that this is an important part of the system simulation and all parameters must be provided.

6. *Post-processing:* a post-processing tool is included in where the results can be visualized. The amount of results depends on the type of complexity chosen. The results correspond mainly to the states of the system such as displacements, velocities, accelerations, vibration and loads.

The use of the tool follows the flow chart presented in Figure D-1. Once the input parameters are defined, the tool creates the system matrices of the specified drive-train configuration and runs the simulation. The flowchart sequence is true assuming that the input file to HAWC2 is already defined.

Once the simulation is done, it is possible to analyze the results from the drive-train in Matlab using the post-processing class that is available with the tool. This is not a strict requirement, however, since the system variables and results are available in Matlab's workspace.

D.2 Models description

This section presents the general idea behind the models used in this tool. All of the gearbox models are based on lumped-parameter theory, in where every flexibility is represented as a linear spring. In the case of the connecting shafts in each stage, a torsional spring is used to represent the coupling.

To model the internal flexibilities of the gearbox, different assumptions are made:

- each gear body, or a state on the system, is assumed to be rigid.
- the gear mesh due to teeth flexibility is represented by a linear spring (Figure 3-14). In reality, this is a non-linear parameter that varies in time as there is single or double contact in the meshing teeth. However, it is considered linear initially in this tool. This assumption is valid for both levels of complexity on the models.
- the bearings are represented by linear springs that support the gears. The bearing stiffness parameter needs to be provided in the input file. This assumption is only valid for the 2D model since it models the translational DOFs of each body.
- all the shafts connecting the gearbox stages, generator and wind turbine rotor are assumed to be torsional springs.

The interaction with between Matlab and HAWC2 is done through a DLL in charge of the communication of the the two tools. Each software solves the EOM at the time step set by HAWC2 and share the information of the states upon convergence. The diagram in Figure 3-22 shows an example of the variables interacting between the two tools. The coupler block estimates the LSS torque given changes in the rotor speed. The coupler equation (3.77) calculates in reality the torsion at the carrier side. This is the results of the analysis of a two mass model in free-free condition, where the reaction forces on each mass are equivalent in magnitude. Therefore, the torsion (T_r)seen at the carrier is of the same value of the LSS.

where K_s is the LSS stiffness, C_s is the LSS damping, ω_r is the rotor speed,ω_c is the carrier speed, J_r is the rotor inertia and J_{gb} is the gearbox inertia refereed to the low-speed side. In order to keep the torque balance in the wind turbine's rotor, the calculated torsion is applied to the main shaft. This replaces the torque demand from the controller (T_{ref}) which is usually applied to the main shaft to keep the equilibrium in the rotor, when doing only aeroelastic simulations with HAWC2.

The generator model calculates the electromagnetic torque based on the speed in the HSS. The other inputs to the model are the excitation voltages, which are controlled by the machine controller to maintain the torque commanded by the wind turbine controller. The resulting electromagnetic torque is the second input to the gearbox. Since it is a free-free conditions, it is paramount to maintain a dynamic equilibrium between the two inputs and the reaction forces generated inside the gearbox due to the flexibilities. This is achieved by the combined work of the coupler equation and the machine controller for the generator.

D.3 Outputs

As mentioned before, it is possible to obtain a different set of results depending on the level of complexity chosen in the gearbox specification. The information presented in Table D.1 shows the results available depending on the model complexity.

Table D.1: Results available after simulation depending on the level of complexity of the gearbox model.

Result type	Torsional-1D	Translational/rotational-2D
Displacements	x	x
Vibration	x	x
Velocities	x	x
Accelerations	x	x
Torsional loads	x	x
Gear mesh loads	x	x
Bearing loads		x
Low-speed torque	x	x
High-speed torque	x	x
Voltages	x	x
Currents	x	x
Power production	x	x
Flux linkages	x	x

Appendix E

Dynamic model of a permanent magnet synchronous generator

This section presents the typical model found in literature that deals with the dynamics of a PMSG in wind energy applications [78, 12, 110, 77, 79]. This model is defined in the *dq0*-frame for ease on the calculations, since this coordinate transformation transforms the three phase system (abc) that varies with time in to a rotating frame of reference that rotates along with the three-phase system, and therefore, produces three DC voltages. This results in an elimination of the time-varying terms in inductance matrix in the (abc) model.

The model of the PMSG uses the variations of flux linkages as states to fins the currents in the stator, electric torque and electric power. The model is implemented in Simulink and the corresponding equations can be expressed as follows:

$$\begin{aligned} \dot{\psi_{sd}} = & \quad -R_s i_{sd} + \omega_e \psi_{sq} + u_{sd} \\ \dot{\psi_{sq}} = & \quad -R_s i_{sq} - \omega_e \psi_{sd} + u_{sq} \end{aligned} \tag{E.1}$$

and the stator current components as:

$$\begin{aligned} i_{sd} = & \quad \frac{\psi_{sd} - \psi_{pm}}{L_d} \\ i_{sq} = & \quad \frac{\psi_{sq}}{L_q} \end{aligned} \tag{E.2}$$

where ψ_{sd} and ψ_{sq} as the stator flux components; u_{sd} and u_{sq} are the terminal stator voltages; R_s is the stator resistance; L_d and L_q are the stator inductances in the *dq0*-frame.

The electrical torque of the generator is expressed as:

$$T_e = \frac{3}{2} p \psi_{pm} i_{sq} \tag{E.3}$$

and the generated power is defined as:

$$P = T_e \omega_r \eta \tag{E.4}$$

where ω_r is the mechanical rotational speed of the machine, p is the number of pole pairs, ψ_{pm} is the permanent magnet flux linkage constant[1] and η is the efficiency of the machine.

E.1 Physical Parameters

The design of an electrical machine is not a trivial task and it is not the purpose of this project. However, many models and design work has been done and it is available in the literature. For instance, Roshanfekr et. al., studied the performance of two different types of PMSG in [12]. The two 5MW generators studied were the surface mounted permanent magnets (SPMSG) and for the interior permanent magnet machine (IPMSG). The parameters for this implementation are taken from the former SPMSG and are shown in Table E.1.

Table E.1: The 5 WM PMSG parameters used in this dissertation [12].

Parameter	Value
Rated Output Power	5 MW
Rated Torque on generator	64 kNm
Armature phase resistance	0.00125 Ω
D-Axis main Reactance	0.111974 Ω
Q-Axis main Reactance	0.111974 Ω
Synchronous Speed	750 rpm
Number of poles	8
Efficiency	99%
Permanent Magnet Flux Linkage (ψ_{pm})	2.0215

E.2 Results

First, the generator was simulated at rated conditions using as an input the three-phase voltages, with the corresponding coordinate transformation to the dq-frame. The transformation from the abc frame results into two stator voltages, namely v_{sd} and v_{sq}. Furthermore, the model was tested at rated values to:

- verify the convergence of the simulation to a steady-state value,

[1] This value was estimated since the paper did not provided the value that it was used for their computations.

- find the operation points of torque, currents and produced power. These values are to be validated with those found by [12].

The results are shown in Figures E-1 and E-2.

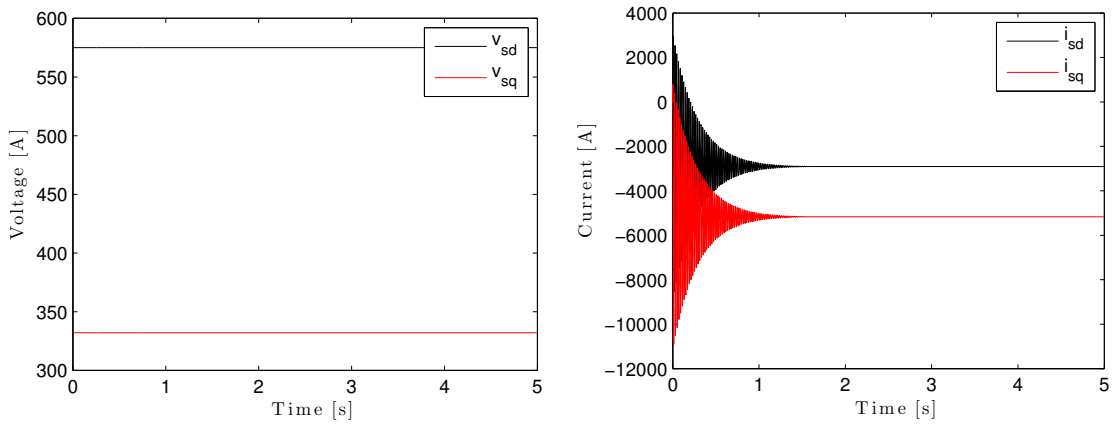

Figure E-1: (a) Stator voltages in the dq-reference. (b) Machine current in the dq-reference.

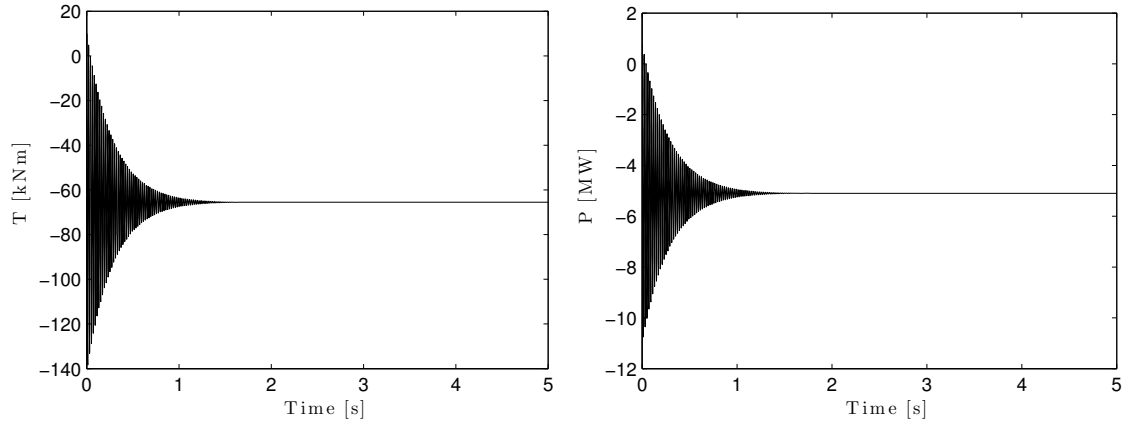

Figure E-2: (a) Machine torque. (b) Generated power.

From the results in Table E.2, it is seen that the model is accurate enough given the low percentage of error, which might be due to the estimation of the ψ_{pm}. It is important to highlight that the values for the flux linkages are unknown, and therefore, the initial conditions for these states are treated as zero for this set of results. This is the reason why there seem to be a transient behavior in the results before reaching steady-state, and it is due to convergence. However, the steady-state condition found in these results can be used as initial conditions in future simulations that include the entire drive-train and the

Table E.2: Validation of results are rated conditions

Parameter	**Reference**	**Implemented**	**Error** (%)
Torque [kNm]	64	65.53	2.3
Power [MW]	5	5.095	1.9

turbine. As it has been experienced before, the initial conditions are very important to simulate larger systems in order to avoid convergence issues and faster transient period.

Bibliography

[1] V. AA., "UpWind - Design limits and solutions for very large wind turbines," tech. rep., 2011.

[2] F. Oyague, "Gearbox Modeling and Load Simulation of a Baseline 750-kW Wind Turbine Using State-of-the- Art Simulation Codes," Tech. Rep. February, National Renewable Energy Laboratory, Golden, CO, 2009.

[3] J. Peeters, D. Vandepitte, and P. Sas, "Analysis of internal drive train dynamics in a wind turbine," *Wind Energy*, vol. 9, pp. 141–161, Jan. 2006.

[4] E. Pierce, "Epicyclic gear ratios," 2006.

[5] J. Lai, T. Lund, K. Rydén, A. Gabelli, and I. Strandell, "The fatigue limit of bearing steels - Part I: A pragmatic approach to predict very high cycle fatigue strength," *International Journal of Fatigue*, vol. 38, pp. 155–168, 2012.

[6] F. Iov, A. D. Hansen, P. Sø rensen, and N. A. Cutululis, "Mapping of grid faults and grid codes," Tech. Rep. July, RisøNationa Laboratory, Technical University of Denmark, Roskilde, Denmark, 2007.

[7] H. O. Madsen, S. Krenk, and N. C. Lind, *Methods of Structural Safety*. Mineola, New York: Dover Publications, Inc., 2006.

[8] N. K. Dimitrov, "Probabilistic Methods in Wind Engineering. Lecture Notes. Technical University of Denmark, DTU Wind Energy.," tech. rep., Technical University of Denmark, DTU Wind Energy, 2014.

[9] S. P. Radzevich, *Dudley's Handbook of Practical Gear Design and Manufacture*. CRC Press, 2 ed., 2012.

[10] International Electrotechnical Commision, "IEC 61400-1. Wind turbines - Part 1: Design requirements.," 2005.

[11] SKF Group, "SKF high-capacity cylindrical roller bearings Higher load ratings and longer service life," tech. rep., 2010.

[12] P. Roshanfekr, T. Thiringer, M. Alatalo, and S. Lundmark, "Performance of two 5 MW permanent magnet wind turbine generators using surface mounted and interior mounted magnets," in *2012 XXth International Conference on Electrical Machines*, (Marseille), pp. 1041–1047, IEEE, Sept. 2012.

[13] M. Z. Jacobson and M. A. Delucchi, "A Path to Sustainable Energy by 2030," *Scientific American*, Nov. 2009.

[14] S. Shuangwen, M. Mcdade, and R. Errichello, "Wind Turbine Gearbox Failure Modes – A Brief," in *ASME/STLE 2011 International Joint Tribology Conference*, (Los Angeles, CA), 2011.

[15] P. Moriarty and S. Butterfield, "Wind Turbine Modeling Overview for Control Engineers Simulation Requirements," in *2009 American Control Conference*, (St. Louis, Missouri), 2009.

[16] J. Jonkman and W. Musial, "IEA Wind Task 23 Offshore Wind Technology and Deployment," tech. rep., National Renewable Energy Laboratory, Golden, CO, 10.

[17] T. J. Larsen and A. M. Hansen, "How 2 HAWC2, the user's manual," Tech. Rep. April, DTU Wind Energy, Roskilde, Denmark, 2012.

[18] B. Barahona, *Integrated analysis of wind turbines.* Phd, Technical University of Denmark, 2012.

[19] J. M. Jonkman and M. L. J. Buhl, "FAST User's Guide," tech. rep., National Renewable Energy Laboratory, Golden, CO, 2005.

[20] P. Passon and M. Kuhn, "State-of-the-art and Development Needs of Simulation Codes for Offshore Wind Turbines," in *IEA Wind Meeting, Task 23 Subtask 2 Code Comparison Collaborative (OC3)*, (Roskilde, Denmark), pp. 1–12, 2005.

[21] DNV-GL, "Bladed - Wind Turbine Design Software," 2014.

[22] MSC Software, "AdWiMo: Advanced Windturbine," 2012.

[23] SIMPACK, "Multi-body Simulation Software - Wind."

[24] Y. Xing and T. Moan, "Multi-body modelling and analysis of a planet carrier in a wind turbine gearbox," *Wind Energy*, 2012.

[25] Siemens, "LMS Samtech Samcef Wind Turbines," 2014.

[26] Y. Guo and R. G. Parker, "Dynamic modeling and analysis of a spur planetary gear involving tooth wedging and bearing clearance nonlinearity," *European Journal of Mechanics - A/Solids*, vol. 29, pp. 1022–1033, Nov. 2010.

[27] H. Link, W. Lacava, J. V. Dam, and B. Mcniff, "Gearbox Reliability Collaborative Project Report: Findings from Phase 1 and Phase 2 Testing Gearbox Reliability Collaborative Project Report : Findings from Phase 1 and Phase 2 Testing," no. June, 2011.

[28] J. Helsen, *The dynamics of high power density gear units with focus on the wind turbine application.* Phd, Katholieken Universiteit Leuven, 2012.

[29] W. Lacava, J. Keller, and B. Mcniff, "Gearbox Reliability Collaborative: Test and Model Investigation of Sun Orbit and Planet Load Share in a Wind Turbine Gearbox," in *53rd Structures, Structural Dynamics and Materials Conference*, no. April, (Honolulu, Hawaii), 2012.

[30] J. Lin and R. G. Parker, "Analytical Characterization of the Unique Properties of Planetary Gear Free Vibration," *Journal of Vibrations and Acoustics*, 1999.

[31] J. Lin and R. Parker, "Planetary Gear Parametric Instability Caused By Mesh Stiffness Variation," *Journal of Sound and Vibration*, vol. 249, pp. 129–145, Jan. 2002.

[32] A. Kahraman, "Load Sharing Characteristics of Planetary Transmissions," *Mechanical Machine Theory*, vol. 29, no. 8, 1994.

[33] A. Kahraman, "Planetary Gear Train Dynamics," *Journal of Mechanical Design*, no. September 1994, 1994.

[34] A. Kahraman and G. W. Blankenship, "Effect of Involute Contact Ratio on Spur Gear Dynamics," *Journal of Mechanical Design*, vol. 121, no. 1, pp. 112–118, 99.

[35] Y. Guo, J. Keller, and R. Parker, "Dynamic Analysis of Wind Turbine Planetary Gears Using an Extended Harmonic Balance Approach Preprint," in *International Conference on Noise and Vibration Engineering*, no. June, (Leuven, Belgium), 2012.

[36] J. Keller, Y. Guo, W. Lacava, and H. Link, "Gearbox Reliability Collaborative Phase 1 and 2: Testing and Modeling Results Preprint," in *Leuven Conference on Noise and Vibration Engineering*, no. May, (Leuven, Belgium), 2012.

[37] J. Helsen, F. Vanhollebeke, B. Marrant, D. Vandepitte, and W. Desmet, "Multibody modelling of varying complexity for modal behaviour analysis of wind turbine gearboxes," *Renewable Energy*, vol. 36, pp. 3098–3113, Nov. 2011.

[38] J. Helsen, F. Vanhollebeke, F. De Coninck, D. Vandepitte, and W. Desmet, "Insights in wind turbine drive train dynamics gathered by validating advanced models on a newly developed 13.2MW dynamically controlled test-rig," *Mechatronics*, vol. 21, pp. 737–752, June 2011.

[39] G. Mandic, A. Nasiri, E. Muljadi, and F. Oyague, "Active Torque Control for Gearbox Load Reduction in a Variable-Speed Wind Turbine," *IEEE Transactions on Industry Applications*, vol. 48, no. 6, pp. 2424–2432, 2012.

[40] M. Singh, E. Muljadi, and J. Jonkman, "Simulation for Wind Turbine Generator — With FAST and MATLAB-Simulink Modules," Tech. Rep. November, NREL, Golden, CO, 2013.

[41] B. Barahona, R. You, A. D. Hansen, N. A. Cutululis, and P. Sø rensen, "Assessment of the impact of frequency support on DFIG wind turbine loads," in *12th International Workshop on Large-Scale Integration of Wind Power into Power Systems as well as on Transmission Networks for Offshore Wind Power Plants*, (London), 2013.

[42] I. P. Girsang, J. S. Dhupia, E. Muljadi, M. Singh, and L. Y. Pao, "Gearbox and Drivetrain Models to Study Dynamic Effects of Modern Wind Turbines Preprint," in *IEEE Energy Conversion Congress and Exposition*, no. October, (Denver, Colorado), 2013.

[43] G. Joós, "Wind Turbine Generator Low Voltage Ride through Requirements and Solutions," *2008 IEEE Power and Energy Society General Meeting*, vol. 1-11, pp. 1470–1476, 2008.

[44] International Electrotechnical Commision, *IEC 61400-4. Wind turbines - Part 4: Design requierements for wind turbine gearboxes.* 2012.

[45] J. Gallego-Calderon, K. Branner, A. Natarajan, N. Cutululis, and J. Hansen, "Electromechanical drivetrain simulation," in *Proceedings of the 9th PhD Seminar on Wind Energy in Europe*, (Gotland, Sweden), 2013.

[46] J. Gallego-Calderon and A. Natarajan, "Assessment of Wind Turbine Drive-train Fatigue Loads under Torsional Excitation," *Under review in Engineering Structures*, 2014.

[47] J. Gallego-Calderon, A. Natarajan, and N. K. Dimitrov, "Effects of bearing configuration in wind turbine gearbox reliability," *Under review in Energy Procedia*, 2015.

[48] T. Burton, N. Jenkins, D. Sharpe, and E. Bossanyi, *Wind Energy Handbook.* John Wiley & Sons, 2 ed., 2011.

[49] J. Jonkman, S. Butterfield, W. Musial, and G. Scott, "Definition of a 5-MW Reference Wind Turbine for Offshore System Development," Tech. Rep. February, National Renewable Energy Laboratory, Golden, CO, 2009.

[50] S. Schmidt and A. Vath, "Comparison of Existing Medium-speed Drive Train Concepts with a Differential Gearbox Approach," in *EWEA*, 2012.

[51] D. Bang, H. Polinder, G. Shrestha, and J. A. Ferreira, "Review of Generator Systems for Direct-Drive Wind Turbines," in *European Wind Energy Conference & Exhibition*, (Belgium), 2008.

[52] P. Eschmann, L. Hasbargen, and K. Weigand, *Ball and Roller Bearings. Theory, Design, and Application.* John Wiley & Sons, 2 ed., 1985.

[53] J. F. Gieras, *Advances in Electric Machines.* Springer Netherlands, 2008.

[54] A. D. Hansen, F. Iov, P. Sø rensen, C. Jauch, F. Blaabjerg, and R.-r. En, "Dynamic wind turbine models in power system simulation tool DIgSILENT," Tech. Rep. August, DTU Wind Energy, Roskilde, Denmark, 2007.

[55] T. A. Harris and R. M. Barnsby, "Life ratings for ball and roller bearings," *Proceedings of the Institution of Mechanical Engineers, Part J: Journal of Engineering Tribology*, vol. 215, pp. 577–595, 2001.

[56] G. Lundberg and A. Palmgren, *Dynamic capacity of roller bearings.* Ingeniörsvetenskapakademiens handlingar, Generalstabens litografiska anstalts förlag, 1947.

[57] T. A. Harris, *Rolling Bearing Analysis.* Wiley-Interscience publication, John Wiley & Sons, 3rd ed., 1991.

[58] J. E. Shigley and C. R. Mischke, *Mechanical Engineering Design.* McGraw-Hill, 6th ed., 2003.

[59] S. Yagi, "Bearings for Wind Turbine," Tech. Rep. 71, NTN, 2004.

[60] K. Shiozawa, L. Lu, and S. Ishihara, "S-N curver characteristics and subsurface crack initiation behaviour in ultra-long ling fatigue of a high carbon-chromium bearing steel," *Fatigue Fract. Eng. Struct.*, vol. 24, pp. 781–90, 2001.

[61] R. P. L. Nijssen, *Fatigue Life Prediction and Strength Degradation of Wind Turbine Rotor Blade Composites.* Ph.d., Delft University of Technology, 2006.

[62] M. A. Miner, "Cumulative Damage in Fatigue," *Journal of Applied Mechanics*, vol. 12, pp. A159–A164, 1945.

[63] P. E. Nikravesh, *Computer-aided Analysis of Mechanical Systems.* Englewood Cliffs, New Jersey: Prentice Hall, 1987.

[64] D. Vlasenko and R. Kasper, "Spatial Kinematics of Gears in Absolute Coordinates," in *Proceedings of Industrial Simulation Conference*, 2009.

[65] M. F. Jø rgensen, N. L. Pedersen, J. N. Sø rensen, and U. S. Paulsen, "Rigid MATLAB drivetrain model of a 500 kW wind turbine for predicting maximum gear tooth stresses in a planetary gearbox using multibody gear constraints," *Wind Energy*, vol. 2, 2013.

[66] Y. Guo and R. G. Parker, "Sensitivity of General Compound Planetary Gear Natural Frequencies and Vibration Modes to Model Parameters," *Journal of Vibration and Acoustics*, vol. 132, no. 1, p. 011006, 2010.

[67] Y. Guo, *Multi-body and Nonlinear Dynamics of Planetary Gear Drivetrains Considering Bearing Clearance and Acoustics*. Ph.d., Ohio State University, 2011.

[68] D. Qin, J. Wang, and T. C. Lim, "Flexible Multibody Dynamic Modeling of a Horizontal Wind Turbine Drivetrain System," *Journal of Mechanical Design*, vol. 131, no. 11, p. 114501, 2009.

[69] R. Pedersen, *Gearboxes and Experimental Validation*. Ph.d., Technical University of Denmark, 2010.

[70] D. Qin, J. Wang, and T. C. Lim, "Flexible Multibody Dynamic Modeling of a Horizontal Wind Turbine Drivetrain System," *Journal of Mechanical Design*, vol. 131, no. 11, p. 114501, 2009.

[71] D. Ji, Y. Song, and J. Zhang, "Dynamics of the Gear Train Set in Wind Turbine," *Materials Science Forum*, vol. 697-698, pp. 701–705, Sept. 2012.

[72] J. Rao, T. Shiau, and J. Chang, "Theoretical analysis of lateral response due to torsional excitation of geared rotors," *Mechanism and Machine Theory*, vol. 33, pp. 761–783, Aug. 1998.

[73] M. I. Friswell, J. E. T. Penny, S. D. Garvey, and A. W. Lees, *Dynamics of Rotating Machines*. New York, NY: Cambridge University Press, 2010.

[74] B. Ghalamchi, J. Sopanen, and A. Mikkola, "Simple and Versatile Dynamic Model of Spherical Roller Bearing," *International Journal of Rotating Machinery*, vol. 2013, pp. 1–13, 2013.

[75] T. C. Lim and R. Singh, "Vibration Transmission Through Rolling Element Bearings, Part I: Bearing Stiffness Formulation," *Journal of Sound and Vibration*, vol. 139, no. 2, pp. 179–199, 1990.

[76] H. Link, J. Keller, and Y. Guo, "Gearbox Reliability Collaborative Phase 3 Gearbox 2 Test Plan," Tech. Rep. April, National Renewable Energy Laboratory, Golden, CO, 2013.

[77] A. D. Hansen and G. Michalke, "Multi-pole permanent magnet synchronous generator wind turbines' grid support capability in uninterrupted operation during grid faults," *IET Renewable Power Generation*, vol. 3, no. 3, p. 333, 2009.

[78] A. M. Hemeida, W. A. Farag, and O. A. Mahgoub, "Modeling and Control of Direct Driven PMSG for Ultra Large Wind Turbines," *Worlk Academy of Science*, vol. 59, pp. 918–924, 2011.

[79] R. Melício, V. M. F. Mendes, and J. a. P. S. Catalão, "Wind Turbines with Permanent Magnet Synchronous Generator and Full-Power Converter: Modelling, Control and Simulation," *IREE*, vol. 5, no. 2, 2010.

[80] F. Oyague, "Progressive Dynamical Drive Train Modeling as Part of NREL Gearbox Reliability Collaborative Preprint," in *WINDPOWER 2008 Conference and Exhibition. Houston, Texas.*, no. July, 2008.

[81] Y. Guo, J. Keller, and W. Lacava, "Planetary gear load sharing of wind turbine drivetrains subjected to non-torque loads," *Wind Energy*, 2014.

[82] J. Wang, Y. Wang, and Z. Huo, "Analysis of dynamic behavior of multiple-stage planetary gear train used in wind driven generator.," *The Scientific World Journal*, Jan. 2014.

[83] A. M. Hansen, F. Rasmussen, and T. J. Larsen, "Gearbox loads caused by double contact simulated with," in *EWEC 2011*, (Brussels), 2011.

[84] J. G. Holierhoek, D. J. Lekou, T. Hecquet, H. Söker, and B. Ehlers, "PROcedures for TESTing and measuring wind turbine components ; results for yaw and pitch system and drive train," *Wind Energy*, no. July 2012, pp. 827–843, 2013.

[85] M. H. Hansen and L. C. Henriksen, "Basic DTU Wind Energy controller," Tech. Rep. January, DTU Wind Energy, Roskilde, Denmark, 2013.

[86] A. R. Nejad, Z. Gao, and T. Moan, "Long-term Analysis of Gear Loads in Fixed Offshore Wind Turbines Considering Ultimate Operational Loadings," *Energy Procedia*, vol. 35, pp. 187–197, Jan. 2013.

[87] E. Muljadi, N. Samaan, V. Gevorgian, J. Li, and S. Pasupulati, "Different factors affecting short circuit behavior of a wind power plant," *IEEE Transactions on Industry Applications*, vol. 49, no. 1, pp. 284–292, 2013.

[88] E. Muljadi and Y. C. Zhang, "Wind Power Plant Voltage Stability Evaluation Preprint," in *International Conference on Wind Energy Grid-adaptive Technologies*, (Jeju, Korea), 2014.

[89] A. D. Hansen and G. Michalke, "Fault ride-through capability of DFIG wind turbines," *Renewable Energy*, vol. 32, pp. 1594–1610, July 2007.

[90] M. Singh, E. Muljadi, and V. Gevorgian, "Test cases for wind power plant dynamic models on real-time digital simulator," *2012 IEEE Power Electronics and Machines in Wind Applications*, no. June, pp. 1–7, 2012.

[91] G. Ramtharan, N. Jenkins, O. Anaya-lara, and E. Bossanyi, "Influence of Rotor Structural Dynamics Representations on the Electrical Transient Performance of FSIG and DFIG Wind Turbines," *Wind Energy*, vol. 10, no. March, pp. 293–301, 2007.

[92] A. D. Hansen, N. A. Cutululis, H. Markou, and P. E. Sø rensen, "Impact of fault ride-through requirements on fixed-speed wind turbine structural loads," *Wind Energy*, vol. 14, no. April 2010, pp. 1–11, 2011.

[93] DIgSilent GmbH, "PowerFactory 15.1," 2014.

[94] B. Barahona, N. A. Cutululis, A. D. Hansen, and P. Sø rensen, "Unbalanced voltage faults: the impact on structural loads of doubly fed asynchronous generator wind turbines," *Wind Energy*, no. June 2013, pp. 1123–1135, 2014.

[95] I. P. Girsang, S. Member, J. S. Dhupia, E. Muljadi, M. Singh, and J. Jonkman, "Modeling and Control to Mitigate Resonant Load in Variable-Speed Wind Turbine Drivetrain," *IEEE Journal of Emerging and Selected Topics in Power Electronics*, vol. 1, no. 4, pp. 277–286, 2013.

[96] I. P. Girsang, J. Dhupia, M. Singh, V. Gevorgian, E. Muljadi, and J. Jonkman, "Impacts of Providing Inertial Response on Dynamic Loads of Wind Turbine Drivetrains Preprint," in *IEEE Energy Conversion Congress and Exposition*, no. September, (Pittsburgh, Pennsylvania), 2014.

[97] P. C. Krause, O. Wasynczuk, S. D. Sudhoff, and I. P. E. Society, *Analysis of electric machinery and drive systems*. IEEE Press, 2002, 2 ed., 2002.

[98] O. Anaya-Lara, X. Wu, P. Cartwright, J. Ekanayake, and N. Jenkins, "Performance of doubly fed induction generators (DFIG) during network faults," vol. 29, no. 1, pp. 49–66, 2005.

[99] J. B. Ekanayake, S. Member, L. Holdsworth, X. Wu, and N. Jenkins, "Dynamic Modeling of Doubly Fed Induction Generator Wind Turbines," *IEEE Transactions on Power Systems*, vol. 18, no. 2, pp. 803–809, 2003.

[100] P. Sø rensen, A. D. Hansen, T. Lund, and H. Bindner, "Reduced Models of Doubly Fed Induction Generator System for Wind Turbine Simulations," *Wind Energy*, vol. 9, no. October 2005, pp. 299–311, 2006.

[101] C. L. Bottasso, a. Croce, and C. E. D. Riboldi, "Optimal shutdown management," *Journal of Physics: Conference Series*, vol. 524, p. 012050, 2014.

[102] K. G. e. a. Scott, "Effects of Extreme and Transient Loads on Wind Turbine Drive Trains," in *50th AIAA Aerospace Science Meeting including the New horizons Forum and Aerospace Exposition*, (Nashville, Tennessee), pp. 1–24, 2012.

[103] D. Dabrowski and A. Natarajan, "Assessment of Gearbox Operational Loads and Reliability under High Mean Wind Speeds," *Submitted to Energy Procedia*, 2015.

[104] M. Singh, V. Gevorgian, E. Muljadi, and E. Ela, "Variable-speed wind power plant operating with reserve power capability," *2013 IEEE Energy Conversion Congress and Exposition, ECCE 2013*, no. October, pp. 3305–3310, 2013.

[105] A. R. Nejad, Z. Gao, and T. Moan, "On long-term fatigue damage and reliability analysis of gears under wind loads in offshore wind turbine drivetrains," *International Journal of Fatigue*, vol. 61, pp. 116–128, Apr. 2014.

[106] J. V. D. Tempel and D.-p. Molenaar, "Wind Turbine Structural Dynamics – A Review of the Principles for Modern Power Generation, Onshore and Offshore," *Wind Engineering*, vol. 26, no. 4, pp. 211–220, 2002.

[107] Det Norske Veritas, "Guideline for Offshore Structural Analysis: Application to Jackets Platforms," tech. rep., DNV, Høvik, Norway, 1996.

[108] DIN, "Calculation of load capacity of cylindrical gears," tech. rep., Deutsches Institut für Normung DIN 3990, 1987.

[109] A. Kahraman, "Free torsional vibration characteristics of compound planetary gear sets," *Mechanism and Machine Theory*, vol. 36, pp. 953–971, Aug. 2001.

[110] A. D. Hansen and G. Michalke, "Modelling and control of variable-speed multi-pole permanent magnet synchronous generator wind turbine," *Wind Energy*, vol. 11, pp. 537–554, Sept. 2008.